

B0 Shimming of the Human Brain at Ultrahigh Field MRI
with a Multi-Coil Shim Setup

Dissertation

zur Erlangung des Grades eines
Doktors der Naturwissenschaften

der Mathematisch-Naturwissenschaftlichen Fakultät
und
der Medizinischen Fakultät
der Eberhard-Karls-Universität Tübingen

vorgelegt

von

Ali Aghaeifar
aus *Naghadeh, Iran*

May – 2019

Tag der mündlichen Prüfung: 16.10.2019

Dekan der Math.-Nat. Fakultät:

Prof. Dr. W. Rosenstiel

Dekan der Medizinischen Fakultät:

Prof. Dr. I. B. Autenrieth

1. Berichterstatter:

Prof. Dr. Klaus Scheffler

2. Berichterstatter:

Prof. Dr. Fritz Schick

Prüfungskommission:

Prof. Dr. Klaus Scheffler

Prof. Dr. Fritz Schick

Prof. Dr. Wolfgang Grodd

PD. Dr. Maxim Zaitsev

Erklärung / Declaration:

Ich erkläre, dass ich die zur Promotion eingereichte Arbeit mit dem Titel:

„B0 Shimming of the Human Brain at Ultrahigh Field MRI with a Multi-Coil Shim Setup“

selbständig verfasst, nur die angegebenen Quellen und Hilfsmittel benutzt und wörtlich oder inhaltlich übernommene Stellen als solche gekennzeichnet habe. Ich versichere an Eides statt, dass diese Angaben wahr sind und dass ich nichts verschwiegen habe. Mir ist bekannt, dass die falsche Abgabe einer Versicherung an Eides statt mit Freiheitsstrafe bis zu drei Jahren oder mit Geldstrafe bestraft wird.

I hereby declare that I have produced the work entitled “B0 Shimming of the Human Brain at Ultrahigh Field MRI with a Multi-Coil Shim Setup”, submitted for the award of a doctorate, on my own (without external help), have used only the sources and aids indicated and have marked passages included from other works, whether verbatim or in content, as such. I swear upon oath that these statements are true and that I have not concealed anything. I am aware that making a false declaration under oath is punishable by a term of imprisonment of up to three years or by a fine.

Tübingen, den

Datum / Date

Unterschrift /Signature

Summary

Magnetic resonance imaging (MRI) is widely used for contemporary diagnostics and research. Higher static magnetic field enables imaging with a higher resolution because of the increased signal-to-noise-ratio in comparison to low field MRI. However, this benefit is not cost-free. Less B_1^+ field uniformity, higher B_0 inhomogeneity, higher specific absorption rate (SAR), and shortened T_2 and T_2^* are some of the challenges of measurement at ultrahigh-field (UHF). The aim of this thesis is to address higher B_0 inhomogeneity at a magnet with a strength of 9.4 tesla. To this end, the shimming hardware and software required for homogenization of the B_0 field were designed, and the performance of the constructed setups has been validated by simulation and in vivo measurements.

The first part of the thesis (Chapter 1) describes the source of B_0 inhomogeneity, how it changes the FID signal, its consequences, and why UHF intensifies the B_0 inhomogeneity. Then, the process of field homogenization, known as shimming, is introduced, and shimming with spherical harmonics is explained. Next, the standard method for B_0 field measurement and inhomogeneity quantification is presented, and least squares minimization is described in order to optimal currents calculation for a constrained shimming. Then, dynamic slice-wise shimming is introduced as an approach to achieve a better B_0 uniformity by breaking VOI to sub-volumes. Finally, the multi-coil shim setup is presented which benefits from small local coils for a more efficient shimming.

The second part of the thesis (Chapter 2) focuses on construction and application of multi-coil shim setup as achievements of this thesis. First, the construction process of the setup and comparison with spherical harmonic basis sets are provided. Later, the impact of the improved B_0 uniformity with the dynamic multi-coil shimming on fMRI contrast is studied. Finally, a novel multi-coil design approach is presented in which a multi-coil shim setup is optimized for shimming of the human brain. Sections 3.4 and 3.5 present a summary of the collaborations in other related projects. First, a novel method to design the shim coils' wiring pattern based on stream function is introduced which allows higher order shimming with limited number of the coils to be achieved.

Next, an application of the small local coils for parallel imaging is demonstrated. Small local coils are employed for a local modulation of the magnetic field and superimpose a unique phase variation to the spin distribution that can be used to disentangle different part of the object.

The last part of the thesis starts with conclusions and outlook. Later, the resultant publications are listed, and the relevant publications are appended at the end.

Contents

1	Introduction	1
1.1	MRI Basics.....	1
1.2	Shimming Basics	4
1.3	Dynamic Slice-wise Shimming.....	9
1.4	Multi-Coil Method	10
2	Summary of Publications	12
2.1	Publication 1: A 16-Channel Multi-Coil Shim Setup.....	12
2.2	Publication 2: Shimming Impact on Functional MRI.....	16
2.3	Publication 3: A 32-Channel Optimized Multi-Coil.....	19
2.4	Publication 4: A Shim Array Based on Brain Anatomy	23
2.5	Publication 5: Beyond B_0 Shimming	25
3	Conclusions and Outlook	27
4	Acknowledgments	29
5	References	30
6	List of Publications	34
6.1	Appended Publications	34
6.2	Other Recent Publications.....	34
6.2.1	Journal Articles	34
6.2.2	Talks	35

6.2.3	Posters	36
7	Statement of Contributions	39
7.1	Dynamic B0 shimming of the human brain at 9.4T with a 16-channel multi-coil shim setup	39
7.2	Dynamic B0 shimming of the motor cortex and cerebellum with a multi-coil shim setup for BOLD fMRI at 9.4T.....	39
7.3	A 32-channel multi-coil setup optimized for the human brain shimming at 9.4T.	40
7.4	Design of a shim coil array matched to the human brain anatomy.....	40
7.5	Spread-Spectrum Magnetic Resonance Imaging	40
8	Appended Publications	41

List of Figures

1. Examples of artifacts induced by inhomogeneities in static field. A) Reference shimmed image acquired with FLASH sequence. B) Inhomogeneity in slice selection direction causes shift of the slice and signal loss. C) Inhomogeneity in frequency encoding direction shrinks or stretches image. D) Inhomogeneity in phase encoding direction causes shearing in the image plane. E) Global off-resonance offset results in image shift. F) B_0 inhomogeneity results in distortions in EPI..... 2
2. Graphic of the spherical harmonic functions up to third order..... 5
3. Schematic diagram of monopolar triple-echo GRE sequence 8
4. Comparison of static global and dynamic slice-wise shimming of the human brain in simulation for different spherical harmonic shim orders. B_0 map of the human brain is acquired at 9.4T MR scanner. Standard deviation of off-resonance is provided as a performance benchmark..... 10
5. A) Photograph of the 16-channel multi-coil shim array. B) Schematic of the employed setup designed in CATIA. C) Photograph of the completely assembled setup with the chassis used to fix the setup in the patient table 12
6. Visualization of the magnetic field produced by 16-channel multi-coil shim setup 13
7. Comparison of the observed geometric distortions for EPI acquisition when shimming is performed with global 2nd order spherical harmonics (gSH), global multi-coil shimming (gMC), and dynamic multi-coil shimming (dMC) 15
8. Histogram of voxels with t-value between 2 and 16 during the breath holding task. While the number of voxels with a lower level of significance decreased, the number of voxels with a higher t-value increased when a large portion of B_0 uniformity was compensated by dynamic multi-coil shimming 18
9. A) The arrangement of the coils on the cylinder surface after optimization. B) Experimental realization of the optimized 32-channel multi-coil..... 20
10. Comparison of the simulated shimming performance between optimized multi-coil, multi-coils with a different number of coils, and spherical harmonics basis set. Shimming is carried out in global and dynamic slice-wise fashion while the current is constrained and unconstrained. Only unconstrained shimming with spherical harmonics is performed since the sensitivity maps are not available. The shimming is performed on 14 brain B_0 maps which were acquired at 9.4T..... 22

11. Effect of the improved B_0 homogeneity with optimized 32-channel multi-coil on banding artifacts in bSSFP images	22
12. A) An example of the current density map for the largest singular value. B) The current density map in (A) is transformed into a plane. C) Corresponding wiring pattern of the current density map shown in (B).....	24

1 Introduction

1.1 MRI Basics

A nucleus with a non-zero spin quantum number is NMR-active and, in the presence of an external magnetic field \vec{B} , its spins start to align (parallel or antiparallel) and precess along \vec{B} . The precession frequency, known as the Larmor frequency, can be explained by the gyromagnetic ratio (γ) of the nucleus and the magnetic field strength (B_0) via the following equation:

$$f = \frac{\gamma}{2\pi} B_0 \quad (1)$$

The Larmor equation is an important fundamental equation in MR imaging and shows that the precession frequency varies for different nuclei and scales with the magnetic field. The spatial selection and encoding employed in MR imaging are based on the manipulation of the precession frequency. Accordingly, it is essential to have a homogenous magnetic field in the region of interest in order to avoid an unwanted shift in Larmor frequency. In practice, however, spins in an object may precess within a range of frequencies due to static field inhomogeneities.

There are several well-known adverse effects that arise from B_0 inhomogeneities. The effects' form and severity depend on the employed sequence. For MR spectroscopy, field inhomogeneities broaden the spectral linewidth and degrade water suppression quality which results in unreliable spectrum quantification and detection of fewer metabolites [1]. For MR imaging, B_0 inhomogeneity affects the spatial encoding and, therefore, causes distortions and misregistration [2]. Additionally, significant intravoxel dephasing in the local intense inhomogeneities may void the signal completely. Gradient echo planar imaging (EPI) is one of the most sensitive sequences to the B_0 inhomogeneity due to its long echo time. EPI images typically have areas with distortion or signal loss that are influenced by magnetic field inhomogeneity [3]. Some of the consequences

of the B_0 inhomogeneity are depicted in Figure 1. Equation (2) mathematically explains how off-resonance modifies the phase evolution of the MR signal, which leads to the subsequent artifacts.

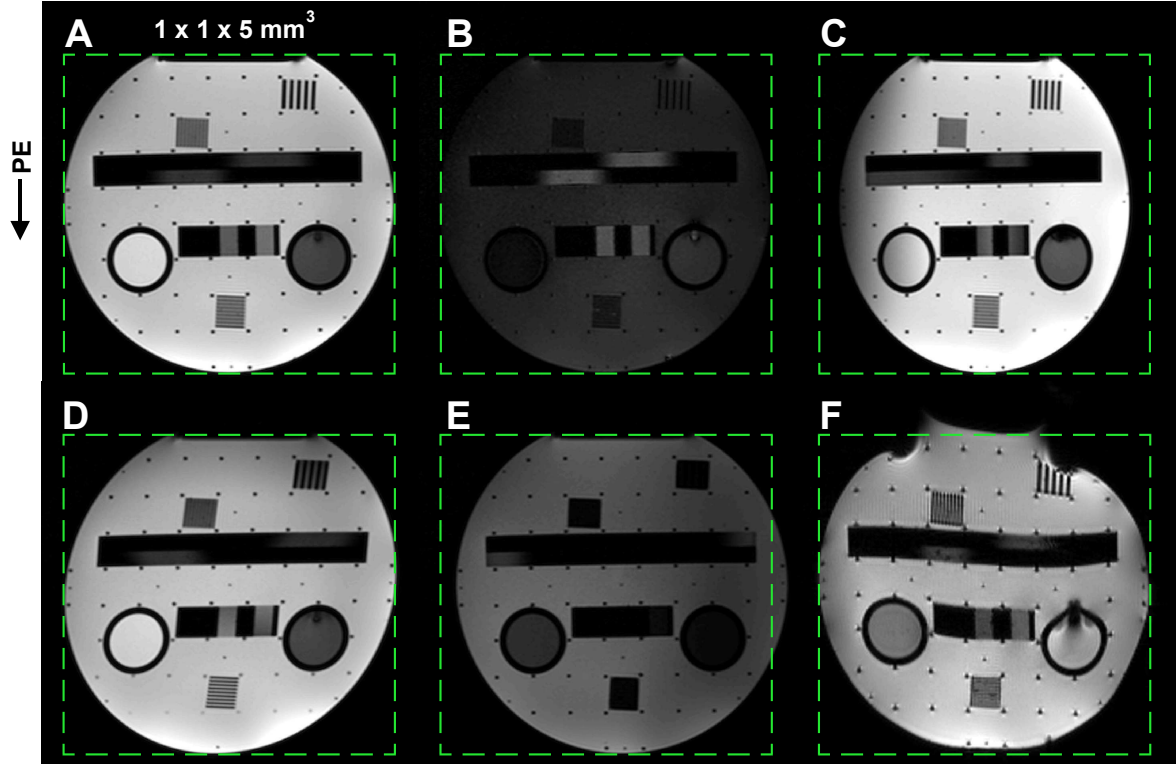


Figure 1. Examples of artifacts induced by inhomogeneities in static field. A) Reference shimmed image acquired with FLASH sequence. B) Inhomogeneity in slice selection direction causes shift of the slice and signal loss. C) Inhomogeneity in frequency encoding direction shrinks or stretches image. D) Inhomogeneity in phase encoding direction causes shearing in the image plane. E) Global off-resonance offset results in image shift. F) B_0 inhomogeneity results in distortions in EPI.

$$S(t) = \iiint M_{xy}(x, y, z) e^{-i\gamma \int_0^t (G_x(\tau)x + G_y(\tau)y + G_z(\tau)z + \Delta B_0(x, y, z)) d\tau} dx dy dz \quad (2)$$

The field strength and its inhomogeneity are two important characteristics of a magnet. There are several sources that cause inhomogeneity in the static field that can be divided into two categories. First, magnet imperfection and some sources cause a constant perturbation in field homogeneity

(e.g. patient table, gradients and other large objects inside or close to the magnet). The second source of the inhomogeneity is the object undergoing an experiment. The perturbations originating from the objects are variable and can even be dynamic. They depend on the geometry and orientation of the object. The magnetic field inside a material placed in a homogenous magnetic field B_0 is given by

$$B_{sum} \approx (1 + \chi)B_0 \quad (3)$$

Where B_0 is the magnetic field in a vacuum and χ is the magnetic susceptibility. Equation (3) shows that the magnetic field inside the material can be slightly altered based on the sign and magnitude of the magnetic susceptibility.

From an NMR perspective, materials with negative and positive magnetic susceptibility are referred to as diamagnetic and paramagnetic, respectively. Most of the tissues are diamagnetic because water is diamagnetic ($\chi = -9.05 \text{ ppm}$). Air is a well-known paramagnetic material ($\chi = +0.36 \text{ ppm}$). The materials with a very large positive magnetic susceptibility are called ferromagnetic and are not generally MR-compatible. According to Equation (3), the magnetic field inside the body is smaller than the nominal value of the magnet strength but will not cause a large off-resonance. Magnetic field perturbations occur considerably at the boundaries, where two materials with different magnetic susceptibility meet. Having a map of the magnetic susceptibility, spatial magnetic field distribution can be calculated numerically based on fast Fourier transform [4] given by

$$\Delta B_z(r) = B_0 FT^{-1} \left\{ \left(\frac{1}{3} - \frac{k_z^2}{k_x^2 + k_y^2 + k_z^2} \right) FT(\Delta\chi(r)) \right\} \quad (4)$$

Where k indicates coordinates in k-space and FT and FT^{-1} are forward and inverse Fourier transformations, respectively. The Equation (4) indicates that field inhomogeneity originating from susceptibility differences scales with the magnetic field (i.e., stronger field inhomogeneity is expected when moving toward the higher static field).

1.2 Shimming Basics

In the context of the MRI, the term “shimming” describes the process of static field homogenization in a volume of interest. After measuring the field inhomogeneity, the goal becomes the generation of a magnetic field with an opposite sign that cancels out the field perturbations. The question of the extent to which the static field should be homogenized is still open; however, the efforts are toward minimizing the inhomogeneity with the available solutions (i.e., hardware and algorithms). After magnet installation, the passive shimming is performed through strategic placement of the ferromagnetic pieces in the bore of the magnet to reduce field inhomogeneities caused by magnet imperfection and surrounding objects. This is a one-time procedure and will remain fixed, and users cannot change it. There is another level of the shimming with active elements to create an additional magnetic field which superimposed to the static B_0 field. The active shimming is performed by passing currents into inductive coils to generate a magnetic field which can be explained through Biot-savart law. The strength of the produced field can be adjusted by altering the amount of current fed into the coils that make it flexible to adapt for different patterns of inhomogeneities. The problem of the shimming with the active elements (shim coils) can be described as follows:

$$B_{0,shimmed} = B_0(x, y, z) - \sum_{n=1}^{\infty} C_n F_n(x, y, z) \quad (5)$$

Where $F_n(x, y, z)$ is basis shim function and C_n represents the current which should be calculated. A variety of the basis sets are available for $F_n(x, y, z)$, but the suitable one should satisfy orthogonality and be experimentally feasible to construct in a cylindrical geometry. Hence, the solution of the Laplace’s equation for the magnetic field $\nabla^2 B_0 = 0$ (i.e. spherical harmonics) is chosen and can be expressed in Cartesian coordinates system by

$$\Delta B_0(x, y, z) = B_{0,offset} + \sum_{n=1}^{\infty} \sum_{m=0}^n C_{n,m} F_{n,m}(x, y, z) \quad (6)$$

Here, $C_{n,m}$ is constant, $F_{n,m}$ is given in Table 1 up to $n=3$ and graphically depicted in Figure 2, and n and m are order and degree of spherical harmonics, respectively. Most clinical scanners are equipped with a shim system that can generate spherical harmonics up to the second order.

Table 1. Shim terms for spherical harmonics up to third order

Order n	Degree m	F(x,y,z)	Common name
0	0	1	Z0
1	0	z	Z
1	1	x	X
1	-1	-y	Y
2	0	$2z^2-(x^2+y^2)$	Z2
2	1	zx	ZX
2	-1	-zy	ZY
2	2	x^2-y^2	C2
2	-2	-xy	S2
3	0	$2z^3-3z(x^2+y^2)$	Z3
3	1	$4z^2x-x(x^2+y^2)$	Z2X
3	-1	$-4z^2y+y(x^2+y^2)$	Z2Y
3	2	$z(x^2-y^2)$	ZC2
3	-2	-zxy	ZS2
3	3	$x(x^2-3y^2)$	X3
3	-3	$y(y^2-3x^2)$	Y3

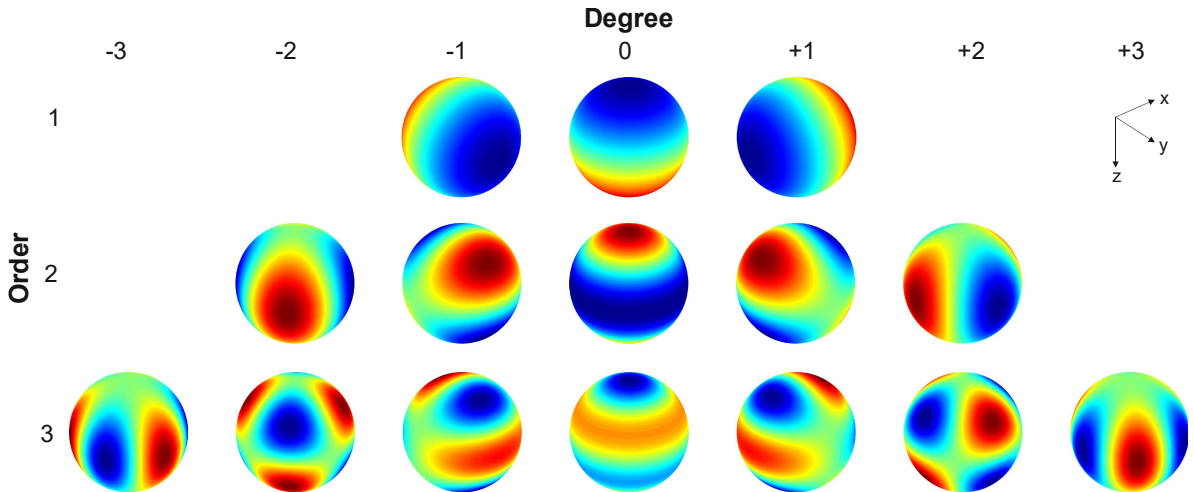


Figure 2. Graphic of the spherical harmonic functions up to third order

Having a controllable shim setup, the next important step will be the characterization of the current magnetic field distribution. The field inhomogeneity should be quantified first in terms of the volume of the interest by magnetic field mapping in order to find a proper scaling of the shim basis sets. It is possible to use an array of NMR field sensors to measure the magnetic field at a variety of spatial positions [5]. Even though the field sensors are a suitable choice to capture the field dynamic and give a high temporal resolution, the spatial resolution of the quantification is limited to the array size. Measurement of the field distribution can be also accomplished by employing a proper pulse sequence and processing the acquired signal. Among several existing pulse sequences, the gradient-recalled-echo (GRE) sequence with multiple echoes is the method of choice for routine usage due to reasonable running time and sufficiently accurate quantification [2]. The GRE-based field mapping acquires two or more images at distinct echo times, i.e. at TE , $TE + \tau_1$, $TE + \tau_2$ (Figure 3). Each echo gives a different T_2^* weighting image in which the phase difference of two images ($\Delta\varphi$) reflects the strength of inhomogeneity. The phase difference can be transformed to off-resonance map in the unit of Hertz as follows:

$$\Delta B_0 = \frac{\text{angle}(I_{echo\ n} * \text{conj}(I_{echo\ m}))}{2\pi(TE_{echo\ n} - TE_{echo\ m})} = \frac{\Delta\varphi}{2\pi\Delta TE} \quad (7)$$

Where $I_{echo\ n}$ is the complex image obtained from n^{th} echo. A perfect homogenous field results in an equal phase for all the echoes and, accordingly, the $\Delta\varphi$ and ΔB_0 will be zero. An additional phase will be accumulated for a voxel with an off-resonance. Increasing ΔTE will cause a larger phase difference and higher sensitivity. At a minimum, two echoes are sufficient for the field mapping; however, more echoes can help facilitate temporal phase unwrapping in the areas with a pronounced off-resonance.

Calculation of the currents required to feed into the current amplifiers will be straightforward after acquiring the ΔB_0 map and basis-set of the shim coils. The solution of the closed-form expression of the shimming problem which is provided in Equation (5) is as follows

$$\Delta B_0(x, y, z) + C * F(x, y, z) = 0 \quad (8)$$

$$* F(x, y, z) * F(x, y, z)^T = -\Delta B_0(x, y, z) * F(x, y, z)^T \quad (9)$$

$$C = -\Delta B_0(x, y, z) * F(x, y, z)^T * (F(x, y, z) * F(x, y, z)^T)^{-1} \quad (10)$$

$$C = -\Delta B_0(x, y, z) * F^\dagger(x, y, z) \quad (11)$$

Where C is the required currents for the amplifiers, $F(x,y,z)$ is the basis-map of the shim coils (the generated magnetic field while 1A is passed into the single coil), and $F^\dagger(x,y,z)$ is the pseudo-inverse of the matrix $F(x,y,z)$. The unconstrained pseudo-inverse approach theoretically yields the best achievable shimming quality; however, the calculated currents are not always feasible to produce due to the current amplifier limitations or heating issue. The unconstrained shimming typically does not exceed the amplifiers' supported range for shimming of the large VOI like the whole brain, but it is more probable to occur for smaller VOI like a single slice. Thus, an alternative approach must be used, one that can take the amplifier restrictions into account. To this end, the shimming problem can be framed as an ordinary least square problem as follows

$$\sum_{v_i \in V} \left[\Delta B_0(v) + \sum_{n=1}^N C_n F_n(v) \right]^2 \quad (12)$$

Where N is the total number of shim coils, and v_i includes the set of voxels in the VOI. The optimal current can be determined through least squares minimization given by

$$\min_C \|\Delta B_0 + CF\|^2 \quad lb \leq C \leq ub \quad (13)$$

Where C is a $I \times N$ row vector bounded between lb ($I \times N$ lower bound) and ub ($I \times N$ upper bound) and N is the overall number of shim coils. ΔB_0 and F are a $I \times V$ vector and an $N \times V$ matrix, respectively and V is the total number of the voxels in the VOI. As the problem can be rephrased to the quadratic form and quadratic problems are convex, the problem therefore has a unique solution that is the global minimum (i.e. regardless of the given starting point, it must converge to the identical results).

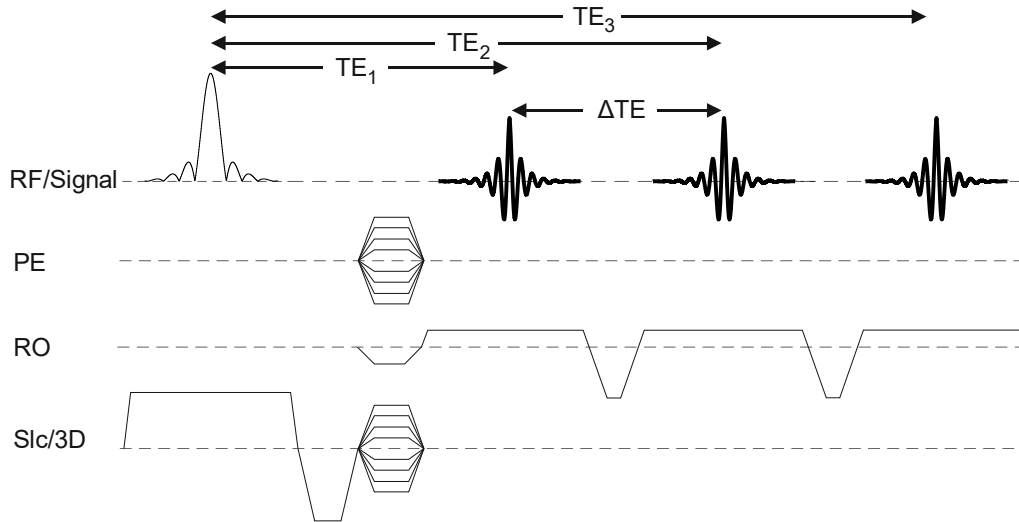


Figure 3. Schematic diagram of monopolar triple-echo GRE sequence

MR imaging at higher field benefits from higher signal-to-noise (SNR). Higher SNR mainly allows for higher image resolution. However, the B_0 field inhomogeneity originated from magnetic susceptibility differences scales with B_0 field, as well. In the human brain, the proximity of the tissue with air in ear canals, sinuses, and nasal cavities results in a severe local B_0 perturbation. The inhomogeneity exceeds 500 Hz in the frontal cortex of the human brain at the magnet with a strength of 9.4T which is target field of this thesis. The standard deviation of inhomogeneity for the whole brain at 9.4T (on average ≈ 80 Hz) is much higher compared to clinical 3T MR scanners (≈ 25 Hz), and the conventional static 2nd order shimming does not satisfy the requirements of some applications at 9.4T. In conventional static shimming, the scanner's 2nd order shim setup is adjusted once for the whole brain and remains fixed during the entire study. Furthermore, inhomogeneity can be correlated with respiration and motion. Literature reported small head movement at 7T leads to field variation of about 10Hz which will be even stronger at 9.4T. In any case, the scope of this thesis is not to resolve the issue of the dynamic field alteration; it does, however, nonetheless exist and affect the measurements, but is negligible in comparison to the susceptibility induced fluctuations.

1.3 Dynamic Slice-wise Shimming

The performance of the static shimming with the scanner's built-in 2nd order setup is not adequate for the sequences susceptible to the B_0 inhomogeneity, and improving the shimming quality is essential. One solution would be to break the VOI to smaller independent sub-volumes which is the principle parts of the dynamic shimming [6]. Due to the fact that the shimming volume decreases, it is typically simpler to approximate field inhomogeneity with a fewer shim coils (e.g. there are only eight channels for 2nd order shim). In MR imaging, all 2D sequences are capable of benefiting dynamic shimming because signal is not acquired from the entire VOI, but rather from just a single slice. This method can be used for multi-voxel experiments or even multi-slab 3D sequences, as well. A comparison of shimming performance between static global and dynamic slice-wise shimming is depicted in Figure 4. Lower order dynamic slice-wise shimming yield a similar result of higher order static global shimming.

Employing dynamic shim update (DSU), the optimal shim settings are required to be calculated for individual slices using equation (13). The current amplifiers are synchronized with the sequence to update the shim during the measurement. A trigger signal (usually a TTL pulse) from the sequence commands the amplifiers to update the shim setting's prior measurement of the next slice and thereby provide an optimal field homogeneity for the slice undergoing the excitation. Utilizing DSU greatly reduces the magnetic field inhomogeneity and always delivers an enhanced field homogeneity compared to the static global shimming. However, there are some challenges for the experimental realization of DSU that must be taken into account.

The synchronization signal is sent out before the onset of the next RF pulse, and there is a short dead zone between these two events. The amplifiers must update the shim and stabilize the currents feeding into the shim coils in the short interval between the trigger signal and the RF pulse. First, DSU requires powerful amplifiers capable of switching quickly between two states in a fraction of a millisecond. Second, and more importantly, rapid magnetic field alteration induces eddy currents in the surrounding conductive structures according to Faraday's law of induction. It is reported in the literature that induced eddy-current due to rapid switching of input for a channel of order n not only can generate another magnetic field similar to the same channel (self-term), but also orders

smaller than n (cross-terms) [6]. In other words, plenty of cross-terms can be formed for a higher order DSU. The eddy-current-induced magnetic fields can significantly perturb the static field and even degrade field homogeneity to a level worse than before. Even though these induced magnetic fields are temporary, they decay with time constants ranging from hundreds of milliseconds to a few seconds [6–8] and therefore must be characterized and minimized for DSU applications. There are several methods proposed to characterize the induced eddy currents [6,9,10]. Compensation circuits known as pre-emphasis are employed to counteract and reduce them. A full compensation of all self and cross terms needs to construct an $n \times n$ interaction matrix where n is the number of shim coils. This may require a large number of the pre-emphasis circuits, which experimentally are difficult to manage. Recent publications demonstrate successful implementation of pre-emphasis for DSU up to 3rd order, while weak interactions are excluded [9].

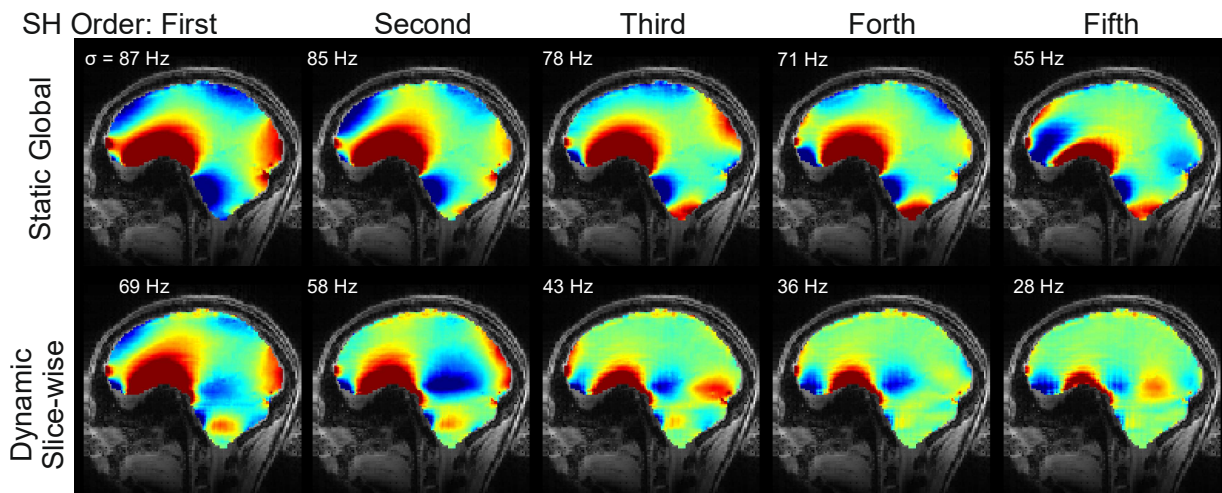


Figure 4. Comparison of static global and dynamic slice-wise shimming of the human brain in simulation for different spherical harmonic shim orders. B_0 map of the human brain is acquired at 9.4T MR scanner. Standard deviation of off-resonance is provided as a performance benchmark.

1.4 Multi-Coil Method

Although dynamic slice-wise shimming improves B_0 homogeneity, the remaining fluctuations after DSU at ultrahigh field are still much larger than static global shimming at lower fields ($\leq 3T$).

The need for a better shim encourages the use of higher order spherical harmonics, but there are a few restrictions that limit shimming with higher order spherical harmonics:

- The space limitations in the scanner's body does not permit the installation of many large shim coils
- Difficulties related to the design of a winding to generate perfect spherical harmonics in the desired diameter of spherical volume (DSV)
- Large inductance which leads to eddy-current induced magnetic fields

The demands for a better shim and the aforementioned limitations for spherical harmonic based shimming lead to the creation an approach called multi-coil shimming [11,12] which is the subject of this thesis. The multi-coil shimming method is an extended version of local active shim coils which were placed in the mouth cavity to mitigate signal loss in the frontal cortex [13,14]. The multi-coil shim setup benefits from an array of small and local coils, typically circular loops, which surround the brain or other organs. In comparison to spherical harmonics-based shimming, shim fields generated with multi-coil are not necessarily orthogonal and the coil size and the inductance are much smaller, and consequently less susceptible to the unwanted eddy currents.

Passing a current into the coils generates a magnetic field $B(r)$ at position r according to the Biot-savart law as follows:

$$B(r) = \frac{\mu_0}{4\pi} \int_C \frac{Idl \times \hat{r}}{|r|^2} \quad (14)$$

Where dl is a vector along the path C and \hat{r} is the unit vector of the r . The equation (14) shows that the produced magnetic field is proportional to the amount of applied current and inversely proportional to square of the distance to the coil. The geometry of the utilized coils is simple, typically square or circular, and the strength of the magnetic field is only high in vicinity of the loops and decreases rapidly when the distance is increased. Hence, it is advantageous to situate the coils as close as possible to the subject in order to avoid high power dissipation.

2 Summary of Publications

2.1 Publication 1: A 16-Channel Multi-Coil Shim Setup

In publication 1, it was demonstrated how a 16-channel multi-coil shim setup provides a superior field homogeneity at 9.4T for static and dynamic shimming of the human brain. The employed multi-coil (Figure 5) consisted of the 16 identical circular loops with 25 wire turns which were positioned symmetrically in two rows, each with 8 coils, on the surface of a cylinder with a diameter of 370 mm and length of 310 mm [15]. Each coil had a diameter of 100 mm and the coils formed two rows, each coil spaced 20 mm apart. The spatial map of the generated fields by the employed 16-channel multi-coil is depicted in Figure 6.

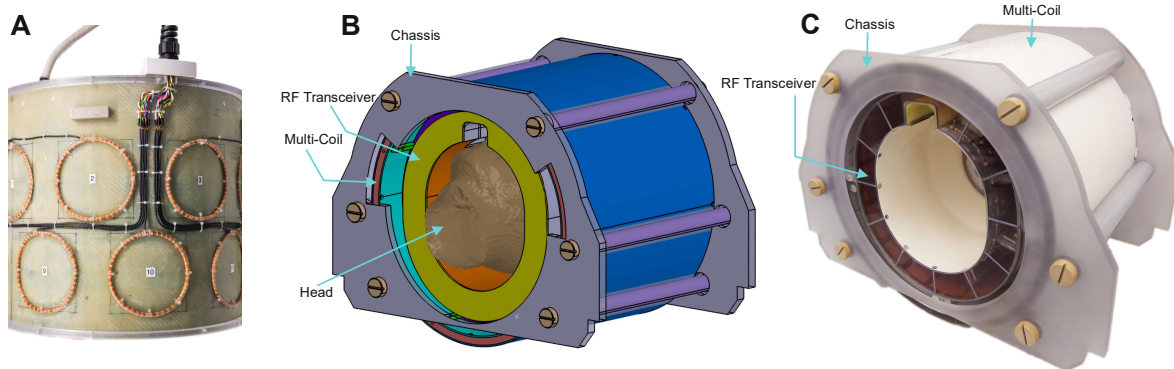


Figure 5. A) Photograph of the 16-channel multi-coil shim array. B) Schematic of the employed setup designed in CATIA. C) Photograph of the completely assembled setup with the chassis used to fix the setup in the patient table

Dedicated homemade current amplifiers were used to supply a current to individual coils (16 amplifiers in total for 16 coils) [16]. The amplifiers were capable of supplying a current up to 5A; however, the permitted current fed into the coils was constrained to $\pm 1.5A$ due to the heating issues and safety of the subjects. There was a 0.1Ω current sensitive resistor in series with the amplifiers' output in order to provide a current feedback. The feedback not only was used for output stabilization, but also provided an interface for online monitoring of the current floating in the coils. The current feedback along with the output voltage monitoring facilitate troubleshooting and

the fixing of failures. An adjustable proportional–integral–derivative (PID) controller was integrated into the amplifier to regulate output for a wide range of the inductive loads. The proper regulation settings enable amplifiers to suppress overshoots and minimize the settling time. The amplifiers were driven by analog signals generated by a PXIe-6738 digital to analog converter (DAC) module. At the user level, a custom-built graphical user interface (GUI) designed with LabVIEW (National Instruments, Austin, TX) controlled the DAC module. The linearity of the amplifiers’ output was evaluated by applying the currents from -2A to +2A in 17 steps and measuring the corresponding magnetic field generated. The linearity was determined by fitting a first-degree polynomial to the measured map and calculating the error. The mean of deviation from linearity was below 4Hz for the studied range, which was more than enough, and the additional amplifiers’ calibration was not necessary.

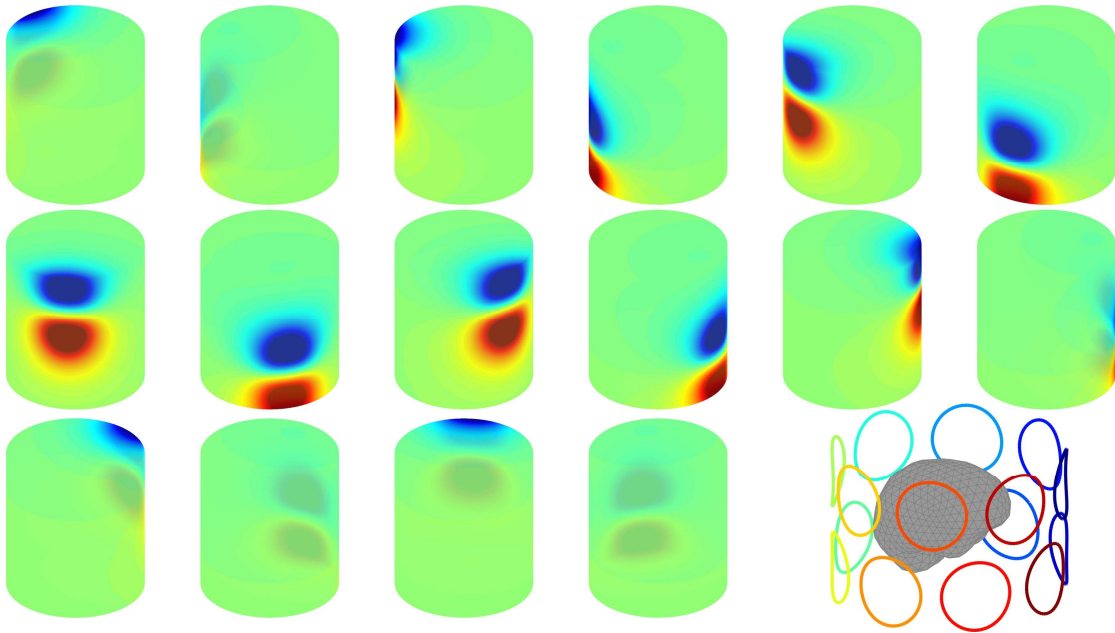


Figure 6. Visualization of the magnetic field produced by 16-channel multi-coil shim setup

In contrast to the setup proposed in the literature (in which the multi-coil is in inner layer relative to the RF coil [12]), the multi-coil is in outer layer in our design and covers the RF coil. This arrangement has two advantages. First, the RF transmit field will not be damped or altered. Second,

different RF coil can be mounted into the multi-coil house without a substantial modification. The entire setup was fixed in the patient table with a chassis to hinder setup vibration during the rapid switching. All of the studies were performed with 18 transmit/32 receive channels home-made shielded RF coil [17]. The shield eliminates interaction between the multi-coil and RF coil.

A custom-built interface was programmed in MATLAB for the required calculations and evaluations. Then, the process of the shimming consists of the following steps:

- 1) Shim coils basis-map measurement (only once for all the studies)
- 2) Whole brain shimming with the scanner's 2nd order shim setup
- 3) Measurement of brain B_0 map
- 4) Apply equation (13) in dynamic or static fashion and save the shim settings
- 5) Measure B_0 map while shimming is being performed with multi-coil
- 6) Compare the measurement from step 5 with the simulation from step 4

All of the sequences requiring dynamic shimming were modified to enable broadcasting the synchronization signal. In our design, synchronization is implemented through transmitting commands via UDP protocol. The commands include information about the next slice undergoing the acquisition and the corresponding shim settings. The shim settings are imported from a text file during the sequence preparation step and sent out a few milliseconds (the exact timer period can be adjusted by the user) before the next RF pulse. On the other side, the LabVIEW program listening to the network receives the commands and immediately updates the current amplifiers. Ramp up and ramp down timing is adjustable through the implemented multistep transition between two states. Faster transition leads to stronger vibration.

The performance of the multi-coil setup can be compared with spherical harmonics with different orders or even with other multi-coils with different numbers or arrangements of the coils. The efficiency can also depend on the shimming ROI (i.e. size, position and orientation of the volume). The basis-sets for the spherical harmonics are analytically computed while those of the multi-coil are experimentally measured. For a fair and true comparison, the 16-channel multi-coil setup was compared with a 28-channel insert-shim (Resonance Research Inc, Billerica, MA). The insert-shim consisted of the full to 4th and partial 5th and 6th order spherical harmonics terms;

however, only up to the full 4th order was used for the comparison. The data acquisition was then performed with various sequences with two different shimming strategies and the results were compared [18,19].

As an application, EPI sequence was employed to evaluate shimming performance. EPI is susceptible to geometric distortion because of long readout. Improving the B₀ homogeneity yields a less distortion in EPI. An anatomy scan was acquired as a reference distortion-free image. Figure 7 shows the amount of distortion in EPI after different shimming strategies with the corresponding B₀ maps.

As previously noted, an important advantage of a multi-coil setup over a spherical harmonics-based approach is the small coil size. Small coil size and, accordingly, smaller inductance not only allows for fast switching with a low-cost amplifier but also diminishes coupling between coils. Lower coupling between two inductors leads to less eddy-current induction. Although experimental DSU measurements with a multi-coil showed no artifacts in the images, the behavior of the setup was characterized by spatiotemporal magnetic field monitoring. To this end, a step input was applied to the individual channels and the field swing was monitored with ¹⁹F field probes. No oscillation was observed in the range of the field probes' sensitivity.

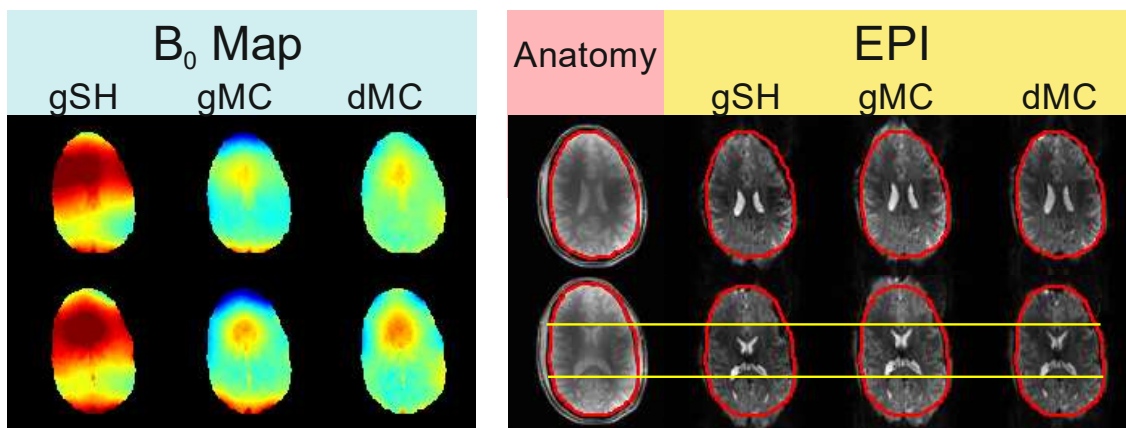


Figure 7. Comparison of the observed geometric distortions for EPI acquisition when shimming is performed with global 2nd order spherical harmonics (gSH), global multi-coil shimming (gMC), and dynamic multi-coil shimming (dMC)

2.2 Publication 2: Shimming Impact on Functional MRI

SNR enhancement at ultrahigh field improves sensitivity to detect blood oxygenation level dependent (BOLD) signal change [20]. Echo planar imaging (EPI) as a T_2^* -weighted sequence has a high sensitivity to BOLD signal and is the sequence of the choice in most fMRI applications. However, long readout in EPI makes it susceptible to geometric distortions and signal loss, which originates from B_0 inhomogeneities. As mentioned previously, B_0 inhomogeneities increase at a higher magnetic field and, therefore, the EPI artifacts get worse. Several retrospective approaches were proposed to correct the geometric distortions (e.g. using point-spread function [21] or B_0 field map [22]). Another method suggests decreasing the echo spacing – and consequently the readout length – by employing a high slew rate head only gradient [23]. However, a more reasonable solution would be to address the problem from its origin (i.e. remove magnetic field perturbations and enhance B_0 homogeneity). A few studies demonstrated the impact of the better shimming on the quality of the EPI images [24–26]. However, to the best of our knowledge, no quantitative comparison about influences of the dynamic shimming on an fMRI study is presented. Two fMRI tasks including finger tapping and breath holding were studied with two different shimming strategies (i.e. using the scanner’s 2nd order shim setup and dynamic shimming with a 16-channel multi-coil setup). The measured data were analyzed with SPM and the results were compared for two shimming approaches.

Two separated regions in brain (the motor cortex and the cerebellum) were covered during the finger-tapping experiment. The cerebellum plays, in conjunction with the motor cortex, an important role in movement organization and their interaction is still not fully understood. Therefore, it is beneficial to study both areas in an fMRI experiment. In total, 40 slices were measured which were split into 22 and 18 slices to partially cover the motor cortex and the cerebellum, respectively. The slices covering the cerebellum were tilted a few degrees for a better coverage. Not only shimming was performed slice by slice in this experiment but also the slices had different orientations. A single-shot EPI was employed for this study with the following parameters: an acceleration factor of 3, $TE/TR = 21/2000$ ms and isotropic voxel size of 1.2 mm.

Prior to the task, the same slices were measured with the same acquisition protocol (except with less repetitions) during rest to evaluate temporal SNR (tSNR). After that, tSNR was calculated as the ratio of the mean signal to the standard deviation over the volumes for the individual voxels in the ROI. Higher tSNR allows the acquisition of fewer volumes while keeping the statistical power of BOLD signal detection. For the case of better field homogeneity provided by dynamic multi-coil shimming, the higher tSNR was observed in both the motor cortex and the cerebellum.

The amount of voxel shifts based on the acquired B_0 map and the effective echo spacing of the employed EPI sequence was calculated. Afterwards, boundaries of the geometric distortions in the both areas for the two shimming approaches were compared with the anatomic images of the same slices. The reduction of the voxel shifts and geometric distortion for the case of multi-coil shimming were apparent.

Single subject (first level) fMRI data analysis was performed on the acquired data from the finger tapping study. The activation in contralateral primary motor cortex, supplementary motor area and ipsilateral superior cerebellum was evident. The number of the voxels with higher t-value increased when multi-coil setup was employed and when dynamic slice-wise shimming was performed. In publication 2 histograms of the t-values for all the attended subject are depicted [27].

Evaluation of impact of the improved B_0 homogeneity on the whole brain fMRI study was performed with a breath-holding experiment. Inadequate respiration leads to an increase in concentration of the carbon dioxide (CO_2) in the blood stream. Increased concentration of CO_2 changes the vessel diameter which leads to a change in blood flow and, accordingly, a change in the BOLD signal intensity [28]. BOLD signal change is global in breath-holding experiment and can be captured for the whole brain in a healthy volunteer. The produced BOLD signal depends on the respiration phase when breath holding starts – i.e. after inhale (end-inspiration) or exhale (end-expiration). Additionally, a relatively long breath hold and paced breathing allows for an increase in the amplitude of the BOLD signal [29].

In our design, the paradigm consisted of a 40-second period of rest (normal breathing) followed by a 20-second task (breath-holding) and started with rest. The subjects were asked to hold their breath after the end-expiration. The complexity of the BOLD signal changes after end-expiration

is reported to be less in comparison to the end-inspiration breath holding. Additionally, end-respiration breath holding is prone to produce variable BOLD signal intensity between trials [30]. Similar to a standard fMRI study, the acquired data was evaluated using a generalized linear model (GLM). In this analysis, HRF response was used; however, the exact response to breathe holding is slightly different. Furthermore, the response to the stimulus in breath holding studies is generally more delayed in comparison to the standard fMRI tasks. The lag on average has been reported to be around 11 seconds and slightly different reaction times for different areas of the brain have been observed. In this analysis, a range of the delays were tried and the one which resulted in higher statistical power was used (in these experiments it was about 13 seconds). We modeled the lag by shifting onset time of the task. An elastic respiratory belt was employed to monitor and log the subjects' respiration performance. Similar to the finger rapping experiments, employing multi-coil in order to dynamic slice-wise shimming resulted in an increase in the number of the voxels with higher t-value. Results of the statistical analysis of the breath holding experiments are shown in Figure 8.

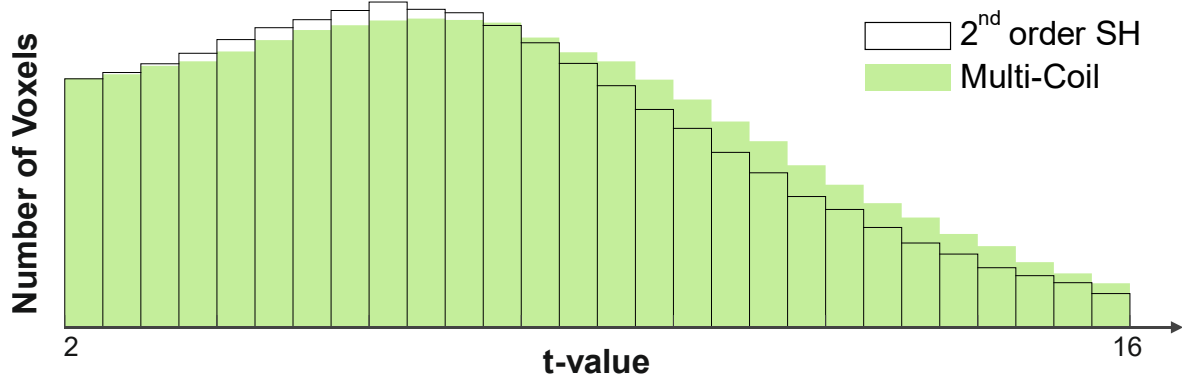


Figure 8. Histogram of voxels with t-value between 2 and 16 during the breath holding task. While the number of voxels with a lower level of significance decreased, the number of voxels with a higher t-value increased when a large portion of B_0 uniformity was compensated by dynamic multi-coil shimming

2.3 Publication 3: A 32-Channel Optimized Multi-Coil

The acquired brain B_0 maps reveal a similar pattern of inhomogeneity for all human brains; a strong local inhomogeneity exists in the prefrontal cortex and near the ear canals while relatively a uniform field is being observed in other areas of the brain. The measured B_0 inhomogeneities pattern can be justified by the human brain anatomy. Air cavities, sinuses, and ear canals in proximity to tissue have a different susceptibility, and the large susceptibility differences between air and tissue result in a local perturbation in B_0 field. Hence, we can optimize the multi-coil setup to adopt with its target when a similar pattern exists in the shimming VOIs.

With a creative manual arrangement of the coils, one can remove some of the shim coils in the posterior where B_0 field in the brain is fairly homogeneous and add more coils in anterior to have a more power to eliminate severe B_0 perturbations in PFC. However, in publication 3, we performed an optimization to obtain an accurate solution [31]. Three parameters of each coil have been considered to optimize as follows:

- Size of the coil
- Axial position of the coil on the cylinder surface
- Angular position of the coil on the cylinder surface

Size and axial position of the coils were constrained while angular position was not constrained in the optimization routing. A cylinder with a diameter of 323 mm and a length of 400 mm was chosen as skeleton of the multi-coil. Part of the cylinder in rear with a length of 70 mm was preserved for the wires going outside. Therefore, the axial position of the coils was bounded to the remaining 330 mm of the cylinder. The lower and upper bound of constraint for the coil size were 20 mm and 100 mm, respectively. The optimization started from a symmetric positioning of the 32 square coils with a side length of 60 mm in four rows. Eight human brain B_0 maps acquired at a magnet with a static field of 9.4T were used as training data. The loss of the cost function was calculated after each successful iteration by:

$$Loss(x) = \sum_{i=1}^8 \sum_{j=1}^{32} (c_{ij}m_j + b_i) \quad (15)$$

Where b_i is the B_0 map of the i^{th} brain, m_j is the basis-map of the j^{th} coil, and c_{ij} is the current of the j^{th} coil calculated for the i^{th} brain. Current of the coils (c_{ij}) is calculated through a constrained linear least-squares optimization.

Several coils were overlapped after optimization. The coils' overlapping can be adjusted by including an additional loss term in the cost function at the cost of degrading the final performance. We permitted for the coils' overlapping without any restrictions but layered the overlapped coils in the construction step. Coils were arranged in four layers while only a few coils were in the third and fourth layers. A 3D support was designed to avoid the bowing of the overlapped coils and to fasten the coils to the cylinder.

Coils' arrangement after optimization (Figure 9) showed an agreement with pattern of B_0 inhomogeneity in the human brain. Overall, the optimized multi-coil consisted of eight, nine, and ten coils placed in the top (anterior), right and up-right and left and up-left, respectively. These coils can counteract the severe B_0 inhomogeneities in the PFC and in the vicinity of the ear canals. Only five coils are placed in bottom (posterior) of the cylinder where B_0 is acceptably uniform in the brain.

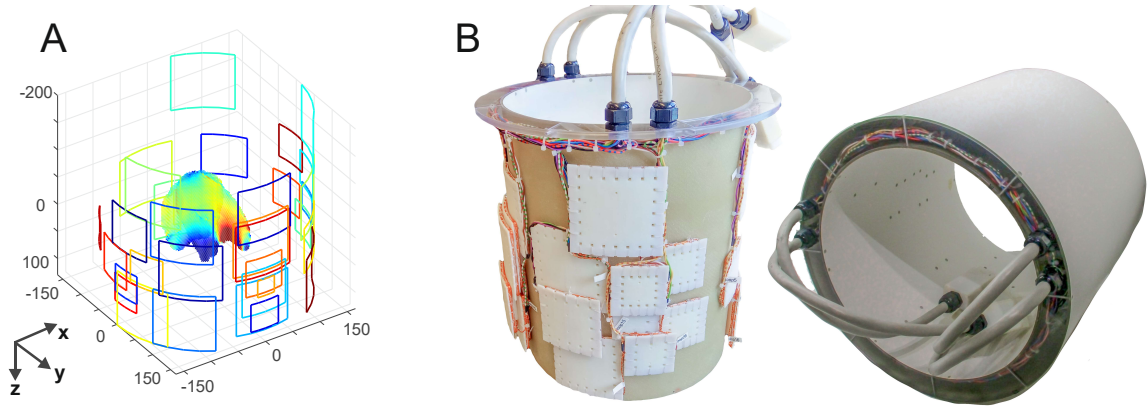


Figure 9. A) The arrangement of the coils on the cylinder surface after optimization. B) Experimental realization of the optimized 32-channel multi-coil

The performance of the optimized 32-channel multi-coil has been compared with multi-coils with different numbers of coils (8, 16, 24, 32, 48, 65 and 96 coils) which are arranged symmetrically on the surface of the same cylinder used for optimization. As a benchmark, comparison with spherical harmonics basis sets up to full sixth order was carried out, as well (Figure 10). Simulations were performed on 14 brain B_0 maps which were not used in training. The performance of the 32-channel optimized multi-coil was comparable with that of the 65-channel multi-coil with a symmetric design (standard deviation of 50.4 Hz for constrained global shimming). In comparison to the spherical harmonics, shimming performance was similar to that of the full fifth order when unconstrained global shimming has been accomplished. Sensitivity of the spherical harmonic terms was not attainable due to analytical calculation of the maps; hence, constrained shimming was not possible to perform. In comparison to the symmetric 32-channel multi-coil which was used as starting point of the optimization, the optimized coil performed better by 12.7% and 19.1% in constrained and unconstrained global shimming, respectively (which decreased to 10.5% and 18.3%, respectively, after layering the coils). The criterion of the improvement was standard deviation of the off-resonance in the whole brain.

The performance of the constructed multi-coil has been evaluated in vivo with multiple sequences that are sensitive to B_0 inhomogeneity. Results of EPI, balanced SSFP and multi-echo GRE sequences were used to evaluate image distortion, banding artifact, and T_2^* quantification, respectively. Multi-echo GRE was used not only for T_2^* calculation, but also for the estimation of B_0 field with and without multi-coil shimming. Details of the acquisition protocols are provided in publication 3. Figure 11 demonstrates reduction of banding artifact in balanced SSFP for two representative slices in prefrontal cortex and ear canals after employing optimized multi-coil.

The designed and constructed multi-coil has been optimized for global shimming of the human brain (i.e., the whole brain). The first benefit of considering such a scope for optimization is the compatibility with the whole brain 3D sequences. Nevertheless, the results showed small improvement in dynamic slice-wise shimming, as well. One can optimize the multi-coil for dynamic slice-wise shimming or specific regions of the brain. However, it is expected that different coils configuration will be obtained for different slice orientations, making the design only suitable for specific applications.

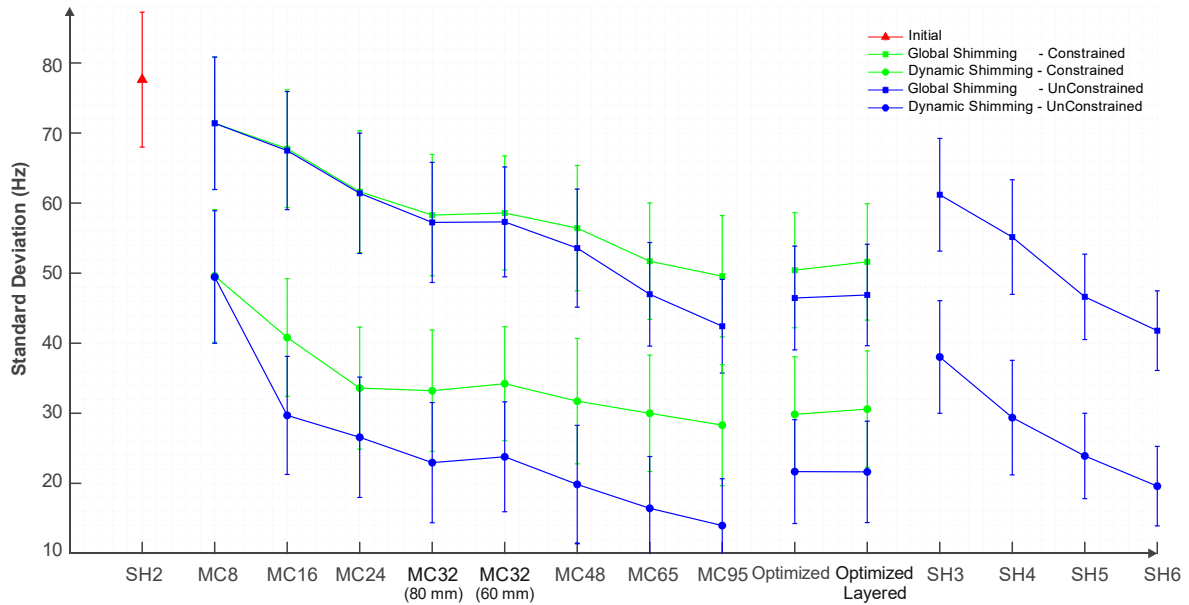


Figure 10. Comparison of the simulated shimmming performance between optimized multi-coil, multi-coils with a different number of coils, and spherical harmonics basis set. Shimmming is carried out in global and dynamic slice-wise fashion while the current is constrained and unconstrained. Only unconstrained shimmming with spherical harmonics is performed since the sensitivity maps are not available. The shimmming is performed on 14 brain B_0 maps which were acquired at 9.4T.

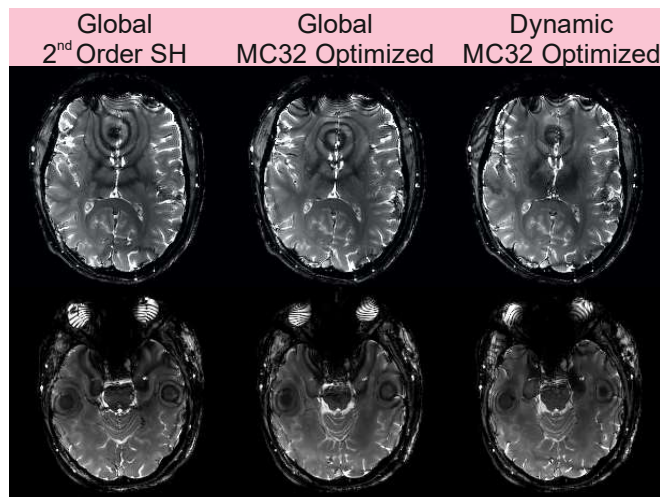


Figure 11. Effect of the improved B_0 homogeneity with optimized 32-channel multi-coil on banding artifacts in bSSFP images

2.4 Publication 4: A Shim Array Based on Brain Anatomy

We introduced an optimized 32-channel multi-coil in the previous subsection. The channels arrangement was adapted to pattern of B_0 inhomogeneity of the brain. Although this approach can effectively improve the shimming performance, but it may not be the most optimum design to yield the maximum achievable B_0 uniformity due to the fixed square shape of the coils. We can use irregular coils with a certain number of nodes [32]; however, an optimum solution would be to find a wiring pattern that can generate inverse of its shimming target. To this end, stream function method [33] has been used in publication 4 to determine optimal surface currents on the cylindrical skeleton which can efficiently generate a field map with the reversed polarity of the brain B_0 map [34].

Field map of the 12 human brains in seven head positions (one reference and three clockwise and three counterclockwise rotations along X, Y, and Z axes) has been acquired. An optimal current density map for every volunteer in every position was calculated. The stream function was optimized on the cylindrical surface with a diameter of 360 mm and a length of 300 mm considering the maximum power dissipation as follow:

$$F = \underset{\psi}{\operatorname{argmin}}(\|B_z(\psi) + B_z^m\|_2^2) \quad \text{subject to} \quad \frac{1}{\tau\sigma} \int_{\Gamma} |\vec{J}(\psi)|^2 \leq P_{max} \quad (16)$$

Where ψ is stream function of the current density $\vec{J}(\psi)$ on surface Γ and B_z^m is the measured field map. τ and σ are thickness and electrical conductivity of the surface, respectively, which in the simulations were 1 mm and 5.998×10^7 S/m.

The same current-carrying surface (cylinder) and mesh were used for all the stream functions. Later, all stream functions formed an $n \times m$ matrix when n denotes number of the nodes and m is total number of the field maps. The singular value decomposition was performed on the matrix and certain numbers of the largest singular values (components) were used to obtain the wiring pattern as shown in Figure 12 for the largest value. The amount of the power dissipation (P_{max}) and total number of components were two adjustable parameters affecting the shimming performance. Choosing a high P_{max} may require a dedicated cooling system or results in

impractical shim coil, while strict constraint on P_{max} can degrade shimming performance. To trade-off between P_{max} , components and the shimming capability, the P_{max} and components were increased in a separate step. Afterward, standard deviation of the residual off-resonance was compared for shimming with the obtained wiring pattern as well as with unconstrained SH shimming with a given order.

In summary, using 12 and 24 components yield a coil design that outperforms fourth and fifth order SH shimming, respectively, for all the 84 brain B_0 map. Furthermore, 12 and 24 components resulted in a better shimming capability for 39% and 90% of the field maps in comparison to the fifth and sixth order SH shimming, respectively.

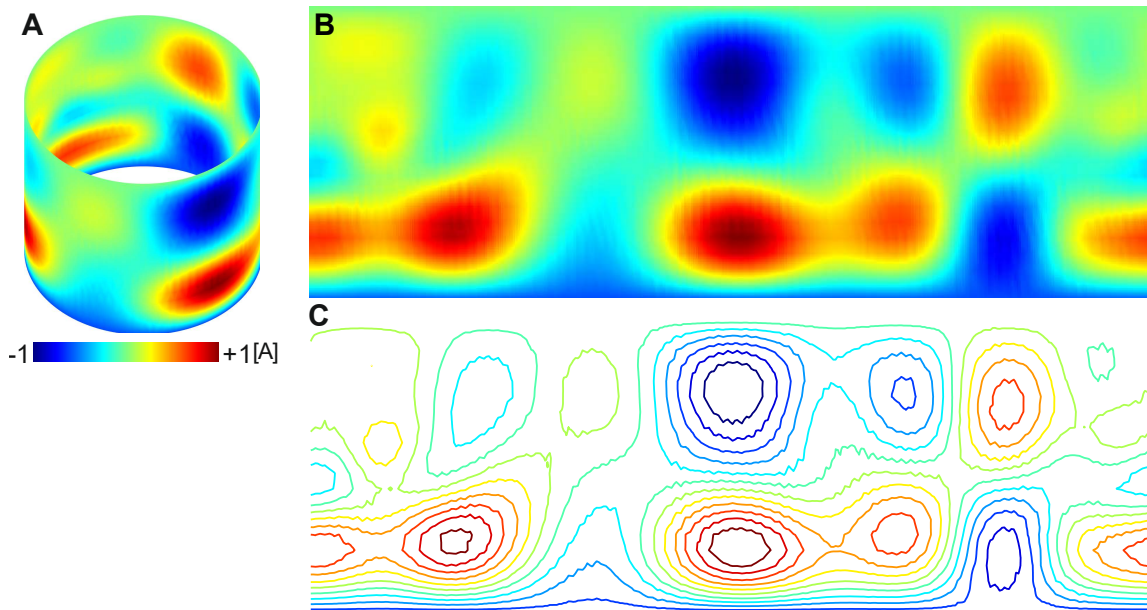


Figure 12. A) An example of the current density map for the largest singular value. B) The current density map in (A) is transformed into a plane. C) Corresponding wiring pattern of the current density map shown in (B).

2.5 Publication 5: Beyond B₀ Shimming

The application of the small local coils is not limited to the B₀ shimming. One can bypass gradient coils and employ local coils for linear and non-linear spatial encoding [35,36]. Another recent study demonstrates how small local coils can be employed as an alternative for saturation pulse in zoomed epi [37]. Here, in publication 5 [38] a novel approach for acceleration of MR imaging was introduced with the aim of rapid dynamic modulation of local magnetic field using small local coils which are called spread-spectrum MRI. Dynamic local magnetic field is produced to superimpose a unique phase evolution during the signal sampling. The injected information, which serves as unique fingerprint into confined area, is utilized to extricate different parts of the object, and thus accelerate imaging.

An array of eight local B₀ coil with a side length of 50 mm and 50 wire turns are placed in a single row on the surface of a cylinder with a diameter of 140 mm to produce local magnetic field modulation patterns. A current waveform controller programmed in LabVIEW played out specified pattern of modulation (5 kHz / 6A peak-to-peak sine wave) concurrently to signal acquisition with a GRE sequence. A phase increment of 45° is applied for the adjacent coils. The sensitivity profile of each local coil has been measured beforehand. The acquired signal can be described with equation (2) but the additive ΔB_0 must be replaced with $\sum_c B_c(r) \int_{t_1}^t f_c(\tau) d\tau$, where B_c is profile of the coil element c and f_c is the arbitrary waveform (here a sine waveform). Therefore, the reconstruction problem for 2D imaging can be describe by $s = Em$, where $s \in \mathbb{C}^{k_x \times k_y}$ is the acquired samples, $m \in \mathbb{C}^{N_x \times N_y}$ is the image and $E \in \mathbb{C}^{k_x \times k_y \times N_x \times N_y}$ is defined as follows:

$$E = F \exp \left(-\frac{i\gamma}{\omega} \sum_c (a_c B_c (\cos(2\pi\omega t_1 + \theta_c) - \cos(2\pi\omega t_i + \theta_c))) \right) \quad (17)$$

Where F denotes the Fourier transform. When g-factor is close to unity, the linear equation system $s = Em$ can be solved simply by calculating the pseudoinverse of the encoding matrix E ; however, the following regularized optimization problem has to be used when g-factor is larger than unity and inversion of the system can be unstable.

$$\hat{m} = \underset{m}{\operatorname{argmin}} (||s - Em||_2^2 + \lambda|TV(m)|) \quad (18)$$

Where total variation term $TV(m)$ penalizes blurring and ghosting artifacts in the reconstruction. Matrix E can be pre-calculated and stored in a look-up table to save the computation time. Experimental results of reconstructed images using the proposed method with acceleration factor of one to four are provided in publication 5. Numerical simulations showed that employing higher modulation frequency and amplitude decreases the normalized mean square error between reference and accelerated image.

3 Conclusions and Outlook

This thesis focuses on inhomogeneity of static field (B_0) and how to address this long-standing challenge at UHF. A design and construction process of a 16-channel multi-coil shim setup has been presented. The setup consisted of several small local shim coils in which each coil shims a confined region. The constructed multi-coil has been used for global static whole brain and dynamic slice-wise shimming at 9.4T MR scanner. The shimming performance was similar to the 3rd order spherical harmonics. Subsequently, a new 32-channel multi-coil shim setup was introduced which is optimized for human brain shimming. The new design improved the performance of the shimming without employing additional coils. The performance of the optimized multi-coil evaluated with several sequences sensitive to B_0 inhomogeneity. Both setups introduced in this thesis have passed the regular safety and quality tests before in vivo measurements. Although a large portion of the B_0 inhomogeneity in human brain can be shimmed with the proposed multi-coil shim setups, the achievable B_0 uniformity at 9.4T is still far away from the conventional 3T scanners. Dynamic shimming with the proposed optimized multi-coil yields a sufficiently homogeneous magnetic field for many applications at UHF.

Despite the remarkable advances in the field of B_0 shimming with multi-coil, there are still some aspects to progress and further improvements. One main issue would be the coil vibration because of electromagnetic force (according to the Lorentz force law). Further optimization can be performed to smooth interstice current change and harness coil vibration. Although the setup can be fixed firmly to the table, some subjects felt like knocking on the helmet. Another exciting progress would be the integration of the amplifier into the multi-coil. Since the coils are small, low-cost and small current amplifier can be designed to integrate into the multi-coil setup and bypass passive electronic elements in the penetration panel. As a further step, combining the amplifiers, shim coil and RF receiver can be an ideal standalone setup for routine research and clinical usages. Finally, the applications beyond B_0 shimming with local coils are expanding. Linear and nonlinear imaging, lipid suppression, local excitation for zoomed imaging, and

acceleration of acquisition by superimposing a unique local magnetic field are some of the applications published in the last two years and more creative ideas are expected to emerge soon.

We hope the proposed setup and results presented in this thesis can further facilitate studies at UHF and bring UHF one step closer to its application in investigations of brain function and clinical diagnostics.

4 Acknowledgments

Praise belongs to God, who guided us unto this; had God not guided us, we had surely never been guided. (Holy Qur'an, Ch. 7, Ver. 43)

whoever is not grateful to the people, he is ungrateful to the creator. (Prophet Mohammad)

This work would not have been possible without the help and support from a lot of people. Therefore, I want to dedicate a few lines to express my tremendous gratitude towards all of them.

I would first like to thank my supervisor, Prof. Dr. Klaus Scheffler, for giving me the opportunity to perform my PhD studies at MPI, for his committed supervision, and for creating a unique research environment full of scientific vision, rigor, and freedom.

I would like to wish my deepest thanks to Dr. Christian Mirkes and Jonas Bause for all the knowledge they provided. I learned a lot from both. Thanks also to my colleagues and friends (present and past) Martin, Alex, Mario, Marlon, Kai, Rolf, Mihai, Philipp, Theodor, Joshi, Mirsat, Dario, Nikolai, Rahel, Jiazheng, and the rest of the MR group at MPI. I'll never forget the hours I spent with you and many wonderful activities we've done together. A big thank you is also due to Tina Schröder for her great support in the last several years.

Last, but by far not least, I am forever thankful to my family for their unconditional support throughout all the years of my education. This thesis would not have been possible without the inspiration of my wife, Azadeh, who believed in me through the past years. Thank you for all of your moral supports. Thanks to my parents whose hearts beat for me from thousands of miles away.

5 References

- 1 De Graaf, R.A. (2018) *In Vivo NMR Spectroscopy : Principles and Techniques*. 3rd ed., Wiley. <https://doi.org/10.1002/9781119382461>.
- 2 Finsterbusch, J. (2014) B0 Inhomogeneity and Shimming. *Quantitative MRI of the Spinal Cord*, Academic Press, 68–90. <https://doi.org/10.1016/B978-0-12-396973-6.00006-X>.
- 3 Schmitt, F., Stehling, M.K. and Turner, R. (1998) *Echo-Planar Imaging: Theory, Technique and Application*. Berlin Heidelberg New York: Springer. <https://doi.org/10.1177/004057368303900411>.
- 4 Marques, J.P. and Bowtell, R. (2005) Application of a Fourier-Based Method for Rapid Calculation of Field Inhomogeneity Due to Spatial Variation of Magnetic Susceptibility. *Concepts in Magnetic Resonance Part B: Magnetic Resonance Engineering*, **25**, 65–78. <https://doi.org/10.1002/cmr.b.20034>.
- 5 Barmet, C., Zanche, N. De and Pruessmann, K.P. (2008) Spatiotemporal Magnetic Field Monitoring for MR. *Magnetic Resonance in Medicine*, **60**, 187–197. <https://doi.org/10.1002/mrm.21603>.
- 6 Juchem, C., Nixon, T.W., Diduch, P., Rothman, D.L., Starewicz, P. and De Graaf, R.A. (2010) Dynamic Shimming of the Human Brain at 7 T. *Concepts in Magnetic Resonance Part B: Magnetic Resonance Engineering*, **37B**, 116–128. <https://doi.org/10.1002/cmr.b.20169>.
- 7 Sengupta, S., Welch, E.B., Zhao, Y., Foxall, D., Starewicz, P., Anderson, A.W., Gore, J.C. and Avison, M.J. (2011) Dynamic B0 Shimming at 7 T. *Magnetic Resonance Imaging*, Elsevier Inc., **29**, 483–496. <https://doi.org/10.1016/j.mri.2011.01.002>.
- 8 Koch, K.M., McIntyre, S., Nixon, T.W., Rothman, D.L. and de Graaf, R.A. (2006) Dynamic Shim Updating on the Human Brain. *Journal of Magnetic Resonance*, Academic Press, **180**, 286–296. <https://doi.org/10.1016/j.jmr.2006.03.007>.
- 9 Fillmer, A., Vannesjo, S.J., Pavan, M., Scheidegger, M., Pruessmann, K.P. and Henning, A. (2015) Fast Iterative Pre-Emphasis Calibration Method Enabling Third-Order Dynamic Shim Updated FMRI. *Magnetic Resonance in Medicine*, **1131**, 1119–1131. <https://doi.org/10.1002/mrm.25695>.
- 10 Jehenson, P., Westphal, M. and Schuff, N. (1990) Analytical Method for the Compensation of Eddy-Current Effects Induced by Pulsed Magnetic Field Gradients in NMR Systems. *Journal*

- of Magnetic Resonance (1969)*, **90**, 264–278. [https://doi.org/10.1016/0022-2364\(90\)90133-T](https://doi.org/10.1016/0022-2364(90)90133-T).
- 11 Juchem, C., Nixon, T.W., McIntyre, S., Rothman, D.L. and Graaf, R.A. De. (2010) Magnetic Field Modeling with a Set of Individual Localized Coils. *Journal of Magnetic Resonance*, Elsevier Inc., **204**, 281–289. <https://doi.org/10.1016/j.jmr.2010.03.008>.
 - 12 Juchem, C., Nixon, T.W., McIntyre, S., Boer, V.O., Rothman, D.L. and De Graaf, R.A. (2011) Dynamic Multi-Coil Shimming of the Human Brain at 7 T. *Journal of Magnetic Resonance*, Elsevier Inc., **212**, 280–288. <https://doi.org/10.1016/j.jmr.2011.07.005>.
 - 13 Hsu, J.-J.J. and Glover, G.H. (2005) Mitigation of Susceptibility-Induced Signal Loss in Neuroimaging Using Localized Shim Coils. *Magnetic Resonance in Medicine*, Wiley-Blackwell, **53**, 243–248. <https://doi.org/10.1002/mrm.20365>.
 - 14 Wong E. C, M.Y. (2004) Shimming of the Inferior Frontal Cortex Using an External Local Shim Coil. Proceedings of the Int. Soc. Magn. Reson. Med.
 - 15 Aghaeifar, A., Mirkes, C., Bause, J., Steffen, T., Avdievitch, N., Henning, A. and Scheffler, K. (2018) Dynamic B₀ Shimming of the Human Brain at 9.4 T with a 16-Channel Multi-Coil Shim Setup. *Magnetic Resonance in Medicine*, **80**, 1714–1725. <https://doi.org/10.1002/mrm.27110>.
 - 16 Aghaeifar, A., Zivkovic, I., Steffen, T., Mirkes, C. and Scheffler, K. (2017) Flexible Gradient Driver System for a Multi-Coil Setup; Design Considerations and Implementation. 34th Annual Scientific Meeting of the European Society for Magnetic Resonance in Medicine and Biology, Barcelona, Spain, 50.
 - 17 Avdievich, N.I., Giapitzakis, I.-A., Bause, J., Shajan, G., Scheffler, K. and Henning, A. (2019) Double-Row 18-Loop Transmit-32-Loop Receive Tight-Fit Array Provides for Whole-Brain Coverage, High Transmit Performance, and SNR Improvement near the Brain Center at 9.4T. *Magnetic Resonance in Medicine*, John Wiley & Sons, Ltd, **81**, 3392–3405. <https://doi.org/10.1002/mrm.27602>.
 - 18 Chang, P., Nassirpour, S., Aghaeifar, A., Scheffler, K. and Henning, A. (2018) Dynamic B₀ Shimming for Multi-Slice Metabolite Mapping at Ultra-High Field in the Human Brain: Very High Order Spherical Harmonics vs. Multi-Coil. 26th Annual Meeting and Exhibition of the International Society for Magnetic Resonance in Medicine, Paris, 0833.
 - 19 Aghaeifar, A., Chang, P., Nassirpour, S., Eschelbach, M., Henning, A. and Scheffler, K. (2018) A True Comparison of B₀ Shimming with a Very High Order Spherical Harmonic Based Setup and a Multi-Coil Shim Array. 26th Annual Meeting and Exhibition of the International Society for Magnetic Resonance in Medicine, Paris, 4422.

- 20 Uğurbil, K. (2018) Imaging at Ultrahigh Magnetic Fields: History, Challenges, and Solutions. *NeuroImage*, **168**, 7–32. <https://doi.org/10.1016/j.neuroimage.2017.07.007>.
- 21 Zaitsev, M., Hennig, J. and Speck, O. (2004) Point Spread Function Mapping with Parallel Imaging Techniques and High Acceleration Factors: Fast, Robust, and Flexible Method for Echo-Planar Imaging Distortion Correction. *Magnetic Resonance in Medicine*, **52**, 1156–1166. <https://doi.org/10.1002/mrm.20261>.
- 22 Jezzard, P. (2012) Correction of Geometric Distortion in FMRI Data. *NeuroImage*, Elsevier Inc., **62**, 648–651. <https://doi.org/10.1016/j.neuroimage.2011.09.010>.
- 23 Tan, E.T., Lee, S.K., Weavers, P.T., Graziani, D., Piel, J.E., Shu, Y., Huston, J., Bernstein, M.A. and Foo, T.K.F. (2016) High Slew-Rate Head-Only Gradient for Improving Distortion in Echo Planar Imaging: Preliminary Experience. *Journal of Magnetic Resonance Imaging*, **44**, 653–664. <https://doi.org/10.1002/jmri.25210>.
- 24 Kim, T., Lee, Y., Zhao, T., Hetherington, H.P. and Pan, J.W. (2017) Gradient-Echo EPI Using a High-Degree Shim Insert Coil at 7 T: Implications for BOLD FMRI. *Magnetic Resonance in Medicine*, **78**, 1734–1745. <https://doi.org/10.1002/mrm.26563>.
- 25 Juchem, C., Umesh Rudrapatna, S., Nixon, T.W. and de Graaf, R.A. (2015) Dynamic Multi-Coil Technique (DYNAMITE) Shimming for Echo-Planar Imaging of the Human Brain at 7 Tesla. *NeuroImage*, Elsevier Inc., **105**, 462–472. <https://doi.org/10.1016/j.neuroimage.2014.11.011>.
- 26 Balteau, E., Hutton, C. and Weiskopf, N. (2010) Improved Shimming for FMRI Specifically Optimizing the Local BOLD Sensitivity. *NeuroImage*, Elsevier Inc., **49**, 327–336. <https://doi.org/10.1016/j.neuroimage.2009.08.010>.
- 27 Aghaeifar, A., Bause, J., Leks, E., Grodd, W. and Scheffler, K. (2019) Dynamic B0 Shimming of the Motor Cortex and Cerebellum with a Multi-Coil Shim Setup for BOLD FMRI at 9.4T. *Magnetic Resonance in Medicine*. <https://doi.org/10.1002/mrm.28044>.
- 28 Birn, R.M., Smith, M.A., Jones, T.B. and Bandettini, P.A. (2008) The Respiration Response Function: The Temporal Dynamics of FMRI Signal Fluctuations Related to Changes in Respiration. *NeuroImage*, **40**, 644–654. <https://doi.org/10.1016/j.neuroimage.2007.11.059>.
- 29 Magon, S., Basso, G., Farace, P., Ricciardi, G.K., Beltramello, A. and Sbarbati, A. (2009) Reproducibility of BOLD Signal Change Induced by Breath Holding. *NeuroImage*, Elsevier Inc., **45**, 702–712. <https://doi.org/10.1016/j.neuroimage.2008.12.059>.
- 30 Pinto, J., Jorge, J., Sousa, I., Vilela, P. and Figueiredo, P. (2016) Fourier Modeling of the BOLD Response to a Breath-Hold Task: Optimization and Reproducibility. *NeuroImage*, **135**,

223–231. <https://doi.org/10.1016/j.neuroimage.2016.02.037>.

- 31 Aghaeifar, A., Zhou, J., Heule, R., Tabibian, B., Schölkopf, B., Jia, F., Zaitsev, M. and Scheffler, K. (2020) A 32-channel Multi-coil Setup Optimized for Human Brain Shimming at 9.4T. *Magnetic Resonance in Medicine*, **83**, 749–764. <https://doi.org/10.1002/mrm.27929>.
- 32 Zivkovic, I., Tolstikhin, I., Schölkopf, B. and Scheffler, K. (2016) B0 Matrix Shim Array Design-Optimization of the Position, Geometry and the Number of Segments of Individual Coil Elements. 33rd Annual Scientific Meeting of the European Society for Magnetic Resonance in Medicine and Biology.
- 33 Peeren, G.N. (2003) Stream Function Approach for Determining Optimal Surface Currents. *Journal of Computational Physics*, **191**, 305–321. [https://doi.org/10.1016/S0021-9991\(03\)00320-6](https://doi.org/10.1016/S0021-9991(03)00320-6).
- 34 Jia, F., Elshatlawy, H., Aghaeifar, A., Chu, Y.-H., Hsu, Y.-C., Littin, S., Kroboth, S., Yu, H., Amrein, P., Gao, X., Yang, W., LeVan, P., Scheffler, K. and Zaitsev, M. (2019) Design of a Shim Coil Array Matched to the Human Brain Anatomy. *Magnetic Resonance in Medicine*. <https://doi.org/10.1002/mrm.28016>.
- 35 Littin, S., Jia, F., Layton, K.J., Kroboth, S., Yu, H., Hennig, J. and Zaitsev, M. (2018) Development and Implementation of an 84-Channel Matrix Gradient Coil. *Magnetic Resonance in Medicine*, **79**, 1181–1191. <https://doi.org/10.1002/mrm.26700>.
- 36 Umesh Rudrapatna, S., Fluerebrock, F., Nixon, T.W., de Graaf, R.A. and Juchem, C. (2019) Combined Imaging and Shimming with the Dynamic Multi-coil Technique. *Magnetic Resonance in Medicine*, **81**, 1424–1433. <https://doi.org/10.1002/mrm.27408>.
- 37 Stockmann, J., Arango, N.S., Poser, B., Witzel, T., White, J., Wald, L.L. and Polimeni, J.R. (2018) Spatially-Selective Excitation Using a Tailored Nonlinear ΔB_0 Pattern Generated by an Integrated Multi-Coil $\Delta B_0/R_x$ Array. 26th Annual Meeting and Exhibition of the International Society for Magnetic Resonance in Medicine, Paris, 0170.
- 38 Scheffler, K., Loktyushin, A., Bause, J., Aghaeifar, A., Steffen, T. and Schölkopf, B. (2019) Spread-spectrum Magnetic Resonance Imaging. *Magnetic Resonance in Medicine*, **82**, 877–885. <https://doi.org/10.1002/mrm.27766>.

6 List of Publications

6.1 Appended Publications

1. **Aghaeifar, A.**; Mirkes, C.; Bause, J.; Steffen, T.; Avdievitch, N.; Henning, A.; Scheffler, K.: Dynamic B0 shimming of the human brain at 9.4 T with a 16-channel multi-coil shim setup. *Magnetic Resonance in Medicine* 80 (4), pp. 1714 - 1725 (2018)
2. **Aghaeifar, A.**; Bause, J.; Leks, E.; Grodd, W.; Scheffler, K.: *Dynamic B0 shimming of the motor cortex and cerebellum with a multi-coil shim setup for BOLD fMRI at 9.4T*. *Magnetic Resonance in Medicine* (2019) DOI: 10.1002/mrm.28044
3. **Aghaeifar, A.**; Zhou, J., Heule, R., Tabibian, B., Schölkopf, Jia, F.; Zaitsev, M.; Scheffler, K.: *A 32-channel multi-coil setup optimized for the human brain shimming at 9.4 T*. *Magnetic Resonance in Medicine* 83 (2), pp. 749-764 (2020)
4. Jia, F.; Elshatlawy, H.; **Aghaeifar, A.**; Chu, Y.; Hsu, Y.; Littin, S.; Kroboth, S.; Yu, H.; Amrein, P.; Gao, X.; Yang, W.; LeVan, P.; Scheffler, K.; Zaitsev, M.: Design of a shim coil array matched to the human brain anatomy. *Magnetic Resonance in Medicine* (2019) DOI: 10.1002/mrm.28016
5. Scheffler, K.; Bause, J.; Loktyushin, A.; **Aghaeifar, A.**; Steffen, T.; Schölkopf, B.: Spread-Spectrum Magnetic Resonance Imaging. *Magnetic Resonance in Medicine* 82 (3), pp. 877-885 (2019)

6.2 Other Recent Publications

6.2.1 Journal Articles

1. Bause, J.; Polimeni, J.; Stelzer, J.; Ehses, P.; In, M.; Kraemer-Fernandez, P.; **Aghaeifar, A.**; Pohmann, R.; Scheffler, K.: *Understanding factors influencing the spatial specificity of laminar BOLD fMRI: Gradient echo EPI acquisition and post-processing*. *Neuroimage* (Under review)

2. Eschelbach, M.; **Aghaeifar, A.**; Bause, J.; Handwerker, J.; Anders, J.; Engel, E.-M.; Thielscher, A.; Scheffler, K.: *Comparison of prospective head motion correction with NMR field probes and an optical tracking system*. *Magnetic Resonance in Medicine* 81 (1), pp. 719 - 729 (2019)
3. Kühne, M.; Eschelbach, M.; **Aghaeifar, A.**; von Pflugk, L.; Thielscher, A.; Himmelbach, M.; Scheffler, K.; van der Smagt, P.; Peer, A.: *An MR-Compatible Haptic Interface with Seven Degrees of Freedom*. *IEEE/ASME Transactions on Mechatronics* 23 (2), pp. 624 - 635 (2018)

6.2.2 Talks

1. **Aghaeifar, A.**; Bause, J.; Leks, E.; Grodd, W.; Scheffler, K.: *Impact of Dynamic Multi-Coil Shimming on BOLD fMRI Contrast at 9.4T*. In *ISMRM Workshop on Ultrahigh Field Magnetic Resonance: Technological Advances, Translational Research Promises & Clinical Applications*, Dubrovnik, Croatia. (2019)
2. Scheffler, K.; Bause, J.; **Aghaeifar, A.**; Steffen, T.; Schölkopf, B.; Loktyushin, A.: *Spread-spectrum MRI: acceleration of image acquisition using locally modulated magnetic fields*. 27th Annual Meeting and Exhibition of the International Society for Magnetic Resonance in Medicine, Montréal, QC, Canada (2019)
3. **Aghaeifar, A.**; Mirkes, C.; Scheffler, K.: *Joint dynamic shimming using the scanner's spherical harmonic shim combined with a local multi-coil shim array*. Joint Annual Meeting ISMRM-ESMRMB 2018, Paris, France. (2018)
4. Chang, P.; Nassirpour, S.; **Aghaeifar, A.**; Scheffler, K.; Henning, A.: *Dynamic B0 Shimming for Multi-Slice Metabolite Mapping at Ultra-High Field in the Human Brain: Very High Order Spherical Harmonics vs. Multi-Coil*. Joint Annual Meeting ISMRM-ESMRMB 2018, Paris, France. (2018)
5. **Aghaeifar, A.**; Zivkovic, I.; Steffen, T.; Mirkes, C.; Scheffler, K.: *Flexible gradient driver system for a multi-coil shim setup: design considerations and implementation*. 34th Annual Scientific Meeting of the European Society for Magnetic Resonance in Medicine and Biology, Barcelona, Spain. (2017)

6. Bause, J.; **Aghaeifar, A.**; In, M.-H.; Engel, E.-M.; Ehses, P.; Eschelbach, M.; Scheffler, K.; Pohmann, R.: Distortion and prospective motion corrected zoomed functional imaging of the human brain at 9.4 Tesla. 34th Annual Scientific Meeting of the European Society for Magnetic Resonance in Medicine and Biology, Barcelona, Spain. (2017)
7. Bause, J.; **Aghaeifar, A.**; Hagberg, G.; Engel, E.-M.; Avdievitch, N.; Scheffler, K.; Pohmann, R.: 350 μ m Isotropic Whole-Brain MP2RAGE without Averaging. ISMRM Workshop on Motion Correction in MRI MRS, Cape Town, South Africa. (2017)
8. **Aghaeifar, A.**; Eschelbach, M.; Scheffler, K.: Multi-Modality Prospective Motion Correction of Human Head. ISMRM Workshop on Motion Correction in MRI MRS, Cape Town, South Africa. (2017)
9. **Aghaeifar, A.**; Eschelbach, M.; Bause, J.; Thielscher, A.; Scheffler, K.: AMoCo, a software package for prospective motion correction. 25th Annual Meeting and Exhibition of the International Society for Magnetic Resonance in Medicine, Honolulu, HI, USA. (2017)
10. **Aghaeifar, A.**; Eschelbach, M.; Scheffler, K.: Real time communications over UDP protocol. European IDEA Users Group Meeting 2016, Maastricht, Netherlands. (2016)
11. **Aghaeifar, A.**; Loktyushin, A.; Mirkes, C.; Thielscher, A.; Scheffler, K.: Fast B0 first order inhomogeneity estimation using radial acquisition. 24th Annual Meeting and Exhibition of the International Society for Magnetic Resonance in Medicine, Singapore. (2016)
12. Kühne, M.; Ergin, M.; Klare, S.; Eschelbach, M.; **Aghaeifar, A.**; Thielscher, A.; Peer, A.: Towards an MR-compatible Haptic Interface with Seven Actuated Degrees of Freedom. In: . IEEE International Conference on Robotics and Automation (ICRA 2015), Seattle, WA, USA. (2015)

6.2.3 Posters

1. **Aghaeifar, A.**; Zhou, J.; Zivkovic, I.; Walzog, J.; Memaj, M.; Steffen, T.; Heule, R.; Jia, F.; Zaitsev, M.; Scheffler, K.: A 32-channel multi-coil shim setup optimized for the human brain, pushing the limits of shimming at 9.4T. 27th Annual Meeting and Exhibition of the International Society for Magnetic Resonance in Medicine, Montréal, QC, Canada (2019)

2. Jia, F.; Elshatlawy, H.; **Aghaeifar, A.**; Littin, S.; Kroboth, S.; Chu, Y.; Hsu, Y.; Gao, X.; Yu, H.; Amrein, P.; Yang, W.; Zhou, J.; Levan, P.; Scheffler, K.; Zaitsev, M.: Design of a shimming coil matched to the human brain anatomy. 27th Annual Meeting and Exhibition of the International Society for Magnetic Resonance in Medicine, Montréal, QC, Canada (2019)
3. Zhou, J.; **Aghaeifar, A.**; Bause, J.; Loktyushin, A.; Hagberg, G.; Scheffler, K.: Magnetic field estimation with ultrashort echo time (UTE) imaging.. 27th Annual Meeting and Exhibition of the International Society for Magnetic Resonance in Medicine, Montréal, QC, Canada (2019)
4. **Aghaeifar, A.**; Chang, P.; Nassirpour, S.; Eschelbach, M.; Henning, A.; Scheffler, K.: A true comparison of B₀ shimming with a very high order spherical harmonic based setup and a multi-coil shim array. Joint Annual Meeting ISMRM-ESMRMB, Paris, France (2018)
5. **Aghaeifar, A.**; Loktyushin, A.; Eschelbach, M.; Scheffler, K.: Improving performance of linear field generation with multi-coil setup by optimizing coils position. 34th Annual Scientific Meeting of the European Society for Magnetic Resonance in Medicine and Biology, Barcelona, Spain (2017)
6. Eschelbach, M.; **Aghaeifar, A.**; Engel, E.-M.; Scheffler, K.: Prospective Head Motion Correction Using Multiple Tracking Modalities. 34th Annual Scientific Meeting of the European Society for Magnetic Resonance in Medicine and Biology, Barcelona, Spain (2017)
7. Mirkes, C.; Shajan, G.; **Aghaeifar, A.**; Zivkovic, I.; Buckenmaier, K.; Scheffler, K.: Dual-layered multi-channel B₀ and RF coil setup for an improved shimming performance at 9.4 Tesla. 25th Annual Meeting and Exhibition of the International Society for Magnetic Resonance in Medicine, Honolulu, HI, USA (2017)
8. **Aghaeifar, A.**; Zivkovic, I.; Mirkes, C.; Steffen, T.; Scheffler, K.: Global and dynamic shimming with the scanner's inbuilt shim system and a custom-made multi-coil setup at 9.4 T. 25th Annual Meeting and Exhibition of the International Society for Magnetic Resonance in Medicine, Honolulu, HI, USA (2017)

9. **Aghaeifar, A.**; Moghaddam, A.; Scheffler, K.: Motion simulation and correction validation using MR tagging. 25th Annual Meeting and Exhibition of the International Society for Magnetic Resonance in Medicine, Honolulu, HI, USA (2017)
10. Eschelbach, M.; **Aghaeifar, A.**; Bause, J.; Handwerker, J.; Anders, J.; Thielscher, A.; Scheffler, K.: A Comparison of Prospective Motion Correction with ¹⁹F NMR Field Probes and an Optical Camera. 25th Annual Meeting and Exhibition of the International Society for Magnetic Resonance in Medicine, Honolulu, HI, USA (2017)

7 Statement of Contributions

7.1 Dynamic B0 shimming of the human brain at 9.4T with a 16-channel multi-coil shim setup

- **A. Aghaeifar:** Performed measurements, developed post-processing techniques, analyzed the data, and wrote major part of the manuscript
- **C. Mirkes:** Prepared dynamic shimming sequence, wrote part of the manuscript and proofread the manuscript
- **J. Bause:** Prepared EPI sequence
- **T. Steffen:** Built the amplifier
- **N. Avdievitch:** Built the RF coil
- **A. Henning:** Supervised on the construction of RF coil
- **K. Scheffler:** Supervised the project and proofread the manuscript

7.2 Dynamic B0 shimming of the motor cortex and cerebellum with a multi-coil shim setup for BOLD fMRI at 9.4T

- **A. Aghaeifar:** Prepared the sequences, performed measurements, analyzed the data, and prepared the manuscript
- **J. Bause:** Helped with measurements and preparing the manuscript
- **E. Leks:** Helped with measurements
- **W. Grodd:** Helped with data analyzing
- **K. Scheffler:** Supervised and advised the project and proofread the manuscript

7.3 A 32-channel multi-coil setup optimized for the human brain shimming at 9.4T

- **A. Aghaeifar:** Performed the simulation, designed the coil, performed the experiments, analyzed the data, and wrote the manuscript
- **J. Zhou:** Helped on measurement and preparing the manuscript
- **R. Heule:** Provided the bSSFP sequence and proofread the manuscript
- **B. Tabibian:** Helped on optimization process
- **B. Schölkopf:** Supervised the optimization process
- **F. Jia & M. Zaitsev:** Provided consultations on data analyzing
- **K. Scheffler:** Supervised and advised the project

7.4 Design of a shim coil array matched to the human brain anatomy

- **F. Jia:** Performed simulation and the coil design and prepared the manuscript
- **H. Elshatlawy:** Performed pre-processing of the data
- **A. Aghaeifar:** Performed the measurements, data collection and pre-processing
- **Y. Chu, Y. Hsu, S. Littin, S. Kroboth, H. Yu, P. Amerein, X. Gao, W. Yang, and P. Levant:** Collaborated in simulation
- **K. Scheffler and M. Zaitsev:** Supervised and advised on the project

7.5 Spread-Spectrum Magnetic Resonance Imaging

- **K. Scheffler:** Created the main idea, performed the measurements and wrote the manuscript
- **J. Bause:** Prepared the setup and measurements hardware
- **A. Loktyushin:** Analyzed the data and prepared reconstruction routine
- **A. Aghaeifar:** Prepared the sequence and designed the software for controlling the coils
- **T. Steffen:** Prepared the amplifier
- **B. Schölkopf:** Supervised on machine learning algorithms

8 Appended Publications

Publication I


“Dynamic B₀ shimming of the human brain at 9.4 T with a 16-channel multi-coil shim setup”

A. Aghaeifar, C. Mirkes, J. Bause, T. Steffen, N. Avdievitch, A. Henning, K. Scheffler

Magnetic Resonance in Medicine, 80 (4), pp. 1714-1725 (2018)

DOI: [10.1002/mrm.27110](https://doi.org/10.1002/mrm.27110)

Dynamic B_0 shimming of the human brain at 9.4 T with a 16-channel multi-coil shim setup

Ali Aghaeifar^{1,2}  | Christian Mirkes³ | Jonas Bause^{1,2} | Theodor Steffen¹ | Nikolai Avdievitch^{1,4} | Anke Henning^{1,4} | Klaus Scheffler^{1,5}

¹Max Planck Institute for Biological Cybernetics, Tuebingen, Germany

²IMPRS for Cognitive and Systems Neuroscience, University of Tuebingen, Tuebingen, Germany

³Skope Magnetic Resonance Technologies AG, Zurich, Switzerland

⁴Institute of Physics, Ernst-Moritz-Armdt University, Greifswald, Germany

⁵Department of Biomedical Magnetic Resonance, University of Tuebingen, Tuebingen, Germany

Correspondence

Ali Aghaeifar, High-Field Magnetic Resonance Center, Max Planck Institute for Biological Cybernetics, Max-Planck-Ring 11, 72076 Tuebingen, Germany.
Email: ali.aghaeifar@tuebingen.mpg.de

Funding information

Max Planck Society and the German research foundation (DFG); Grant Numbers SCHE 658/5 and SCHE 658/7

Purpose: A 16-channel multi-coil shimming setup was developed to mitigate severe B_0 field perturbations at ultrahigh field and improve data quality for human brain imaging and spectroscopy.

Methods: The shimming setup consisted of 16 circular B_0 coils that were positioned symmetrically on a cylinder with a diameter of 370 mm. The latter was large enough to house a shielded 18/32-channel RF transceiver array. The shim performance was assessed via simulations and phantom as well as in vivo measurements at 9.4 T. The global and dynamic shimming performance of the multi-coil setup was compared with the built-in scanner shim system for EPI and single voxel spectroscopy.

Results: The presence of the multi-coil shim did not influence the performance of the RF coil. The performance of the proposed setup was similar to a full third-order spherical harmonic shim system in the case of global static and dynamic slice-wise shimming. Dynamic slice-wise shimming with the multi-coil setup outperformed global static shimming with the scanner's second-order spherical-harmonic shim. The multi-coil setup allowed mitigating geometric distortions for EPI. The combination of the multi-coil shim setup with the zeroth and first-order shim of the scanner further reduced the standard deviation of the B_0 field in the brain by 12% compared with the case in which multi-coil was used exclusively.

Conclusion: The combination of a multi-coil setup and the linear shim channels of the scanner provides a straightforward solution for implementing dynamic slice-wise shimming without requiring an additional pre-emphasis setup.

KEYWORDS

B_0 inhomogeneity, B_0 shimming, current amplifier, echo planar imaging, multi-coil, ultrahigh field

1 | INTRODUCTION

A homogenous B_0 field is a key prerequisite for a large set of MRI and MRS methods. Inhomogeneities arise primarily

from varying magnetic susceptibility within the subject. In the human brain, the susceptibility difference between air and tissue, particularly in the temporal lobes and the prefrontal cortex, results in a complex distortion of the magnetic

field. For EPI, which is one of the most widespread sequences used for functional brain imaging, B_0 inhomogeneity causes two critical artifacts: through-slice dephasing for long TEs due to a reduced T_2^* and image distortions due to an accrual of an additional phase to the received signal.^{1,2} For MRS, ultrahigh field allows gaining a higher spectral resolution and SNR, but complicates at the same time the acquisition of high-quality spectra caused by pronounced B_0 field perturbations.^{3,4}

Artifacts arising from nonuniformities of the B_0 field can be mitigated partially by adjusting the acquisition protocol^{5,6} or by using dedicated distortion correction methods in post-processing. However, these methods meet their limits at some point. Therefore, it would be best to address the problem at its origin and aim for a homogeneous field in the first place.

Laplace's equation describes the magnetic field inside the bore, and it is possible to show that the field can be represented by a linear combination of basis functions that are known as spherical harmonics (SHs). Currently, all state-of-the-art MR scanners are equipped with shimming coils that can generate SH terms up to second order (or third order in high-field scanners). Recently, local coils have been proposed in the literature to achieve an enhanced shimming performance.⁷ They enable a flexible design and a simple fabrication process. As they can be installed closer to the subject, they are better suited to counteract local field distortions. However, the fields they generate are not orthogonal anymore. The flexibility of the multi-coil (MC) approach also allows integrating local shim coils into RF coils.^{8,9}

At high field, the B_0 inhomogeneity becomes more pronounced and the limited number of available shimming coils is insufficient to compensate the field distortions. This fact motivates the transition from static global shimming to dynamic slice-wise shimming.^{10,11} The latter consists of dividing the whole volume of interest into smaller subregions that can be homogenized more efficiently. For each slice, the shim settings must then be updated prior to excitation. A requirement for dynamic shimming is the independence of the individual subregions during measurement. The performance of dynamic shimming using a MC approach on mouse brain,¹² rat brain,¹³ and human brain^{10,14} has already been demonstrated in the literature.

Low-order SH terms are well suited to model global, slowly varying field distortions, which extend over the entire imaging volume. With increasing order, the ability to cancel also local inhomogeneities improves.¹⁵ The MC approach is advantageous for local shimming, and its performance is comparable to middle and high-order SHs.⁸ Several individual shim coils can be used to mimic low-order SH terms as well, but at the cost of degrading the local shimming performance. The combination of SH and MC shimming will

further improve B_0 homogeneity. Therefore, the SH shim can be used to homogenize the field on a global level, whereas multiple local coils, with their low inductance, can be used to dynamically shim local regions.

This work introduces a 16-channel MC setup connected to dedicated amplifiers that was designed for dynamic shimming of the brain at ultrahigh field. Furthermore, this study shows how the SH shim system of a scanner in combination with a MC approach can represent a hybrid method for dynamic shimming. The performance of the proposed approach is demonstrated for slice-wise dynamic shimming in the human brain at 9.4 T.

2 | METHODS

2.1 | Hardware

All experiments were performed on a 9.4T whole-body MR scanner (Siemens Healthcare, Erlangen, Germany) that was equipped with a SC72 gradient system having a maximal amplitude and slew rate of 40 mT/m and 200 T/m/s, respectively. The system vendor provided the means to dynamically change the zeroth (i.e., RF frequency) and first-order (i.e., x, y, and z-gradient) shims of the scanner, which included an integrated eddy-current compensation. The higher-order SH shim coils were only used for static shimming, because their large inductances would otherwise require an adequate pre-emphasis setup.

In addition to the scanner's built-in SH shim system, a home-made MC setup was used for homogenizing the B_0 field. It consisted of 16 identical circular coils that were arranged in 2 rows. The 2 rows were spaced by 20 mm and rotated by 22.5° with respect to each other and had a total height of 22 cm. No optimization in terms of coil position nor shape was performed to keep the fabrication process simple.^{16,17} All coils had 25 wire turns and a diameter of 100 mm. The copper wire used for winding had a diameter of 0.6 mm. The coils were mounted in an equally spaced manner on a fiber-glass cylinder with a diameter of 370 mm and a length of 310 mm (Figure 1). The explicit description of the wiring pattern for the MC setup used in this study can be found in Supporting Information Table S1 according to the public multi-coil information policy,¹⁸ together with a MATLAB (MathWorks, Natick, MA) script to visualize it (Supporting Information Data S1). No air or water cooling circuits were built into the setup.

The cylinder of the MC setup was chosen large enough to house an RF coil. The latter consisted of an 18-element transmit/32-element receive home-made tight-fit head coil array.¹⁹ The array consisted of 16 transceiver (TxRx) surface loops positioned in 2 rows on a cylindrical fiberglass holder and circumscribing the head. In addition, 2 perpendicular TxRx loops were placed at the top (most superior location) of

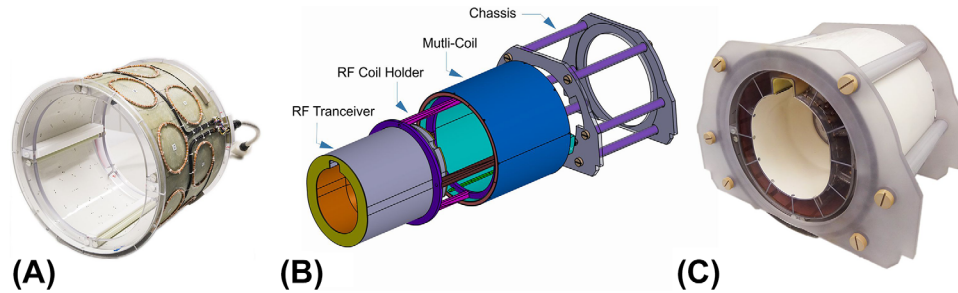


FIGURE 1 A, Photograph of the 16-channel multi-coil shim array. The coils are arranged in 2 rows and spaced equally on the cylinder surface. B, Schematic of the used setup. The setup consists of 4 layers. Starting with the innermost layer, they were RF transceiver coil, RF coil holder, multi-coil shim array, and a chassis to fix the multi-coil setup on the patient table of the scanner. C, Photograph of the assembled setup

the head. To further improve receive (Rx) performance, 14 Rx-only vertical loops were added perpendicularly in the center of the TxRx surface loops, which brings the total count of Rx elements to 32. The array was shielded to minimize radiation losses and improve decoupling of nonadjacent surface loops. At the same time the shield eliminated coupling to the MC setup. During transmission, the tight-fit array was driven using a home-built 16-way Wilkinson splitter with corresponding phase shifts incorporated into the splitter box.

Shim currents were supplied by home-built current amplifiers.²⁰ The amplifier architecture was a modified version of the reported amplifier in Ref 8. Each amplifier module consisted of a pair of OPA549 high-current op-amps to sink or source the current to the load. A 0.1- Ω current sense resistor with a 100 ppm/ $^{\circ}\text{C}$ temperature coefficient in series with the module's output was used to achieve simultaneous current feedback control and real-time monitoring. An adjustable proportional-integral-derivative controller was included in each module to obtain the best performance of each current driver during rapid current switching. The amplifier was equipped with an adjustable power supply and an automatic thermal shutdown mechanism for safety reasons.

2.2 | B_0 mapping and shimming

For B_0 mapping, the raw data of the dual-echo gradient-echo (GRE) scans were exported to MATLAB and a 3D Fourier transform was applied. The individual receiver channels of the RF coil were combined with an adaptive combination method²¹ that preserved the phase information. B_0 maps were generated by taking the phase difference of 2 images acquired at different TEs and dividing by the echo time difference. Strong B_0 inhomogeneities caused phase wraps that had to be unwrapped to ensure a correct calculation of the shim.²² A 3D brain mask was created based on the magnitude image of the first echo with the brain extraction tools²³ of the FMRIB Software Library²⁴ and applied to the map.

Calculation of adequate shim currents requires knowledge about the fields produced by the shim coils. Therefore, B_0 maps per current unit (Hz/A) were acquired on a large oil

phantom for each shim channel of the SH and MC shim setup. The shim maps were interpolated to a common coordinate space that had a FOV of $300 \times 300 \times 300 \text{ mm}^3$ and an isotropic resolution of 1 mm. Any other data (with arbitrary orientation) acquired during the scan session such as shimming regions of interest, masks, and other B_0 maps were transformed to this coordinates space as well.

The shimming process consists in finding the current values I_c for the N_c shim coils that solve the following equation with a minimal norm for the residual vector e :

$$M \cdot I_c = -B + e \quad (1)$$

where M is a rectangular matrix consisting of N_c columns that each list the corresponding shim basis map values for each voxel in the common coordinate space, and B is a column vector listing the measured field inhomogeneity values. The minimum norm least-squares solution can be found by using the pseudo-inverse of M :

$$I_c = -B \cdot M^\dagger \quad (2)$$

This method is computationally efficient and gives reliable results.²⁵ However, it is unconstrained and may return currents that cannot be delivered by the amplifier or that exceed the specified safety constraints. If this was the case, the shim current values were determined by a constraint least-squares optimization based on sequential quadratic programming.²⁶ The latter was implemented using MATLAB's *fmincon* function. The norm least-squares solution (Equation 2) was provided to MATLAB as a starting point for the non-linear optimization. Once shim currents were calculated, they were stored in a plain text file to be read by the scanner. A flowchart of the used shimming workflow is depicted in Figure 2.

2.3 | Imaging protocols

The study included 5 healthy volunteers (average age 26 ± 3 YEARS). In accordance with local research ethics policies and procedures, each of the subjects provided written, informed consent before being scanned.

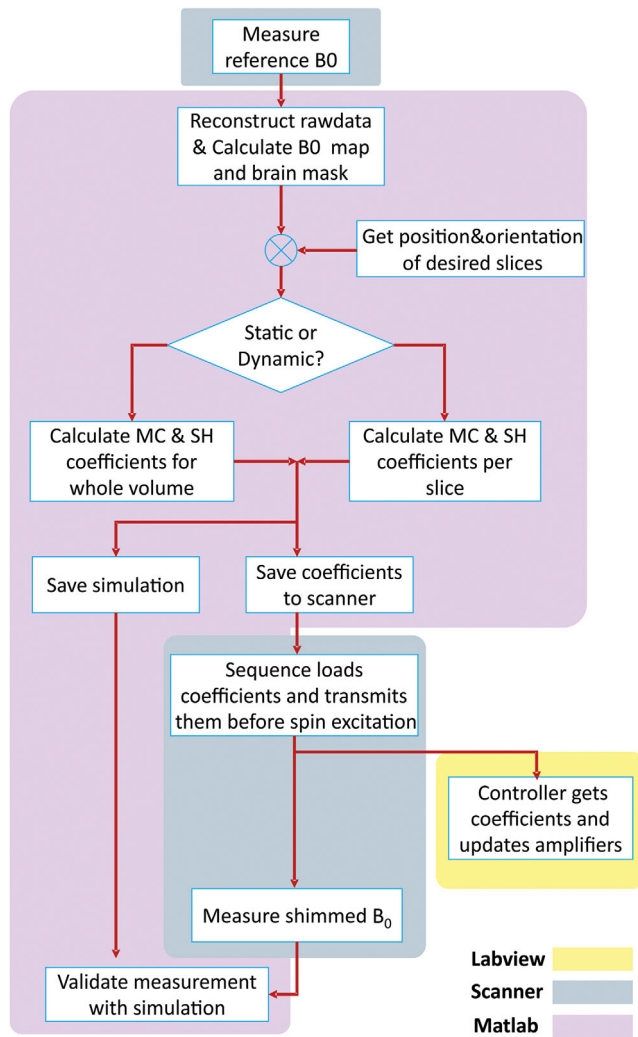


FIGURE 2 Workflow for the shimming process with the multi-coil setup. The whole workload is divided into 3 parts. The offline reconstruction and calculation of the shim currents are performed with MATLAB on a separate PC. The shim currents are exported to the scanner in a text file, which is read by the MR sequence. The sequence sends the shim values for the slice or volume to be measured to a PC that is running LabVIEW, which is used to control the amplifier. MC, multi-coil; SH, spherical harmonics

A modified 3D dual-echo GRE sequence with monopolar readout gradients and TEs of 1.92 and 3.56 ms was used to measure the magnetic field distribution in phantoms and in vivo. The measurement protocol was optimized (TR = 11 ms, flip angle = 7°, matrix = 128 × 128, slice thickness = 2.00 mm, and FOV 220 × 220 × 144 mm³) to scan the whole-brain volume and took 1 minute and 43 seconds.

All imaging sequences used in this study were modified to enable communication with external devices through a standard user datagram protocol (UDP), and could read shim coefficients from a text file before the start of the measurement. While running, the sequence broadcasted the shim information of the next slice to be imaged to all connected network devices. To compensate for a small lag in the whole workflow, the requested

shim current values were sent 10 ms before the first RF pulse of the next slice was played out. If the RF pulse thereafter belonged to the same slice, no new UDP package was sent.

A custom-build LabVIEW (National Instruments, Austin, TX) program was listening to these broadcasts of the sequence, and after reception of a new data package, it updated the output of a PXIe-6738 unit, a high-density analog output module. The PXIe-6738 was connected directly to the MC current driver, which immediately applied the new current settings. For static global shimming with the MC setup, the amplifier current values were broadcasted only once before the very first RF pulse.

The effectiveness of 4 different shimming strategies was evaluated based on 2 EPI scanning protocols. The resulting geometric distortions were compared after B₀ field homogenization using (1) global shimming up to second order with the scanner's built-in SH setup, (2) additional global shimming with the 16 channels of the MC setup, (3) dynamic slice-wise shimming with the 16 channels of the MC setup, and (4) dynamic slice-wise shimming with the 16 channels of the MC setup and the scanner's built-in SH setup up to first order. The first imaging protocol consisted of a 2-mm isotropic single-shot EPI scan with 12 axial slices. Further imaging parameters were flip angle = 80°, FOV = 220 × 220 mm, 6/8 phase partial Fourier, bandwidth = 1894 Hz/pixel, echo spacing = 0.59 ms, and TE/TR = 25/2000 ms. For the second protocol, the in-plane resolution was reduced to 1 mm and a GRAPPA²⁷ acceleration factor of 3 was used. Compared with the previous protocol, the following parameters had to be adapted: bandwidth = 1420 Hz/pixel and echo spacing = 1 ms. For both scans, the bandwidth was optimized to get the shortest echo spacing, and consequently minimal geometric distortions. To ensure enough brain coverage, a gap of 3 mm was introduced between slices.

The performance of the proposed shimming setup was also tested for single-voxel spectroscopy using a STEAM sequence. For this experiment, a voxel with a volume of 30 × 30 × 30 mm³ was selected in the prefrontal cortex, and a region slightly larger than the excitation volume was first shimmed with the scanner's second-order SH shim setup. Spectra were then acquired with and without using the MC setup. The used sequence parameters were chosen as follows: TE/TR = 20/4000 ms, bandwidth = 8000 Hz, vector size = 4096, 4 averages, and no water suppression. The spectra were reconstructed offline, and a phase and frequency drift correction was applied using the FID-A toolkit.²⁸ The full-width-at-half-maximum of the water spectra was evaluated to determine the degree of B₀ homogeneity and consequently MC performance.

2.4 | Setup characterization and safety tests

The settling time of the amplifier was measured by applying a step function as input and monitoring the amplifier's

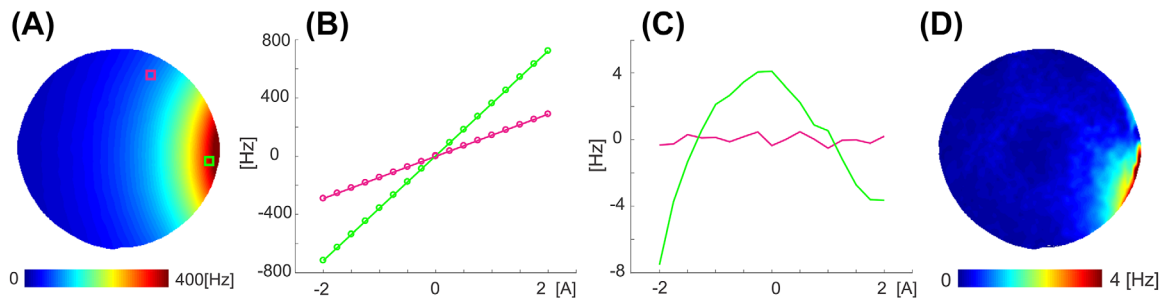


FIGURE 3 Amplifier output linearity was evaluated by applying currents in the range of -2 to 2 A and by measuring the corresponding B_0 map. Because all amplifiers are identical, analysis of an example channel is shown. A, Basis map produced by applying 1 A. B, Plot of the measured field for the 2 marked points in (A) and their first-order polynomial fit. C, Difference between the measured values and fit for inputs from -2 to 2 A for the same points. D, Mean of the absolute deviation from linearity among all input currents

output. Additionally, the step response of the amplifier was characterized by monitoring the B_0 fields produced by the MC setup with ^{19}F field probes.²⁹ The proportional-integral-derivative controller of the amplifiers was adjusted on a channel-by-channel basis to decrease oscillations and achieve a minimum settling time. Rapid gradient switching can induce high voltages in conducting structures; therefore, the behavior of the MC setup was examined while running EPI scans with different orientations of the readout gradient.

The linearity of the amplifier was tested by acquiring B_0 field maps of each shim channel for different current values ranging from -2 A to $+2$ A (step size 0.25 A). This acquisition was repeated twice: one time from -2 A to $+2$ A, and then in reversed order to evaluate the output hysteresis of the drivers as well.

Resistive heating of the B_0 coils is a major concern for subject safety and limits the amount of current that can be safely applied. Bench measurements were performed to determine the maximal allowed current. A constant current (1 , 2 , and 3 A) was passed simultaneously through all channels of the MC setup for 60 minutes while logging the temperature with several temperature sensors that were attached to the setup. Moreover, infrared (E6 thermal imager, FLIR Systems, Wilsonville, OR) images were acquired at the end of each measurement to visualize the heat distribution. The temperature measurements were repeated in the scanner bore using fiber optic temperature sensors while the scanner's ventilator was switched off. During the measurement, no power was transmitted through the RF coil.

Another safety-relevant test consisted of investigating the effect of the MC setup on the B_1^+ field distribution of the RF coil. An actual flip angle imaging sequence³⁰ was used to measure the B_1^+ field in a head-and-shoulder phantom filled with equivalent tissue properties ($\epsilon = 58.6$, $\sigma = 0.64$ S/m)³¹ with and without the MC setup being present.

Moreover, the SNR, the temporal SNR, and the noise correlation matrix of the transceiver array were measured in the absence and presence of the MC setup. The SNR was calculated based on the pseudo multiple replica approach.³²

For this purpose, a GRE image of the head-shaped phantom and a noise-only (flip angle = 0°) image were acquired. The temporal SNR was determined in a spherical agar phantom from 100 measurements.

2.5 | Shim performance

The performance of the MC setup was compared in simulations to a shimming setup with spherical harmonics up to sixth order. Additionally, basis maps of a commercial insert shim setup (MX10W-28, Resonance Research Inc, Billerica, MA) with a complete fourth-order and partial fifth-order and sixth-order set of SH shims was used in simulation as well.³³ Simulations for global and slice-wise shimming were performed based on 10 human brain B_0 maps that were acquired at 9.4 T and already shimmed with the scanner's second-order SH setup.

3 | RESULTS

The coils of the MC setup had an average inductance of 128 μH . When they were used as a load for the amplifier, a minimum settling time of 50 μs could be achieved by adjusting the proportional-integral-derivative controllers on a channel-by-channel basis when switching the output current from -1 A to $+1$ A. A maximum induced open-circuit voltage of approximately 4.5 V was measured for the MC setup when running an EPI sequence with very fast gradient switches from -32 to $+32$ mT/m in 350 μs . The induced voltage can be readily suppressed by an adjustable output voltage provided by the shim amplifier (maximum of 25 V). Running the same EPI sequence with the MC setup being connected to the amplifier led to peak current variations of approximately 40 mA. This value is small compared with the amplifier's current output range of ± 5 A. No image artifacts caused by these small current variations could be detected in any in vivo or phantom measurement. The measured B_0 maps for a set of current values showed that the output of each amplifier channel is linear in the requested range

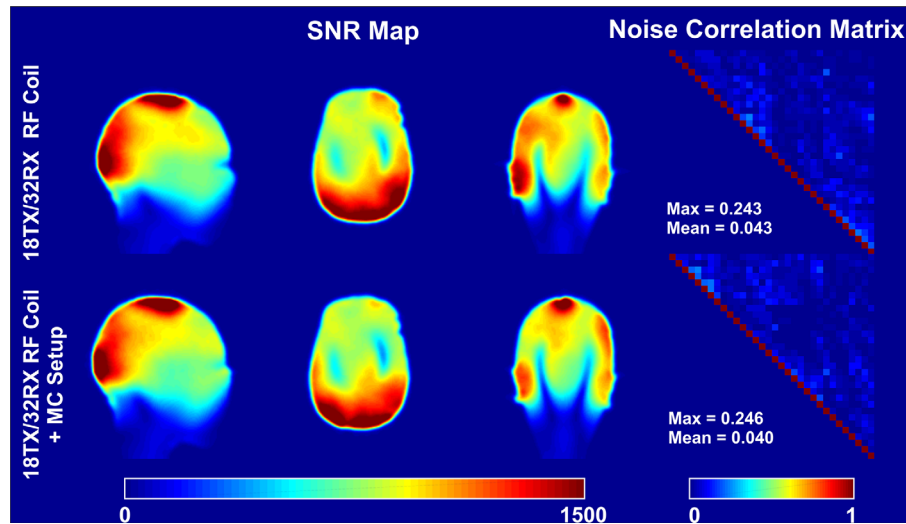


FIGURE 4 Comparison of SNR maps and noise correlation matrix in a head-shaped phantom. The observed differences can be attributed to discrepancies in positioning of the phantom

and that no additional nonlinearity calibration is needed (Figure 3).

The temperature measurements revealed that currents of 1, 2, and 3 A lead to a maximal surface temperature of the coil housing of 33°C, 38°C and 43°C, respectively. Aside from the MC setup, the RF coil is another heat source. Considering that the increase in temperature produced by the RF coil is below 4°C, an amperage of 1.5 A can be considered safe for human measurement.^{34,35}

Figure 4 demonstrates that the addition of the MC setup (connected to the amplifiers, all currents 0 A) does not significantly influence the SNR of the RF coil. Small deviations can be explained by differences in positioning the phantom in the coil. The noise correlation matrix does not exhibit any major changes either when the MC setup is added. The maximum correlation value is approximately 0.24 in both cases. The shield of the RF coil also prevents the MC setup from having an effect on B_1^+ field distribution (Supporting Information Figure S1). The observed small discrepancies may arise from differences in repositioning and/or B_0 shimming. No considerable alteration can be detected in the spatial distribution of temporal SNR (Supporting Information Figure S2). However, the presence of the MC setup appears to improve the temporal stability of the measurement as

indicated by the slightly higher temporal SNR values in some regions.

Table 1 lists the result of the simulation performed for 10 different whole-brain B_0 maps. The achieved mean standard deviation (SD) is reported for global and slice-wise shimming. The MC setup performs better than the third-order SH setup in case of slice-wise shimming. For global shimming, the MC setup can only outperform the third-order setup if the linear gradient terms are added and used in the optimization process. As expected, increasing the number of SH terms results in a better shim performance. A principal component analysis of the basis maps^{8,36} resulted in 8 independent components for the 16-channel MC setup, which agrees well with its performance close to the third-order SH setup.

Figure 5 shows a comparison of the different shimming scenarios that were examined in this study. A range of transversal slices is depicted to evaluate the shimming performance in the upper and lower brain. Large B_0 inhomogeneities persist after global shimming with the SH setup (Figure 5A, row 2), especially above the nasal cavities and around the ear canals. Global shimming with the MC setup permits reducing the field distortions further (Figure 5A, row 3). The standard deviation in some slices is higher for global MC than for global SH, because the optimization was performed on the

TABLE 1 Simulation of global and dynamic shimming for 10 whole-brain (including cerebrum, cerebellum, and brain stem) B_0 maps acquired at 9.4 T

	Initial	MC 16-channel	SH third	MC 16-channel + SH first	SH fourth	Insert shim	SH fifth	SH sixth
Global	94 ± 8	79.7 ± 8	82.6 ± 9	77.2 ± 8	72.5 ± 7	66.9 ± 6	63.3 ± 6	60.8 ± 7
Slice-wise		54.9 ± 5	51 ± 4	49.4 ± 5	44.9 ± 4	38.1 ± 3	37.7 ± 3	32.6 ± 3

Note. All B_0 maps were initially shimmed with the scanner's second-order shim setup. The performance of the 16-channel MC setup and spherical harmonics up to sixth order were evaluated. The mean SD achieved in the entire brain for all subjects is reported. For dynamic shimming, axial slices with 2-mm thickness were used.

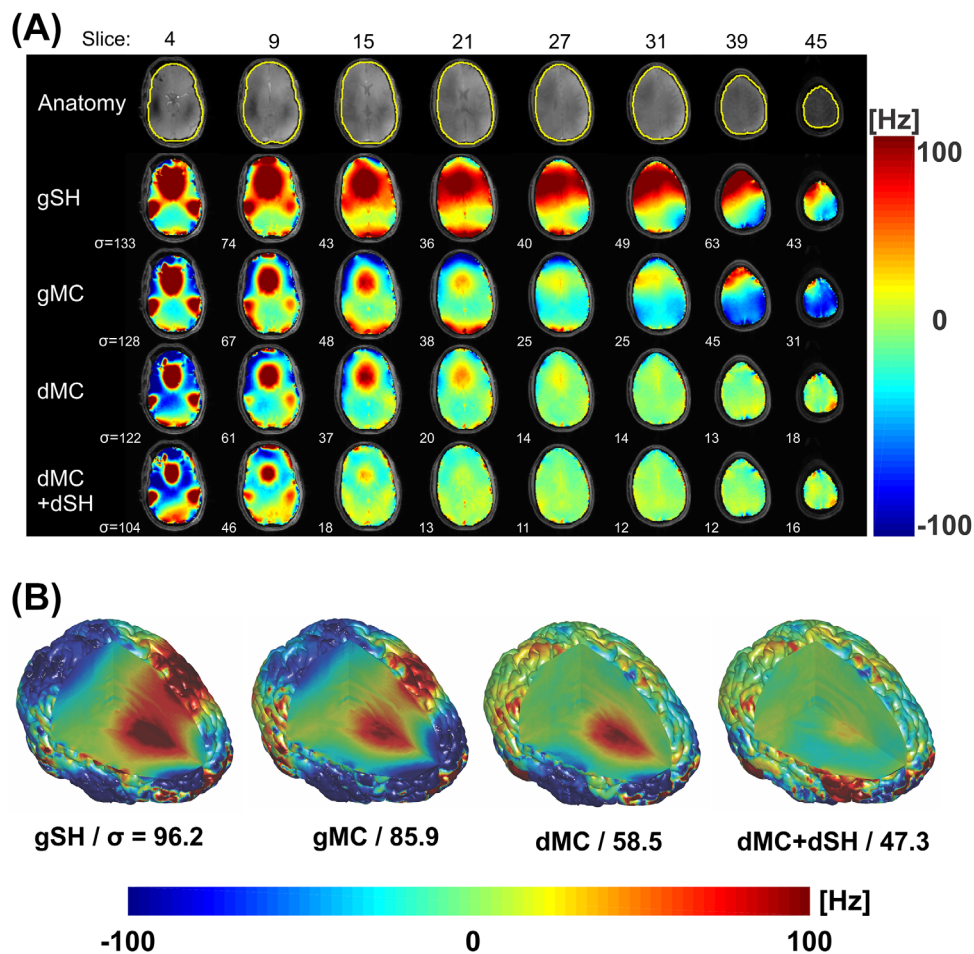


FIGURE 5 A, Comparison of different shimming strategies in several transversal slices. The first row shows an anatomical reference image and the volume of interest, which is indicated by a yellow line. The other 4 rows depict the B_0 field after using global SH shimming (gSH), global MC shimming with the previous settings of the SH shim (gMC), global SH shimming and dynamic slice-wise MC shimming (dMC), and dynamic slice-wise MC shimming together with adaptable zeroth and first-order SH shims (dMC + dSH), respectively. B, Field inhomogeneities mapped to the brain surface with 3 orthogonal cuts to demonstrate shimming performance in the depth of the brain. The SD is calculated for the whole brain

whole brain and not for each slice individually. The result of dynamic MC shimming is shown in Figure 5A, row 4. If the zeroth and first order of the SH shim are also adapted on a slice-by-slice basis, an average improvement of 12% in SD could be achieved for the 5 volunteers who participated in this study (Figure 5A, row 5). For better visualization, Figure 5B illustrates a comparison of the whole-brain B_0 map with 3 orthogonal cuts for each of the 4 shimming methods. A summary of the whole-brain B_0 SD for the 4 shimming scenarios of all 5 subjects is provided in Table 2.

Figure 6 and Supporting Information Figures S4 and S5 demonstrate the benefit of MC shimming for EPI acquisitions. The performance of the MC setup was evaluated for the 4 shimming methods for 2 different EPI scans. A GRE image, which is free of geometry distortions, is displayed in Figure 6, column 1, and serves as anatomical reference. Supporting Information Figure S4, which contains all acquired EPI images for a single subject, shows that the lower brain slices exhibit the strongest geometric distortions. These can be reduced with dynamic slice-wise shimming. The

accelerated EPI scan (Supporting Information Figure S4 on the right) shows even fewer artifacts as a result of a reduced phase-encoding time. Still, some distortions at the edge of

TABLE 2 Measured whole-brain B_0 SD for the 4 shimming strategies

	B_0 SD in the whole brain (Hz)			
	gSH	gMC	dMC	dMC + dSH
Subject 1	92.6	83.5	62.6	59.1
Subject 2	69.7	57.3	43.1	41.1
Subject 3	82.3	65.4	44.3	41.8
Subject 4	96.7	87.0	66.5	60.1
Subject 5	99.7	89.9	56.3	46.1
Average(μ/σ)	88.2/10.0	76.6/11.7	54.6/8.6	49.6/7.6

Note. The average and SD for each strategy is stated in the last row. There is a good agreement between the group-averaged shimming results and the simulated field deviations given in Table 1.

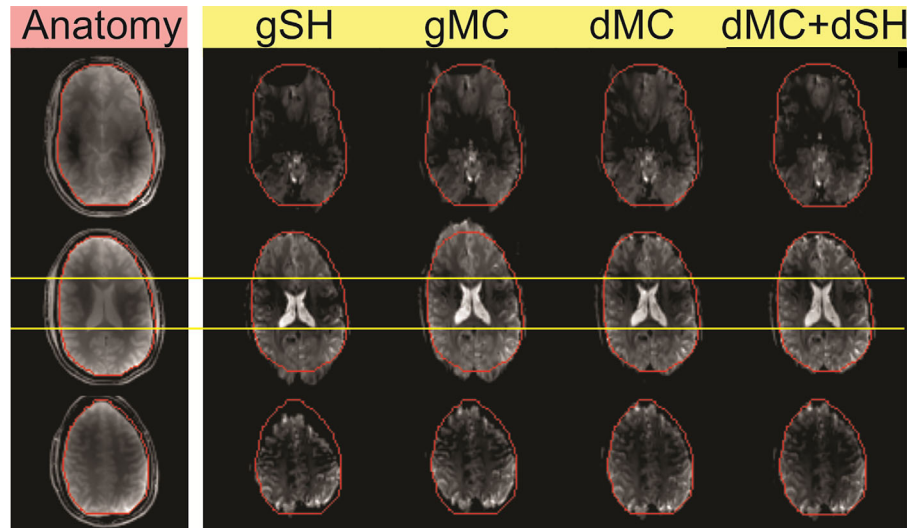


FIGURE 6 Evaluation of the observed geometric distortions for EPI acquisition in bottom, middle, and top slices and for different shimming strategies. The first column shows a gradient-echo (GRE) image for anatomical reference, and the last 4 columns depict the EPI images after global shimming with the scanner's second-order shim (gSH), global MC shimming (gMC), dynamic slice-wise MC shimming (dMC), and dynamic slice-wise MC shimming together with adaptable zeroth and first-order SH shims (dMC + dSH), respectively

the brain persist and cannot be undone even with dynamic shimming. Supporting Information Figure S5 includes 2 slices of EPI images for the 5 volunteers. The B_0 fields present during the EPI acquisitions are displayed in Supporting Information Figure S5, columns 1 to 4.

Table 3 summarizes the results of the single-voxel spectroscopy experiments performed on the 5 volunteers. The voxel position within the brain and spectra after shimming with scanner's second-order SH shim and the MC setup are shown in Figure 7. On average, the signal width of the water peak could be narrowed by a factor of 0.51. The average B_0 standard deviation of the voxel before and after shimming with MC setup was 37 and 16 Hz, respectively.

TABLE 3 Water peak full-width-at-half-maximum value from single voxel spectroscopy experiments before and after static shimming with the MC setup

	FWHM (Hz)		
	Scanner second order	MC 16-channel	Ratio
Subject 1	48.50	24.60	0.50
Subject 2	68.21	32.93	0.48
Subject 3	45.43	16.95	0.37
Subject 4	39.58	24.36	0.61
Subject 5	34.76	20.55	0.59
Average(μ/σ)	47.3/12.8	23.9/5.9	0.51/0.09

Note. The shimming was limited to a small region around the target voxel in the prefrontal cortex. On average, the width of the water peak could be narrowed by approximately 50%. FWHM, full width at half maximum

4 | DISCUSSION

The combination of RF coil and local B_0 shim array into 1 compact device has several advantages compared with other approaches in terms of handling, easy applicability, and full compatibility to rapid imaging such as EPI and SSFP. The results of the presented B_0 shim array with 16 circular loops demonstrate a performance similar to a full third-order SH shim system. In contrast to the latter, the MC coil setup can

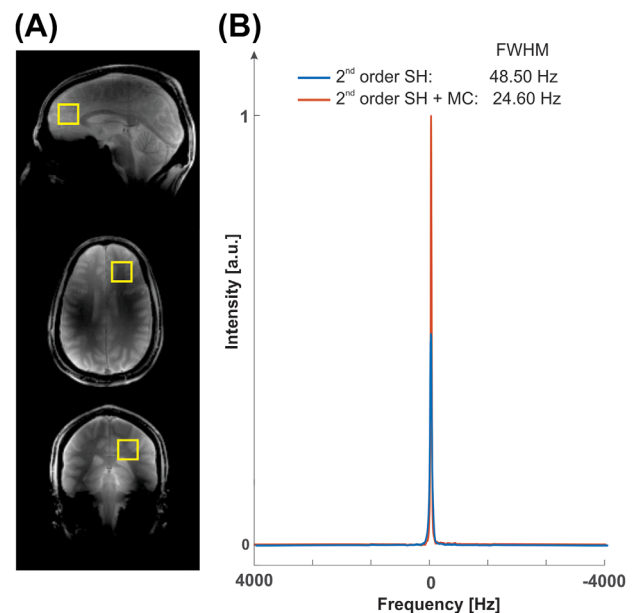


FIGURE 7 Single-voxel spectroscopy experiment. A, Position of the MRS voxel (30 mm^3) in the prefrontal cortex. B, Proton spectrum acquired after shimming with the scanner's second-order shim setup (blue) and additionally with the MC setup (red). FWHM, full width at half maximum

be used for dynamic shimming in a straightforward manner, owing to the small inductance of the circular B_0 coils. Moreover, the spatial distance of the MC setup from conducting materials such as the gradient shield, makes dedicated eddy current and cross-talk compensation unnecessary. Dynamic switching of the zeroth and first-order SH shim (i.e., frequency and linear gradients) provides an additional performance benefit by adding 4 extra degrees of freedom to the optimization process. In all experiments, the B_0 field was first homogenized with a standard second-order SH shim. Thereafter, MC shim currents were calculated for the entire brain or individual slices. It would also have been possible to determine both SH and MC shim currents concurrently, but this was not done to keep the workflow simple.

Unlike a previously reported design¹⁴ in which the MC setup was positioned inside of the RF coil, the design presented here used a shim matrix that surrounds the RF coil. There are several reasons for choosing this arrangement. On the one hand, this configuration allows one to easily mount a variety of different RF coils inside the shim array without requiring fundamental technical changes. One requirement, however, is that the RF coil is shielded; otherwise, interactions between the RF and B_0 coil are very likely. On the other hand, having the shim coil as an outer layer gives full flexibility regarding the positioning of the RF transceiver loops. The latter permits one to optimize the transmit efficiency and SNR, as placing conducting structures between the subject and the RF coil sometimes results in a dampening of the RF field due to shielding effects.⁷ It has been also proposed to use the same conducting structures for B_0 shimming and RF transmission.⁸ However, such a design is very hard to realize for a multichannel RF coil at ultrahigh field, because of the large number of capacitors that must be bridged. Furthermore, the proposed modular design easily allows one to exchange the outermost MC cylinder with other more sophisticated MC designs.^{16,17}

A downside of the used configuration is of course the fact that the shim coils are further away from the subject and a higher current is required to produce the same field. However, moving the loops further away from the subject and placing them in a separate outer tube that allows thermal conduction with the surrounding air provides an additional safety benefit. The *in vivo* and phantom measurements showed that a maximal current of ± 1.5 A per channel is sufficient in most cases. A total current of $9.5 \text{ A} \pm 1.1$ (mean \pm SD) for all channels was required to perform global shimming with the MC setup on the 5 subjects. The required total shim currents for slice-wise shimming amounted to $15.7 \text{ A} \pm 1.5$ in lower brain areas (including the temporal lobe), $13.1 \text{ A} \pm 2.8$ in the middle of brain (frontal lobe), and $11.8 \text{ A} \pm 2.6$ for upper brain slices.

The total number of coils was chosen based on design, fabrication, and cost considerations. First, the number and size of the B_0 coils must be chosen such that the entire surface of the mounting tube can be covered. Because each shim coil requires a dedicated amplifier, a higher number of coils can become very expensive and complicates the fabrication process. Still, the count of channels must be high enough to provide sufficient degrees of freedom for efficient shimming. In addition, a small number of large coils requires a more sophisticated amplifier design, because gradient switching induces in this case higher voltages that need to be counteracted. However, an increase of the coil count does not linearly improve shimming performance (e.g., increasing the number of coils from 8 to 32 results in an improvement of only 5% for global and 23% for dynamic shimming).^{8,37} The number and size of the coils as well as the number of wire turns used for this setup reduced the average required current to 1.5 A. Although the shim amplifiers can supply up to ± 5 A per channel, only their very linear operation range was used for the measurements and no extra calibration was needed.

The switching of the MC shim currents results in a torque on the shim coils and on the whole setup. The vibrations and the acoustic noise caused by electromotive forces was reduced by a heavy frame that was fixed to the patient table. In addition, current changes were implemented as 1-ms ramps with 128 intermediate steps. Nevertheless, subjects still reported a slight vibration of the setup. These vibrations can lead to a mismatch between B_0 field prediction and measurement for 2 reasons: First, the coil might slightly shift during the measurement; and second, subject discomfort can elicit involuntary movements. In fact, long experiments are prone to larger mismatch errors, as subjects are likely to move at some point during the measurement. This issue is especially critical for slice-wise shimming and thin slices. Ideally, the B_0 maps should be updated once in a while during long studies. However, in this study, the maps were only acquired at the very beginning of the scan session that lasted approximately 60 minutes. Reproducible positioning of the coil setup itself is also very important, because the basis maps for the shim coils and the actual B_0 map are not acquired in the same scan session. Therefore, the position of the MC was marked on the patient table to minimize positioning inaccuracies and to ensure the validity of the previously acquired basis maps.

The performance comparison of the different shimming strategies (global SH, global MC, dynamic MC, and dynamic MC + dynamic SH) shows that global shimming with the MC setup results in a 15% improvement compared with the second-order shim of the scanner. Dynamic slice-wise shimming provides an improvement of 61% if the MC setup is used on its own, and 78% if it is combined with the zeroth

and first-order of the SH shim setup. Geometric distortions of the EPI images could not be reduced to an acceptable level with global shimming. With slice-wise shimming, high geometric fidelity could be achieved in mid and upper brain slices. Although lower slices could not be shimmed to the same degree, a tangible improvement can be noticed compared with the globally shimmed scenario.

The shimmed B_0 field was compared with simulations to validate the calculated shim currents. The predicted field agreed very well with the measured B_0 map. In rare cases, a small frequency offset in the acquired field map was detected for dynamic slice-wise shimming, even though the SD of the simulated and acquired field was similar. This discrepancy could be corrected by adjusting the excitation/reception frequency.

Remarkably, the dynamic shimming performance was much higher for transversal slices in comparison to slices with the same FOV in sagittal orientation. This observation is probably related to the distribution of the individual coils on the cylinder surface. If a transversal orientation is chosen, a large number of coils can efficiently contribute to the homogenization of the slice. With the current arrangement of 8 coils in each of the 2 rows, sagittal and coronal slices are far away from most of the coils, and the optimization under current constraints become more challenging. In addition, the shape of the field inhomogeneity of the human brain in the transversal plane is generally easier for the optimizer to solve. In the sagittal plane, strong field distortions in the frontal and temporal lobe with opposite off-resonance values have to be mitigated. Rapid variations and changes of the sign of the field inhomogeneity results in a lower shimming efficiency.

5 | CONCLUSIONS

In this study, we designed a 16-channel MC setup for B_0 shimming of human brain at ultrahigh field. However, the plan to design a setup with more shim coils, which brings more degrees of freedom, is underway. The MC setup was combined successfully with the scanner's built-in shim coils up to the first order for dynamic shimming. A different arrangement of the coils and optimization of the shape of the coils may improve the shimming performance further.

ACKNOWLEDGMENTS

We thank Martin Eschelbach for his help in measuring B_0 temporal variation with field probes, and Paul Chang and Sahar Nassirpour for providing insert-shim basis maps. We also acknowledge Azadeh Nazemorroaya for the great support during the experiments.

ORCID

Ali Aghaeifar  <http://orcid.org/0000-0002-6964-0992>

REFERENCES

- [1] Jezzard P, Balaban RS. Correction for geometric distortion in echo planar images from B_0 field variations. *Magn Reson Med.* 1995;34:65-73.
- [2] Sekihara K, Kohno H. Image restoration from nonuniform static field influence in modified echo-planar imaging. *Med Phys.* 1987;14:1087-1089.
- [3] Lemke C, Hess A, Clare S, Bachtiar V, Stagg C, Jezzard P, Emir U. Two-voxel spectroscopy with dynamic B_0 shimming and flip angle adjustment at 7 T in the human motor cortex. *NMR Biomed.* 2015;28:852-860.
- [4] Juchem C, de Graaf RA. B_0 magnetic field homogeneity and shimming for in vivo magnetic resonance spectroscopy. *Anal Biochem.* 2017;529:17-29.
- [5] Deichmann R, Gottfried JA, Hutton C, Turner R. Optimized EPI for fMRI studies of the orbitofrontal cortex. *NeuroImage.* 2003;19:430-441.
- [6] Olman CA, Davachi L, Inati S. Distortion and signal loss in medial temporal lobe. *PLoS One.* 2009;4:e8160.
- [7] Juchem C, Nixon TW, McIntyre S, Rothman DL, Graaf RA De. Magnetic field modeling with a set of individual localized coils. *J Magn Reson.* 2010;204:281-289.
- [8] Stockmann JP, Witzel T, Keil B, Polimeni JR, Mareyam A, Lapiere C, Setsompop K, Wald LL. A 32-channel combined RF and B_0 shim array for 3T brain imaging. *Magn Reson Med.* 2016;75:441-451.
- [9] Truong T-KK, Darnell D, Song AW. Integrated RF/shim coil array for parallel reception and localized B_0 shimming in the human brain. *NeuroImage.* 2014;103:235-240.
- [10] Juchem C, Umesh Rudrapatna S, Nixon TW, de Graaf RA. Dynamic multi-coil technique (DYNAMITE) shimming for echo-planar imaging of the human brain at 7 Tesla. *NeuroImage.* 2015;105:462-472.
- [11] Blamire AM, Rothman DL, Nixon T. Dynamic shim updating: a new approach towards optimized whole brain shimming. *Magn Reson Med.* 1996;36:159-165.
- [12] Juchem C, Brown PB, Nixon TW, McIntyre S, Rothman DL, De Graaf RA. Multicoil shimming of the mouse brain. *Magn Reson Med.* 2011;66:893-900.
- [13] Juchem C, Herman P, Sanganahalli BG, Brown PB, McIntyre S, Nixon TW, Green D, Hyder F, de Graaf RA. DYNAMIC Multi-coil TEchnique (DYNAMITE) shimming of the rat brain at 11.7T. *NMR Biomed.* 2014;27:897-906.
- [14] Juchem C, Nixon TW, McIntyre S, Boer VO, Rothman DL, De Graaf RA. Dynamic multi-coil shimming of the human brain at 7 T. *J Magn Reson.* 2011;212:280-288.
- [15] Kim T, Lee Y, Zhao T, Hetherington HP, Pan JW. Gradient-echo EPI using a high-degree shim insert coil at 7 T: implications for BOLD fMRI. *Magn Reson Med.* 2017;78:1734-1745.
- [16] Zivkovic I, Mirkes C, Scheffler K. B_0 shimming at 9.4T using a multicoil approach—coil design with genetic algorithm. In

- Proceedings of 24th Annual Meeting of ISMRM, Singapore, 2016. Abstract 1152.
- [17] Zivkovic I, Tolstikhin I, Schölkopf B, Scheffler K. B0 matrix shim array design-optimization of the position, geometry and the number of segments of individual coil elements. In: Proceedings of the 33rd Annual Scientific Meeting of the European Society for Magnetic Resonance in Medicine and Biology, Vienna, Austria, 2016. Abstract 36.
- [18] Juchem C, de Graaf RA. The public multi-coil information (PUMCIN) policy. *Magn Reson Med*. 2017;78:2042-2047.
- [19] Avdievich, Nikolai Giapitzakis, Ioannis Henning A. Double-row 16-element tight-fit transceiver phased array with high transmit performance for whole human brain imaging at 9.4T. In: Proceedings of the 25th Annual Meeting of ISMRM, Honolulu, HI, 2017. Abstract 759.
- [20] Aghaeifar A, Zivkovic I, Steffen T, Mirkes C, Scheffler K. Flexible gradient driver system for a multi-coil setup; design considerations and implementation. In: Proceedings of the 34th Annual Scientific Meeting of the European Society for Magnetic Resonance in Medicine and Biology, Barcelona, Spain, 2017. Abstract 50.
- [21] Walsh DO, Gmitro AF, Marcellin MW. Adaptive reconstruction of phased array MR imagery. *Magn Reson Med*. 2000;43:682-690.
- [22] Abdul-Rahman HS, Gdeisat MA, Burton DR, Lalor MJ, Lilliey F, Moore CJ. Fast and robust three-dimensional best path phase unwrapping algorithm. *Appl Opt*. 2007;46:6623-6635.
- [23] Smith SM. Fast robust automated brain extraction. *Hum Brain Mapp*. 2002;17:143-155.
- [24] Smith SM, Jenkinson M, Woolrich MW, et al. Advances in functional and structural MR image analysis and implementation as FSL. *NeuroImage*. 2004;23:208-219.
- [25] Nassirpour S, Chang P, Fillmer A, Henning A. A comparison of optimization algorithms for localized in vivo B0 shimming. *Magn Reson Med*. 2018;79:1145-1156.
- [26] Bonnans J-F, Gilbert JC, Lemarechal C, Sagastizábal CA. *Local methods for problems with equality constraints*. In: Numerical optimization. Berlin: Springer; 2006. pp 215-253.
- [27] Griswold MA, Jakob PM, Heidemann RM, Nittka M, Jellus V, Wang J, Kiefer B, Haase A. Generalized autocalibrating partially parallel acquisitions (GRAPPA). *Magn Reson Med*. 2002;47:1202-1210.
- [28] Simpson R, Devenyi GA, Jezzard P, Hennessy TJ, Near J. Advanced processing and simulation of MRS data using the FID appliance (FID-A)—an open source, MATLAB-based toolkit. *Magn Reson Med*. 2017;77:23-33.
- [29] Eschelbach M, Aghaeifar A, Bause J, Handwerker J, Anders J, Scheffler K. A comparison of prospective motion correction with 19F NMR field probes and an optical camera. In: Proceedings of the 25th Annual Meeting of ISMRM, Honolulu, HI, 2017. Abstract 1304.
- [30] Yarnykh VL. Actual flip-angle imaging in the pulsed steady state: a method for rapid three-dimensional mapping of the transmitted radiofrequency field. *Magn Reson Med*. 2007;57:192-200.
- [31] Beck BL, Jenkins KA, Rocca JR, Fitzsimmons JR. Tissue-equivalent phantoms for high frequencies. *Concepts Magn Reson Part B Magn Reson Eng*. 2004;20:30-33.
- [32] Robson PM, Grant AK, Madhuranthakam AJ, Lattanzi R, Sodickson DK, McKenzie CA. Comprehensive quantification of signal-to-noise ratio and g-factor for image-based and k-space-based parallel imaging reconstructions. *Magn Reson Med*. 2008;60:895-907.
- [33] Chang P, Nassirpour S, Henning A. Modeling real shim fields for very high degree (and order) B0 shimming of the human brain at 9.4T. *Magn Reson Med* 2018;79:529-540.
- [34] Hoffmann J, Henning A, Giapitzakis IA, Scheffler K, Shajan G, Pohmann R, Avdievich NI. Safety testing and operational procedures for self-developed radiofrequency coils. *NMR Biomed*. 2016;29:1131-1144.
- [35] Anon. IEC (Edition 3.1 2013) 60601-2-33 Medical electrical equipment. Part 2-33: particular requirements for the basic safety and essential performance of magnetic resonance equipment for medical diagnosis, Geneva, Switzerland.
- [36] Breuer FA, Blaimer M, Mueller MF, Heidemann RM, Griswold MA, Jakob PM. The use of principal component analysis (PCA) for estimation of the maximum reduction factor in 2D parallel imaging. In: Proceedings of the 13th Annual Scientific Meeting of the European Society for Magnetic Resonance in Medicine and Biology, Miami, FL, 2005. Abstract 2668.
- [37] Stockmann JP, Wald LL. In vivo B0 field shimming methods for MRI at 7T. *NeuroImage*. 2017. <https://doi.org/10.1016/j.neuroimage.2017.06.013>.

SUPPORTING INFORMATION

Additional Supporting Information may be found in the supporting information tab for this article.

FIGURE S1 Comparison of B_1^+ as a safety relevant parameter in the absence and presence of the MC setup according to the institute's safety procedure.³⁴ The measured field remains very similar regarding spatial distribution and strength

FIGURE S2 Comparison of temporal SNR as a quality relevant parameter in the absence and presence of the MC setup. The signal appears to be slightly more stable in the presence of the MC setup. An apparent reason can be the result of a heavier setup, which diminishes vibration

FIGURE S3 Comparison of the B_0 SD for several slices after shimming with the scanner's second-order SH shims and after shimming with the MC setup in simulation and measurement. The direction of slice sequence is from inferior to superior

FIGURE S4 Evaluation of the observed geometric distortions for 2 EPI sequence settings and different shimming conditions. Echo spacing was 0.59 and 1 ms for nonaccelerated and accelerated EPI, respectively. The first column shows a GRE image for anatomical reference. The other 2 blocks of images correspond to a fully acquired and an accelerated EPI scan, respectively. Four horizontal lines have been added to mark the location of the ventricles as observed in the GRE. Global MC shimming (gMC) mitigates some distortions in the center of slices, but does not

perform well at the boundaries of the brain for both EPI scans. Dynamic MC shimming (dMC) improves image quality considerably. The latter can be further enhanced by dynamically adapting the zeroth and first-order SH shim as well

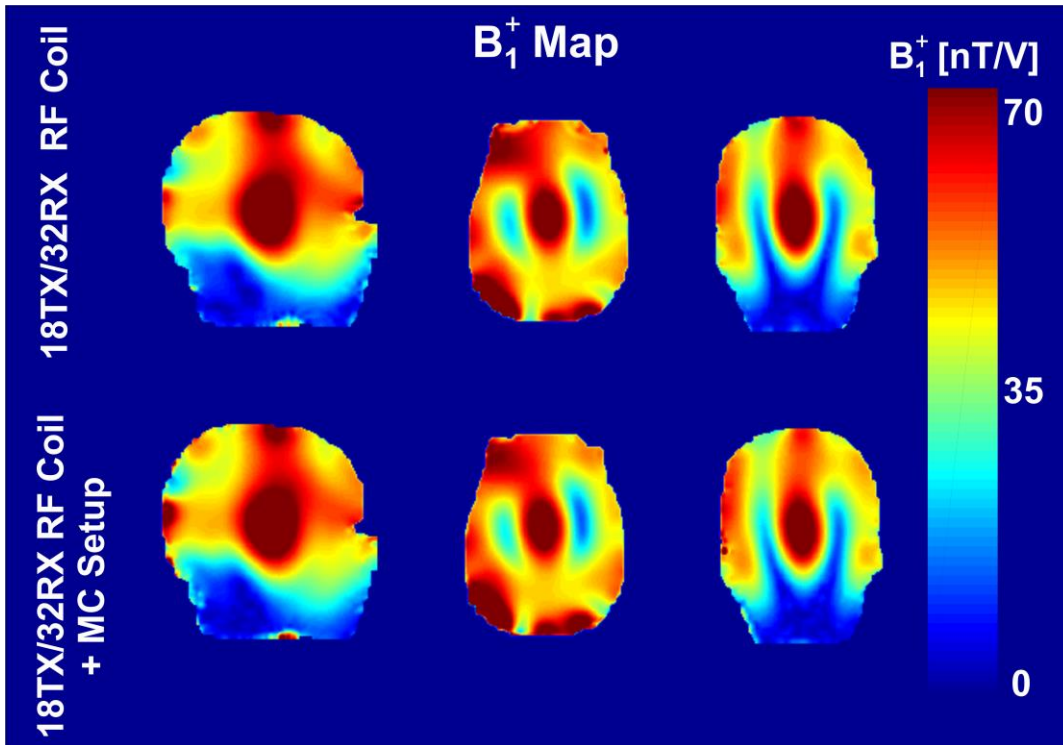
FIGURE S5 Evaluation of the observed geometric distortions for EPI acquisition across all 5 subjects of the study and for different shimming strategies. The first 4 columns show B_0 maps after global shimming with the scanner's second-order shim (gSH), global MC shimming (gMC), dynamic slice-wise MC shimming (dMC), and dynamic slice-wise MC shimming together with adaptable zeroth and first-order SH shims (dMC + dSH), respectively. The fifth column shows a GRE image for anatomical reference, and the last 4 columns depict the EPI images. In subject 5,

echo spacing was deliberately increased from 0.59 to 1 ms to exacerbate distortion. Still, dMC could eliminate many artifacts and enhanced the image quality

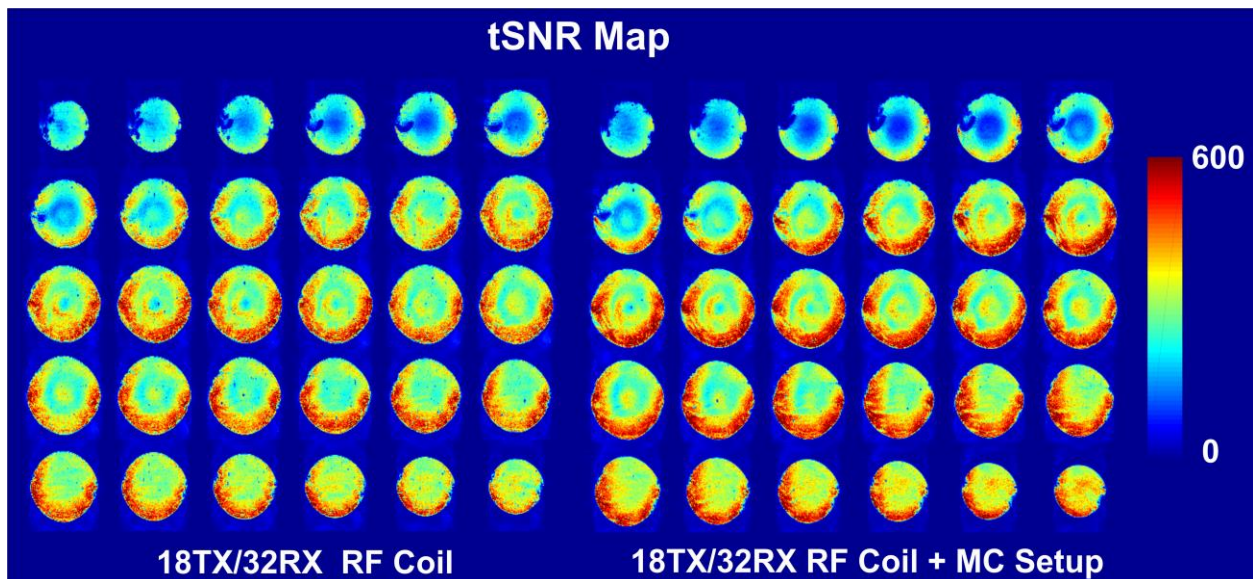
TABLE S1 Sixteen-channel multi-coil wire pattern used in this study

DATA S1 MATLAB script to read and visualize wire pattern of the multi-coil in Supporting Information Table S1

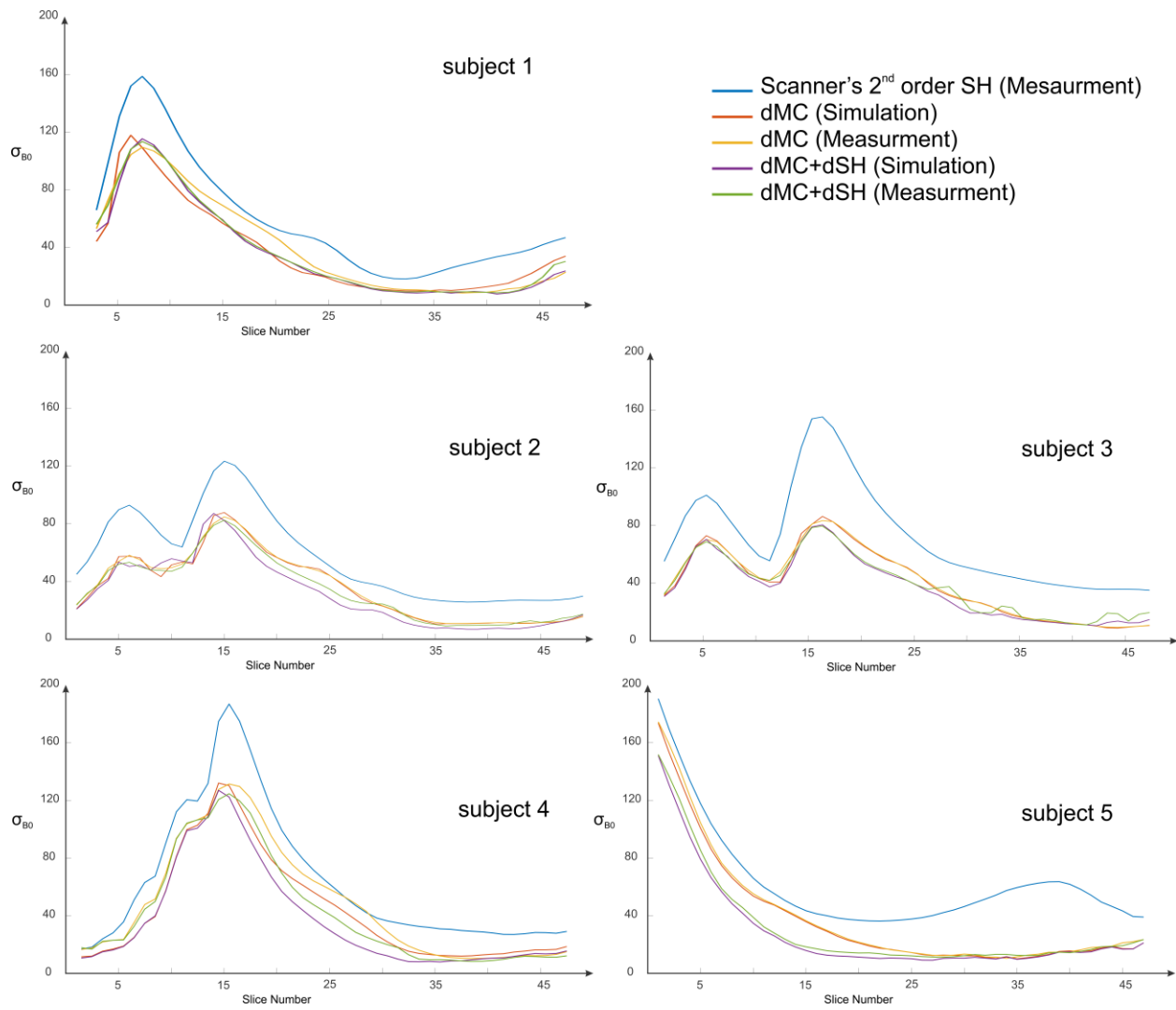
How to cite this article: Aghaeifar A, Mirkes C, Bause J, et al. Dynamic B_0 shimming of the human brain at 9.4 T with a 16-channel multi-coil shim setup. *Magn Reson Med*. 2018;80:1714–1725. <https://doi.org/10.1002/mrm.27110>



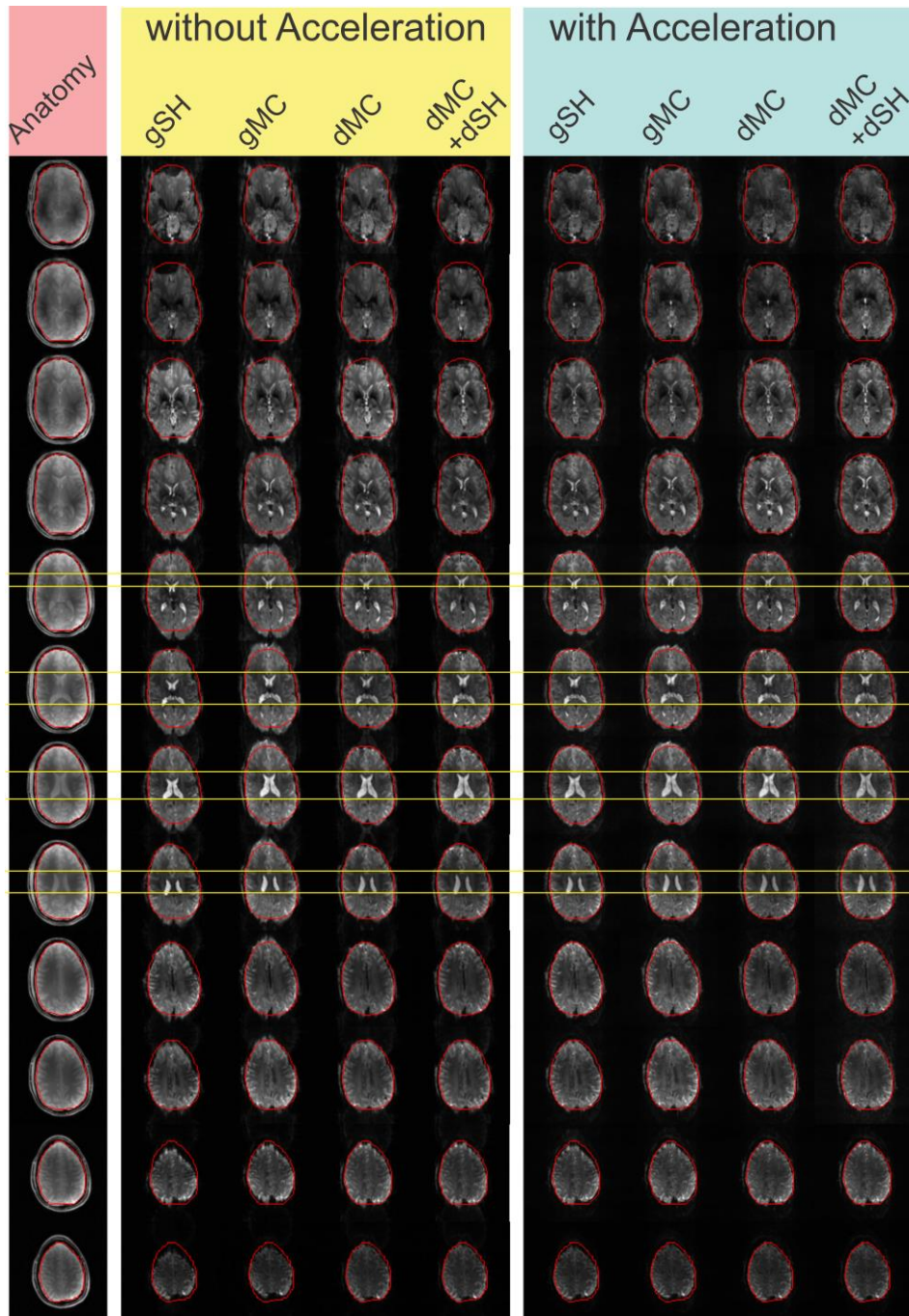
Supporting Figure S1. Comparison of B_1^+ as a safety relevant parameter in the absence and presence of the MC setup according to the institute's safety procedure [34]. The measured field remains very similar regarding spatial distribution and strength.



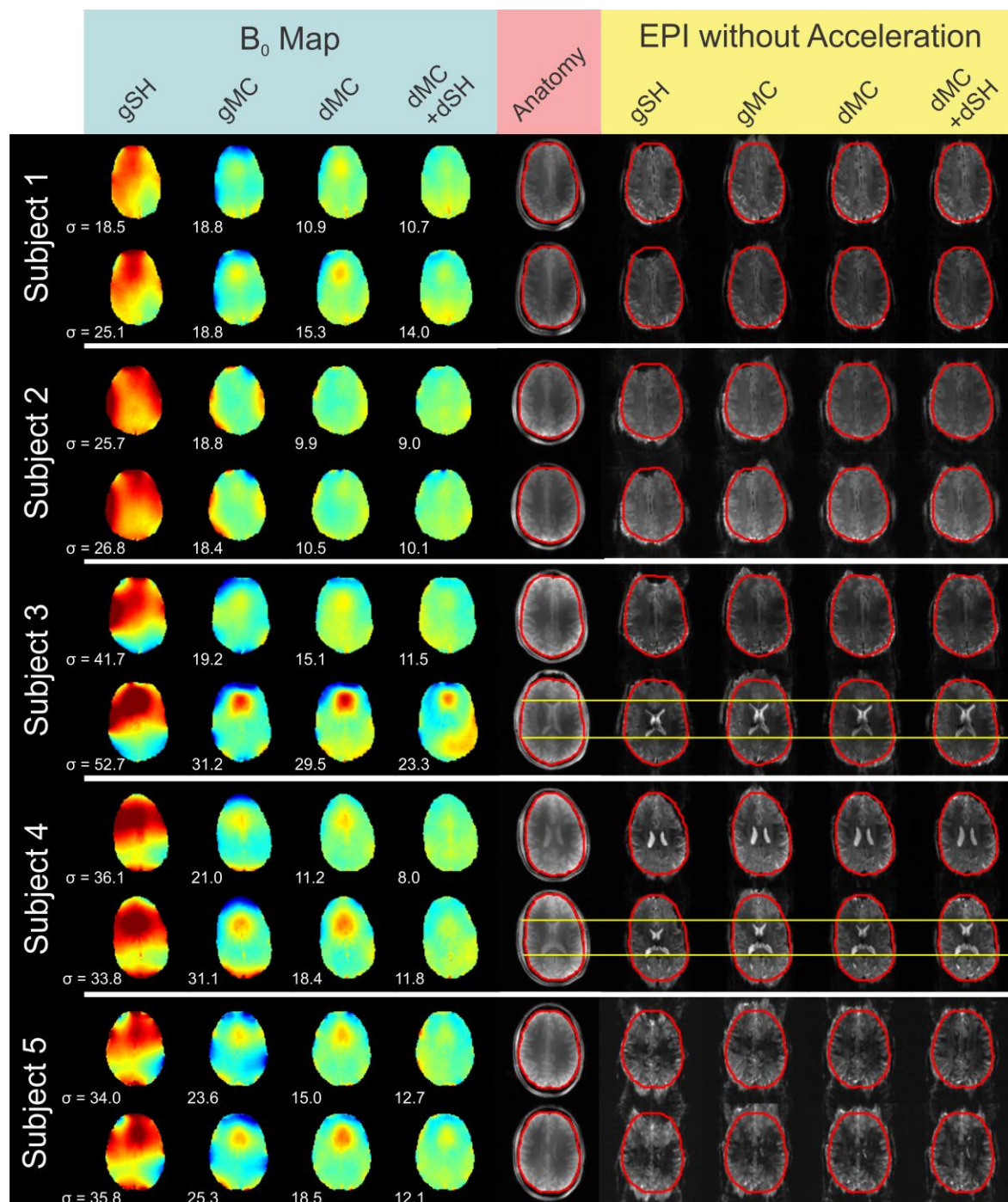
Supporting Figure S2. Comparison of tSNR as a quality relevant parameter in the absence and presence of the MC setup. The signal appears to be slightly more stable in the presence of the MC setup. An apparent reason can be due to a heavier setup which diminishes vibration.



Supporting Figure S3. Comparison of the B_0 standard deviation for several slices after shimming with scanner's 2nd order SH shims as well as after shimming with the MC setup in simulation and measurement. The direction of slice sequence is from inferior to superior.



Supporting Figure S4. Evaluation of the observed geometric distortions for two EPI sequence settings and different shimming conditions. Echo-spacing was 0.59 ms and 1 ms for un- accelerated and accelerated EPI respectively. The first column shows a GRE image for anatomical reference. The other two blocks of images correspond to a fully acquired and an accelerated EPI scan, respectively. Four horizontal lines have been added to mark the location of the ventricles as observed in the GRE. Global MC (gMC) shimming mitigates some distortions in the center of slices but does not perform well at the boundaries of the brain for both EPI scans. Dynamic MC (dMC) shimming improves image quality considerably. The latter can be further enhanced by dynamically adapting the zeroth and first order SH shim as well.



Supporting Figure S5. Evaluation of the observed geometric distortions for EPI acquisition across all five subjects of the study and for different shimming strategies. The first four columns show B₀ maps after global shimming with scanner's 2nd order shim (gSH), global MC shimming (gMC), dynamic slice-wise MC shimming (dMC) and dynamic slice-wise MC shimming together with adaptable 0th and 1st order SH shims (dMC + dSH) respectively. The fifth column shows a GRE image for anatomical reference and the last four columns depict the EPI images. In subject 5, echo-spacing was deliberately increased from 0.59 ms to 1 ms to exacerbate distortion. Still, dMC could eliminate many artifacts and enhanced image quality.

Supporting Data S1. Matlab script to read and visualize wire pattern of the multi-coil in supporting Table S1.

```

classdef PUMCIN_OBJ
% Read and plot PUMCIN formatted file
% Author: Ali Aghaeifar (ali.aghaeifar@tuebingen.mpg.de)
% Example:
% myaddr = 'c:\mc.txt';
% mcObj = PUMCIN_OBJ(myaddr);
% mcObj.plotCoils;
properties
    filepath;
    coilpos;
    wireRad = 0.6; % mm
end % properties
methods
function obj = PUMCIN_OBJ(fileadd)
    if nargin < 1
        info = 'Please select PUMCIN file to read';
        [FileName,PathName,FilterIndex] = uigetfile('*.txt',info);
        if FilterIndex == 0
            return;
        end
        obj.filepath = fullfile(PathName, FileName);
    else
        if exist(fileadd, 'file') ~= 2
            error('Input is not a valid file address');
        end
        obj.filepath = fileadd;
    end
    obj.coilpos = importPUMCIN(obj);
end

function coilpos = importPUMCIN(obj)
    fileID = fopen(obj.filepath);
    rawdata = textscan(fileID,'%d %f %f %f %d','CommentStyle','%');
    fclose(fileID);
    if numel(rawdata) ~= 5 % There is 5 columns
        error('Non-standard input file');
    end

    ind = [find(~rawdata{5}); numel(rawdata{5})+1]; % [find zeros ; index of the last
element]
    coilpos = cell(numel(ind)-1,1);
    for i=1:numel(ind)-1
        coilpos{i}.x = rawdata{2}(ind(i):ind(i+1)-1);
        coilpos{i}.y = rawdata{3}(ind(i):ind(i+1)-1);
        coilpos{i}.z = rawdata{4}(ind(i):ind(i+1)-1);
        coilpos{i}.t = rawdata{5}(ind(i):ind(i+1)-1);
    end
end

function plotCoils(obj)
    widthDef = 2*obj.wireRad;
    myCMap = jet(numel(obj.coilpos));
    for c=1:numel(obj.coilpos)
        for d=1:numel(obj.coilpos{c}.x)-1
            h=line([obj.coilpos{c}.x(d); obj.coilpos{c}.x(d+1)], [obj.coilpos{c}.y(d);
obj.coilpos{c}.y(d+1)], [obj.coilpos{c}.z(d); obj.coilpos{c}.z(d+1)]);
            set(h,{'LineWidth', 'Color'}, {widthDef*sqrt(double(obj.coilpos{c}.t(d+1))),
myCMap(c,:)});
        end
    end
    view(-30, 45);
    xlabel('X'); ylabel('Y'); zlabel('Z');
    axis image;
end

end % methods
end % classdef

```

Publication II

“Dynamic B0 shimming of the motor cortex and cerebellum
with a multi-coil shim setup for BOLD fMRI at 9.4T”


A. Aghaeifar, J. Bause, E. Leks, W. Grodd, K. Scheffler

Magnetic Resonance in Medicine, (2019)

DOI: 10.1002/mrm.28044

NOTE

Dynamic B_0 shimming of the motor cortex and cerebellum with a multicoil shim setup for BOLD fMRI at 9.4T

Ali Aghaeifar^{1,2}  | Jonas Bause^{1,2,3} | Edyta Leks^{1,2,3} | Wolfgang Grodd¹ | Klaus Scheffler^{1,3}

¹High-Field Magnetic Resonance Center, Max Planck Institute for Biological Cybernetics, Tuebingen, Germany

²IMPRS for Cognitive and Systems Neuroscience, University of Tuebingen, Tuebingen, Germany

³Department of Biomedical Magnetic Resonance, University of Tuebingen, Tuebingen, Germany

Correspondence

Ali Aghaeifar, High-Field Magnetic Resonance Center, Max Planck Institute for Biological Cybernetics, Max-Planck-Ring 11, 72076 Tuebingen, Germany.
Email: ali.aghaeifar@tuebingen.mpg.de

Funding information

Deutsche Forschungsgemeinschaft, Grant/Award Number: DFG SCHE 658/12 (Reinhart Koselleck); Max-Planck-Gesellschaft

Purpose: We assessed how improved static magnetic field (B_0) homogeneity with a dynamic multicoil shimming can influence the blood oxygen level dependent (BOLD) contrast to noise when echo planar imaging (EPI) sequence is used for a motor task functional MRI study. We showed that a multicoil shim setup can be a proper choice for dynamic shimming of 2 spatially distant areas with different inhomogeneity distributions.

Methods: A 16-channel multicoil shim setup is used to provide improved B_0 homogeneity by dynamic slice-wise shimming. The performance of dynamic B_0 shimming was investigated in 2 distinct brain regions, the motor cortex and the cerebellum, in the same experiment during a finger-tapping task. Temporal SNR (tSNR), geometric distortion of the EPIs, and results of an analysis with a general linear model before and after shimming with the multicoil were compared.

Results: Reduced B_0 deviation by 30% and 52% in the cerebellum and motor cortex, respectively, resulted in higher tSNR and a reduction of distortions in the EPI. Statistical analysis applied to the EPIs showed higher t values and increased number of voxels above significance threshold when shimming with the multicoil setup.

Conclusions: Improved B_0 homogeneity leads to higher tSNR and enhances the detection of BOLD signal.

KEYWORDS

B_0 inhomogeneity, BOLD signal, multicoil, shimming, temporal SNR, ultrahigh field

1 | INTRODUCTION

In most applications, functional MRI (fMRI) is performed with gradient echo planar imaging (EPI), a fast T_2^* -weighted sequence which has a high sensitivity to blood oxygen level dependent (BOLD) signal changes. EPI possesses a long

readout duration, which makes the images susceptible to geometric distortion¹ and signal loss because of B_0 inhomogeneity. These effects are even more pronounced at ultra-high fields (UHF) given that the magnetic field variations induced from susceptibility differences linearly increase with the magnetic field strength.

A recent quantitative comparison between a high-order shim insert and the scanner's second-order shim demonstrated the influence of shimming on BOLD fMRI.² The static magnetic field can be additionally optimized to enhance BOLD sensitivity over a region of interest and improve BOLD response detection.³ MR scanners are equipped with dedicated coils for shimming of the static field, in which superposition of the magnetic fields produced by the individual shim coils is used to shape a reverse field and cancel existing field perturbations. However, because of the limited number of the coils and difficulties in dynamic driving of large coils, the current scanner's built-in shim setup (up to the second- or third-order spherical harmonic) is not sufficient at UHF, and thus the use of additional shim equipment is inevitable.

A more cost-effective and flexible shimming approach is a multicoil shim setup,⁴ which benefits from an array of small local coils. These local coils can even be integrated into the radiofrequency (RF) coil for joint reception, excitation, and shimming⁵ or even used for acceleration of MRI acquisition.⁶ For example, the application of a 16-channel multicoil setup for dynamic shimming of the human brain at 9.4T showed approximately 40% improvement in B_0 field uniformity.⁷ In another study, dynamic multicoil shimming was used for T_2^* mapping and EPI at 7T, which produced 10% to 50% longer T_2^* values for voxels in the prefrontal and temporal cortices and reduced the average voxel shifts from 8 to 3 mm.⁸ Such a shim setup can be further optimized for a superior performance in human brain shimming.^{9,10}

fMRI of long-range connectivity between 2 spatially distant cortical regions is one of the key applications of dynamic shimming. Both regions need to be stimulated and acquired within 1 measurement for a reliable estimation of functional connectivity. Therefore, it would be beneficial to exclude parts of the brain between distant volumes of interest (VOIs) to achieve higher temporal resolution. Even if 2 VOIs are small, the effectiveness of the standard scanner's built-in global shimming process can be dramatically reduced if there is a large gap between them. In one of the first applications of dynamic shimming, a dynamic first-order shim update was performed at 3T for a combined measurement of the human brain and the cervical spinal cord¹¹; this was recently also achieved with dynamic slice-by-slice shimming.¹² Another interesting application is studying the connection between motor cortex and cerebellum, which plays an essential role in the coordination of voluntary movements.^{13,14} By receiving direct afferences from the motor cortex, the cerebellum regulates the accurate planning and online control of active and passive movements. To better understand these mechanisms and changes during diseases, it is therefore important to capture both areas in functional MRI experiments. To this end, simultaneous EPI of the motor cortex and cerebellum with 2D-selective excitation and parallel transmission has already shown superior temporal signal-to-noise ratio (tSNR) performance.¹⁵

In this work, we compare geometric distortions, tSNR, and the results of fMRI experiment at 9.4T with and without dynamic shimming using a 16-channel multicoil shim setup. Dynamic shimming in this context describes slice-specific shimming, that is, the shim values are optimized for individual slices and rapidly switch to proper settings from slice to slice. An fMRI study with 2 slice groups covering the motor cortex and the cerebellum was performed during a finger-tapping task. Finger tapping is an appropriate way to target the cerebellar-motor cortex network, given that it represents an excellent motor task which requires precise control of speed, force, and range of movement. Amount of residual image distortions and improvement in tSNR in the case of dynamic shimming were investigated for all the measurements. Shim settings were optimized for each slice individually and applied using the multicoil shim setup during measurement. Both regions were covered within the same measurement for reliable evaluation.

2 | METHODS

All experiments were performed on a 9.4T whole-body MRI system (Siemens Healthcare, Erlangen, Germany). The scanner is equipped with a shim setup, which generates full second-order spherical harmonic (SH) functions. A custom-built, shielded head coil with 18 transmit and 32 receive channels was used for RF transmission and signal reception.¹⁶ Five healthy volunteers (average age, 27 ± 4 years) participated in this study, and informed consent was provided in accord with the local ethics committee regulations before the experiments.

2.1 | B_0 shimming

A home-made 16-channel multicoil setup was used for dynamic shimming of the human brain.⁷ Briefly, 16 identical circular loops, each with 25 wire turns and a diameter of 100 mm, were symmetrically positioned in 2 rows on the surface of a cylinder with a diameter of 370 mm. The transceiver array was mounted inside this multicoil arrangement, and RF interference with the multi-coil was avoided by the shield of the RF coil. Dedicated in-house developed current amplifiers were used to supply current to the multicoil.¹⁷ The amplifiers were driven through analog signals provided by 16-bit digital-to-analog converters (DACs). The current of all the shim channels was limited to ± 1.5 A to prevent excessive heating, and the amplifier allowed a highly linear output and switching in <100 μ s for the desired range. The MR scanner broadcasted a trigger signal preceding each RF pulse, which initiated a LABVIEW-based (National Instruments, Austin, TX) program to change the state of the DAC and, accordingly, the amplifier's output.

The vendor provided an interface for performing global shimming of a VOI with the scanner's built-in second-order SH

shim setup. A rectangular volume that covers the whole brain was chosen to shim the brain of each subject before shimming with the multicoil setup. A 3D dual-echo gradient recalled echo (GRE) sequence with TE1/TE2/TR = 3.6/8.4/15 ms (flip angle [FA] = 12°, resolution = 2 mm isotropic), without acceleration, and total acquisition time of 2 minutes was used to map the B_0 inhomogeneity after shimming with the scanner's second-order shims. For B_0 mapping, the gradient shapes were adapted to low bandwidth and slightly longer rise time in order to avoid eddy current perturbation. The acquired B_0 map was used as a reference for all of the following calculations and measurements unless the subject needed to reposition his or her head, which required reacquisition of the reference B_0 map.

Before any calculation, a brain mask was generated with a brain extraction tool,¹⁸ and spatial phase unwrapping was performed in the VOI.¹⁹ Based on the preprocessed reference B_0 maps and the basis maps of individual multicoil channels, a constrained least-squares optimization was performed to calculate the currents required to minimize the deviation of the B_0 field across the individual slices. The calculated current values were stored in a text file, which was read by the sequence and broadcasted alongside with the trigger signal. The shimming target VOI for the individual slices consisted of the slice itself and the corresponding adjacent slices. This helped to overcome 2 probable issues in thin slices: having an ill-conditioned problem^{20,21} and leading to degeneracy.^{22,23}

As an additional shimming strategy, which can be simply used in every scanner, dynamic zeros and first-order shimming have been performed for tSNR evaluation (see below) as well. To this end, excitation frequency and offset in linear gradients have been updated slice by slice. Finally, the performance is compared with global second-order SH and dynamic multicoil shimming.

2.2 | MRI parameters

Single-shot EPI with generalized autocalibrating partially parallel acquisition (GRAPPA) = 3 was used for the fMRI experiment with the following parameters: TE/TR = 24/2500 ms, FA = 60°, resolution = 1.2 mm isotropic, matrix size = 170 × 170, 6/8 partial Fourier, bandwidth = 1132 Hz/Px, and echo spacing = 1.01 ms. In total, 40 slices were acquired with an interleaved slice excitation order which were split into 2 groups to cover part of the motor cortex and the cerebellum with 22 and 18 slices, respectively. The update of the dynamic shims was performed in the remaining 5-ms gap between the end of the current slice readout and the excitation pulse for the next slice. Dynamic multicoil shimming was executed not only for imaging, but also for the acquisition of the GRAPPA reference lines and dummy scans. tSNR calculation and geometric distortion evaluation were later performed on data which were derived from the data of fMRI experiments and acquired with the EPI sequence. The experiments

were repeated with 2 different shimming approaches, global shimming with scanner's second-order SH, and dynamic slice-wise shimming with a 16-channel multicoil setup. The settings for the scanner's second-order shim were kept constant during the multicoil shimming. All experiments started first with dynamic multicoil shimming and then global second-order SH shimming. However, multicoil shimming was performed before and after global second-order SH shimming in 2 volunteers to show that order effects are not relevant for the difference between results of the 2 measurements.

A 2D double echo GRE sequence (TE1/TE2/TR = 4/8.4/20 ms and FA = 12°) with identical field of view and resolution because the EPI scan, which is primarily used for validation of shimming, was used for a separate acquisition of the GRAPPA reference lines too.²⁴ This approach is beneficial in comparison to the native GRAPPA calibration scan, which is based on a segmented multishot EPI. Such a prescan is acquired over multiple TR and thus prone to breathing and motion, which can result in artifacts and tSNR variations across different slices.²⁵ In addition, the images acquired from the GRE sequence were used as an anatomical reference image to extract brain borders and qualitatively assess the geometric distortions in EPIs. The acquired B_0 map before and after multicoil shimming was used to estimate the magnitude of the voxel shift through the formula $d_{pe} = \Delta B_0 \cdot T_{acq}$, where d_{pe} is the amount of voxel shift in the phase-encoding direction and T_{acq} is the time required for the full-Fourier acquisition.

EPI is vulnerable to N/2 ghosting arisen from the inconsistency in the odd/even echoes (attributable to gradient delay, induced eddy current, and B_0 inhomogeneities). A simple and robust method for correction of such N/2 ghost is to use additional reference data to correct the phase and shift the position of the echoes. To this end, bipolar navigators are acquired immediately after RF pulse for phase correction of EPIs. Constant and linear phase correction terms were calculated by weighted fitting of the phase difference of 2 navigators with a first-degree polynomial. The weight of the fits was obtained from the magnitude of the navigators. EPIs were reconstructed offline using in-house routines developed in Matlab (The MathWorks, Inc., Natick, MA).

2.3 | Finger tapping experiment and tSNR

Given that the RF coil was surrounded by the multicoil cylinder, the use of a conventional mirror setup for fMRI stimulation and task indication was not feasible. Thus, a 3 × 3 cm opaque polycarbonate sheet was attached to the coil ceiling above the subject's nose. This sheet was illuminated by an optical fiber, which was connected to a triggerable light-emitting diode outside of the scanner room. This simple setup was used to indicate the subjects when to start and end the

tasks. The display was bright enough that no direct line of sight was required to know the task condition. The subjects were asked to perform a finger-tapping task with the thumb and index fingers of their right hand at a rate of approximately 1 tap per second. The paradigm consisted of a block design of 25 seconds task and 25 seconds rest and started with a rest period of 150 seconds. The trial was repeated 8 times, and the whole scan lasted approximately 10 minutes, including the dummy scans and the GRAPPA calibration measurements. The experiment was performed with and without dynamic multicoil shimming, to investigate the performance of multicoil shimming in comparison to static global shimming with the built-in second-order shims of the scanner.

The functional data were preprocessed and analyzed using SPM12.²⁶ The preprocessing pipeline is comprised of retrospective motion correction and slice timing correction (no spatial smoothing). Afterward, a high-pass filter with a cut-off period of 120 seconds was applied to remove low-frequency drifts. The absolute value of motion was compared by calculating the root-sum-of-squares of all translation and rotation terms for both shimming approaches.

Signal stability, a crucial metric for fMRI, can be quantified by measuring the tSNR. tSNR determines how many volumes are required to have enough statistical power for BOLD signal detection.²⁷ The data acquired during the initial rest period of 150 seconds (60 volumes in total) were additionally used for tSNR evaluation. The tSNR was then calculated as the ratio of the mean and standard deviation over time for the individual voxels.

3 | RESULTS

3.1 | Geometric distortions

The main visible effect of improved shimming with the multicoil is a reduction of geometric distortions. In Figure 1, the contours of the anatomical masks derived from the GRE measurements are overlaid onto the EPIs to visualize the boundary of a nondistorted image. The direction of distortions follows the background B_0 perturbation. The voxels with negative and positive off-resonance are shifted in the anterior and posterior directions, respectively, when phase encoding is in the anteroposterior direction. Dynamic multicoil shimming reduces the distortions for both slice groups, covering cerebellum and motor cortex, compared to shimming with conventional second-order SH. Even though parallel acquisition significantly decreases the readout length, the geometric distortion is still evident when only second-order shimming is used. Calculating the voxel shifts based on the acquired B_0 map shows that the number of voxels with a displacement larger than 6.0 mm (5 voxels) decreases by 44% and 97% for the slices covering cerebellum and motor cortex, respectively, when shimming is performed dynamically with

the multicoil. Supporting Information Table S1 compares the standard deviations of B_0 inhomogeneities measured with the double-echo GRE with and without dynamic multicoil shimming. A mean reduction of 30% and 52% in the field variation was observed for the slices covering the cerebellum and motor cortex, respectively, when dynamic multicoil shimming was used.

3.2 | tSNR experiment

Dynamic multicoil shimming enhances tSNR in both slice groups that cover cerebellum and motor cortex regions (Figure 2 and Supporting Information Figure S1). On average, over the 5 volunteers, multicoil shimming improved tSNR by 34% and 35% for cerebellum and motor cortex, respectively. Because of different static field inhomogeneities, images acquired with and without multicoil exhibit different signal intensities and image distortions. Therefore, the obtained EPI masks are slightly different. Figure 2 shows that improvement of tSNR in gray matter (GM) is more pronounced relative to white matter (WM). The slices mask was shrunk to cover a major part of WM. The improvement of tSNR in the shrunk masks, which only includes WM, was 20%, on average, over the 5 volunteers. Supporting Information Figure S2 shows that the order of the measurement does not significantly affect the tSNR improvement. Dynamic multicoil shimming was performed before and after shimming with second-order SH. Both dynamic shimming with multicoil eventuated in a better tSNR with respect to the global second-order shimming.

Figure 3 shows a possible reason behind the tSNR improvement. Overall, temporal deviation of voxel intensities is reduced for the cerebellum and the motor cortex with the multicoil setup, indicating an improved shimming (Figure 3A). The signal magnitude slightly increased and decreased in the cerebellum and motor cortex, respectively, for some subjects. Figure 3B shows that phase correction samples acquired before EPI readout is smoother and a better estimation of constant and linear phase correction can be obtained. On average, for all slices, the deviation of the fitted values for constant and linear phase correction over repetitions is 40% less for the case of dynamic multicoil shimming in comparison to the global second-order shimming. Figure 3C shows the value of 0th and first-order phase correction for different repetitions. Improved shimming with multicoil resulted in more stable values. Windowing EPI images acquired with both shimming techniques reveals a shift of fat signal in the motor cortex and a high temporal deviation in the cerebellum when shimming is performed with second-order SH. No significant difference in the intensity of N/2 or GRAPPA ghost in the motor cortex for both shimming techniques is observed; however, the noise level in the background is higher for the shimming with second-order SH (Supporting Information

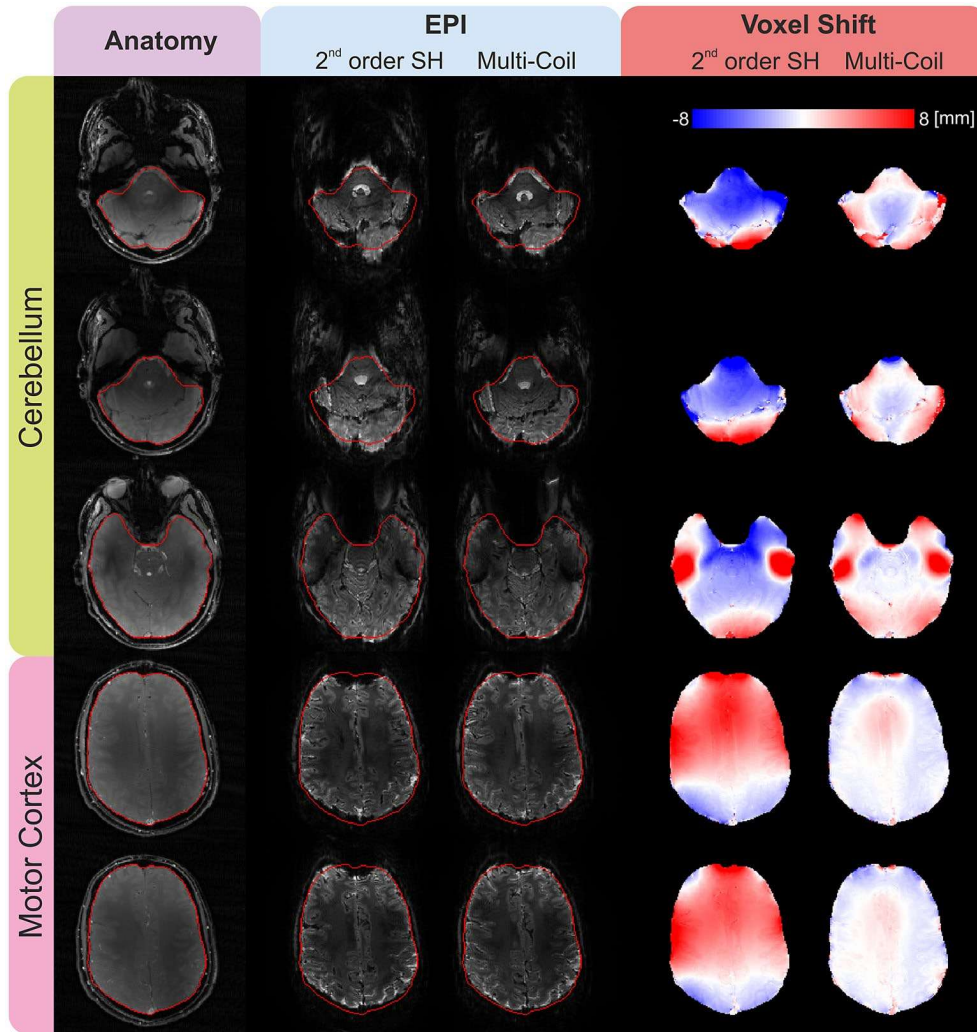


FIGURE 1 Improvement of geometric distortions with improved B_0 homogeneity by dynamic multicoil shimming. EPIs are compared with a distortion-free anatomical image of the same slice. One can see that the geometric distortions in the anterior part of the slices covering the motor cortex and close to the frontal cortex are more pronounced when conventional second-order SH shimming is used. However, the severe inhomogeneities in the vicinity of ear canals cause signal voids in these regions and cannot be recovered even with the dynamic multicoil shimming technique. The last 2 columns represent corresponding simulated voxel shift maps, which were calculated based on the B_0 inhomogeneity and the bandwidth in the phase-encoding direction. The color map is restricted to ± 8 mm to improve visualization of smaller displacements

Figure S3). This seems to indicate that the less-stable phase correction signals for the shimming with second-order SH does not cause ghosting, but an increased noise level in the reconstructed EPI.

3.3 | Finger tapping experiment

Figure 4 illustrates how the uniformity of the B_0 field can ultimately affect the BOLD statistics for an example subject. The circumscribed activation in the contralateral primary sensorimotor cortex and supplementary motor area (SMA) as well as in the ipsilateral superior cerebellum are evident. The session with dynamic multicoil shimming produced activated voxels with higher t-values in the cerebellum and the motor cortex. Having a better B_0 uniformity with dynamic

multicoil shimming, the SMA activation map aligned better with the GM in the structural images while no coregistration was applied. Histograms of t-values for all subjects are depicted in Figure 4B. The values are normalized between 0 and 1 with respect to the highest t-value for better comparison. Considering voxels having a t-value >3 as significant, the number of activated voxels in the cerebellum increased by 240%, 165%, 290%, 520%, and 80% for subjects 1 to 5, respectively, using dynamic shimming with the multicoil instead of using only the static second-order SH shim. Similarly, the number of voxels with t-value >3 in the motor cortex region increased by 135%, 170%, 360%, 145%, and 145% for subjects 1 to 5, respectively, when multicoil was used for the shimming. On average, for all subjects, shimming with multicoil increased the population of voxels with

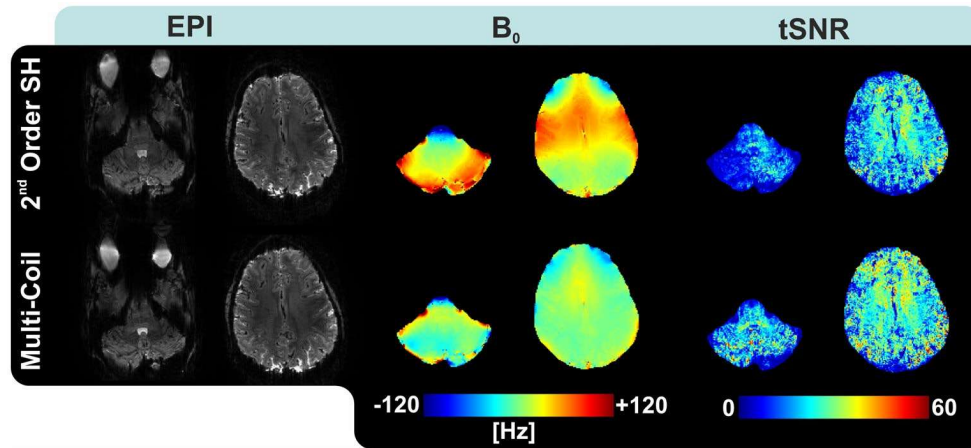


FIGURE 2 tSNR map for a representative volunteer. The same sequence and acquisition protocol for the finger-tapping experiment with an isotropic resolution of 1.2 mm was used for the comparison of the second-order SH and the dynamic multicoil shimming. Because of different degrees of distortions, different masks were created. Higher tSNR can be observed when shimming with the multicoil. These increases are especially pronounced in the cerebellum. tSNR map for other volunteers is represented in Supporting Information Figure S1

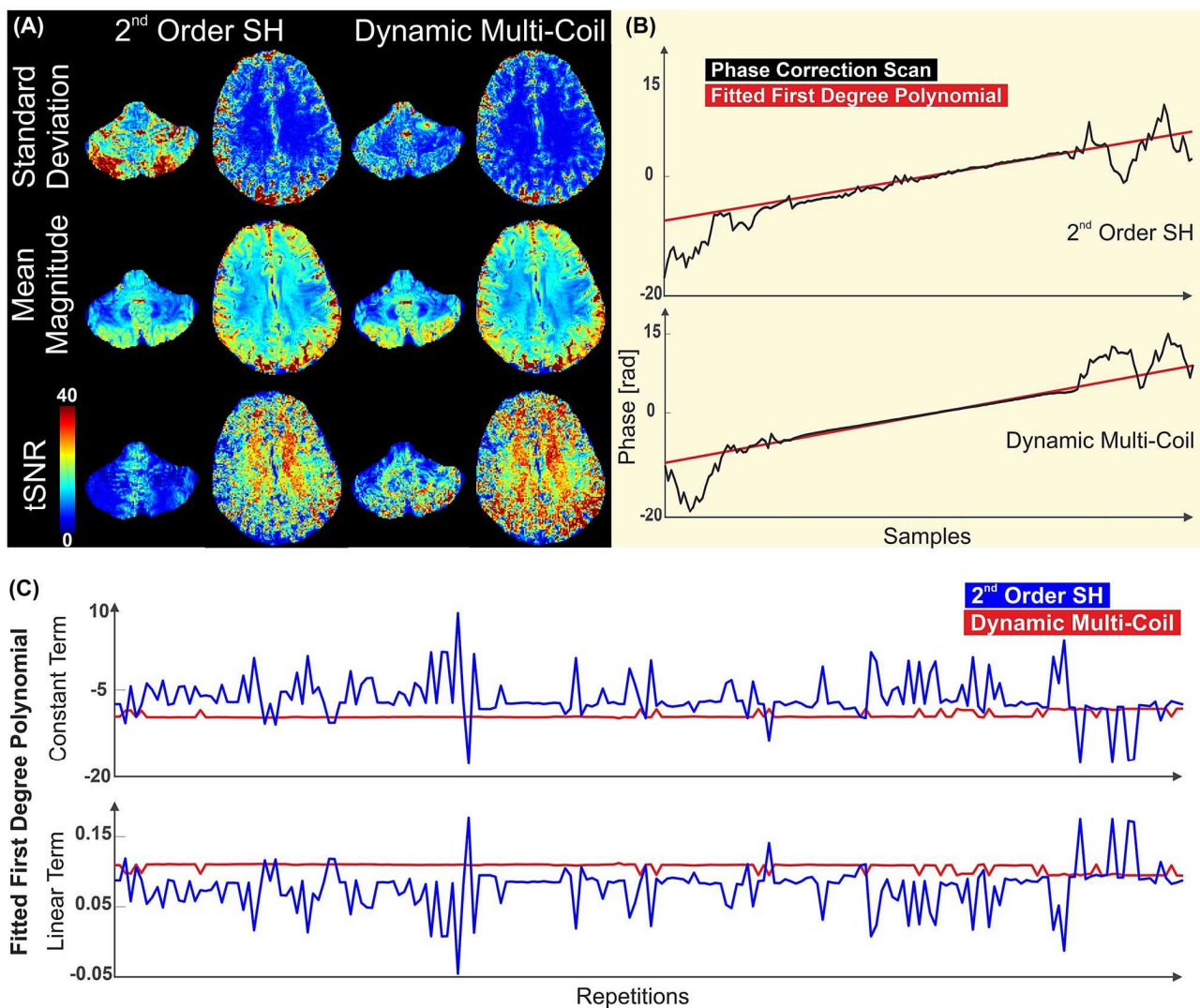


FIGURE 3 Investigating the reasons of the tSNR gain attributed to improved B_0 homogeneity. A, Mean and standard deviation over time as 2 components affecting tSNR are depicted. B, Phase correction data for 2 different shimming approaches (same slice and repetition number). The corresponding weighted fits are plotted in red. C, Calculated constant and linear terms of phase correction for several consecutive repetitions

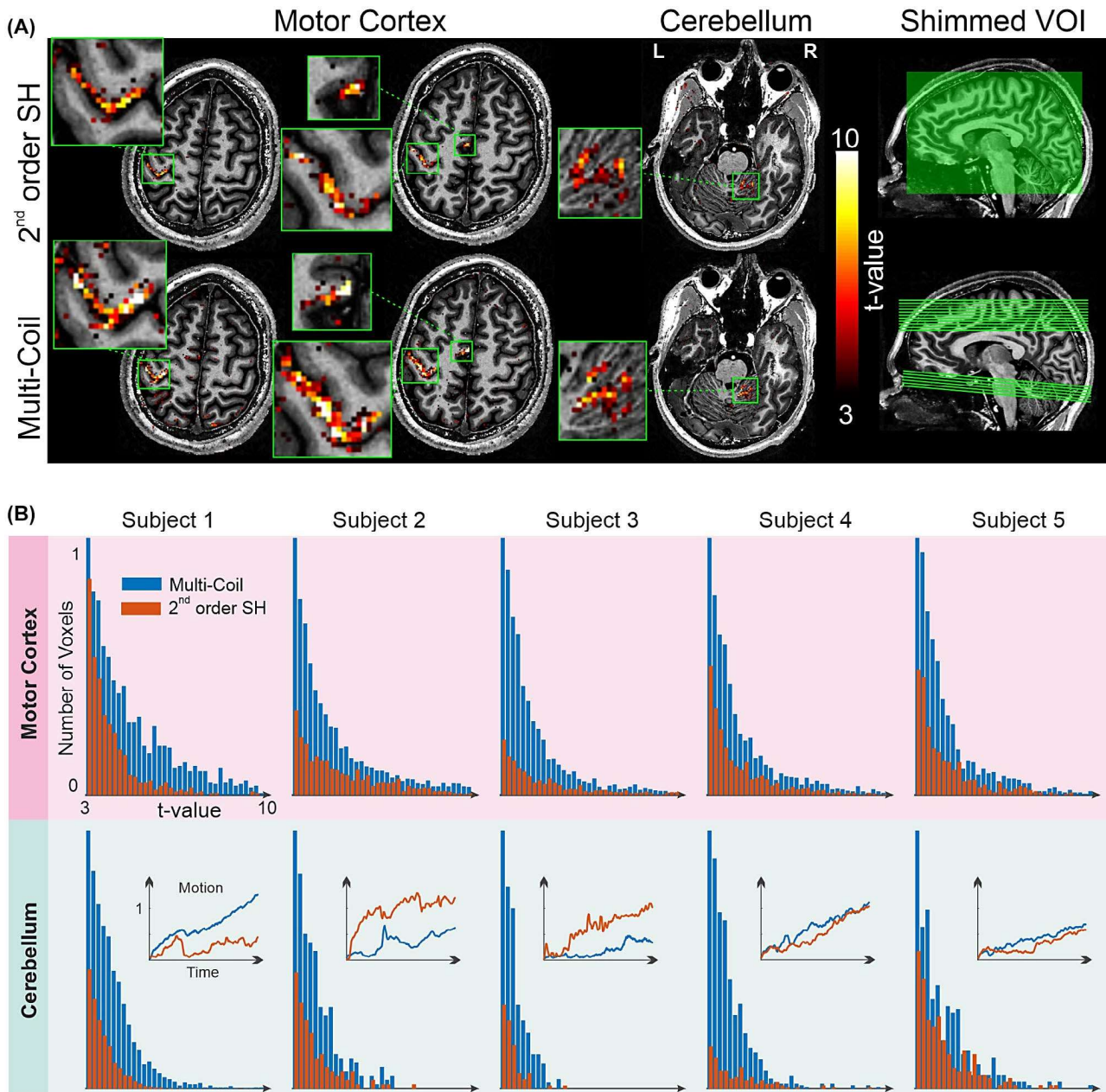


FIGURE 4 A, BOLD activation map in motor cortex and cerebellum during finger tapping from a single subject. The overlaid t-value map is restricted to the voxels with $t > 3$ ($P < .001$ uncorrected). Better shimming with the multicoil is reflected in a larger activated cluster with higher t-values. Activation maps are slightly smoothed for a better presentation. B, Histogram of the voxels with $t > 3$ in the finger-tapping experiment across all 5 subjects of the study. All values are normalized to be between 0 and 1. The number of voxels with a higher t-value increased in both regions, the cerebellum and the motor cortex, when the dynamic multicoil technique was applied

t-value > 3 by 240% and 180% for the cerebellum and motor cortex, respectively.

4 | DISCUSSION

The main benefit of the multicoil shim setup in comparison to the scanner's second-order shim coils is the potential for fast switching, which allows for rapid slice-wise shimming of the brain, independent of individual slice positions and

orientations. The 2 slice groups that cover the cerebellum and motor cortex were separated by a gap of approximately 6 cm and exhibited a completely different profile of B_0 inhomogeneity. Therefore, global shimming with the scanner's built-in setup cannot effectively improve B_0 inhomogeneity, even if the gap between the slice groups was excluded for the shim current calculation. Especially in the cerebellum, strong local inhomogeneities were observed, which were beyond the capability of the utilized multicoil setup to compensate. However, more degrees of freedom can be achieved by using

additional shim coils and supplying additional current, which may lead to a better shimming.

Geometric distortions are well-known effects of poor B_0 field homogeneity in sequences with long readout durations like EPI. The corresponding voxel shifts are proportional to the background B_0 inhomogeneity and the effective echo spacing. In this study, all EPI protocols had an acceleration factor of 3 in phase-encoding direction, which reduced the readout length to one-third of the nominal value. Assuming the same protocol settings, measuring with such readout durations at 9.4T is expected to produce similar distortion as at 3T without parallel imaging. One can use a hybrid approach and combine dynamic shimming with a distortion correction method in postprocessing. An additional issue can be slice bending of the thin slices attributed to strong B_0 inhomogeneity.²⁸ For the settings used in this study (slice thickness 1.2 mm and slice selection gradient of 35 mT/m), a bandwidth of approximately 1790 Hz/slice is obtained. With a maximum B_0 inhomogeneity of approximately 850 Hz after second-order shim, slice bending of half of a voxel is expected.

An increased tSNR was obtained with dynamic multicoil shimming. The sources of signal fluctuations can be generally classified as thermal noise, scanner-related noise (e.g., gradient instability), physiological noise, and signal from non-task-related processes. In general, there is no direct relation between the field homogeneity and the aforementioned noise sources except for scanner-related noise. To achieve fast spatial encoding, EPI acquires signal during both polarities of the readout gradient. Therefore, any gradient delay and eddy current can lead into an alternating offset between odd and even lines and result in $N/2$ Nyquist ghosts.²⁹ B_0 inhomogeneity may further amplify this artifact by delaying or advancing the spin rephasing (actual echo time) in the GRAPPA calibration scan, phase correction scan, or EPI readout. Phase of the signal from phase correction scans is extracted and used for phase correction. Hence, they are sensitive to B_0 inhomogeneities even at the very short echo time. In contrast to the gradient delays, which add a constant phase shift to all excited spins, the field inhomogeneity is spatially variant and phase accrual is a function of spatial position. As shown in Figure 3, improved shimming allows calculation of phase correction terms with higher accuracy attributed to a smoother phase difference signal. Phase correction navigators are basically a projection of the slice along phase-encoding direction. Inhomogeneities of different areas sum up and are reflected as fluctuations into the phase of projection signal. Although the signal is 1-dimensional, small fluctuations may hamper a reliable phase unwrapping. One may avoid ramp sampling in phase correction scans for accurate calculation of phase shifts, which cannot be achieved with regridding of the samples. Alternatively, nuclear MR field probes may be used during scans to track gradient waveform and extract delays which are not affected by the static inhomogeneities in the brain.³⁰

Improved shimming can reduce macroscopic magnetic field inhomogeneity and therefore increases T_2^* , which increases signal strength and tSNR accordingly. This effect is somewhat evident in the cerebellum represented in Figure 3. Improving signal magnitude requires through-plane shimming and considering gradient of inhomogeneities in the slice direction³¹ and cannot be guaranteed with in-plane shimming. Additionally, T_2^* gain may not be also notable in the small voxels after shimming.⁸ Supporting Information Figure S4 shows that increasing the thickness of the shim volume per slice can preserve or improve T_2^* values after in-plane shimming of a thin slice. However, as Figure 3A represents, signal magnitude is not a dominant factor in tSNR changes in this study.

The depicted results in Figure 2 represent a higher tSNR gain in GM in comparison to WM when the multicoil setup is used. This indicates that signal variations in different repetitions may emanate from blood or cerebrospinal fluid (CSF) flow, which are somehow suppressed during slice-wise multicoil shimming. Supporting Information Figure S5 displays spatial distribution of B_0 inhomogeneity when a single slice is shimmed with the utilized multicoil setup. Supporting Information Figure S5 represents that magnetic field steeply increases or decreases in the vicinity of target slice. The strong magnetic field produced by multicoil outside of the slice of interest can spoil the magnetization in blood/CSF flow, which may be produced from excitation of previous slices. An additional tSNR measurement was performed without using multicoil setup to support this hypothesis. To this end, spoiler gradients in read and slice direction are embedded into the sequence, which are executed immediately after readout. For an efficient spoiling, gradient moment of spoilers was adjusted to produce phase dispersion of 4π across the voxel. Figure 5 compares the tSNR change between 4 strategies: shimming with scanner's second-order SH; dynamic slice-wise shimming with zeros and first-order SH; spoiling the magnetization after EPI readout; and dynamic slice-wise shimming with multicoil. Dynamic first-order SH improved tSNR; however, geometric distortion is still severe and background noise level also elevated. Effects of spoiler gradients are not constant for all the slices. In some regions, tSNR improvement is apparent and in other regions degraded. One should consider some dead time after strong spoiler gradients to avoid eddy-current artifacts, which will increase the minimum TR. tSNR gain with multicoil shimming is higher than other strategies, and level of background noise is also smaller and more stable during the repetitions.

The electromagnetic force (according to the Lorentz force law) from static currents does not produce any vibration in the coils. However, rapid change of shim currents leads to vibrations of the coil and additional acoustic noise. The resulting vibration and noise are more severe when changing the slice position from the cerebellum to

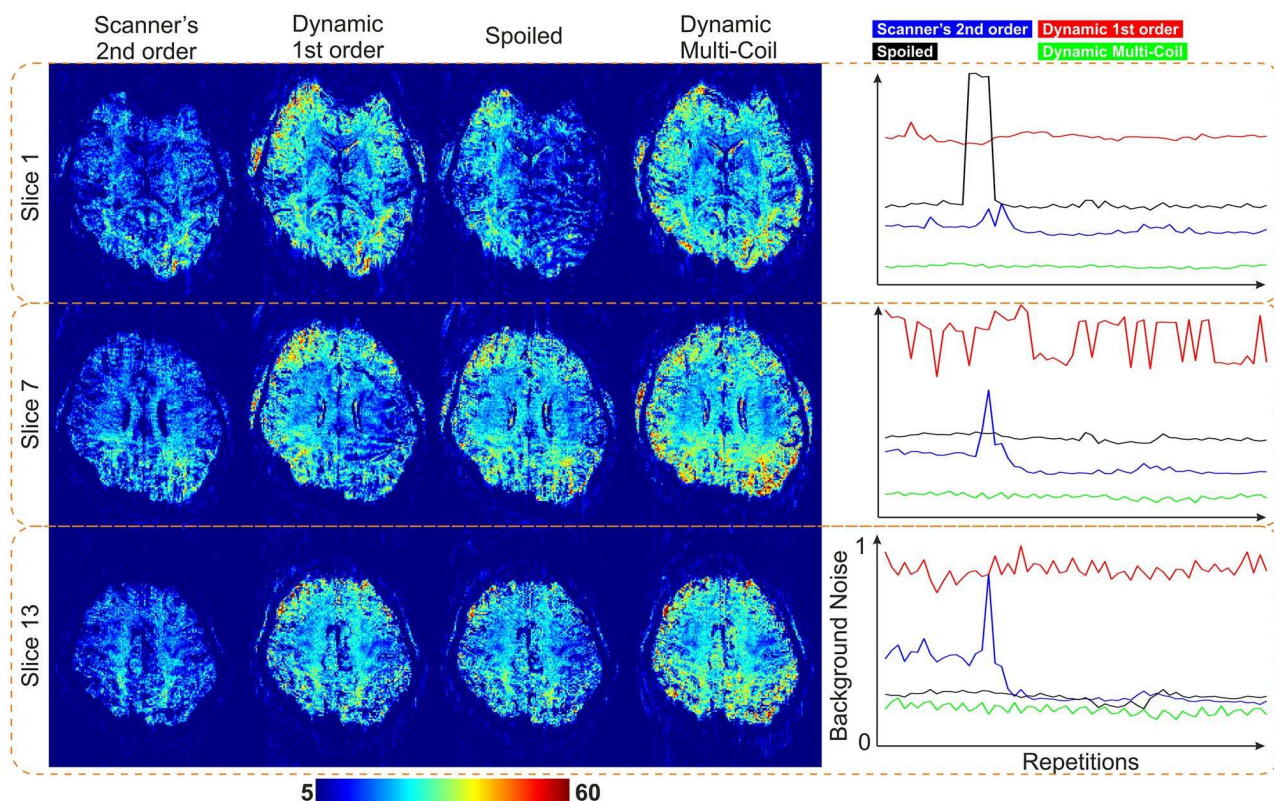


FIGURE 5 Comparison of the tSNR changes between 4 acquisition strategies and their corresponding background noise level. Three representative slices after global second-order SH shimming, dynamic 0th and first-order SH shimming, spoiling the magnetization after EPI readout, and dynamic multicoil shimming are presented. A mask is generated to exclude the brain and fat before calculating the background noise level. The values are normalized to the maximum. Dynamic multicoil shimming yielded a higher tSNR gain and less background noise

the motor cortex given that the current alteration is larger for non-neighboring slices in the brain, which have different profiles of inhomogeneity. The calculated current for 1 of the finger-tapping experiments is depicted in Supporting Information Figure S6. The slices were acquired in an interleaved manner to reduce the amount of signal saturation attributed to imperfect excitation profiles of adjacent slices. Thus, this leads to 4 large vibrations in the shim setup during the finger-tapping experiment. The level of acoustic noise was comparable to gradients noise in some experiments. One can apply a constraint for interslice current change similar to a previous work³² to have smoother change in currents.

Simultaneous acquisition of slices in multiband (MB) sequences can overshadow the performance of slice-wise shimming. However, simulations yielded a similar shimming outcome between MB factors of 1 and 2.^{33,34} The performance of slice-wise shimming will decrease by increasing the MB factor and will be similar to global shimming for MB factor higher than 4. The distance between slices undergoing a simultaneous excitation is another factor that may affect the efficiency of slice-wise shimming for MB factor ≥ 2 . The slices close together exhibit same pattern of inhomogeneity and can probably be shimmed more efficiently.

ACKNOWLEDGMENTS

This work was funded, in part, by DFG SCHE 658/12 (Reinhart Koselleck) and the Max Planck Society. The authors acknowledge Dr Nikolai Avdievitch and Theodor Steffen for all the support regarding the RF coil and the shim amplifier. The authors thank Dr Anagha Deshmane for careful proof-reading of the manuscript, Dr Philipp Eshes for providing the MATLAB script in order to reconstruct EPIs, and Azadeh Nazemorroaya for the support during the experiments.

ORCID

Ali Aghaeifar  <https://orcid.org/0000-0002-6964-0992>

REFERENCES

1. Jezzard P. Correction of geometric distortion in fMRI data. *NeuroImage*. 2012;62:648–651.
2. Kim T, Lee Y, Zhao T, Hetherington HP, Pan JW. Gradient-echo EPI using a high-degree shim insert coil at 7 T: implications for BOLD fMRI. *Magn Reson Med*. 2017;78:1734–1745.
3. Balteau E, Hutton C, Weiskopf N. Improved shimming for fMRI specifically optimizing the local BOLD sensitivity. *NeuroImage*. 2010;49:327–336.

4. Juchem C, Nixon TW, McIntyre S, Boer VO, Rothman DL, De Graaf RA. Dynamic multi-coil shimming of the human brain at 7 T. *J Magn Reson*. 2011;212:280–288.
5. Darnell D, Truong TK, Song AW. Integrated parallel reception, excitation, and shimming (iPRES) with multiple shim loops per radio-frequency coil element for improved B₀ shimming. *Magn Reson Med*. 2017;77:2077–2086.
6. Scheffler K, Loktyushin A, Bause J, Aghaeifar A, Steffen T, Schölkopf B. Spread-spectrum magnetic resonance imaging. *Magn Reson Med*. 2019;82:877–885.
7. Aghaeifar A, Mirkes C, Bause J, et al. Dynamic B₀ shimming of the human brain at 9.4 T with a 16-channel multi-coil shim setup. *Magn Reson Med*. 2018;80:1714–1725.
8. Juchem C, Umesh Rudrapatna S, Nixon TW, de Graaf RA. Dynamic multi-coil technique (DYNAMITE) shimming for echo-planar imaging of the human brain at 7 Tesla. *NeuroImage*. 2015;105:462–472.
9. Aghaeifar A, Zhou J, Heule R, et al. A 32-channel multi-coil setup optimized for human brain shimming at 9.4T. *Magn Reson Med*. 2019 Sep 4. doi: <https://doi.org/10.1002/mrm.27929>. [Epub ahead of print].
10. Jia F, Elshatlawy H, Aghaeifar A, et al. Design of a shim coil array matched to the human brain anatomy. *Magn Reson Med*. 2019 Sep 30. doi: <https://doi.org/10.1002/mrm.28016>. [Epub ahead of print].
11. Finsterbusch J, Sprenger C, Büchel C. Combined T2*-weighted measurements of the human brain and cervical spinal cord with a dynamic shim update. *NeuroImage*. 2013;79:153–161.
12. Islam H, Law CSW, Weber KA, Mackey SC, Glover GH. Dynamic per slice shimming for simultaneous brain and spinal cord fMRI. *Magn Reson Med*. 2019;81:825–838.
13. Daskalakis ZJ, Paradiso GO, Christensen BK, Fitzgerald PB, Gunraj C, Chen R. Exploring the connectivity between the cerebellum and motor cortex in humans. *J Physiol*. 2004;557:689–700.
14. Grodd W, Hulsmann E, Lotze M, Wildgruber D, Erb M. Sensorimotor mapping of the human cerebellum: fMRI evidence of somatotopic organization. *Hum Brain Mapp*. 2001;13:55–73.
15. Poser BA, Kass AL, Wiggins CJ, Uludug K, Tse DHY. Dual region-selective spiral pTX excitation for digit mapping fMRI in motor cortex and cerebellum. In Proceedings of 26th Annual Meeting of the ISMRM, Honolulu, HI, 2017. p. 0588.
16. Avdievich NI, Giapitzakis IA, Bause J, Shajan G, Scheffler K, Henning A. Double-row 18-loop transceive-32-loop receive tight-fit array provides for whole-brain coverage, high transmit performance, and SNR improvement near the brain center at 9.4T. *Magn Reson Med*. 2019;81:3392–3405.
17. Aghaeifar A, Zivkovic I, Steffen T, Mirkes C, Scheffler K. Flexible gradient driver system for a multi-coil setup; design considerations and implementation. In 34th Annual Scientific Meeting of the European Society for Magnetic Resonance in Medicine and Biology, Barcelona, Spain, 2017. p. 50.
18. Smith SM. Fast robust automated brain extraction. *Hum Brain Mapp*. 2002;17:143–155.
19. Abdul-Rahman HS, Gdeisat MA, Burton DR, Lalor MJ, Lilley F, Moore CJ. Fast and robust three-dimensional best path phase unwrapping algorithm. *Appl Opt*. 2007;46:6623–6635.
20. Kim DH, Adalsteinsson E, Glover GH, Spielman DM. Regularized higher-order in vivo shimming. *Magn Reson Med*. 2002;48:715–722.
21. Finsterbusch J. B₀ inhomogeneity and shimming. In *Quantitative MRI of the Spinal Cord*. Amsterdam: Academic. 2014;68–90.
22. Shen J. Effect of degenerate spherical harmonics and a method for automatic shimming of oblique slices. *NMR Biomed*. 2001;14:177–183.
23. Koch KM, McIntyre S, Nixon TW, Rothman DL, de Graaf RA. Dynamic shim updating on the human brain. *J Magn Reson*. 2006;180:286–296.
24. Talagala SL, Sarlls JE, Liu S, Inati SJ. Improvement of temporal signal-to-noise ratio of GRAPPA accelerated echo planar imaging using a FLASH based calibration scan. *Magn Reson Med*. 2016;75:2362–2371.
25. Polimeni JR, Bhat H, Witzel T, et al. Reducing sensitivity losses due to respiration and motion in accelerated echo planar imaging by reordering the autocalibration data acquisition. *Magn Reson Med*. 2016;75:665–679.
26. Friston KJ, Ashburner JT, Kiebel SJ, Nichols TE, Penny WD. *Statistical Parametric Mapping: The Analysis of Functional Brain Images*. New York, NY: Elsevier/Academic; 2011.
27. Murphy K, Bodurka J, Bandettini PA. How long to scan? The relationship between fMRI temporal signal to noise ratio and necessary scan duration. *NeuroImage*. 2007;34:565–574.
28. Juchem C, Graaf RAD. B₀ magnetic field homogeneity and shimming for in vivo magnetic resonance spectroscopy. *Anal Biochem*. 2017;529:17–29.
29. Schmitt F, Stehling MK, Turner R. *Echo-planar imaging: theory, technique and application*. Berlin; Heidelberg, Germany: Springer-Verlag; 1998.
30. Wilm BJ, Dietrich BE, Reber J, Vannesjo SJ, Pruessmann KP. Gradient response harvesting for continuous system characterization during MR sequences. *IEEE Trans Med Imaging*. 2019 Aug 19. doi: <https://doi.org/10.1109/TMI.2019.2936107>. [Epub ahead of print].
31. Truong TK, Song AW. Single-shot dual-z-shimmed sensitivity-encoded spiral-in/out imaging for functional MRI with reduced susceptibility artifacts. *Magn Reson Med*. 2008;59:221–227.
32. Schwerter M, Hetherington H, Moon CH, et al. Interslice current change constrained B₀ shim optimization for accurate high-order dynamic shim updating with strongly reduced eddy currents. *Magn Reson Med*. 2019;82:263–275.
33. Stockmann JP, Wald LL. In vivo B₀ field shimming methods for MRI at 7 T. *NeuroImage*. 2018;168:71–87.
34. Hetherington H, Moon C, Pan J. Dynamically updated B₀ shimming for multi-band imaging with high order spherical harmonics. In Proceedings of the 27th Annual Meeting and Exhibition of the International Society for Magnetic Resonance in Medicine, Montreal, Quebec, Canada, 2019. p. 1473.

SUPPORTING INFORMATION

Additional supporting information may be found online in the Supporting Information section.

FIGURE S1 EPI, B₀ map, and tSNR map across 4 subjects of the study before and after dynamic multicoil shimming
FIGURE S2 Evaluation of the impact of measurements order in tSNR. Three tSNR measurements with 2 shimming strategies were performed in 2 volunteers. Dynamic multicoil

shimming was performed before and after second-order global shimming. Both measurements with dynamic multicoil shimming yielded a better tSNR in comparison to the second-order SH

FIGURE S3 The contrast and brightness of EPIs acquired with 2 different shimming approaches are adjusted in a sequence of repetitions to compare the background ghosts. Shift of the fat in motor cortex area is visible when shimming is performed with second-order SH, which is well eliminated by multicoil shimming. However, the difference in $N/2$ ghost level is not significant. Ghosts level in the cerebellum is high in some of the repetitions with second-order shimming while it is pretty consistent when multicoil shimming is used. Additionally, level of background noise is higher for the shimming with second-order SH in comparison to the improved shimming with multicoil (also see Figure 5)

FIGURE S4 Impact of shim volume in T_2^* measurements. In-plane shimming with a thin shim volume may degrade T_2^* . In this study, shimming target VOI per slice consisted of the slice itself and the corresponding adjacent slices (thickness of shimming VOI = $3 \times 1.2 \text{ mm} = 3.6 \text{ mm}$). To preserve or improve T_2^* values, one can increase thickness of shimming VOI per slice or include additional regularization term during calculation of shim current to optimize the shim for both in-plane and T_2^* . The details of such a regularization term are described in a previous work.²⁷ However, increasing thickness of shimming VOI or including additional regularization

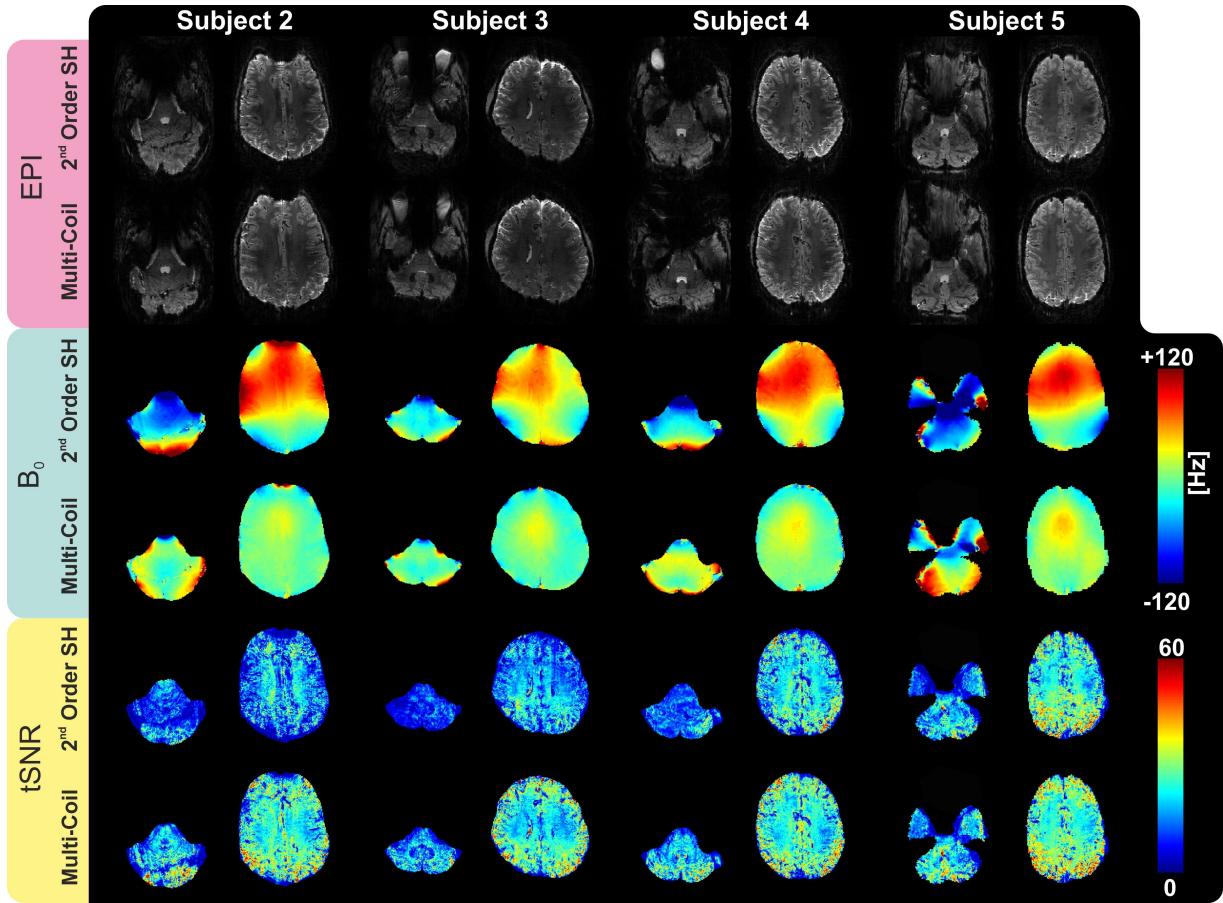
term will decrease efficiency of in-plane shimming and accordingly correction of geometric distortions

FIGURE S5 Spatial distribution of the magnetic field during slice-wise shimming with multicoil. The magnetic field in the slice of interest is well homogeneous; however, it steeply increases/decreases outside of the shimming VOI

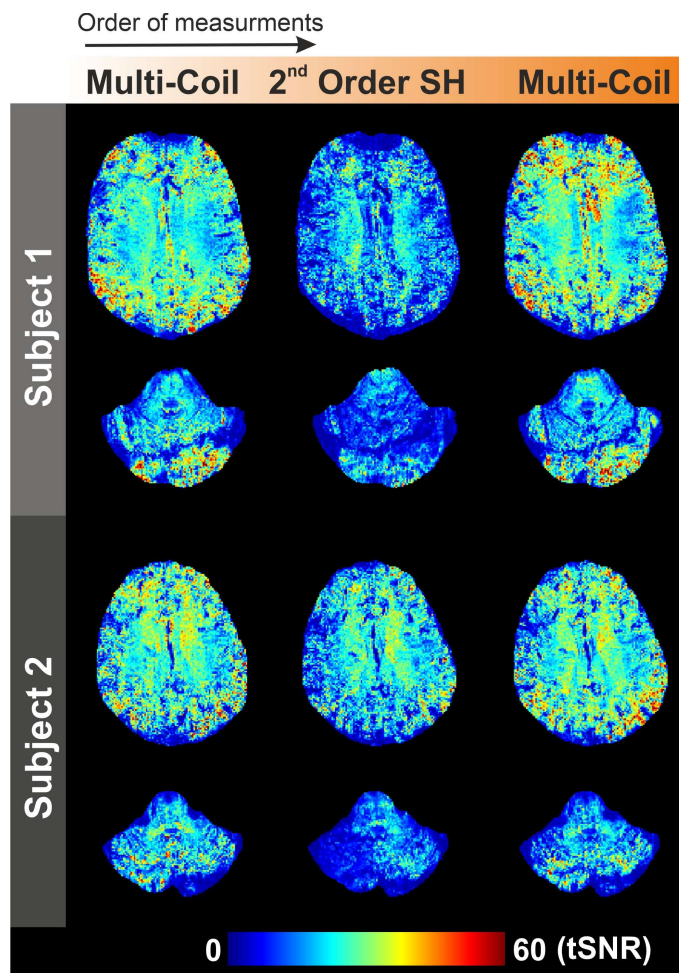
FIGURE S6 Example of the calculated currents for individual channels of the multicoil for all 40 slices in the finger-tapping experiment. The current values were obtained by a constrained least squares optimization and limited to $\pm 1.5 \text{ A}$, and the slice numbers are listed according to the acquisition order (interleaved). The currents changed smoothly when the successive slices to measure were in the same vicinity, but a strong modification was required when the slice group changed from the cerebellum to the motor cortex or vice versa

TABLE S1 B_0 standard deviation (SD) across all volunteers. The SD was calculated for all measured slices in the cerebellum and motor cortex for the individual subjects and averaged over all subjects

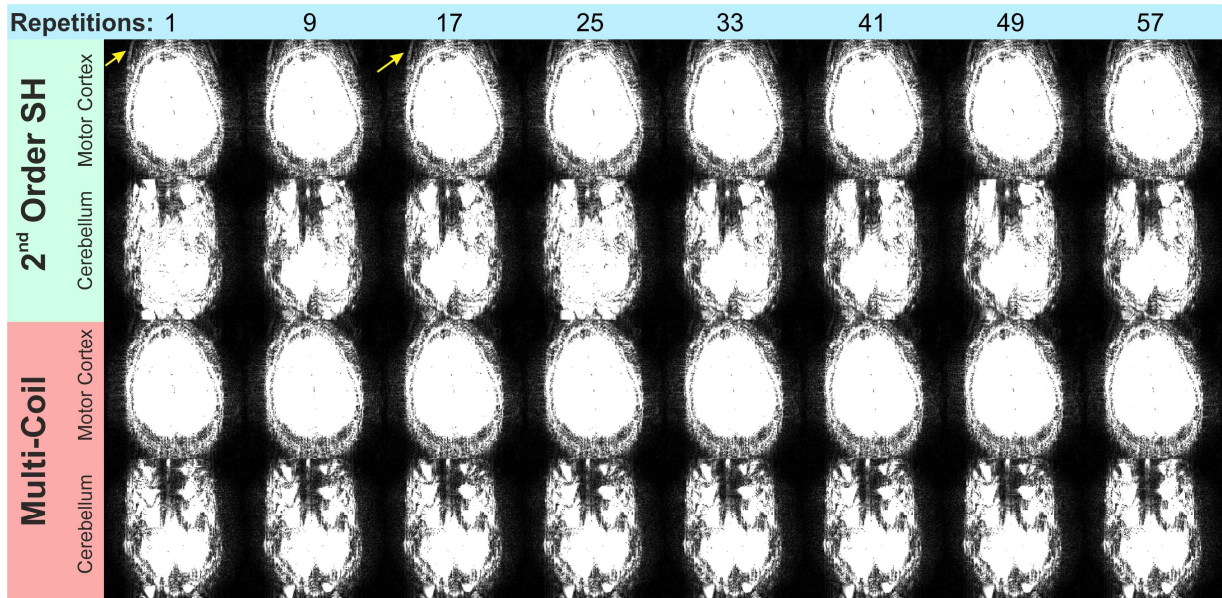
How to cite this article: Aghaeifar A, Bause J, Leks E, Grodd W, Scheffler K. Dynamic B_0 shimming of the motor cortex and cerebellum with a multicoil shim setup for blood oxygen level dependent functional MRI at 9.4T. *Magn Reson Med*. 2019;00:1–11. <https://doi.org/10.1002/mrm.28044>



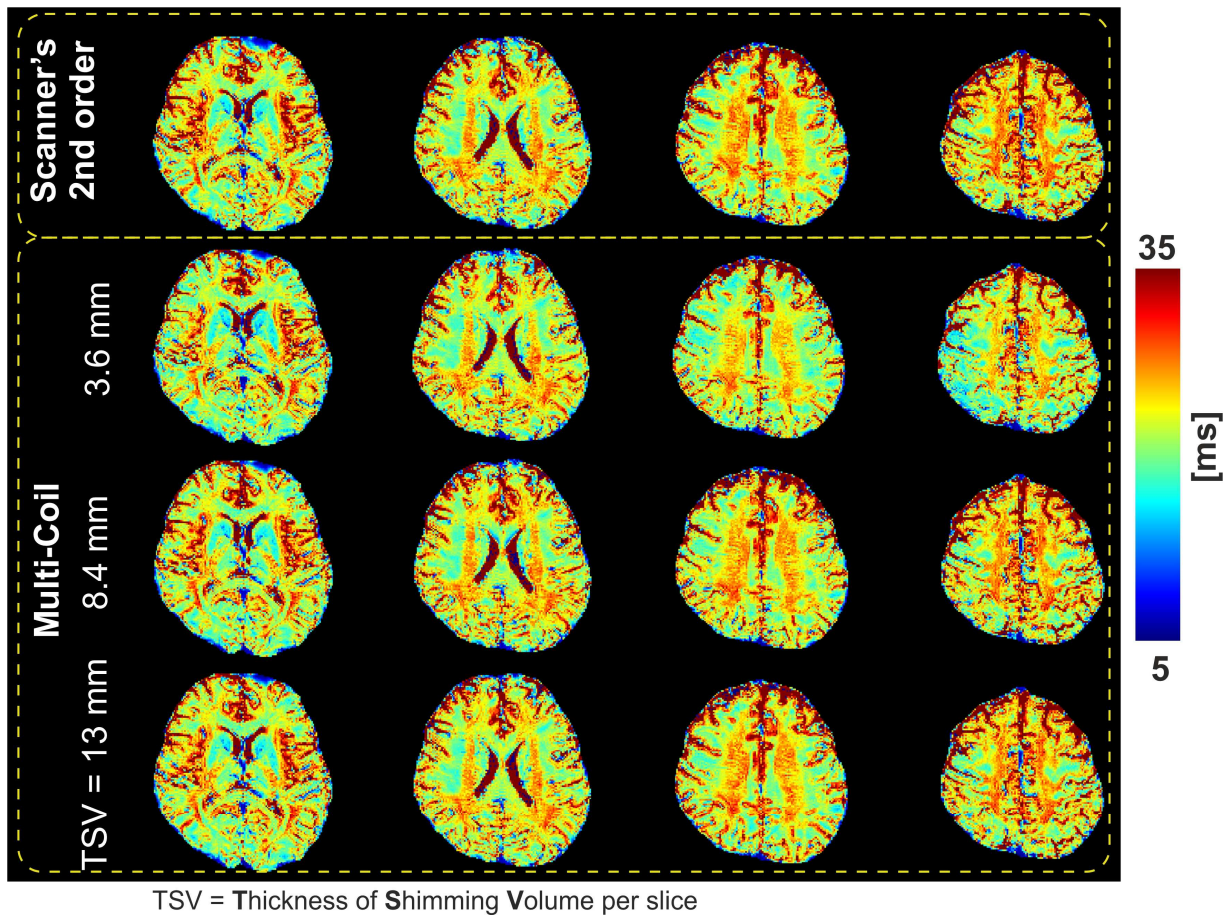
Supporting Information Figure S1. EPI, B_0 map, and temporal SNR (tSNR) map across 4 subjects of the study before and after dynamic multi-coil shimming.



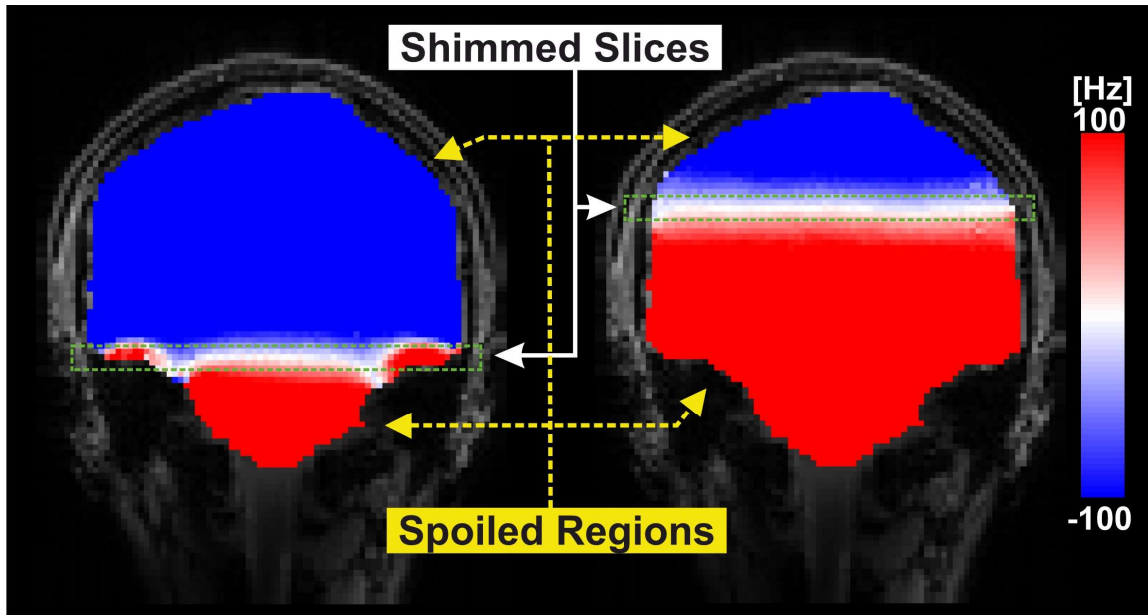
Supporting Information Figure S2. Evaluation of the impact of measurements order in tSNR. Three tSNR measurements with two shimming strategies were performed in two volunteers. Dynamic multi-coil shimming was performed before and after 2nd order global shimming. Both measurements with dynamic multi-coil shimming yielded a better tSNR in comparison to the 2nd order SH.



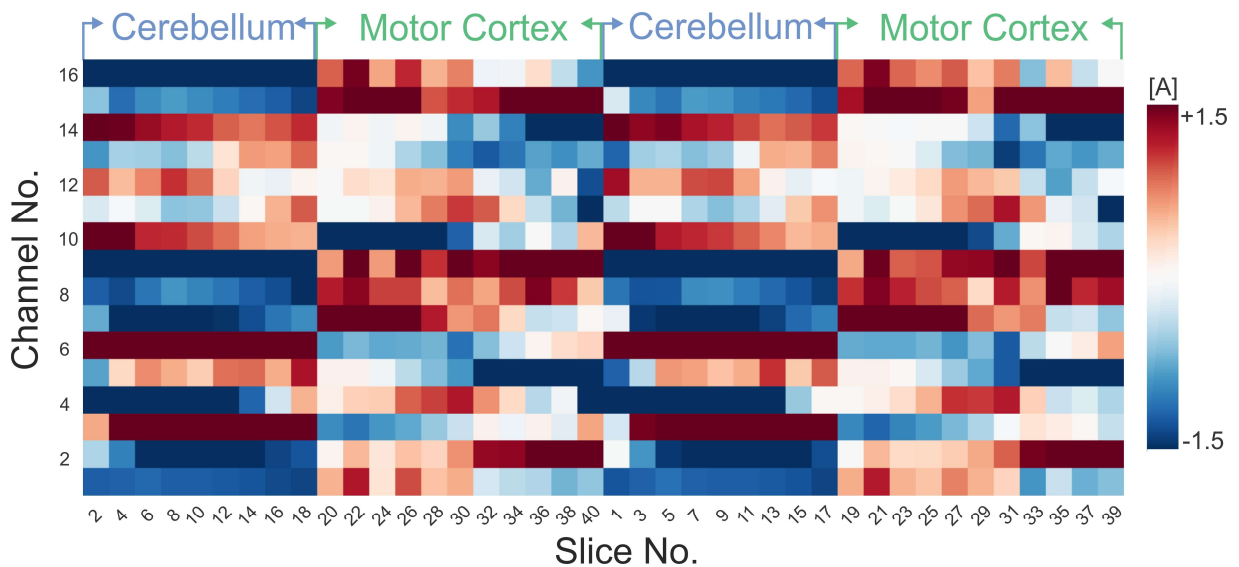
Supporting Information Figure S3. The contrast and brightness of EPIs acquired with two different shimming approaches are adjusted in a sequence of repetitions to compare the background ghosts. Shift of the fat in motor cortex area is visible when shimming is performed with 2nd order SH which is well eliminated by multi-coil shimming. However, the difference in N/2 ghost level is not significant. Ghosts level in the cerebellum is high in some of the repetitions with 2nd order shimming while it is pretty consistent when multi-coil shimming is employed. Additionally, level of background noise is higher for the shimming with 2nd order SH in comparison to the improved shimming with multi-coil (also see Figure 5).



Supporting Information Figure S4. Impact of shim volume in T_2^* measurements. In-plane shimming with a thin shim volume may degrade T_2^* . In this study, shimming target VOI per slice consisted of the slice itself and the corresponding adjacent slices (thickness of shimming VOI = $3 \times 1.2\text{mm} = 3.6\text{mm}$). To preserve or improve T_2^* values, one can increase thickness of shimming VOI per slice or include additional regularization term during calculation of shim current to optimize the shim for both in-plane and T_2^* . The details of such a regularization term are described in Ref. 27. However, increasing thickness of shimming VOI or including additional regularization term will decrease efficiency of in-plane shimming and accordingly correction of geometric distortions.



Supporting Information Figure S5. Spatial distribution of the magnetic field during slice-wise shimming with multi-coil. The magnetic field in the slice of interest is well homogeneous; however, it steeply increases/decreases outside of the shimming VOI.



Supporting Information Figure S6. Example of the calculated currents for individual channels of the multi-coil for all 40 slices in the finger tapping experiment. The current values were obtained by a constrained least squares optimization and limited to ± 1.5 A, and the slice numbers are listed according to the acquisition order (interleaved). The currents changed smoothly when the successive slices to measure were in the same vicinity, but a strong modification was required when the slice group changed from the cerebellum to the motor cortex or vice versa.

Supporting Information Table S1. B_0 standard deviation (SD) across all volunteers. The SD was calculated for all measured slices in the cerebellum and motor cortex for the individual subjects and averaged over all subjects.

Volunteer	Cerebellum		Motor Cortex	
	2 nd order SH (Hz)	Multi-Coil (Hz)	2 nd order SH (Hz)	Multi-Coil (Hz)
1	77.4	61.0	27.1	13.8
2	73.8	44.5	35.8	16.4
3	95.1	70.7	31.4	17.9
4	109.5	67.4	34.1	16.4
5	131.8	102.2	39.9	14.0
Mean	97.5	69.1	33.7	17.7

Publication III




“A 32-channel multi-coil setup optimized for the human brain
shimming at 9.4 T”

A. Aghaeifar, J. Zhou, R. Heule, B. Tabibian, B. Schölkopf, F. Jia, M.
Zaitsev, K. Scheffler

Magnetic Resonance in Medicine, 83 (2), pp. 749-764 (2020)

DOI: [10.1002/mrm.27929](https://doi.org/10.1002/mrm.27929)

A 32-channel multi-coil setup optimized for human brain shimming at 9.4T

Ali Aghaeifar^{1,2}  | Jiazheng Zhou^{1,2} | Rahel Heule¹  | Behzad Tabibian³ |
Bernhard Schölkopf³ | Feng Jia⁴  | Maxim Zaitsev⁴ | Klaus Scheffler^{1,5}

¹High-Field Magnetic Resonance Center, Max Planck Institute for Biological Cybernetics, Tuebingen, Germany

²IMPRS for Cognitive and Systems Neuroscience, University of Tuebingen, Tuebingen, Germany

³Department of Empirical Inference, Max Planck Institute for Intelligent Systems, Tuebingen, Germany

⁴Department of Radiology, Medical Physics, Faculty of Medicine, Medical Center University of Freiburg, University of Freiburg, Freiburg, Germany

⁵Department of Biomedical Magnetic Resonance, University of Tuebingen, Tuebingen, Germany

Correspondence

Ali Aghaeifar, High-Field Magnetic Resonance Center, Max Planck Institute for Biological Cybernetics, Max-Planck-Ring 11, 72076 Tuebingen, Germany.
Email: ali.aghaeifar@tuebingen.mpg.de

Funding information

German Research Foundation, Grant/Award Numbers: Reinhard Kossleck Project, DFG SCHE 658/12, SCHE 658/13, and ZA 422/6-1; Max Planck Society.

Purpose: A multi-coil shim setup is designed and optimized for human brain shimming. Here, the size and position of a set of square coils are optimized to improve the shim performance without increasing the number of local coils. Utilizing such a setup is especially beneficial at ultrahigh fields where B_0 inhomogeneity in the human brain is more severe.

Methods: The optimization started with a symmetric arrangement of 32 independent coils. Three parameters per coil were optimized in parallel, including angular and axial positions on a cylinder surface and size of the coil, which were constrained by cylinder size, construction consideration, and amplifiers specifications. B_0 maps were acquired at 9.4T in 8 healthy volunteers for use as training data. The global and dynamic shimming performance of the optimized multi-coil were compared in simulations and measurements to a symmetric design and to the scanner's second-order shim setup, respectively.

Results: The optimized multi-coil performs better by 14.7% based on standard deviation (SD) improvement with constrained global shimming in comparison to the symmetric positioning of the coils. Global shimming performance was comparable with a symmetric 65-channel multi-coil and full fifth-order spherical harmonic shim coils. On average, an SD of 48.4 and 31.9 Hz was achieved for in vivo measurements after global and dynamic slice-wise shimming, respectively.

Conclusions: An optimized multi-coil shim setup was designed and constructed for human whole-brain shimming. Similar performance of the multi-coils with many channels can be achieved with a fewer number of channels when the coils are optimally arranged around the target.

KEYWORDS

B_0 inhomogeneity, B_0 shimming, echo planar imaging, multi-coil, optimization, ultrahigh field

1 | INTRODUCTION

Ultrahigh field (UHF) MRI has been increasingly used by researchers in the last decade for neuroimaging of the human brain. UHF enables gaining a better understanding of brain functions by means of higher spatial resolution and signal-to-noise ratio (SNR). However, there are several significant challenges for imaging at UHF, for example, inhomogeneity in B_0 and B_1 field and specific absorption rate (SAR).¹⁻³

In particular, static field inhomogeneity is a long-standing issue from the early days of nuclear MR (NMR) imaging,⁴ which is more pronounced at UHF. Challenges originating from B_0 inhomogeneities are anticipated and reported in literature, including geometric distortion,⁵ spectra line broadening and weak water suppression,⁶ shortening T_2^* relaxation time,⁷ or voiding the signal.⁸ There are a few postprocessing approaches which can partially correct the consequences of poor B_0 uniformity.^{9,10} These methods attempt to retrospectively mitigate adverse effects of the static field perturbation rather than to address the problem at its origin.

Shimming—the process of homogenizing the static magnetic field—is a routine solution provided by vendors. One can quantitatively describe the existing B_0 field in the magnet with the aim of Laplace's equation, whose general solution yields a set of basis functions called spherical harmonics (SH). Most state-of-the-art UHF scanners are equipped with shim coils that can model spatial field distribution up to third-order SH. The size and specific winding pattern of such shim coils come along with a large inductance, resulting in long transient times after switching attributed to induced eddy currents and mutual inductance. This limitation makes such coils inflexible, and a pre-emphasis circuit is essential when rapid switching is required.^{11,12}

Another proposed method, known as multi-coil shim array, suggests using a group of small local coils to generate a local magnetic field.¹³ The generated local fields can contribute effectivity to counteract the existing B_0 inhomogeneity. Small size, low inductance, and lower power consumption of such coils make them a suitable choice for dynamic slice-wise shimming,^{14,15} integration into the radiofrequency (RF) receive coil,^{16,17} real-time correction of temporal B_0 alteration,¹⁸ generating spatial encoding magnetic fields,¹⁹ and novel parallel imaging methods.²⁰

The major part of the B_0 field perturbation comes from the sample or subject being imaged rather than the magnet imperfection itself.²¹ The human body is composed of air and water. The magnetic susceptibility difference of 9.41 ppm²² between air and water induces a magnetic field inhomogeneity nearby air-tissue boundaries.²³ This effect scales with the magnetic field strength and becomes more severe at UHF.¹ To overcome this issue, one can increase the number of the local coils or feed more current to the coils, which necessitates taking thermal issues into account. A simulation comparing the

performance of multi-coils with a different number of coils is reported in Stockmann et al.¹⁶ Although increasing the number of coils yields better shimming, it requires more dedicated amplifiers and, consequently, would not be cost-effective. Furthermore, difficulties in maintenance and troubleshooting are expected. A successful combination of a scanner's zeroth and first-order SH shim coils with a 16-channel multi-coil setup for dynamic shimming of the human brain at 9.4T is reported in Aghaeifar et al.,¹⁵ which allowed for more degrees of freedom (DOFs) in shimming at UHF using the scanner's built-in hardware.

In the brain, the strongest field inhomogeneities are found in the temporal lobe (TL) and prefrontal cortex because of proximity to the ear canals and sinuses, respectively.²⁴ In a few studies, active shim coils are placed in the mouth or over the nose to improve B_0 uniformity in the frontal lobe.^{25,26} This procedure can be considered as manual optimization of the coil positioning for local shimming. However, the subject's safety, their comfort, and the stability of the coils are questionable in this case. Given that the overall geometry and structure of the head and skull as well as the relative location of air cavities and ear canals are similar across humans, a similar pattern of B_0 inhomogeneity in the human brain is expected and has been observed. Therefore, the shim array can be modified for better performance on an identified target pattern. Theoretical design of shim arrays with an irregular shape to generate low-order SH²⁷ and to fit with C-type permanent magnet has recently been presented.²⁸ Another study has demonstrated the application of a genetic algorithm to design a coil with an irregular shape, which is optimized only for 4 representative slices of the brain²⁹ and extended later for optimization of position and geometry of 16 coils for 2 slices of a single brain.³⁰

Thus, the aim of the present work was to design and construct an optimized multi-coil shim array to target the B_0 inhomogeneity in the whole human brain. This will help to enhance B_0 shimming at UHF without the need to add more coils. Optimization was performed under specific constraints to keep the construction step simple. The performance of the optimized multi-coil is compared to the conventional symmetric coils arrangement with a different number of local coils and with different orders of SH. The efficiency of the designed and constructed setup is evaluated in vivo with several sequences susceptible to B_0 inhomogeneity.

2 | METHODS

2.1 | Optimizations

In this study, the optimization was performed on a 32-channel multi-coil setup to improve shimming performance for a human brain target. All coils were positioned on a cylinder with a diameter of 323 mm. This is the minimum allowable diameter that can house the utilized RF coil.³¹ Optimization

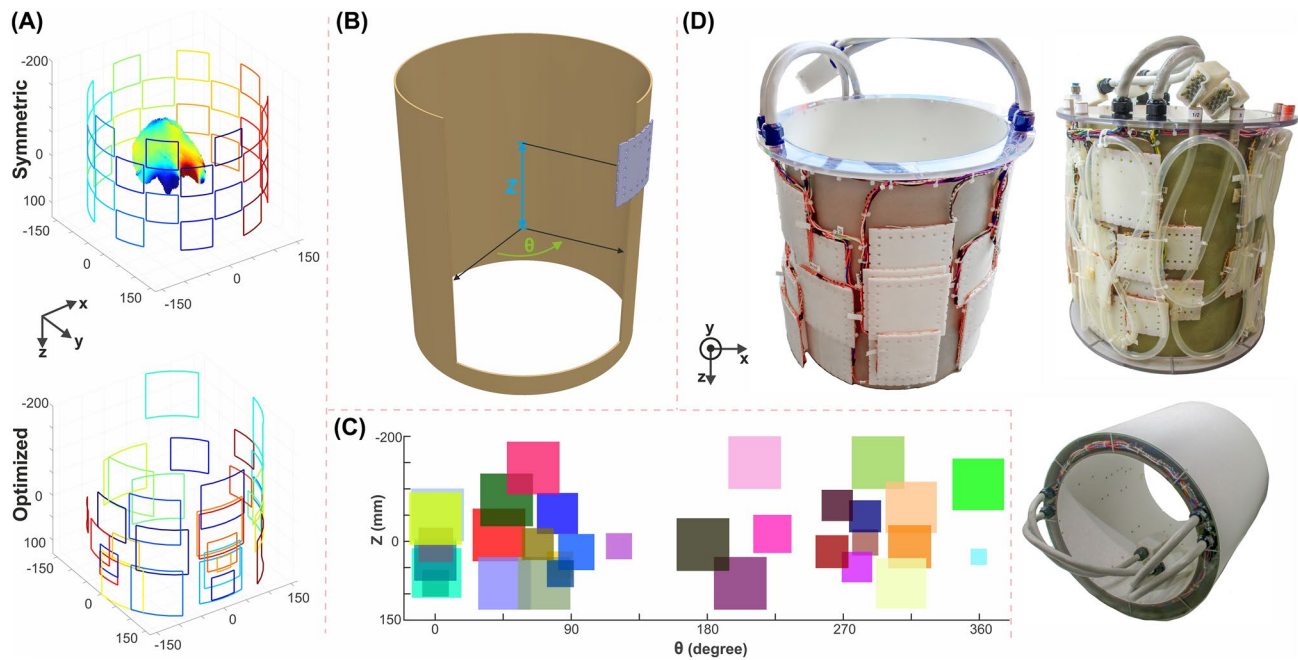


FIGURE 1 A, The arrangement of the coils on the cylinder surface before and after multi-coil optimization. Optimization started from a symmetric arrangement of the 32 coils in 4 rows with a side length of 60 mm. B, DOFs for the position of the coils represented in the cylindrical coordinate system. Axial value (Z) was constrained to the cylinder size, but the angular value (θ) was unconstrained during the optimization. C, The arrangement of the coils of optimized multi-coil in (A), which is transformed into a 2D plane. D, Experimental realization of the optimized 32-channel multi-coil

started from a symmetric arrangement of 32 coils in 4 rows on the surface of the cylinder (Figure 1A). All coils had an identical square shape with an equal side length of 60 mm and 25 wire turn. Because of the cylindrical skeleton, the optimization was performed in a cylindrical coordinate system with 3 DOFs for each coil as follows:

1. Size of the coil (i.e., side length of a square coil) where the shape does not change.
2. Axial coordinate (Z) or height of the center of coils in the cylinder surface.
3. Angular coordinate (θ), the angle between the reference axis on a chosen plane and a line from the origin to the projection of the coil center to that plane (Figure 1B).

The first 2 DOFs (i.e., size and height) were constrained during the optimization while the angular coordinate was unconstrained given that, theoretically, it should lay between $-\pi$ and $+\pi$. The lower and upper bounds for the size of the coils were [20 and 100] mm, respectively, and for the height of the coils were [-150 and +80] mm, respectively. Therefore, based on the maximum side length of the coils, the required overall length for the cylinder would be 330 mm. During the construction, the cylinder length was chosen longer to reserve space for wires going outside the multi-coil (final cylinder length was 400 mm). The initial side length of 60 mm was chosen as the middle of the upper and the lower bound of

the coil size. For the chosen initial coil arrangement, there was no overlapping between the coils and the free spacing between a coil and the next closest coil was negligible.

A nonlinear constrained optimization was implemented in MATLAB (The MathWorks, Inc., Natick, MA) using the function, *fmincon*. The purpose of the nonlinear constrained optimization was to find the most effective configuration of coils. After every successful iteration, new shim basis maps were generated, and the required current per coil was calculated by a constrained linear least-squares optimization (*lsqlin* command in MATLAB). The flowchart of the optimization process is depicted in Figure 2A, where the box with a yellow outline refers to the constrained linear least-squares optimization. Given that the gradient of the objective function with respect to the position of the coils was simply not analytically attainable in a closed-form expression, the choice of solver was limited to one that can numerically estimate the gradient. Two algorithms were utilized to this end: sequential quadratic programming (SQP)³² and interior point.³³ Both algorithms yielded acceptable improvement; however, SQP converged faster and was therefore selected as solver for the final optimization. To calculate shim currents, the bounds were variable according to the coil size. Given that smaller coils produce less heating, the current for the largest coils with a side length of 100 mm was constrained to 1.5 A, and it was modeled to increase linearly with decreasing coil size. The current bound was truncated to 3 A for the coils with side

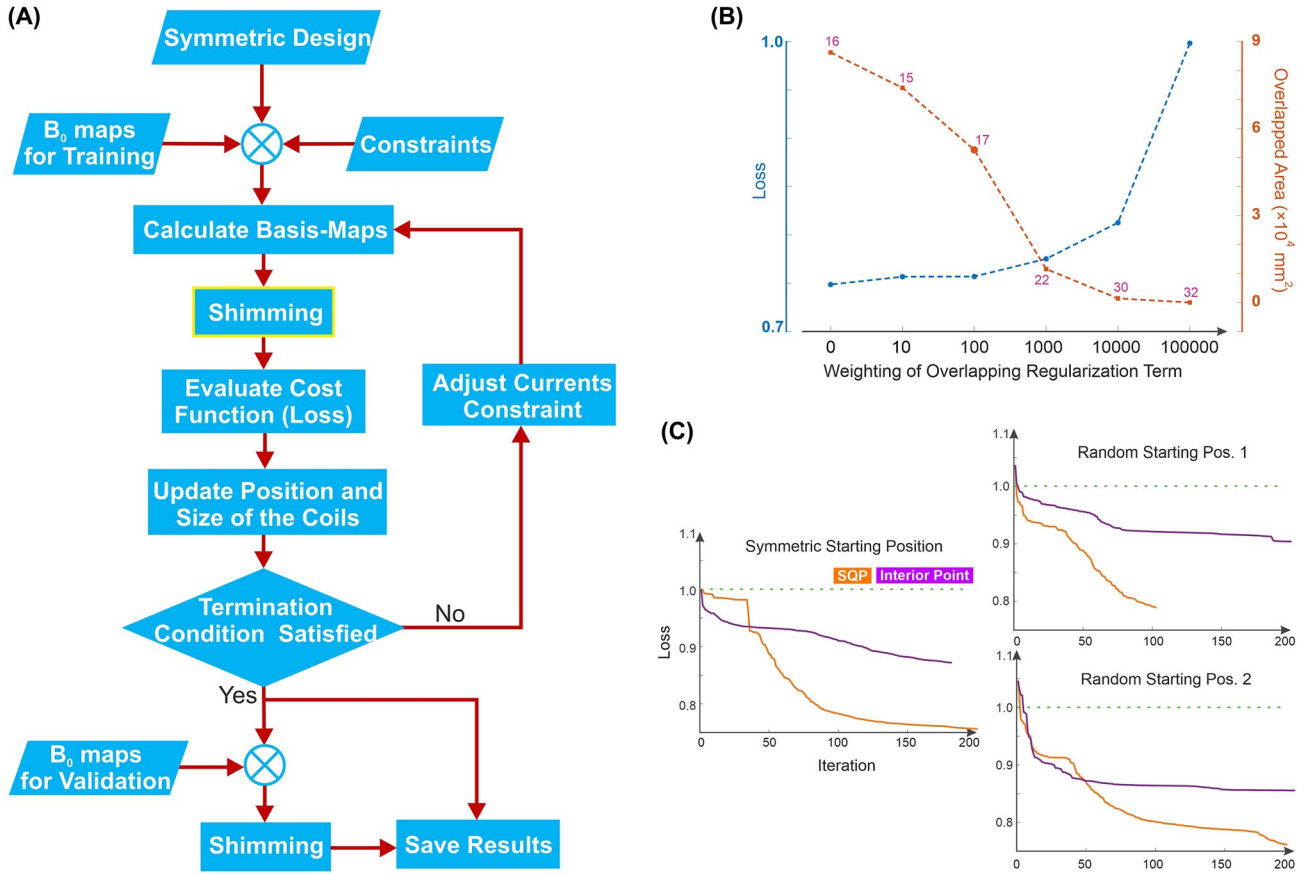


FIGURE 2 A, Flowchart of the optimization process used in this study. There are 3 inputs for the optimizations, including constraints, initial coil arrangement, and the training data. It is permitted to adjust the current constraints based on the coil size. The returned value of the cost function is the sum of the residual off-resonance after shimming in individual training B_0 maps as explained in Equation 1. The optimization will be terminated when the changes in the arrangement and size of the coils are smaller than a defined threshold. B, Impact of the overlapping regularization term on the efficiency of the final design. Increasing the weighting decreases the total overlapped areas, but degrades the final loss (loss: output of cost function defined in Equation 1). The numbers in pink represent the maximum number of the coils that do not need to be moved to outer layers. The loss values are normalized with respect to the loss of the symmetric design. C, Speed of convergence of 2 algorithms, SQP, and interior point, used in this study from symmetric initial coils arrangement and 2 representative random initial coils arrangements. SQP could converge faster and yield a smaller loss for all cases. The values are normalized to the loss obtained from symmetric design

length smaller than 50 mm because of to the employed amplifier specifications (e.g., the currents for coils with a size length of 100, 75, 50, and 30 mm were constrained to 1.5, 2.0, 3.0, and 3.0 A, respectively).

B_0 maps of the brain from 12 volunteers were measured at a magnet with a static field of 9.4T after applying the scanner's second-order SH global shimming. All maps were interpolated into a standard coordinate system with a field of view (FOV) of $300 \times 300 \times 300 \text{ mm}^3$ and isotropic resolution of 3.0 mm. The B_0 maps were split into 2 groups of 8 and 4 maps. The first group with 8 maps was used for optimization (training), and the second group with 4 maps was used for validation of the optimization outcome. The cost function of the optimization is described by Equation 1:

$$\text{cost}(x) = \sum_{i=1}^8 \sum_{j=1}^{32} (c_{ij}m_j + b_i) \quad (1)$$

where x includes the size and position of the coils in the current iteration, b_i is the B_0 map of the i^{th} brain, m_j is the basis-map of the j^{th} coil, and c_{ij} is the current of the j^{th} coil calculated for the i^{th} brain through constrained linear least-squares optimization. Given that the coils may overlap partially or completely after optimization, the overlapping coils were mounted in different layers during the construction. However, it is possible to modify Equation 1 and add an additional regularization term to address coil overlapping, that is, $\text{cost}_{\text{new}}(x) = \text{cost}(x) + kF(x)$, where $F(x)$ is given by the summation of intersections between coils and k represents a weighting factor.

Additionally, the performance of the optimization algorithm was investigated with noisy inputs. Thus, white Gaussian noise with standard deviation (SD) between 0 and 40 Hz was added to the training B_0 maps. The coil optimization was then repeated and the performance of the obtained

optimized coil was compared to the case with 0 additive noise. Given that inaccurate placement of the coils during construction is possible, stability of the optimization output was further investigated. The axial and angular value of the coil locations were shifted randomly in the range of ± 10 mm and $\pm 4^\circ$, respectively. The performance of the shimming after coil repositioning was evaluated and compared with the original optimized multi-coil.

2.2 | Construction

As mentioned in the optimization procedure, smaller coils were allowed to carry higher currents up to 3A. The generated magnetic field is proportional to $n \times I$, where n is the number of turns and I is the passing current, and power dissipation is equal to RI^2 , where R is the resistance of the coil. Therefore, the smaller coils were built with more windings instead of supplying higher current to reduce thermal losses (i.e., all currents were constrained into 1.5 A in experimental measurements because of increasing the coil's winding). A copper wire with a thickness of 0.8 mm was used for coil

winding. A 3D printed support was designed to avoid bowing of the overlapped coils and to fasten the coils to the cylinder (Supporting Information Figure S1). The support was drawn in CATIA (Dassault Systems, Suresnes, France) for each coil while considering the cylinder peripheral curve. A thin plastic pipe split into 3 branches was swirled around the coils for the water cooling of the setup in case it was needed. Later, the whole free space between the inner cylinder (diameter = 323 mm) and the outer cover (diameter = 370 mm) was filled with epoxy (Polytec EP 641; Polytec PT GmbH, Karlsbad, Germany) to prevent mechanical vibration of the coils.

2.3 | Simulations

Basis-maps of the multi-coils with a different number of coils (8, 16, 24, 32, 48, 65, and 96) were analytically calculated using Biot-Savart's law. Individual coils of all multi-coils were symmetrically positioned on the surface of a cylinder with diameter and length of 323 and 330 mm, respectively (Figure 3). All coils were simulated with 25 wire turns and a square shape. The diameter of the coils was adjusted for each

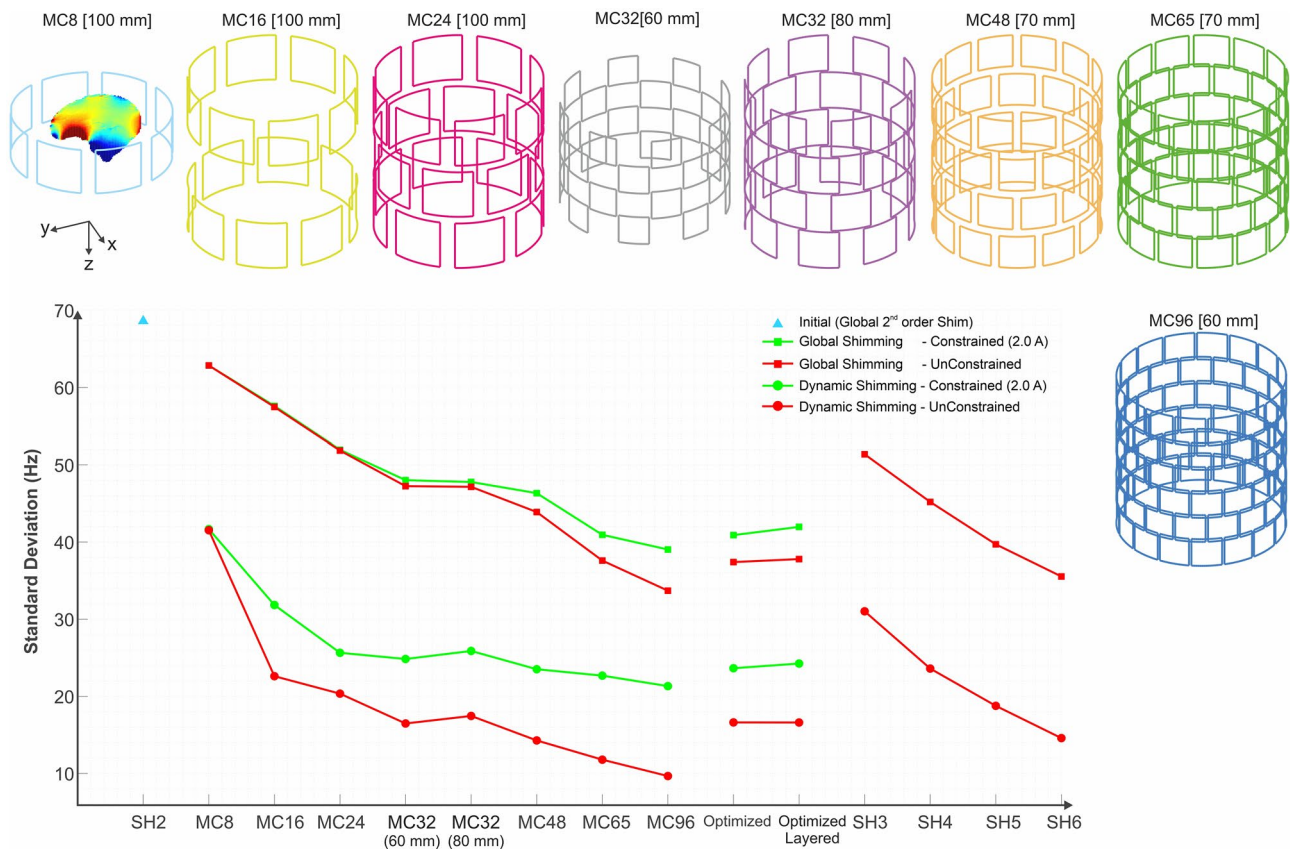


FIGURE 3 Comparison of the simulated shimming performance between optimized multi-coil, multi-coils with a different number of coils, and spherical harmonics basis set. Shimming is carried out in global and dynamic slice-wise fashion while the current is constrained and unconstrained. Only unconstrained shimming with spherical harmonics is performed given that they are calculated analytically. The shimming is performed on 14 brain B_0 maps, which were acquired at 9.4T. All maps are transformed into a standard space with an isotropic resolution of 1.5 mm. The side length of the coils is indicated above each sketched multi-coil. Two different 32-channel multi-coils are simulated, one has larger coils for full coverage of the cylinder, and the other is the one used for optimization

multi-coil to cover the whole cylinder surface with minimal overlapping. Performance of the multi-coils was compared in terms of global and slice-wise shimming for 14 brain B_0 maps while the input current was constrained to 2.0 A and unconstrained. All B_0 maps were interpolated to a standard space with an isotropic resolution of 1.5 mm. The target volume of shimming consisted of $379,555 \pm 28,740$ voxels corresponding to 1282 ± 97 mL (mean \pm SD). The shim currents were optimized for a 4.5-mm slab centered with respect to the slice of interest in case of slice-wise shimming. As a benchmark, unconstrained shimming was performed with SH basis sets up to sixth order as well. ΔB_0 SD and root mean squares (RMS) were calculated after shimming and averaged over all volunteers for whole brain. The shimming performance was further assessed locally within a spherical volume, which had an average diameter of 4 and 2.8 cm around the prefrontal cortex (PFC) and ear canals, respectively.

2.4 | Setup characterization

Home-built amplifiers were used to supply current for the local coils.³⁴ Each channel could supply up to 5 A (120 A in total). The output voltage was adjustable through the user interface to control thermal loss (maximum, 24 V). A current sense resistor of 0.1 Ω in series connected to the output for real-time current monitoring, and feedback control. A 10-Hz square wave signal with an amplitude of 2 V (corresponding to 2 A) and 50- μ s ramp time was applied to the current amplifier while monitoring the output current. Then, the proportional-integral-derivative controller of the amplifiers was adjusted on a channel-by-channel basis to achieve minimum settling time and overshooting for the inductive load of the individual channels. Each control term was adjusted by a digital variable resistor through the user interface. All the adjustment values were saved in the amplifiers' memory for the future experiments. A custom-built LabVIEW program (National Instruments, Austin, TX) received the trigger signal from the scanner and then updated the output of a PXIe-6738 unit (digital to analog output module) to control the amplifiers. All the required currents were imported to the LabVIEW program before start of the scan. The LabVIEW program changes the current within a 2-ms time interval using 200 intermediate steps (where time interval and number of steps were adjustable). The currents passing into the coils were read from the current feedback signal and displayed in the LabVIEW program to discover mismatch between inputs and outputs.

Investigation of the possible interaction between overlapped coils was studied through temporal field monitoring with a field camera.³⁵ The field camera consisted of 16 ^{19}F -NMR sensors (Skopec Magnetic Resonance Technologies, Zurich, Switzerland) tuned for a magnet with a field strength

of 9.4T and distributed on the surface of a sphere with a diameter of 20 cm. A signal consisting of a sequence of alteration between [0, +2, -2, +2, 0] was applied to the amplifier input in 5 steps. The field measurement lasted 20 ms for each step, which started 4 ms before input current alteration and sampled at a temporal resolution of 1 μ s. The resulting time-varying phase was extracted from the signal of the probes, unwrapped, and used for B_0 estimation by linear regression of the phase time course of every 1 ms. Furthermore, gradients waveform estimation with NMR probes was checked in the presence and absence of the multi-coil to test disturbance rejection of the amplifiers and influence of the setup on the produced encoding magnetic fields.

Similar to our previous design,¹⁵ several measurements, including B_1^+ , temporal SNR (tSNR), and SNR, were carried out with and without multi-coil to evaluate the influence of the multi-coil on image quality. Thermal behavior of the setup was characterized by applying the maximum current to all channels for an hour and measuring the temperature on the surface of the setup.

2.5 | B_0 shimming and imaging protocols

Five healthy volunteers participated in the study (average age, 25 ± 4 years) in accord with the local ethics protocol. A dual-echo gradient echo (GRE) sequence was used to measure reference B_0 maps for the subsequent calculations (flip angle [FA], 12° ; $TE_1/TE_2/TR$, 2.8/7.8/15 ms; FOV, $208 \times 208 \times 160$ mm³; isotropic resolution of 2.0 mm). The magnitude images and B_0 maps were reconstructed offline from the raw data. Later, a 3D brain mask was created from the magnitude image using brain extraction tools³⁶ and spatial phase unwrapping was applied to the B_0 maps.³⁷ Then, constrained least-squares optimization was performed on the shimming problem, which can be described by Equation 2:

$$\min_x \|(Ax - B)\|^2 \quad (2)$$

where B is a $v \times 1$ vector representing the unshimmed brain B_0 map (v : number of voxels after masking), A is a $v \times n$ matrix of the shim basis-set (n : number of shim channels), and x is an $n \times 1$ vector containing the unknown shim currents. The MATLAB *lsqlin* function was used to solve this minimization problem. Equation 2 was also used for the shimming of training B_0 maps in every iteration when optimizing the coil arrangement and size as explained above, with the difference that matrix A was updated in every iteration. The calculation of the required shim currents was performed in MATLAB. Once the shim currents were calculated, they were saved as a table in a text file to be used by the LabVIEW program as explained previously.

The performance of global and dynamic slice-wise shimming was evaluated by using multiecho GRE, echo planar imaging (EPI), and balanced steady-state free precession (SSFP) sequences. Multi-echo GRE was not only used for assessment of the dynamic B_0 shimming, but also for T_2^* characterization. All echoes were acquired with monopolar read-out gradients. The acquisition protocol included FOV: $204 \times 204 \text{ mm}^2$, isotropic resolution of 2.0 mm, FA: 20° , TE/TR: [5, 9.5, 15, 22, 30, 40]/80 ms, and 16 slices (slice gap = 200%). EPIs were measured with different isotropic resolutions and acceleration factors. The bandwidth (BW) was adjusted for each EPI to minimize echo-spacing and, accordingly, geometric distortions. The acquisition parameters were FOV: $204 \times 204 \text{ mm}^2$, isotropic resolution of [2.0, 2.0, 1.5, 1.0] mm, FA: 60° , TE/TR: 24/2000 ms, 16 slices (slice gap = [200, 200, 300, 500] %), BW: [2132, 2131, 1838, 1442] Hz/Px, 6/8 partial Fourier, and generalized autocalibrating partially parallel acquisitions (GRAPPA) factor: [1, 2, 2, 3] (parameters between brackets “[]” are ordered consistently with respect to each other). Images with a balanced SSFP (bSSFP) sequence were acquired using sign-alternated RF pulses. The actual image acquisition of each slice was preceded by 16 RF ramp preparation pulses followed by 100 dummy pulses to ensure steady-state conditions. The acquisition protocol included FOV: $204 \times 204 \text{ mm}^2$, isotropic resolution of 1.0 mm, FA: 30° , TE/TR: 7.5/15 ms, and 16 slices (slice gap = 500%). T_2^* and bSSFP data were acquired for 4 subjects. All of the employed sequences were able to send out a trigger signal before RF excitation to synchronize the sequence and the shimming hardware. The trigger signal was followed by a 2-ms delay to compensate for the ramp transition of shim currents between 2 states and any lag in the setup.

3 | RESULTS

Figure 1A demonstrates the result of optimizing the position and size of the coils. The shim coils are depicted in the scanner gradient coordinate system (+Z = feet, -Z = head, +Y = anterior, -Y = posterior, +X = left, and -X = right). Figure 1C shows arrangement of the optimized multi-coil when the cylindrical coordinate is transformed into a 2D plane. Supporting Information Figure S1 shows how the coils' supports with a thickness of ≈ 7.5 mm are layered. Figure 1D displays the constructed 32-channel multi-coil setup optimized for the human brain. Coils were installed in 4 layers including 16, 11, 3, and 2 coils in the layers 1 to 4, respectively. Overall, the optimized multi-coil consisted of 8, 11, 9, and 4 coils placed in the top (anterior), right and up-right, left and up-left, and bottom (posterior) of the cylinder, respectively. The measured inductance and resistance of the coils at 1 kHz was ranging from 108 to 232 μH and from 2.1 to 5.7 Ω , respectively.

The addition of the setup (connected to the amplifier with 0 A in all channels) did not significantly affect the excitation profile (B_1^+ map), SNR, and tSNR (Supporting Information Figures S2, S3, and S4). Supporting Information Figure S5 shows the results of the thermal tests measured with an array of 16 temperature sensors and an infrared camera (images were acquired at the end of measurement). Given that the setup temperature can be considered safe for human measurements with the specified current bounds, no water cooling was used during the experiments.

Figure 2B shows how an increased weighting of the overlapping regularization term, k , affects the final loss, total overlapped areas, and the maximum number of the coils in the first layer. The pink numbers in the plot represent the maximum number of the coils which can be installed in the first layer (their original position). Including an additional regularization term increases the nonlinearity degree of the problem and yields a less effective coil arrangement. Investigating the effect of noisy training B_0 maps shows that adding Gaussian noise with SD below 30 Hz to training data did not affect performance of the obtained optimized coil (changes below 1% on average over 14 brain B_0 maps). However, the shimming performance decreased by 12% for the case comprises Gaussian noise with SD of 40 Hz. The evaluation of the stability of the optimization output reveals that a minor inaccuracy in the placement of the coils can degrade the performance by 1.5% and 0.4% in global and slice-wise shimming, respectively (on average over 5 sets of inaccurate positions).

Summary of the shimming performance in simulation for several symmetric coils arrangements, the 32-channel optimized multi-coil (with and without layering), and SH term is shown in Figure 3. The results correspond to the shimming performance averaged across 14 brain B_0 maps, which were not included into the training. Two different symmetric 32-channel multi-coils are simulated; one has slightly larger coils which cover the cylinder fully, and another one served as initial configuration of the coils for optimization. The performance of the 32-channel optimized coil (with SD of 40.9 and 37.4 Hz for the case of constrained and unconstrained global shimming, respectively) is comparable to the 65-channel symmetric design. In comparison to the SH terms, the performance is slightly better than full fifth-order SH for the case of unconstrained global shimming. Layering the coils resulted in a slight increase of the SD by approximately 1.1 Hz for constrained global shimming. In comparison to the initial symmetric design and based on SD of the residual off-resonance after shimming, performance improved by 14.7% and 20.8% after optimization with constrained and unconstrained global shimming, respectively (which decreased to 12.4% and 19.9% after layering). Table 1 shows the amount of performance

TABLE 1 Different metrics and subregions used to evaluate improvement in shimming performance of the optimized multi-coil with respect to the symmetric design (with side length of 60 mm) in simulation

	Shim scope:	Global [2.0 A, unconstrained] %		Slice-wise [2.0 A, unconstrained] %	
	Criterion:	SD	RMS	SD	RMS
Original	Whole brain	[14.7, 20.8]	[14.7, 20.8]	[8.6, 4.7]	[8.6, 4.7]
	Frontal cortex	[11.5, 20.4]	[14.4, 24.0]	[10.5, 10.7]	[10.9, 11.0]
	Near ear canals	[17.4, 23.3]	[19.4, 25.9]	[6.6, 1.9]	[6.6, 1.9]
Layered	Whole brain	[12.4, 19.9]	[12.4, 19.9]	[6.3, 4.9]	[6.2, 4.9]
	Frontal cortex	[9.3, 19.6]	[11.8, 23.1]	[8.0, 11.3]	[8.4, 11.5]
	Near ear canals	[14.4, 22.7]	[16.0, 25.1]	[4.0, 0.7]	[3.9, 0.6]

Global and dynamic shimming for both the constrained and unconstrained case are studied.

improvement of the optimized multi-coil with respect to the symmetric design based on SD and RMS for different subregions, constrained and unconstrained shimming, as well as global and dynamic slice-wise shimming. The presented results are calculated before and after coil layering. RMS is a better metric for subregions given that it characterizes the off-resonance fully while SD ignores the mean of the off-resonance. Supporting Information Table S1 displays the achieved improvement for 14 individual B_0 maps used in the simulation (the optimized design after layering compared to the symmetric 32-channel). On average, the required shim currents for unconstrained global/slice-wise shimming are in total 47.1/5512 A and 122.5/5457 A for symmetric and optimized multi-coil, respectively.

Redundancy in the magnetic fields generated by the individual coils after optimization is quantified based on correlation coefficient and singular value decomposition. The results are depicted in Supporting Information Figure S6. In summary, 55% of correlation coefficients were between 0 ± 0.25 , and the cumulative sum of the first 10 eigenvalues reached 80% of the total eigenvalues energy. This means that several coils can be replaced with a single coil (probably with an irregular shape) and 1 more powerful amplifier. The obtained results are based on the magnetic field generated in a spherical FOV with a diameter of 200 mm centered on the scanner isocenter.

Figure 4A shows the phase evolution of the NMR field probes during current alteration in channel 29 of the multi-coil. Channel 29 is mounted in the upper part of the cylinder above the frontal cortex of the volunteer and is overlapped with channels 3, 11, 24, and 25. The ΔB_0 estimation from the closest field probe to the coil is plotted. No eddy-current contamination has been observed in the fitted ΔB_0 . Similar results have been achieved for other channels. Furthermore, the estimated gradient waveform reveals that there is a small interaction between gradients and the setup which can be compensated at an acceptable level when the amplifiers are switched on (Figure 4B).

Figure 5 displays the in vivo performance of the 32-channel optimized multi-coil in B_0 shimming. On average over all subjects, the whole-brain SD of off-resonance after performing global and dynamic slice-wise multi-coil shimming decreased from 71.9 to 48.4 Hz and 31.9 Hz, respectively. Table 2 shows SD of off-resonance in the whole brain for all volunteers. The average SD of global shimming in the measurement (48.4 Hz) for 5 volunteers is slightly higher than in the simulation (42.0 Hz); however, the average SD after second-order SH in the measurement (71.9 Hz) is also higher than the average SD of B_0 maps used in the simulations (68.6 Hz).

Figure 6 illustrates the impact of the shimming on correction of the geometric distortion in EPIs and the corresponding voxel shift map. An anatomical image acquired with GRE sequence is used as an undistorted reference image. Ventricles align better with anatomy, and a large portion of the distortion in the frontal cortex is recovered for both global and dynamic multi-coil shimming at the cost of stretching in anterior. On average over all volunteers, voxel shifts larger than 5 mm after global and dynamic slice-wise shimming decreased by 49% and 64%, respectively, for all utilized EPI protocols (discrepancy was below 2.5% for different resolutions). The EPIs for other resolutions and subjects are provided in Supporting Information Figures S7 and S8.

Figure 7 compares the banding artifacts in bSSFP images. Three slices covering the cerebellum, ear canals, and frontal cortex are chosen for the comparison. Global multi-coil shimming reduced the banding artifacts in different areas, and dynamic slice-wise multi-coil shimming was successful in a higher degree to eliminate a large portion of the banding artifacts. The bSSFP images for other subjects are provided in Supporting Information Figure S9.

The outcome of the T_2^* calculation after second-order shimming as well as global and dynamic multi-coil shimming is depicted in Figure 8. Two slices that cover areas of the brain with the highest B_0 inhomogeneity from each subject are shown. Both dynamic slice-wise and global multi-coil shimming resulted in T_2^* gain for the areas with

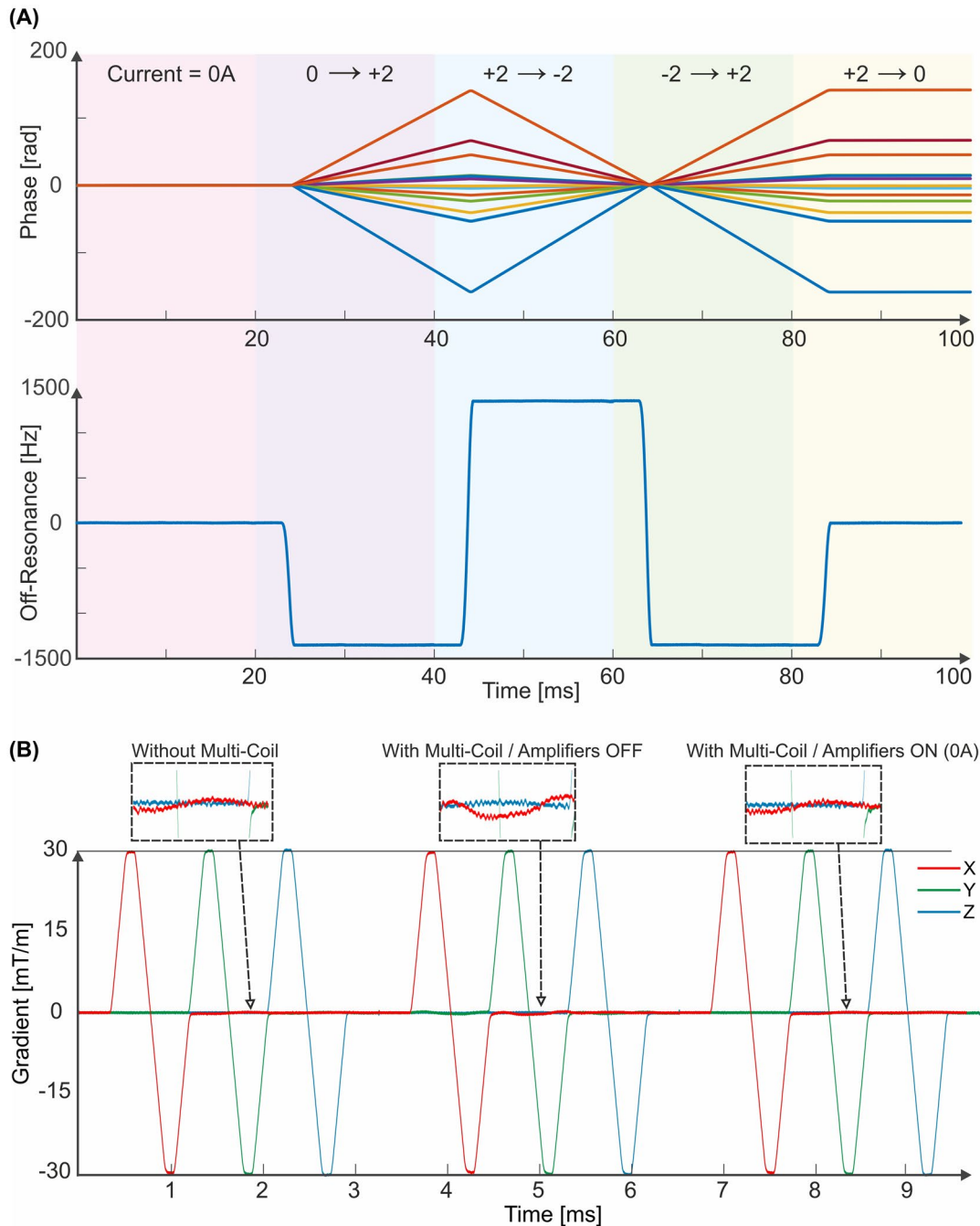


FIGURE 4 A, Temporal field monitoring with NMR field probes during input current alternation for channel 29. Phase evolution of all 16 field sensors during the 5 steps, including 0A input, switching from 0A to 2A, switching from 2A to -2A, switching from -2A to 2A, and switching from 2A to 0A, is depicted. Then, the generated off-resonance during the 5 steps of the current alteration is calculated from the linear regression of every 1 ms of phase data. B, NMR field probes are utilized to calculate gradients waveform in absence of multi-coil, presence of multi-coil, but the amplifiers are off, and presence of multi-coil while the amplifiers are on with 0A inputs. The amplifiers compensated the induced currents arisen from rapid gradients switching. The input waveform consisted of individual gradient axes switching with an amplitude and a rise time of 30 mT/m and 150 μs, respectively

severe B_0 inhomogeneities. The T_2^* ratio increased by 18.1% and 28.0% in the vicinity of the ear canals as well as 8.8% and 12.5% in PFC after global and slice-wise shimming, respectively.

The information of the coils layering and description of wiring pattern according to the public multi-coil information policy³⁸ can be found in Supporting Information Tables S2 and S3, respectively.

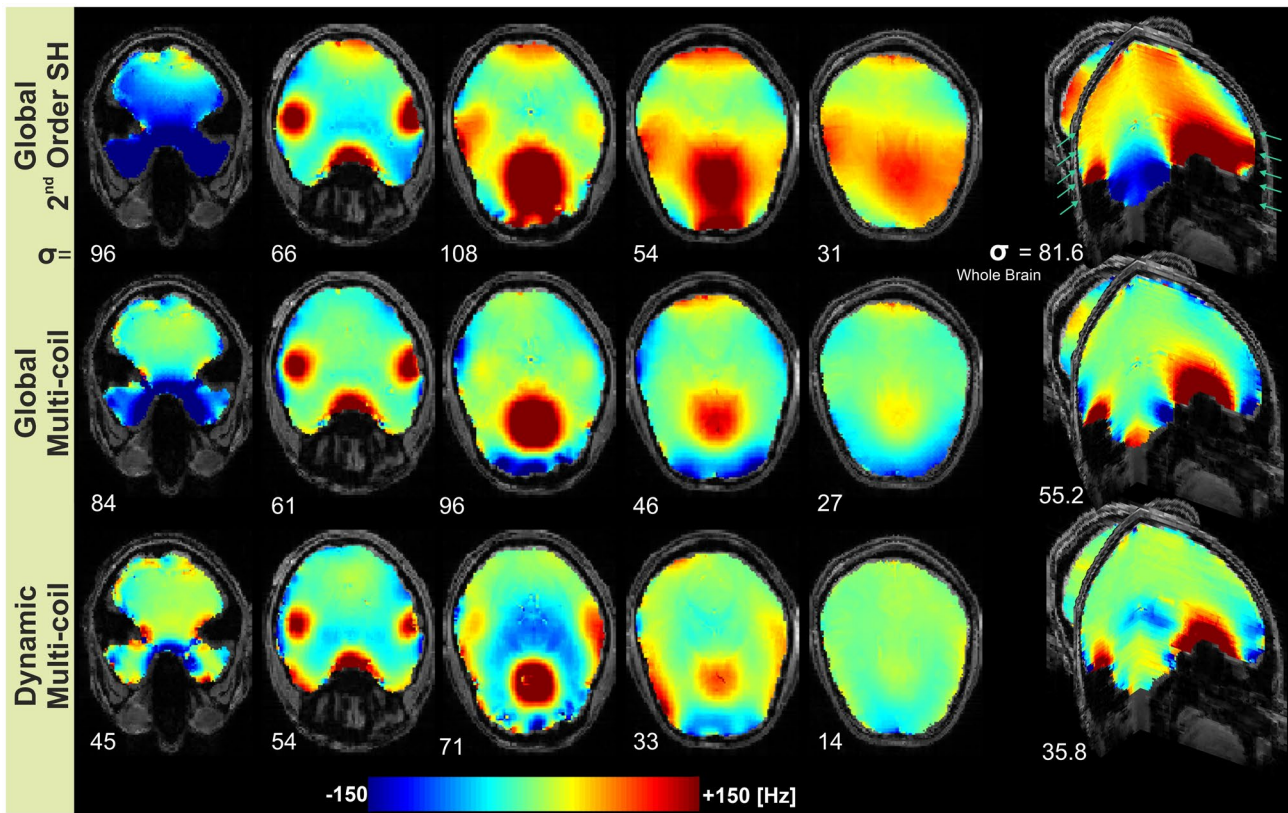


FIGURE 5 Comparison of the residual B_0 inhomogeneity after different shimming approaches. The whole brain is shimmed at the beginning with the scanner's second-order built-in spherical harmonic shims. After having the second-order shim applied, global and dynamic multi-coil shimming is performed

TABLE 2 The SD of B_0 inhomogeneity after different shimming strategies for individual volunteers and on average across all (experimental data)

Subjects No.	Target volume (mL)	Shimming method (STD)		
		Second-order SH	Global multi-coil	Dynamic multi-coil
1	1199	65.8	45.4	28.1
2	1502	75.7	51	32.4
3	1321	75	48	30.1
4	1046	61.5	42.4	33.4
5	1470	81.6	55.2	35.8
Average	1307	71.9	48.4	31.9

4 | DISCUSSION

The aim of this study is to design and construct a prototype of a multi-coil shim setup that is optimized for human brain shimming. The optimization procedure resulted in new coil arrangements and sizes, which allow boosting of shimming performance without increasing the number of coils. The optimization was limited to 3 DOFs per coil; axial and angular value in the cylindrical coordinate system and the coil size. Avoiding constraints in the coil geometry (i.e., permitting for irregular coil shapes) increases the number of DOFs;

however, it may either result in a coil shape with difficulties to build or in overfitting of the model.

The designed multi-coil arrangement in this work may not be suitable for combined RF and B_0 shim array, as is proposed in earlier works^{16,17} attributed to possible degradation in sensitivity profile of the receive coils and more challenges in coils decoupling. Additionally, the optimized multi-coil may not be a proper choice for applications beyond B_0 shimming similar to what is suggested in Umesh Rudrapatna et al¹⁹ for imaging and in Scheffler et al²⁰ for acceleration because of nonuniform coverage of the FOV.

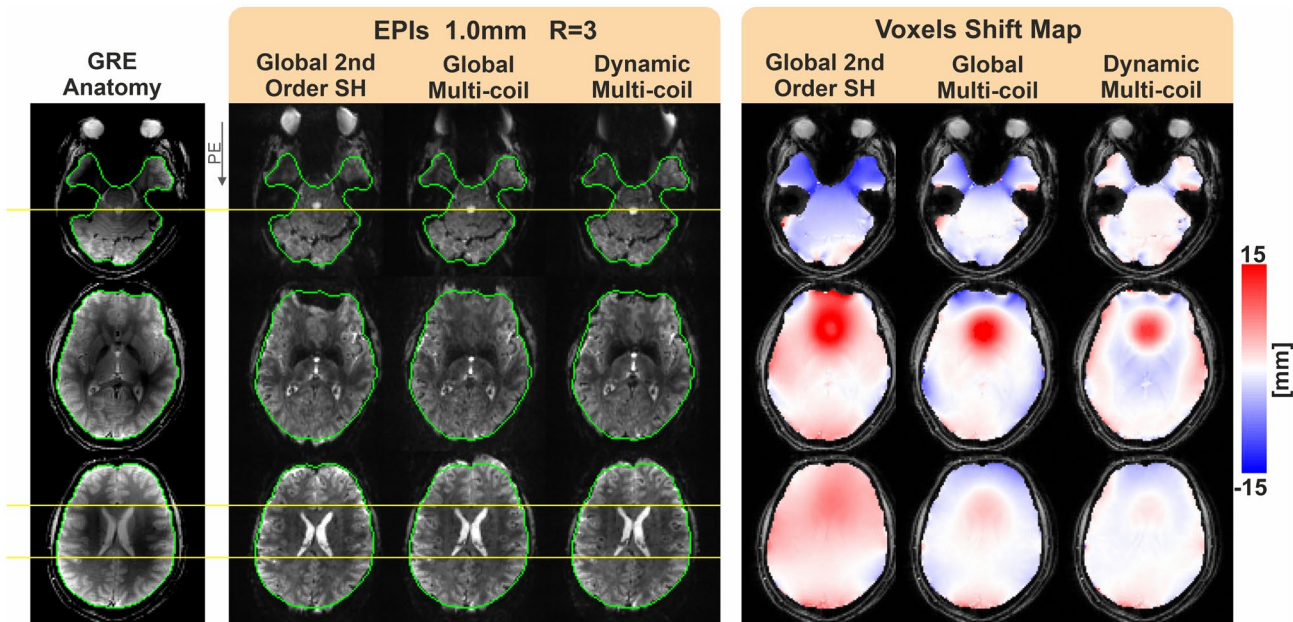


FIGURE 6 Evaluation of the geometric distortion for 3 representative slices of the brain at 1.0-mm isotropic resolution. Voxel shift maps are calculated based on B_0 maps and the EPI acquisition protocol. Better shimming results in less distortion, which is also apparent from the voxels shift maps. The amount of distortion in high-resolution accelerated 1.0 mm imaging is approximately 2 times less than in low-resolution 2.0-mm isotropic EPI without acceleration (depicted in Supporting Information Figure S7)

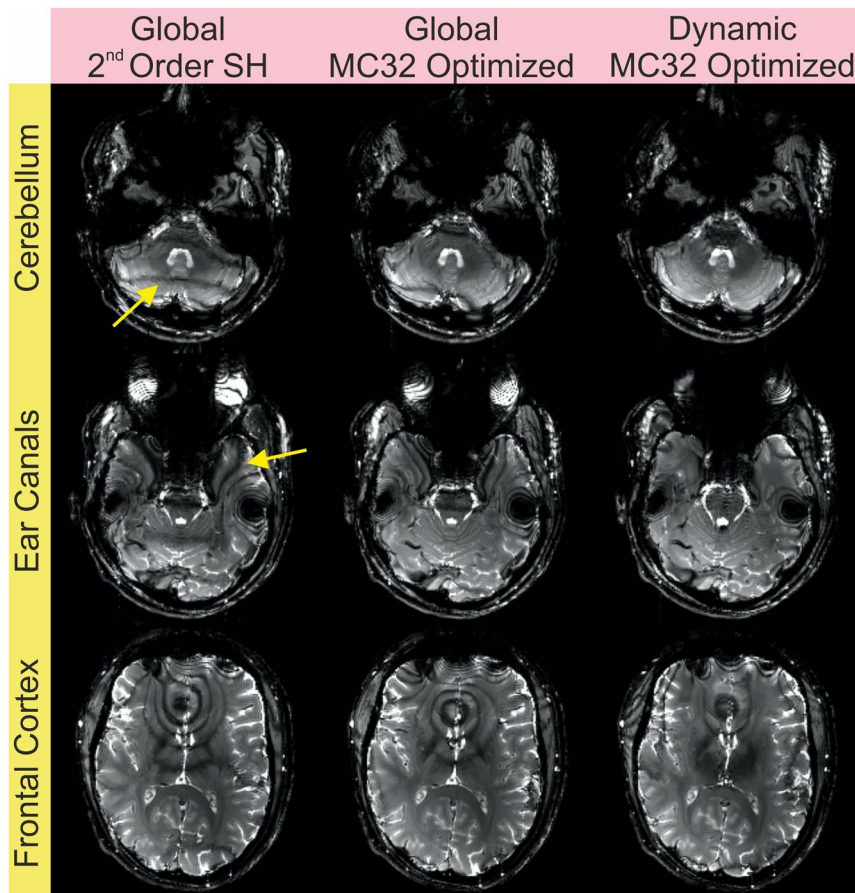


FIGURE 7 Effect of the improved B_0 homogeneity on banding artifacts in bSSFP images. Three representative slices from 3 areas of the brain with the highest B_0 inhomogeneity are selected. Global and dynamic multi-coil shimming apparently reduces banding artifacts

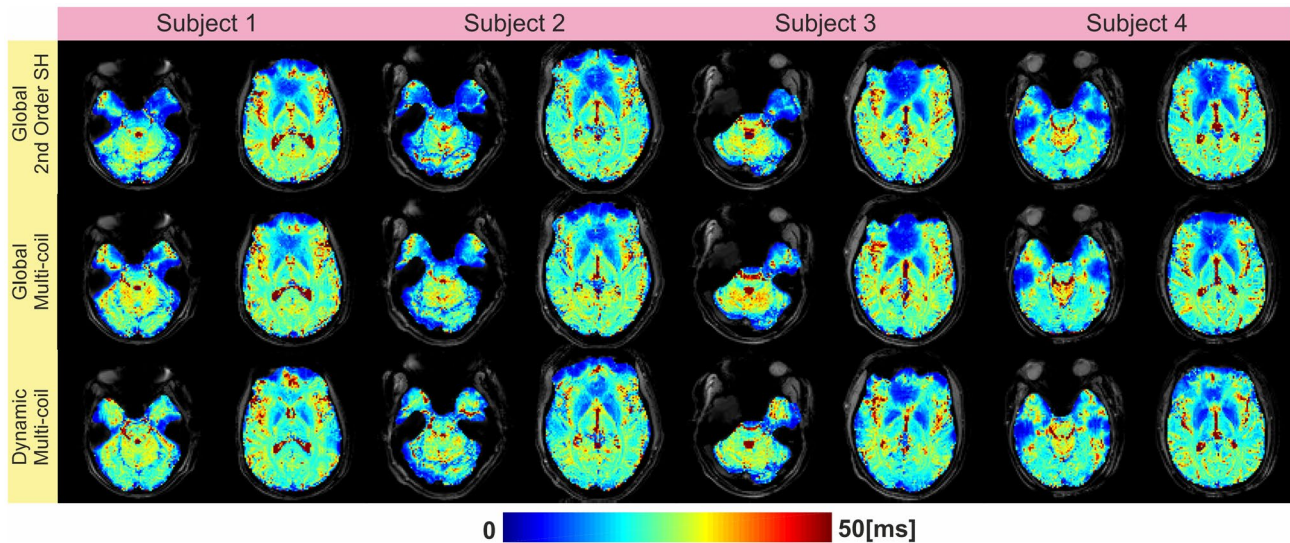


FIGURE 8 Impact of the shimming with the optimized multi-coil on the quality of the T_2^* mapping. Two slices were selected for each volunteer to evaluate the T_2^* increase in the PFC and near the ear canals

Another approach suggests optimizing the wiring pattern with genetic algorithm,²⁹ which can result in a complex design. In contrast, we used simple square coils and optimized the position and size rather than the shape. The optimization of multi-coil for position, geometry, and number of the segments for 2 slices of a human brain B_0 map is also reported in Zivkovic et al.³⁰ However, no in vivo measurement has been reported to date, and neither any performance analysis of the design on the whole brain nor any comparison with higher-order SH and other multi-coils are yet available.

The target of the optimization in this study was global shimming of the human brain, which is more general and applicable for whole-brain 3D sequences or multiband 2D sequences. However, the performance was evaluated for dynamic slice-wise shimming in both simulations and in vivo measurements. The position of the coils could be optimized to improve the performance of dynamic slice-wise shimming, but different results are expected for different slice orientations, which may limit the optimization output for more specific applications. Furthermore, the optimization of the shimming performance for dynamic slice-wise shimming may not result in a significant improvement, because the region of shimming is small and thus symmetric configuration of coils can even yield similar shimming performance.

Optimization of size and position of a limited set of external coils similar to this study is presented in Juchem et al²⁴ for magnetic field homogenization of the human PFC at 4T. However, the optimization routine and the utilized algorithm were not explained clearly enough for proper comparison. The resultant improvement of SD reported in Juchem et al²⁴ for PFC and whole brain with respect to SH shimming is 29% and 3%, respectively, which in this study improvement

for PFC/TL/whole brain with respect to SH shimming is 10.6/9.5/32.7% and 37.6/34.9/55.6% (based on RMS is 30.9/14.8/35.2% and 57.1/38.8/55.1%) with global and slice-wise shimming, respectively (in experimental measurements). However, it has to be noted that the target of optimization for these 2 studies is different. The presented combined 32-channel RF-shim coil setup in Stockmann et al¹⁶ improved the field homogeneity in simulation by 31.1% and 49.0% for constrained global and slice-wise shimming, respectively (magnet strength of 3T and 50 slices with a thickness of 2.0 mm), which in this study is 40% and 65.3% in simulation (after layering) and 32.7% and 55.6% in measurement for constrained global and slice-wise shimming, respectively. In Juchem et al,¹⁴ a SD of 25 Hz was reported in the experimental study after dynamic slice-wise shimming with a 48-channel multi-coil at 7T (100 turns per coil and shimming target volume of 1269 mL), which in this study is 31.9 Hz at 9.4T (25–50 turns per coil and shimming target volume of 1307 mL). A previously reported 16-channel multi-coil setup utilized for shimming of human brain at 9.4T yielded 13.1% and 38.1% improvement with respect to the second-order SH after constrained global and slice-wise shimming, respectively.¹⁵ In Juchem et al,³⁹ where the same multi-coil setup as described in Juchem et al¹⁴ was used, it was reported that the T_2^* ratio increased by approximately 15% and 30% in PFC and TL, respectively, after dynamic multi-coil shimming at 7T, while in the current study the gain is 12.5% and 28% in PFC and TL, respectively (both studies were performed with an isotropic resolution of 2.0 mm). Overall, the achieved results in this study are in agreement with the reports in recent publications. There is an improvement in some of the obtained results, and the rest do not contradict with the results from previous literature.

The utilized solver for optimization was based on the SQP algorithm. The natively implemented SQP algorithm in MATLAB allows for nonlinear constrained optimization, fast execution, less memory usage, and no explicit definition of the gradient of the cost function (the gradient is estimated by finite differences). SQP converged faster than interior point algorithm in MATLAB; however, it may not be the best choice among all published solvers to this end. Figure 2C compares the performance of the 2 nonlinear constrained algorithms, SQP and interior point, in different iterations. Given that SQP updates the Hessian matrix at each major iteration, it performs better in locating the local minima and moves faster to its final result. The runtime of both algorithms at the same number of iterations was similar; however, SQP converged into a lower loss. Using a quad-core 3.5 GHz Intel Xeon processor, computation time to obtain the optimal coil arrangement was approximately 48 hours. The objective function of the problem may not be convex, and therefore the obtained solution may not necessarily be a global minimum. To this aim, optimization with 9 random initial coils positioning was performed. Coil arrangements after optimization for 9 different starting points did not yield an identical result; however, none of them performed considerably better than the case when symmetric coil positioning was chosen as the starting point (Figure 2C). The obtained optimized coil arrangements (with SQP algorithm) starting from random initial positions improved the shim performance by $13.2 \pm 2.8\%$ and $10.9 \pm 3.5\%$ with respect to their initial positions and the symmetric design, respectively. Therefore, it can be concluded that the objective function is not a convex function, and there is no guarantee that the obtained result after optimization (with the initial symmetric coil positioning mentioned earlier) is the most optimal coil arrangement. Nevertheless, there was an improvement and shimming with this new coil arrangement performs better by 14.7% in comparison to the conventional symmetric design. The optimization allowed coil overlapping, which was addressed later by layering the overlapped coils. Two coils may be overlapped entirely during the optimization iterations, which results in a non-full-rank basis-set matrix. However, this is not a problem as long as constrained shimming was performed in every iteration. Unconstrained shimming can also be applied during the iterative optimization process; however, the final arrangement must be evaluated with constrained shimming.

The initial bench test of the setup revealed slight in-place mechanical vibration of some local coils. Although the coils were fixed tightly, small imperceptible local vibration of the coils in outer layers did not allow adjusting the proportional-integral-derivative in the amplifier. As a consequence, the transient time of the output current did not follow a similar pattern after several sharp changes in input and even was getting worse. To address this issue, the free space in the cylinder was filled with an epoxy which eliminated the shaking of the

coils. To be on the safe side, a thin plastic tube was circulated in the cylinder before using epoxy to set up a water-cooling system in the case of overheating. The weight of the setup increased considerably after epoxy filling from 15 to 27.4 kg.

Although the human brain is almost symmetric in anatomy, the coil arrangement shown in Figure 1A is not symmetric with respect to the YZ (sagittal) plane. There are 3 possible reasons. First, the center of the brain in the train data may not agree with the isocenter of the scanner, which is the center of the coordinate system in the optimization. Second, as seen in the first row of Figure 5, the B_0 map of the brain is not perfectly symmetric respect to the center sagittal plane. Magnet imperfection, other contamination sources, and head orientation can cause asymmetric brain B_0 maps. Third, even when ignoring the 2 reasons above, the solver may converge to an asymmetric arrangement to shim a symmetric B_0 map; for example, 2 small coils in the right side can perform equally as well as 1 big coil in the left side. However, the resultant coil arrangement after optimization matches the overall B_0 pattern of the human brain. Several coils are located in the anterior to address the inhomogeneity in the PFC. Some of the coils are small to cancel very local inhomogeneities or compensate for the adverse effect of the large coils in vicinities. On the contrary, only a few large coils are positioned in the posterior. There are also many coils in the left, left-anterior, right, and right-anterior to cancel out inhomogeneities around ear canals and to also support better shimming of the PFC.

The simulation results depicted in Figure 3 reveal that constrained and unconstrained global shimming yielded a similar shim performance for the 32-channel symmetric design. However, unconstrained shimming improved the performance of the optimized design. As a consequence, the performance of the symmetric arrangement is intrinsically limited regardless of current constraints, while the performance of the optimized design is limited by the current bounds. Increasing the current constraints to ± 6.0 A resulted in 19% better performance in global shimming for the optimized design after layering with respect to the symmetric arrangement (which was 12.4% with current constraints based on coil size as reported in Table 1). It has to be noted that the absolute sum of the currents in all channels did not exceed 77.0 A on average over 14 brain B_0 maps. Such a performance gain is simply possible by increasing the coil windings to 100 turns (similar to Juchem et al¹⁴) if supplying higher currents is not desired.

Interestingly, adding more coils increased the difference in shim performance between constrained and unconstrained global shimming as can be observed in Figure 3. Smaller coils have a smaller penetration depth and their shim fields might not contribute to compensate more distant inhomogeneities while in case of unconstrained shimming the shim fields are strong enough to penetrate deeper and contribute

also to compensate more remote inhomogeneity. Another reason might be that smaller coils can more effectively shim small targets (e.g., near ear canals or PFC) without significantly affecting the neighbor voxels and degrading the magnetic field produced by adjacent coils. Therefore, their impact is limited by the supplied current. However, unconstrained shimming is not a realistic solution because of current amplifier limitations and thermal issues. For the case of constrained dynamic slice-wise shimming (axial slices), a multi-coil with 24 channels can shim with the same performance level like a multi-coil with 65 channels (assuming the proposed geometry). Hence, there is no performance gain for multi-coil optimization (with the DOF as mentioned earlier) if dynamic slice-wise shimming is the goal.

Figures 5-8 show the performance of the constructed multi-coil for different applications. The off-resonance level in the PFC and ear canals proximity is remarkably reduced. Although the multi-coil is optimized for global shimming, the performance for dynamic shimming has been preserved as well (and slightly got better). With dynamic shimming, the residual inhomogeneity at 9.4T became very close to what is obtained at the conventional 3T scanner after second-order global shimming.

Considering Figure 7, it is important to note that the bSSFP frequency response is periodic with $1/TR$. Supporting Information Figure S10A displays a simulation of the bSSFP profile based on the utilized acquisition protocol as well as literature white matter and gray matter T_1 and T_2 values at 9.4T. The periodic profile illustrates that even when the field homogeneity is improved, new banding artifacts can be generated for certain areas, which were in the pass-band before shimming and then shifted into the stop-band of the bSSFP profile after shimming. An example for this issue is shown in Supporting Information Figure S10B after global shimming. Therefore, the number, density, and distance of the bandings after shimming have to be considered rather than individual artifacts.

Despite a reduction of the geometric distortion in the center area of some slices covering brain ventricles, some stretching in the anterior is apparent after shimming, which was also observed in other recent studies.^{15,40} The inhomogeneities in the proximity of boundaries in the anterior part are lower than in the inner areas. Nevertheless, the areas, which are closer to the shim coils, feel considerably stronger magnetic fields produced by the local coils. However, the least-square optimization considers the whole target volume for shimming. Although the homogeneity may get worse in some regions, it will be overall improved in the target volume after shimming.

The MATLAB source code of the implemented multi-coil optimization in this study is available under the MIT license from the project website: https://github.com/Aghaeifar/optimized_multi_coil.

5 | CONCLUSIONS

Multi-coil shim setups can be optimized for specific targets to increase shim performance without adding additional coils. The performance of the 32-channel optimized multi-coil which was proposed in this study is comparable to a 65-channel multi-coil with conventional symmetric design. In comparison to the symmetric arrangement with the same number of coils for which constrained and unconstrained global shimming yields similar results, the efficiency of the proposed optimized coil is limited by the supplied current.

ACKNOWLEDGMENTS

We thank Andrew Wright for careful proofreading of the manuscript, Mirsat Memaj for all mechanical design, and Theodor Steffen and Joshi Walzog for help running the shim amplifier and coil winding. We also acknowledge Azadeh Nazemorroaya for her assistance in the measurements.

ORCID

Ali Aghaeifar  <https://orcid.org/0000-0002-6964-0992>

Rahel Heule  <https://orcid.org/0000-0002-4589-6483>

Feng Jia  <https://orcid.org/0000-0003-3593-2513>

REFERENCES

1. Uğurbil K. Imaging at ultrahigh magnetic fields: history, challenges, and solutions. *NeuroImage*. 2018;168:7–32.
2. Fiedler TM, Ladd ME, Bitz AK. SAR simulations & safety. *NeuroImage*. 2018;168:33–58.
3. Stockmann JP, Wald LL. In vivo B_0 field shimming methods for MRI at 7 T. *NeuroImage*. 2018;168:71–87.
4. O'Donnell M, Edelstein WA. NMR imaging in the presence of magnetic field inhomogeneities and gradient field nonlinearities. *Med Phys*. 1985;12:20–26.
5. Jezzard P, Clare S. Sources of distortion in functional MRI data. *Hum Brain Mapp*. 1999;8:80–85.
6. Chen Z, Cai S, Huang Y, Lin Y. High-resolution NMR spectroscopy in inhomogeneous fields. *Prog Nucl Magn Reson Spectrosc*. 2015;90–91:1–31.
7. Chavhan GB, Babyn PS, Thomas B, Shroff MM, Haacke EM. Principles, techniques, and applications of T_2^* -based MR imaging and its special applications. *Radiographics*. 2009;29:1433–1449.
8. Drangova M, Pelc NJ. Artifacts and signal loss due to flow in the presence of B_0 inhomogeneity. *Magn Reson Med*. 1996;35:126–130.
9. Liu Y, Ma C, Clifford BA, Lam F, Johnson CL, Liang ZP. Improved low-rank filtering of magnetic resonance spectroscopic imaging data corrupted by noise and B_0 field inhomogeneity. *IEEE Trans Biomed Eng*. 2016;63:841–849.
10. Jezzard P. Correction of geometric distortion in fMRI data. *NeuroImage*. 2012;62:648–651.

11. Fillmer A, Vannesjo SJ, Pavan M, Scheidegger M, Pruessmann KP, Henning A. Fast iterative pre-emphasis calibration method enabling third-order dynamic shim updated fMRI. *Magn Reson Med*. 2015;1131:1119–1131.
12. Juchem C, Nixon TW, Diduch P, Rothman DL, Starewicz P, De Graaf RA. Dynamic shimming of the human brain at 7 T. *Concepts Magn Reson Part B Magn Reson Eng*. 2010;37B:116–128.
13. Juchem C, Nixon TW, McIntyre S, Rothman DL, De Graaf RA. Magnetic field modeling with a set of individual localized coils. *J Magn Reson*. 2010;204:281–289.
14. Juchem C, Nixon TW, McIntyre S, Boer VO, Rothman DL, De Graaf RA. Dynamic multi-coil shimming of the human brain at 7 T. *J Magn Reson*. 2011;212:280–288.
15. Aghaeifar A, Mirkes C, Bause J, et al. Dynamic B_0 shimming of the human brain at 9.4 T with a 16-channel multi-coil shim setup. *Magn Reson Med*. 2018;80:1714–1725.
16. Stockmann JP, Witzel T, Keil B, et al. A 32-channel combined RF and B_0 shim array for 3T brain imaging. *Magn Reson Med*. 2016;75:441–451.
17. Truong TK, Darnell D, Song AW. Integrated RF/shim coil array for parallel reception and localized B_0 shimming in the human brain. *NeuroImage*. 2014;103:235–240.
18. Topfer R, Foias A, Stikov N, Cohen-Adad J. Real-time correction of respiration-induced distortions in the human spinal cord using a 24-channel shim array. *Magn Reson Med*. 2018;80:935–946.
19. Umesh Rudrapatna S, Fluerebrock F, Nixon TW, de Graaf RA, Juchem C. Combined imaging and shimming with the dynamic multi-coil technique. *Magn Reson Med*. 2019;81:1424–1433.
20. Scheffler K, Bause J, Loktyushin A, Aghaeifar A, Steffen T, Schölkopf B. Spread-spectrum magnetic resonance imaging. *Magn Reson Med*. 2019;82:877–885.
21. De Graaf RA, Juchem C. B_0 Shimming Technology. In: Webb AG, ed. *Magnetic Resonance Technology: Hardware and System Component Design*. Cambridge, UK: The Royal Society of Chemistry; 2016:166–207.
22. Schenck JF. The role of magnetic susceptibility in magnetic resonance imaging: MRI magnetic compatibility of the first and second kinds. *Med Phys*. 1996;23:815–850.
23. de Graaf RA. Hardware 10.1. In *in vivo NMR Spectroscopy*. Chichester, UK; Hoboken, NJ: Wiley; 2007:479–548.
24. Juchem C, Nixon TW, McIntyre S, Rothman DL, De Graaf RA. Magnetic field homogenization of the human prefrontal cortex with a set of localized electrical coils. *Magn Reson Med*. 2010;63:171–180.
25. Hsu JJ, Glover GH. Mitigation of susceptibility-induced signal loss in neuroimaging using localized shim coils. *Magn Reson Med*. 2005;53:243–248.
26. Wong EC, Mazaheri Y. Shimming of the inferior frontal cortex using an external local shim coil. In *Proceedings of the 12th Annual Meeting of the ISMRM*, Kyoto, Japan, 2004. p. 520.
27. While PT, Korvink JG. Designing MR shim arrays with irregular coil geometry: theoretical considerations. *IEEE Trans Biomed Eng*. 2014;61:1614–1620.
28. Chen W, Chen J, Sun H, Chen Z. Simulation and analysis of irregular multi-coil B_0 shimming in C-type permanent magnets using genetic algorithm and simulated annealing. *Appl Magn Reson*. 2019;50:227–242.
29. Zivkovic I, Mirkes C, Scheffler K. B_0 shimming at 9.4T using a multi-coil approach—coil design with genetic algorithm. In *24th Annual Meeting and Exhibition of the ISMRM*, Singapore, 2016. p. 1152.
30. Zivkovic I, Tolstikhin I, Schölkopf B, Scheffler K. B_0 matrix shim array design-optimization of the position, geometry and the number of segments of individual coil elements. In *33rd Annual Scientific Meeting of the European Society for Magnetic Resonance. Medicine and Biology*. Vienna, Austria, 2016:36.
31. Avdievich NI, Giapitzakis IA, Bause J, Shajan G, Scheffler K, Henning A. Double-row 18-loop transceive-32-loop receive tight-fit array provides for whole-brain coverage, high transmit performance, and SNR improvement near the brain center at 9.4T. *Magn Reson Med*. 2019;81:3392–3405.
32. Bonnans JF, Gilbert JC, Lemarechal C, Sagastizábal CA. Local methods for problems with equality constraints. In *Numerical Optimization*. Berlin: Springer; 2006:215–253.
33. Waltz RA, Morales JL, Nocedal J, Orban D. An interior algorithm for nonlinear optimization that combines line search and trust region steps. *Math Program*. 2006;107:391–408.
34. Aghaeifar A, Zivkovic I, Steffen T, Mirkes C, Scheffler K. Flexible gradient driver system for a multi-coil setup; design considerations and implementation. In *34th Annual Scientific Meeting of the European Society for Magnetic Resonance in Medicine and Biology*. Barcelona, Spain: 2017:50–51.
35. Barmet C, De Zanche N, Pruessmann KP. Spatiotemporal magnetic field monitoring for MR. *Magn Reson Med*. 2008;60:187–197.
36. Smith SM. Fast robust automated brain extraction. *Hum Brain Mapp*. 2002;17:143–155.
37. Abdul-Rahman HS, Gdeisat MA, Burton DR, Lalor MJ, Lillie F, Moore CJ. Fast and robust three-dimensional best path phase unwrapping algorithm. *Appl Opt*. 2007;46:6623–6635.
38. Juchem C, de Graaf RA. The public multi-coil information (PUMCIN) policy. *Magn Reson Med*. 2017;78:2042–2047.
39. Juchem C, Umesh Rudrapatna S, Nixon TW, de Graaf RA. Dynamic multi-coil technique (DYNAMITE) shimming for echo-planar imaging of the human brain at 7 Tesla. *NeuroImage*. 2015;105:462–472.
40. Kim T, Lee Y, Zhao T, Hetherington HP, Pan JW. Gradient-echo EPI using a high-degree shim insert coil at 7 T: implications for BOLD fMRI. *Magn Reson Med*. 2017;78:1734–1745.

SUPPORTING INFORMATION

Additional supporting information may be found online in the Supporting Information section at the end of the article.

FIGURE S1 The designed supports allowed easy layering of the overlapping coils. The thickness of the supports was 7.5 mm

FIGURE S2 Comparison of the B_1^+ field in the presence and absence of the constructed multi-coil. The spatial distribution and strength remained similar. An actual flip angle imaging (AFI) sequence was used to measure the B_1 field. The phantom filled with equivalent tissue properties (e558.6, r50.64 S/m)

FIGURE S3 Comparison of the SNR and noise correlation matrix in the presence and absence of the constructed

multi-coil. The difference is minor and may be attributed to discrepancies in the positioning of the phantom. The SNR was calculated based on the pseudo multiple replica approach

FIGURE S4 Comparison of the temporal SNR and noise correlation matrix in the presence and absence of the constructed multi-coil. The temporal SNR was determined in a spherical agar phantom from 100 measurements

FIGURE S5 The produced heating attributed to the resistance of the coils is a major concern. To this end, all channels were fed with 1.5 A for an hour and the temperature was monitored with temperature sensors that were attached to the setup. Furthermore, infrared images with a thermal image (E6 thermal imager; FLIR Systems, Wilsonville, OR) were acquired at the end of the measurement. The hottest point was in the outer surface of the multi-coil where several coils are overlapped in the anterior. However, this area is not in contact with the subject

FIGURE S6 Redundancy in the magnetic fields generated by the individual coils before and after optimization. (A) Matrix of correlation coefficients. Numbers close to zero represent less similarity in the magnetic field generated by 2 individual coils. (B) The cumulative sum of shim coils eigenvalues. Summation of the first 14 and 10 principal components reached to 80% of total eigenvalue energy for symmetric and optimized design, respectively

FIGURE S7 Evaluation of the geometric distortion and voxel shift map at resolution of 1.5-mm isotropic and 2.0-mm isotropic for the same subject depicted in Figure 6. EPIs with 2.0-mm isotropic resolution are acquired without and with an acceleration factor of 2

FIGURE S8 Evaluation of the geometric distortion and voxel shift map at resolution of 1.0-mm isotropic (GRAPPA factor = 3) and 2.0-mm isotropic (no acceleration) for subjects 2 to 5

FIGURE S9 Effect of the improved B_0 homogeneity on banding artifacts in bSSFP images for subjects 2 to 4

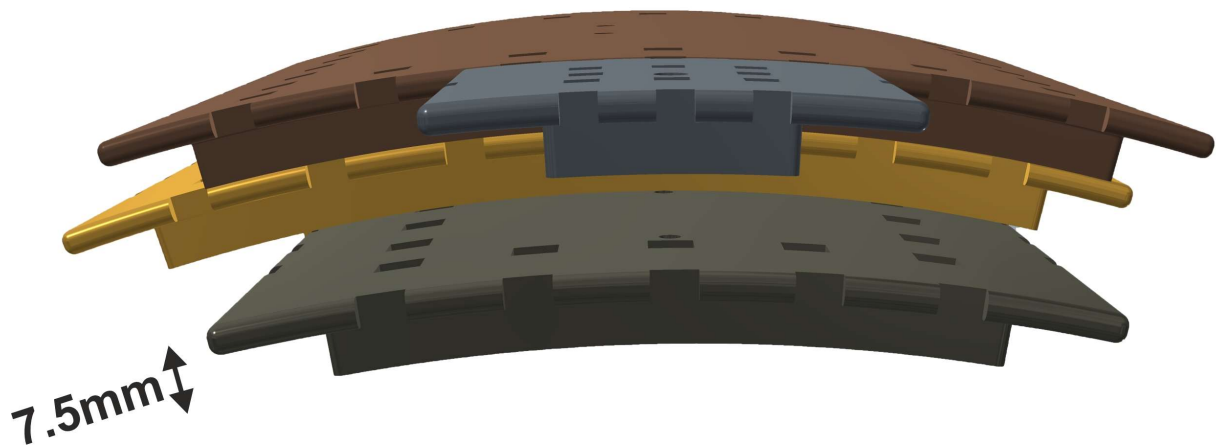
FIGURE S10 (A) The periodic profile of bSSFP frequency response simulated based on the acquisition protocol used in this study (in our case, $1/TR$ corresponds to a periodicity of 66 Hz). (B) An example of generating new banding artifact after global shimming while the shimming is improved. Because of the periodic profile, some areas may be shifted from pass-band into stop-band after shimming

TABLE S1 Evaluation of improvement in shimming performance of optimized multi-coil with respect to the symmetric design in global shimming for individual subjects

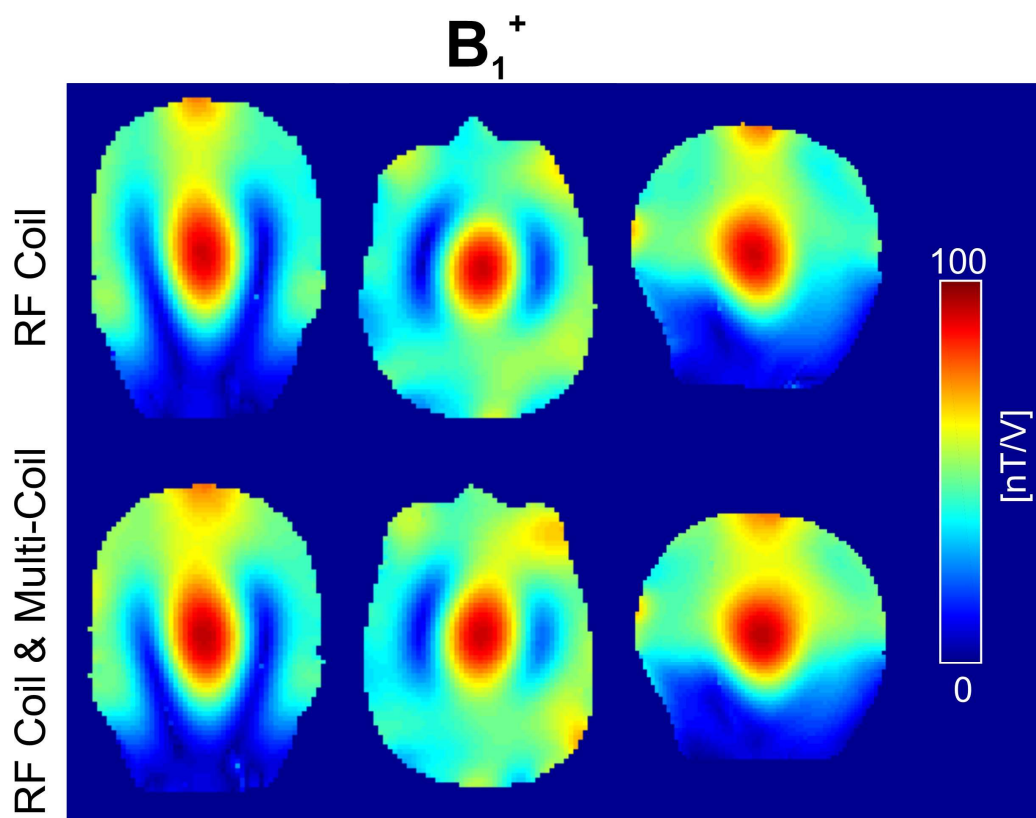
TABLE S2 Information of coils layering to overcome the overlapping between the coils after optimization The base for choosing a layer for a coil was to keep the most coils in layer1, then layer2 and so forth.

TABLE S3 The wiring pattern of the designed 32-channel optimized multi-coil according to the public multi-coil information policy

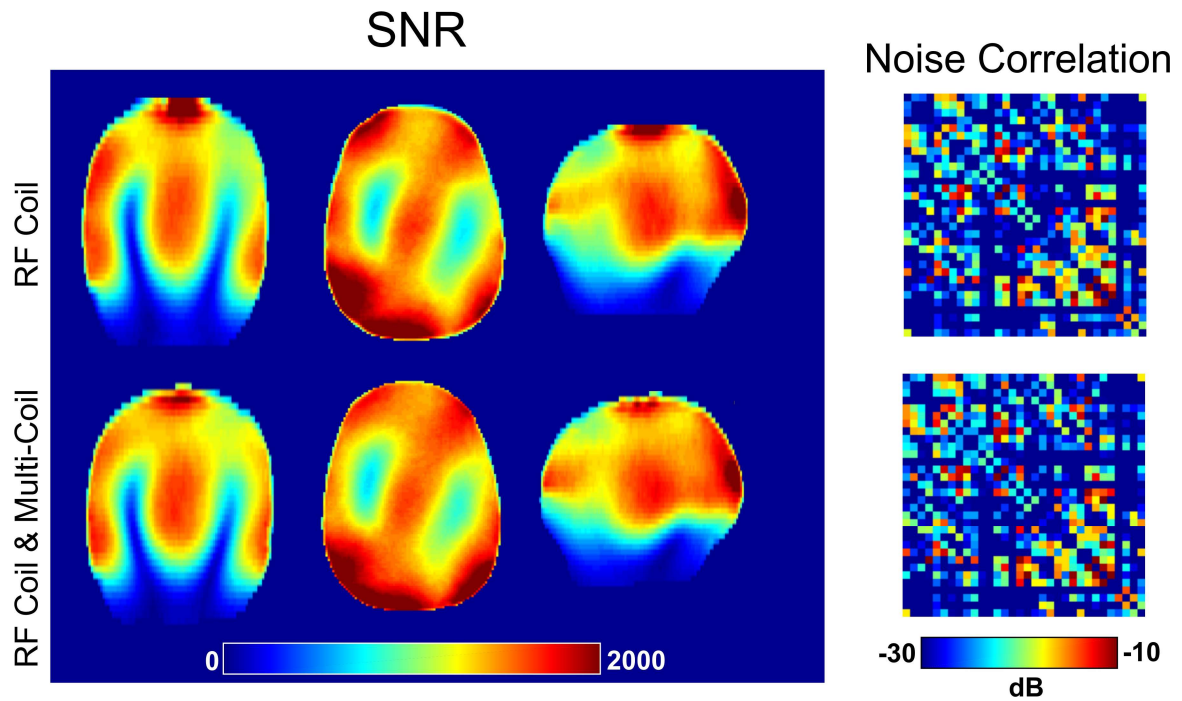
How to cite this article: Aghaeifar A, Zhou J, Heule R, et al. A 32-channel multi-coil setup optimized for human brain shimming at 9.4T. *Magn Reson Med.* 2019;00:1–16. <https://doi.org/10.1002/mrm.27929>



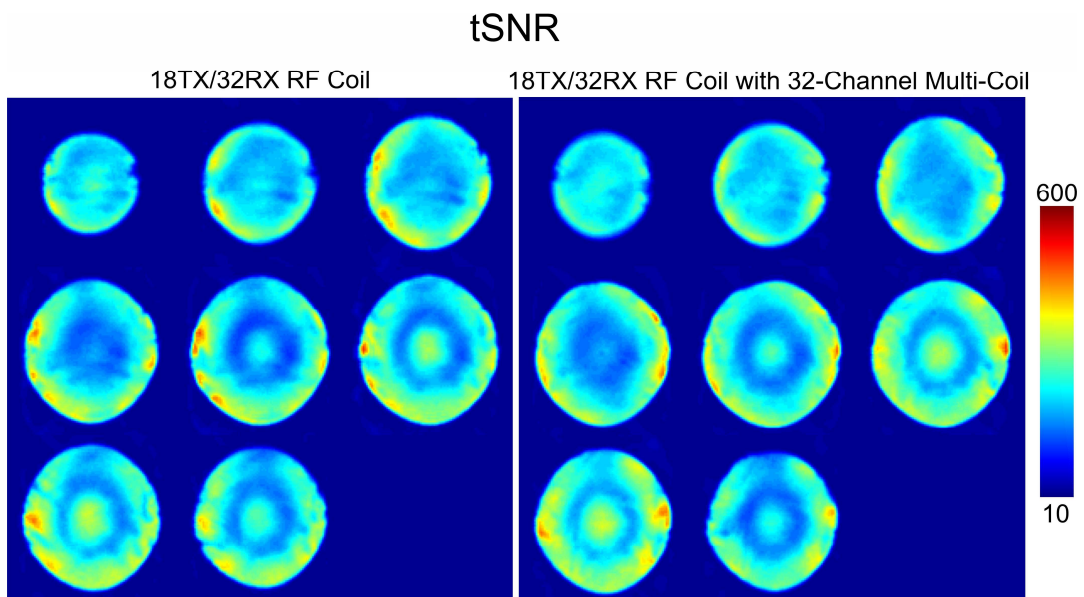
Supporting Information Figure S1. The designed supports allowed easy layering of the overlapping coils. The thickness of the supports was 7.5 mm



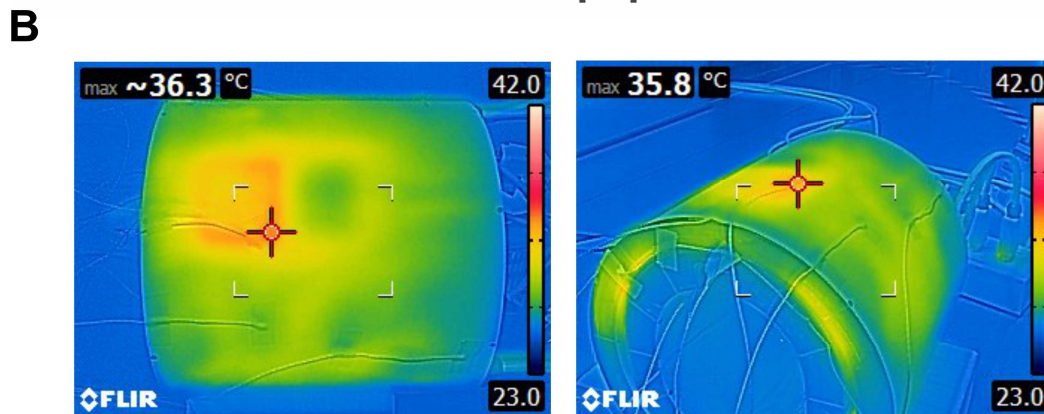
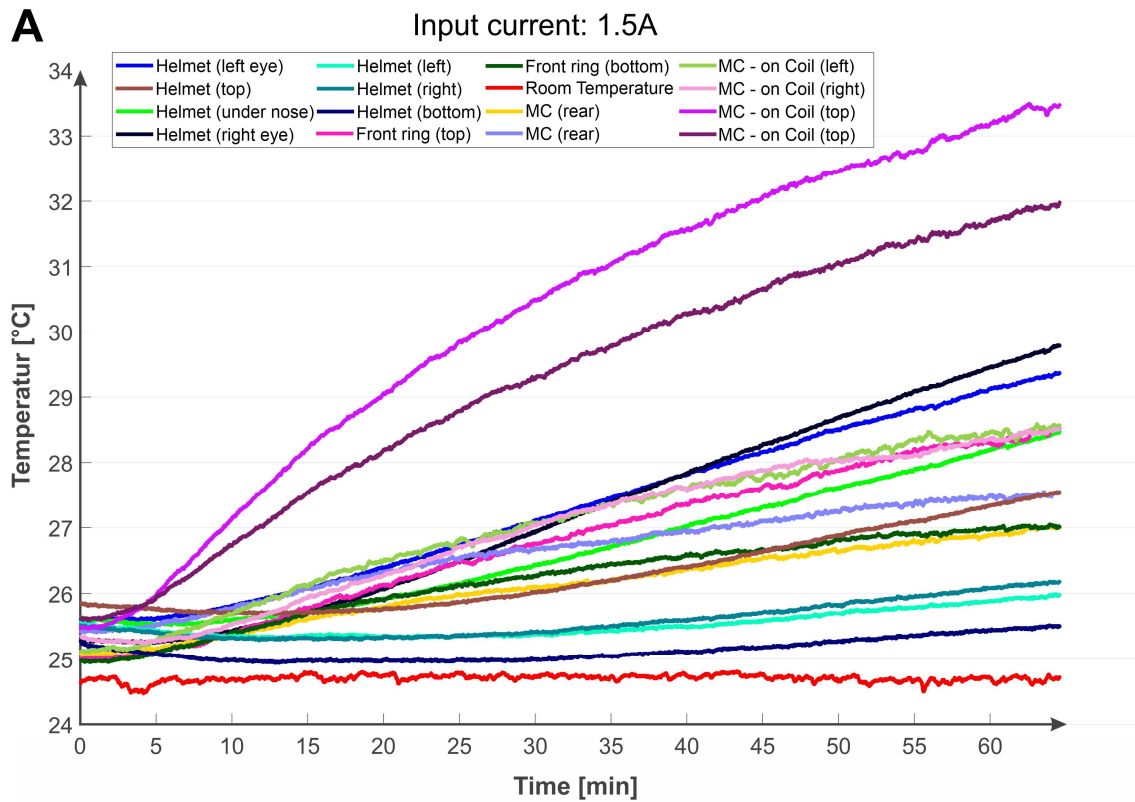
Supporting Information Figure S2. Comparison of the B_1^+ field in the presence and absence of the constructed multi-coil. The spatial distribution and strength remained similar. An actual flip angle imaging (AFI) sequence was used to measure the B_1 field. The phantom filled with equivalent tissue properties ($\epsilon 558.6$, $r 50.64$ S/m).



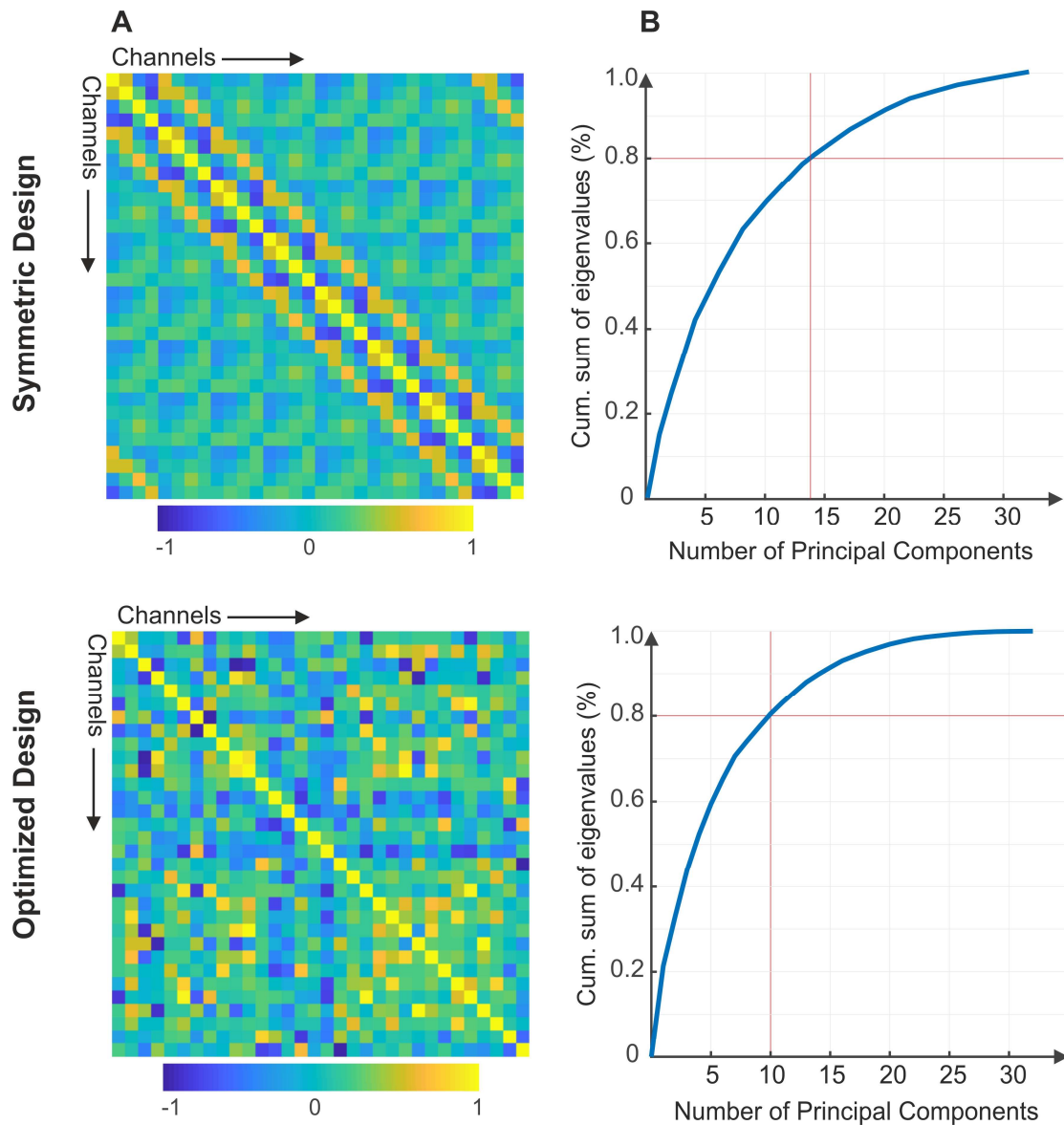
Supporting Information Figure S3. Comparison of the SNR and noise correlation matrix in the presence and absence of the constructed multi-coil. The difference is minor and maybe due to discrepancies in the positioning of the phantom. The SNR was calculated based on the pseudo multiple replica approach.



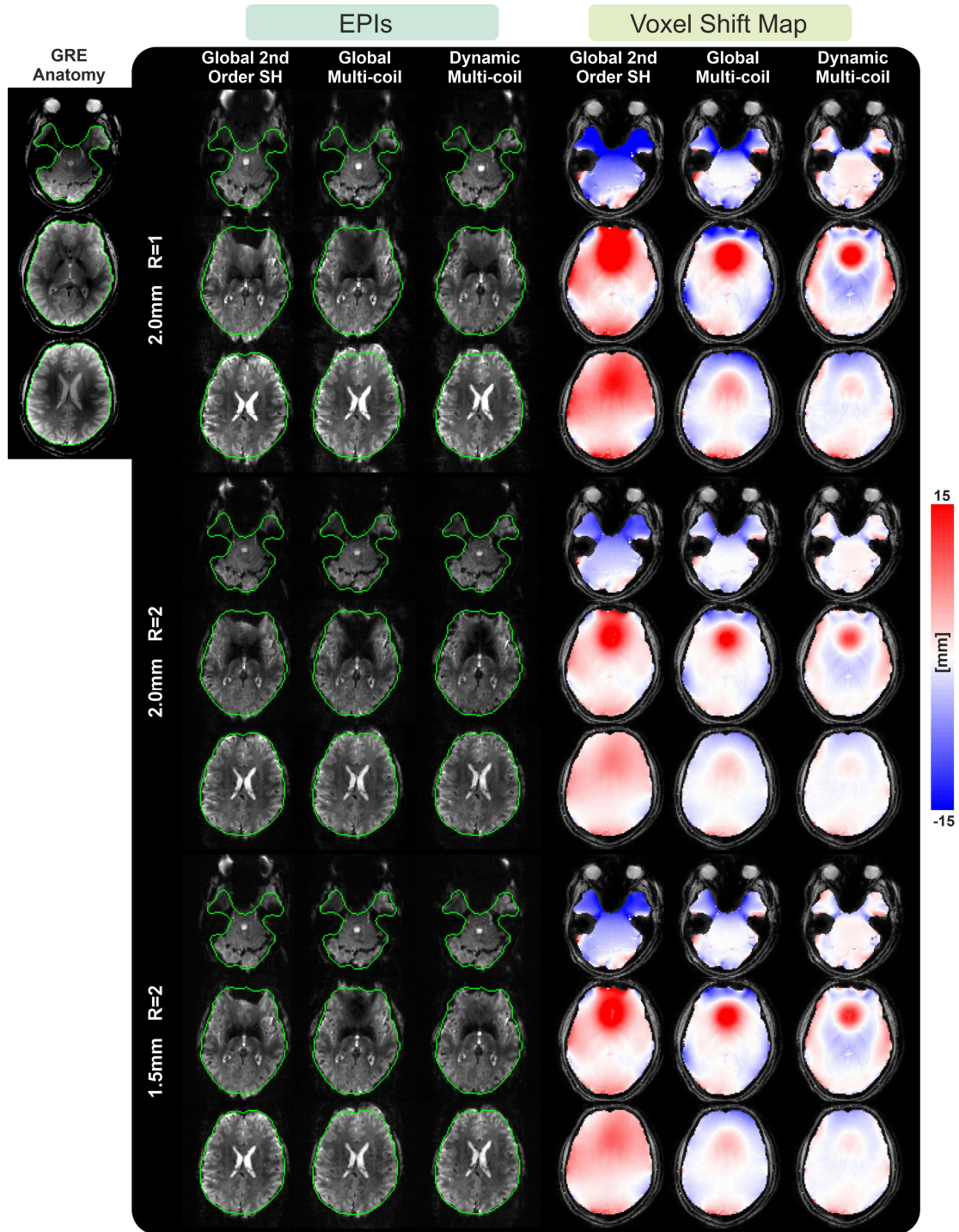
Supporting Information Figure S4. Comparison of the temporal SNR and noise correlation matrix in the presence and absence of the constructed multi-coil. The temporal SNR was determined in a spherical agar phantom from 100 measurements.



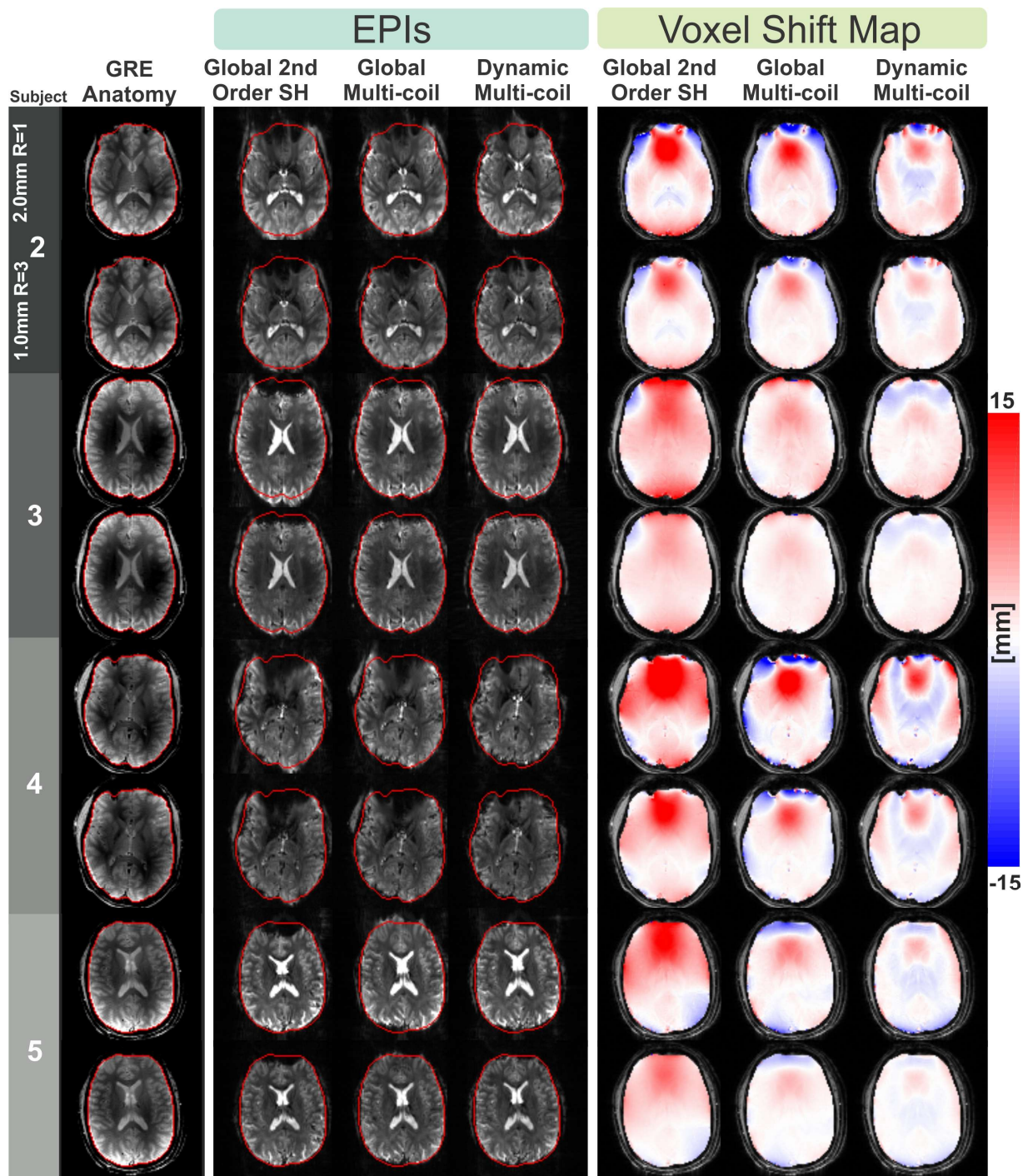
Supporting Information Figure S5. The produced heating due to the resistance of the coils is a major concern. To this end, all channels were fed with 1.5A for an hour and the temperature was monitored with temperature sensors that were attached to the setup. Furthermore, infrared images with a thermal imager (E6 thermal imager, FLIR Systems, Wilsonville, OR) were acquired at the end of the measurement. The hottest point was in the outer surface of the multi-coil where several coils are overlapped in anterior. However, this area is not in contact with the subject.



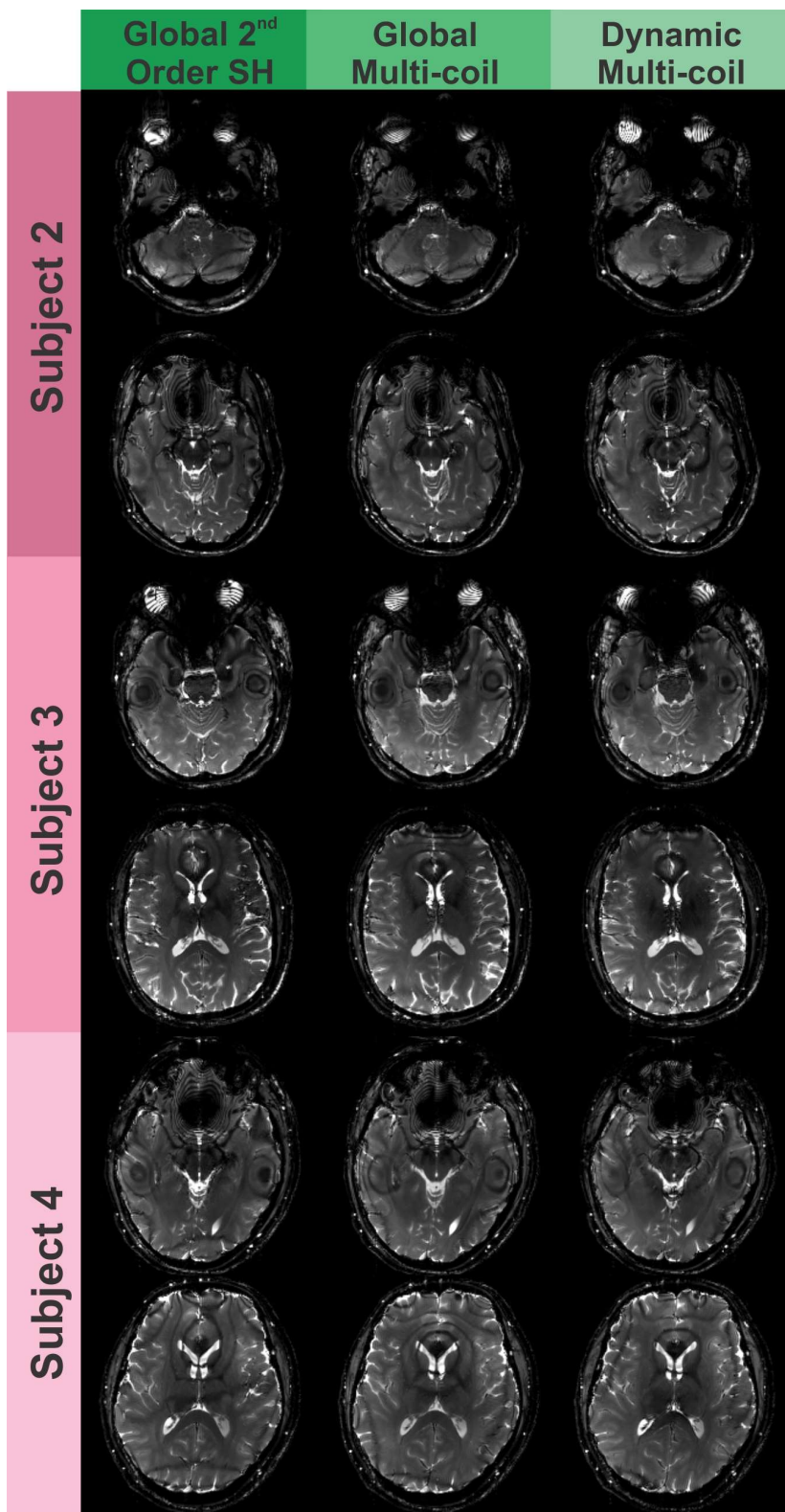
Supporting Information Figure S6. Redundancy in the magnetic fields generated by the individual coils before and after optimization. A) Matrix of correlation coefficients. Numbers close to zero represent less similarity in the magnetic field generated by two individual coils. B) The cumulative sum of shim coils eigenvalues. Summation of the first 14 and 10 principal components reached to 80% of total eigenvalue energy for symmetric and optimized design, respectively.



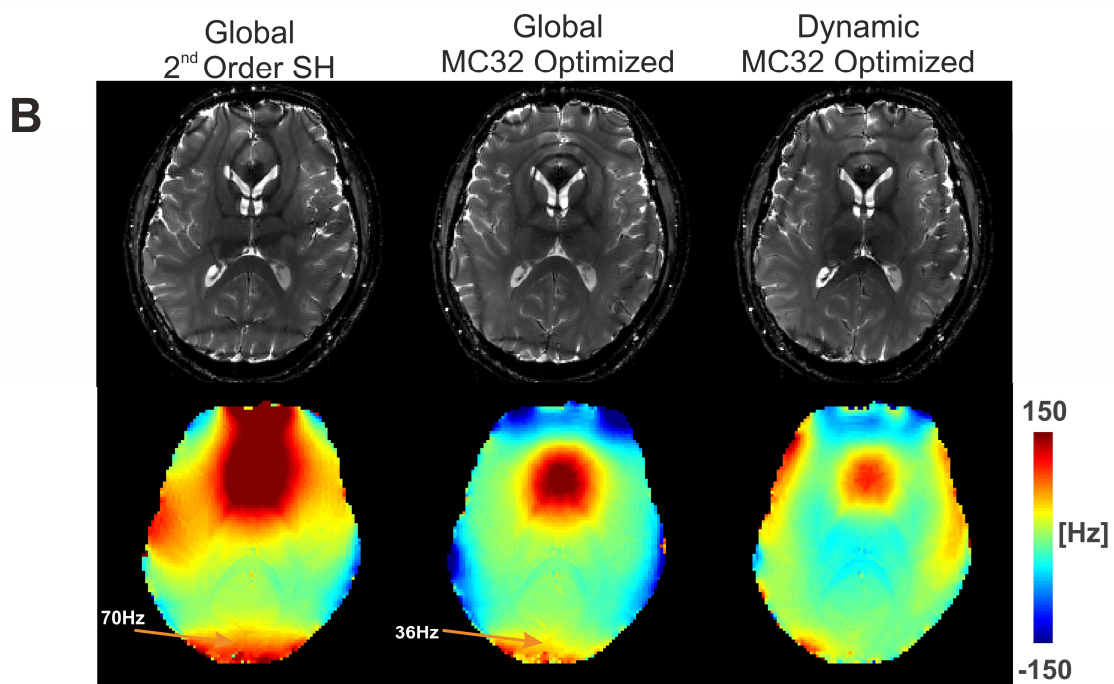
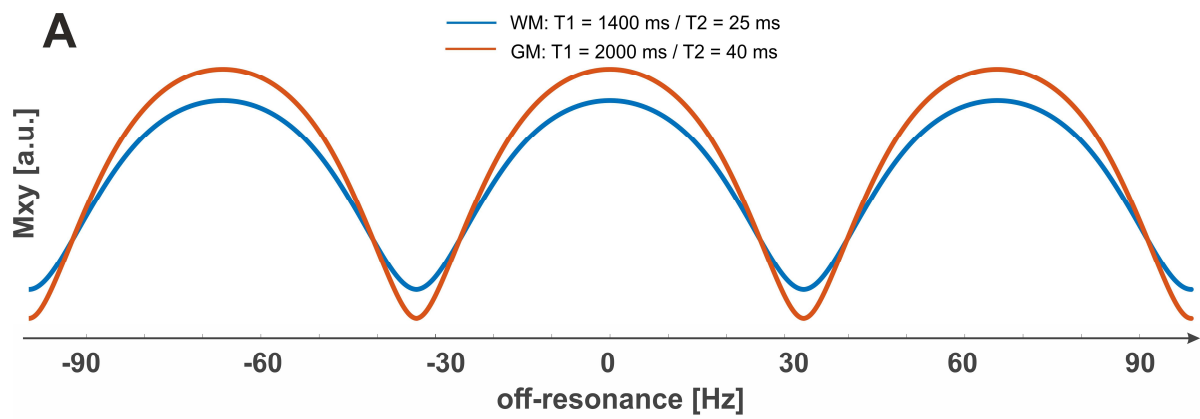
Supporting Information Figure S7. Evaluation of the geometric distortion and voxel shift map at resolution of 1.5 mm isotropic and 2.0 mm isotropic for the same subject depicted in Figure 6. EPIs with 2.0 mm isotropic resolution are acquired without and with an acceleration factor of 2.



Supporting Information Figure S8. Evaluation of the geometric distortion and voxel shift map at resolution of 1.0 mm isotropic (grappa factor = 3) and 2.0 mm isotropic (no acceleration) for subjects two to five.



Supporting Information Figure S9. Effect of the improved B_0 homogeneity on banding artifacts in bSSFP images for subjects two to four.



Supporting Information Figure S10. A) The periodic profile of bSSFP frequency response simulated based on the acquisition protocol employed in this study (in our case, $1/TR$ corresponds to a periodicity of 66 Hz). B) An example of generating new banding artifact after global shimming while the shimming is improved. Because of the periodic profile, some area may be shifted from pass-band into stop-band after shimming.

Supporting Information Table S1. Evaluation of improvement in shimming performance of optimized multi-coil with respect to the symmetric design in global shimming for individual subjects.

Subject		Standard Deviation %			Root-Mean-Square %		
		Whole Brain	Frontal Cortex	Near Ear Canals	Whole Brain	Frontal Cortex	Near Ear Canals
2.0 A	1	15	11	13	15	14	15
	2	10	10	13	10	11	14
	3	5	12	3	5	14	3
	4	7	7	15	7	11	17
	5	16	9	4	16	14	5
	6	11	13	8	11	15	8
	7	14	6	16	14	10	20
	8	10	7	13	10	10	15
	9	12	7	14	12	9	17
	10	9	5	21	9	6	22
	11	6	5	16	6	5	17
	12	19	10	28	19	13	29
	13	24	15	24	24	18	28
	14	15	13	14	15	15	14
Average :		12.4	9.3	14.4	12.4	11.8	16.0
Unconstrained	1	23	25	13	23	29	16
	2	21	23	26	21	25	32
	3	11	13	14	11	16	16
	4	7	9	17	7	12	19
	5	23	14	15	23	21	16
	6	17	22	10	17	25	11
	7	21	18	23	21	24	27
	8	21	19	28	21	23	29
	9	23	23	22	23	25	28
	10	18	15	35	18	18	37
	11	14	18	28	14	20	29
	12	28	24	35	28	29	36
	13	32	30	33	32	33	37
	14	20	21	19	20	24	19
Average :		19.9	19.6	22.7	19.9	23.1	25.1

Supporting Information Table S2. Information of coils layering to overcome the overlapping between the coils after optimization. The base for choosing a layer for a coil was to keep the most coils in layer1, then layer2 and so forth.

Coil No.	1	2	3	4	5	6	7	8	9	10	11	12	13	14	15	16	17	18	19	20	21	22	23	24	25	26	27	28	29	30	31	32		
Layer:	1	2	1	1	1	1	1	1	1	2	4	2	2	1	2	2	2	1	1	4	2	3	2	2	1	1	3	2	3	1	1	1		
Overlapped with Coils	17	7	29	10		28	2	2	12	4	4	31	18		9	19	7	21	16	8	32	8	25	25	23	15	1	6	25		12	21		
	22	8	24	11		20	17	20	15	25	25	9			26		1	13		6	18	1	11	3	11		6	20	3					
	27	22				22		22		11	10									2		6	10	29	10		28	27	24					
		20				27					23	23									28	2		11	24		20		11					
											29										27	20		29										
										24										22														

Supporting Information Table S3. The wiring pattern of the designed 32-channel optimized multi-coil according to the public multi-coil information policy

Please find “Supporting Information Table S3” in the online record of the paper in the journal webpage. This table is too long to be included here.

Publication IV




“Design of a shim coil array matched to the human brain anatomy”

F. Jia, H. Elshatlawy, **A. Aghaeifar**, Y. Chu, Y. Hsu, S. Littin, S. Kroboth, H. Yu, P. Amrein, X. Gao, W. Yang, P. LeVan, K. Scheffler, M. Zaitsev

Magnetic Resonance in Medicine, (2019)

DOI: 10.1002/mrm.28016

Design of a shim coil array matched to the human brain anatomy

Feng Jia¹  | Hatem Elshatlawy¹ | Ali Aghaeifar²  | Ying-Hua Chu¹ |
Yi-Cheng Hsu¹ | Sebastian Littin¹  | Stefan Kroboth¹ | Huijun Yu¹ |
Philipp Amrein¹ | Xiang Gao¹ | Wenchao Yang¹ | Pierre LeVan¹ |
Klaus Scheffler^{2,3} | Maxim Zaitsev¹

¹Department of Radiology, Medical Physics, Faculty of Medicine, Medical Center University of Freiburg, University of Freiburg, Freiburg, Germany

²Max Planck Institute for Biological Cybernetics, Tuebingen, Germany

³Department of Biomedical Magnetic Resonance, University of Tuebingen, Tuebingen, Germany

Correspondence

Feng Jia, Department of Radiology,
Medical Physics, Medical Center University
of Freiburg, Faculty of Medicine,
University of Freiburg, Freiburg, Germany.
Email: feng.jia@uniklinik-freiburg.de

Funding information

German Research Foundation (DFG),
Grant/Award Numbers: ZA 422/5-1, ZA
422/6-1; Reinhart Koselleck Project,
Grant/Award Numbers: DFG SCHE 658/12
and SCHE 658/13-1; European Research
Council, Grant/Award Number: Proof-of-
Concept Grant agreement ID 755466

Purpose: The purpose of this study is to introduce a novel design method of a shim coil array specifically optimized for whole brain shimming and to compare the performance of the resulting coils to conventional spherical harmonic shimming.

Methods: The proposed design approach is based on the stream function method and singular value decomposition. Eighty-four field maps from 12 volunteers measured in seven different head positions were used during the design process. The cross validation technique was applied to find an optimal number of coil elements in the array. Additional 42 field maps from 6 further volunteers were used for an independent validation. A bootstrapping technique was used to estimate the required population size to achieve a stable coil design.

Results: Shimming using 12 and 24 coil elements outperforms fourth- and fifth-order spherical harmonic shimming for all measured field maps, respectively. Coil elements show novel coil layouts compared to the conventional spherical harmonic coils and existing multi-coils. Both leave-one-out and independent validation demonstrate the generalization ability of the designed arrays. The bootstrapping analysis predicts that field maps from approximately 140 subjects need to be acquired to arrive at a stable design.

Conclusions: The results demonstrate the validity of the proposed method to design a shim coil array matched to the human brain anatomy, which naturally satisfies the laws of electrodynamics. The design method may also be applied to develop new shim coil arrays matched to other human organs.

KEYWORDS

cross validation, magnetic resonance imaging, multi-coil, shim coil array design, stream function method

1 | INTRODUCTION

Ultra-high field magnetic resonance imaging (MRI) at field strengths of 7T or above offer a substantially increased

signal- and contrast-to-noise ratio.¹ However, magnetic field inhomogeneity becomes a substantial obstacle for echo planar imaging (EPI),² susceptibility-weighted imaging or T₂* mapping,³ and spectroscopy⁴ because susceptibility-induced

MR frequency variations scale linearly with the main magnetic field.

In order to improve the field homogeneity, conventional second-order spherical harmonic (SH) shim coils are used in routine scanners. Typically, prior to execution of imaging or spectroscopy sequences, the input currents of the shim coils are adjusted to achieve a certain reduction of the field inhomogeneity. However, even after the best possible second-order SH shimming, residual \mathbf{B}_0 inhomogeneity still exists, especially in local regions in the vicinity of air cavities and canals such as frontal lobes or temporal lobes of the human brain. Currently, high-order spherical harmonics coils,^{5,6} multi-coils,⁷⁻¹¹ and integrated RF/ \mathbf{B}_0 shim coil arrays¹²⁻¹⁴ have been proposed and demonstrated to provide better shimming capabilities than the standard manufacturer-provided shimming. The mentioned high-order SH coils were designed to generate magnetic fields with an orthonormal set of pure SH shapes. By contrast, the elements of multi-coil shim arrays and integrated RF/ \mathbf{B}_0 shim arrays typically have a simple fixed shape, such as a circular loop and are distributed in a regular pattern over a surface such as a cylinder or close-fitting helmet. During the design of all these generic coil arrays and their elements, typical \mathbf{B}_0 field maps acquired in human subjects have not been considered explicitly.

In order to reduce the field inhomogeneity over a specific region of the human brain, such as the medial temporal lobe, a single coil shim insert¹⁵ has been proposed and designed for magnetic resonance spectroscopy. During the design, the average of field maps of 10 normal human subjects has been used as a target field over a spherical region. Such an approach, however, is not applicable to whole brain shimming as a fixed mask cannot be applied to each of the 10 subjects since individual brains have different geometries. Moreover, the usage of a fixed mask tends to exclude regions with high inhomogeneities, typically located close to the periphery.

If custom shim coils with more than one channel are designed, averaging is not sufficient. Therefore, alternative approaches^{16,17} were proposed that consider field maps of multiple human subjects simultaneously to find a basis set that represents the particular spatial patterns of field inhomogeneity occurring in the brain using substantially fewer basis field terms than the number of input field maps. In particular, the approach in Li et al¹⁷ relies on a singular value decomposition (SVD) applied to multiple field maps of the brain and uses the singular vectors as shim basis fields. To account for individual shape differences, brain normalization¹⁸ was applied prior to the SVD. The required basis fields could provide better \mathbf{B}_0 homogeneity than the first through third-order SH fields. However, the derived basis field patterns may be challenging to generate by a shim coil in practice and may not even satisfy Maxwell's equations. Furthermore, the validity of the spatial normalization step is questionable. On the one hand, it applies spatial transformations not compatible with

Maxwell's equations. On the other hand, it removes rigid head motion, which makes one of the major factors affecting the susceptibility-induced frequency distribution invisible for the coil design step.

In this work, a design method of a shim coil array specifically optimized for whole-brain shimming in humans is proposed. The shim design is based on the stream function method¹⁹ applied to 84 target field maps acquired in 12 normal volunteers in seven different head positions, followed by the singular value decomposition. The leave-one-out cross validation technique, commonly used in machine learning,²⁰ is applied here to determine the total number of required elements of the coil array. Statistical inference based on a bootstrap approach²¹ is introduced to verify the stability of the coil array design. Numerical results are presented to demonstrate the validity of the proposed design approach.

2 | METHODS

The proposed design method is summarized as follows. First, the field maps of multiple human brains are acquired and pre-processed. The resulting field maps are specified as target fields and a stream function of the electric current density¹⁹ is designed for every field map on a pre-defined current-carrying surface. In this way, for every human brain in every position, a separate optimal shim coil is calculated. All coils share the same current-carrying surface. As the current-carrying surface and its mesh remain the same during the design of all coil layouts, this initial design step maps each individual field map with its specific spatial position and the masked region into the common space of the electric current density on the current-carrying surface. In the following step, the matrix consisting of all resulting stream functions is analyzed by an SVD, and the left singular vectors with the largest singular values are used to obtain the wire patterns of elements of the shim coil array. A leave-one-out cross validation technique is applied to find a suitable number of channels and to verify the generalization ability of the coil array. The bootstrap approach is then used to assess whether the current sample of brain field maps is sufficient and estimate the appropriate sample size for future experiments.

2.1 | Measurement and preprocessing of human brain field maps

In this study, anatomical images and \mathbf{B}_0 field maps of heads of 18 different healthy adult volunteers (age: 30.8 ± 3.97 , gender: 14 males and 4 females) were measured on a 3T scanner (Siemens Healthcare, Erlangen, Germany) by a field mapping sequence based on a multi-echo 3D gradient echo (GRE) sequence. Before these measurements, the heads in the central position were shimmed to the second order using

the routines provided by the scanner. The imaging parameters were TE = 3.84/6.7/10.56 ms, TR = 14 ms, flip angle = 8°, field of view (FOV) = (256 × 256 × 224) mm³, and 128 × 128 × 112 matrix size. The measured maps have an isotropic resolution of 2 mm. The selected FOV was large enough to cover the whole brain (including: cerebellum, midbrain, and pons) of all subjects. All field maps from the 18 subjects were divided into two sets: the field maps from 12 subjects were designated as a training set for designing the shim coil array, while the field maps from the remaining six subjects constituted a test set. The field maps in the test set were only used to assess the performance of the final designed coil array in the following Section 3.4. In other subsections, only the field maps from the training set have been used.

In order to assess the impact of head motion on B_0 maps, each subject was measured seven times in different head positions. The first field map was measured in a reference head position considered optimal by an experienced radiographer. The other six maps were measured after rotation along x , y , and z axes by approximately $\pm 5^\circ$. Here, a 2D multislice echo-planar imaging (EPI) sequence was used to quantify the head movement using a prospective acquisition correction algorithm,²² and the subjects were guided via the intercom system to comply with the requirements of the protocol.

The non-brain areas of all field maps were removed using the BET (Brain Extraction Tool)²³ based on the magnitude images from the scanned field maps at the second echo. The field maps were then unwrapped using the phase unwrapping algorithm in Robinson et al²⁴ based on multi-echo phase images. Magnitude of the three-dimensional gradient of the phase of the unwrapped maps weighted by the magnitude images was used to detect outliers (such as noise pixels at the boundary and occasional residual phase wraps) and modify the usable brain mask. Disconnected regions were removed from the updated mask. No further topologic operations (such as erosion) were applied to the mask to maximally preserve reliably detected field inhomogeneities close to the surface of the brain. A weak 7-voxel median filter constrained to the mask was applied to the unwrapped field maps to remove the residual outliers. Histograms of selected field maps (e.g. with the highest standard deviations within the data set) were visually inspected to confirm the reliable mask generation and the absence of apparent outliers. The processed field maps were downsampled to a 56 × 64 × 64 matrix in order to reduce the computational cost during the shim coil design step. Considering that in modern scanners the subject can be moved along the z -axis of the magnet to the optimal position without manual subject repositioning by adjusting the bed position, the median of the z -coordinates of points in the brain mask was translated to the magnet iso-center along the z -axis. Moreover, since clinical MRI scanners can rapidly adjust a radio-frequency (RF) synthesizer to compensate zeroth-order B_0 offsets²⁵ and gradient offsets for first-order shimming without

any relevant constraints, the translated and masked brain field maps were preprocessed to remove any zeroth- and first-order SH contributions. The residual field inhomogeneities in the whole brain including midbrain, pons, and cerebellum were used for all design and validation tasks. The mean of the root-mean-square (RMS) of the residual field calculated across all 126 data sets was 26.1 ± 3.27 Hz (mean \pm standard deviation).

2.2 | Design method of a shim coil for a specific brain field map

In order to obtain coil arrays for shimming all field maps in the training set, a wire pattern for each individual field map was first designed using the stream function method. The field map with the reversed polarity was used as a target magnetic field. A stream function on a cylindrical surface of certain dimensions (see below) was then optimized to minimize the standard deviation (SD) of the residual magnetic field over the whole brain. During the optimization procedure, the power dissipated by the coil was constrained in order to obtain a physically and technically meaningful solution. Based on the above considerations, the following optimization problem was used to design a shim coil for a field map:

$$\begin{aligned} \min_{\psi} F, F: &= \sum_{\vec{x}_i \in \text{ROI}} (B_z(\psi, \vec{x}_i) + B_z^m(\vec{x}_i))^2, \\ \text{subject to } & \frac{1}{\tau\sigma} \int_{\Gamma} |\vec{J}(\psi)|^2 d\Gamma \leq P_{\max}^T. \end{aligned} \quad (1)$$

Here, ψ denotes the scalar piecewise-linear stream function¹⁹ of the surface electric current density vector $\vec{J}(\psi)$ where

$$\vec{J}(\psi) = \nabla \times (\psi \vec{n}) \quad (2)$$

on a current-carrying surface Γ with a normal unit vector \vec{n} . According to Peeren,¹⁹ ψ is defined as the line integral of the cross product of \vec{n} and \vec{J} along a curve on Γ and $\psi(\vec{x})$ indicates the current through the curve from a fixed point to \vec{x} . B_z is the z -component of the magnetic field \vec{B} generated by current densities \vec{J} on Γ , which is calculated using the Biot-Savart law. B_z^m indicates the measured in vivo ΔB_0 field map. The points $\vec{x}_i = (x_i, y_i, z_i)^T$, $i = 1, \dots, m$ denote the coordinate vectors of m test points in the ROI, τ indicates the thickness of the surface Γ , σ is the electrical conductivity of the surface Γ , and P_{\max}^T denotes the maximum power dissipated by the coil.

In order to house a compact transmit–receive RF head coil assembly used in previous studies,²⁶ a cylindrical surface with a radius of 180 mm and a length of 300 mm was used to design shim coils in this work. The current-carrying surface has a thickness of 1 mm and its material property of copper has an electrical conductivity of 5.998×10^7 S/m. All optimization problems were solved with two routines *cgsvd* and *lsqi* in the MATLAB (The MathWorks, Natick, Massachusetts) package named REGULARIZATION TOOLS.²⁷

TABLE 1 Definition of some useful terms

Term	Definition
T_n	The total number of required singular vectors (=shim channels)
P_{\max}^T	The maximal allowed dissipated power as a constraint parameter in the optimization process of the stream function. This value is chosen for each field map individually.
Target Order	The target order is a chosen SH order which is used to select the maximal dissipated power (P_{\max}^T) as a constraint in the optimization process of the stream function. Strictly speaking P_{\max}^T is chosen to obtain the same standard deviation in the residual field as that of an unconstrained SH shim system with the same order. (=the target order)
Achieved Order	The achieved order corresponds to the equivalent shimming performance of an SH shimming system with unconstrained power dissipation. For a SVD shim system with a given achieved order, the minimal number of singular vectors (=channels) were chosen to obtain the same SH-shimming performance.
P_{\max}^A	The highest dissipated power of all the SVD channels to obtain a certain achieved order SH shimming capability for a field map.

The solution of the optimization problem (1) depends on the selection of P_{\max}^T . Selecting exceedingly high P_{\max}^T values may lead to impractical shim coils with a very high dissipated power. P_{\max}^T constraints that are too strict may result in poor shimming performance. In order to balance the trade-off between the dissipated power and the shimming capability, P_{\max}^T was individually selected for every field map to obtain a dedicated shim coil with the same shimming performance, i.e. the same standard deviation of the residual field, as the unconstrained SH shimming with a given order. In this manuscript, this given order will be referred to as *target order* and is shown in Table 1.

2.3 | Singular value decomposition

For each field map in the training set, a stream function was obtained as described above. All stream functions were used to form a $n \times m$ matrix where n indicates the total number of nodes on the mesh and m corresponds to the total number of field maps entering the basis generation algorithm. A singular value decomposition (SVD) was performed on the matrix, and the resulting left-singular vectors (referred to as *components*) corresponding to a certain number of largest singular values were used to obtain the wire patterns of coil elements of a shim coil array. For each component which can be used as a stream function, field maps per unit current were then calculated by formula (2) and the Biot-Savart law to form a sensitivity matrix. To test the performance of the designed shim array, for each brain field map, the currents flowing through all coil elements were obtained by minimizing the standard deviation of the residual magnetic field over the whole brain.

In the above approach, there is still an open question related to the number of components needed for the coil array. To address this challenge, we gradually increased the number of components used to shim each measured field map until the same or better performance was achieved as the unconstrained SH shimming with a certain order. This type of order is referred to as an *achieved order* (Table 1). P_{\max}^A (Table 1) is

used to indicate the highest dissipated power of all the used SVD components to obtain a given achieved order SH shimming capability for a field map. The value of P_{\max}^A may be different for each field map.

2.4 | Leave-one-out cross validation

The optimal shim design will be achieved if all measured field maps (12 subjects \times 7 positions) in the training set are included in the SVD method. However, it is important to assess the stability of this optimal solution and whether it will perform well in other subjects whose field maps are not included in the design. This property is called the generalization ability of a model in machine learning.²⁸

In order to test the generalization ability of the resulting shim coil array, a leave-one-out cross validation²⁰ was used. In the leave-one-out cross validation technique, out of 12 subjects, 11 subjects (11 \times 7 maps) were assigned to the training group and 1 was assigned to the validation group. All field maps of the training group were used as target fields in problem (1) and the resulting $m = 11 \times 7 = 77$ stream functions entered the SVD design algorithm from Section 2.3. Thereafter for each field map of the validation group, a minimum number of components was determined for the given achieved order, as described in Section 2.3.

The entire leave-one-out cross validation procedure was repeated 12 times, where each subject was sequentially assigned to the validation group. For example, initially, the first subject constituted the validation group and for each of the seven field maps corresponding to the seven different head positions the number of SVD components from the current training group was defined. Thereafter, the second subject was assigned to the validation group and another seven minimum required numbers of components from the new training group were obtained. Note that in these two steps, the SVD components and correspondingly the shim coil designs are generally different. Finally, 84 minimum required numbers of components were obtained and their statistical parameters (maximum, mean, median, etc.) were considered to assess

performance of the proposed SVD algorithm for the given achieved order.

2.5 | Shimming capability and coil element layouts of the designed coil array

As described in the above subsection, 84 separate required numbers of components were calculated after the leave-one-out cross validation. The maximum of these 84 minimum required numbers was used as the final total number (T_n (Table 1)) of elements in the coil array design. The SVD algorithm was executed for all 84 measured field maps in the training set, as described in the Section 2.3, and T_n components corresponding to the largest singular values were selected. Winding patterns of the channels of the final shim coil array were produced as contours of the respective SVD components.¹⁹ All coil elements were then applied to perform shimming for each field map in the training and test set. The standard deviation of the residual field inhomogeneity after shimming for each map was calculated in order to assess the shimming performance of the resulting coil array.

2.6 | Bootstrap approach for testing the stability of the designed coil array

In the above subsections, a shim coil array design method has been proposed using all measured field maps of 12 subjects in the training set which are only a small sample of the population of all human subjects. In the following, we apply an inferential statistical analysis to deduce properties of the population from this sample. In this subsection, we first define a continuous parameter related to the shimming capacity of the designed coil array. Thereafter, the confidence interval of this parameter is calculated and the stability of the designed coil array is analyzed based on that confidence interval. The new parameter is needed because previously used parameters are either discrete integers (e.g. minimum number of components, achieved order, etc.) or contaminated by a bias (e.g. SD of the residual is contaminated by the unshimmable field terms due to local sources⁵) and therefore are unsuitable for statistical analysis.

The parameter is defined as follows: First, for each field map of each subject, shimming using the designed coil array and the target order SH shimming is obtained. The standard deviation of the difference between these two shim fields is then calculated for each field map. Finally, the mean of the standard deviations for all the field maps in the population is specified as the parameter, which is denoted μ_σ . Its corresponding statistical estimate for the sample of the 12 subjects is expressed as $\hat{\mu}_\sigma$. The parameter is used to assess the stability of the designed coil array.

While the calculated parameter $\hat{\mu}_\sigma$ is valid for the given sample of 12 subjects, its distribution over general samples

of field inhomogeneities in the brains of all human beings is unknown. In order to obtain an approximate confidence interval of the parameter μ_σ using the field maps of the 12 measured subjects, we used a bootstrap approach²¹ as described below. First, k subjects, namely a bootstrap sample, are obtained by randomly resampling with replacement from the 12 original subjects. Here, k may not necessarily be equal to 12 and two or more subjects may be repeated. Second, all measured field maps of the k subjects are used in the SVD method from Section 2.3 to generate new T_n components. Finally, these new components are applied to shim all field maps in the training set and $\hat{\mu}_\sigma$ using the new components from the bootstrap sample is then calculated. The whole procedure is repeated b times and $\hat{\mu}_\sigma$ for the b th time is denoted by $\hat{\mu}_\sigma^b$. Here, b is set to 1000, which is a typical number in confidence interval approximations with bootstrap. Thus, sorting all the $\hat{\mu}_\sigma^b$ in ascending order, the approximated bootstrap percentile 95% confidence interval²¹ of the parameter is given by $(\hat{\mu}_\sigma^{25}, \hat{\mu}_\sigma^{975})$ and the significance level α is set to 0.05. The mean of all the $\hat{\mu}_\sigma^b$ is indicated by $\bar{\hat{\mu}}_\sigma$.

The $\hat{\mu}_\sigma$ obtained by the designed coil array and all 84 measured field maps in the original sample is expressed as $\bar{\mu}_\sigma$, which is used to perform a comparison with the upper bound of the confidence interval in order to measure the stability of the designed coil array.

3 | RESULTS

This section consists of five subsections. Example coil layouts for individual brain field maps are shown in the first subsection. The results in the next two subsections are obtained using the SVD method described in Section 2.3 and the leave-one-out cross validation technique described in Section 2.4. Coil element layouts of the designed array and the comparison of shimming capability between the conventional SH method and the SVD method with the selected number of shimming channels are presented in the fourth subsection. The results of the stability of the designed array are described in the fifth subsection.

3.1 | Shim coils for individual field maps

Figure 1A-D shows shim coil layouts for various selected subjects in the reference head positions. Here, P_{\max}^T in problem (1) was selected for each field map to obtain the same shimming performance as the fifth-order SH shimming (target order 5). It can be seen that all coil layouts show some similarities although substantial differences between some layouts, for example as depicted in Figure 1A,C, are visible.

Figure 1E-F presents coil layouts for subject 1 after a rotation around the x and y axes, respectively. Here, the designed coil after the head rotation around the z -axis is

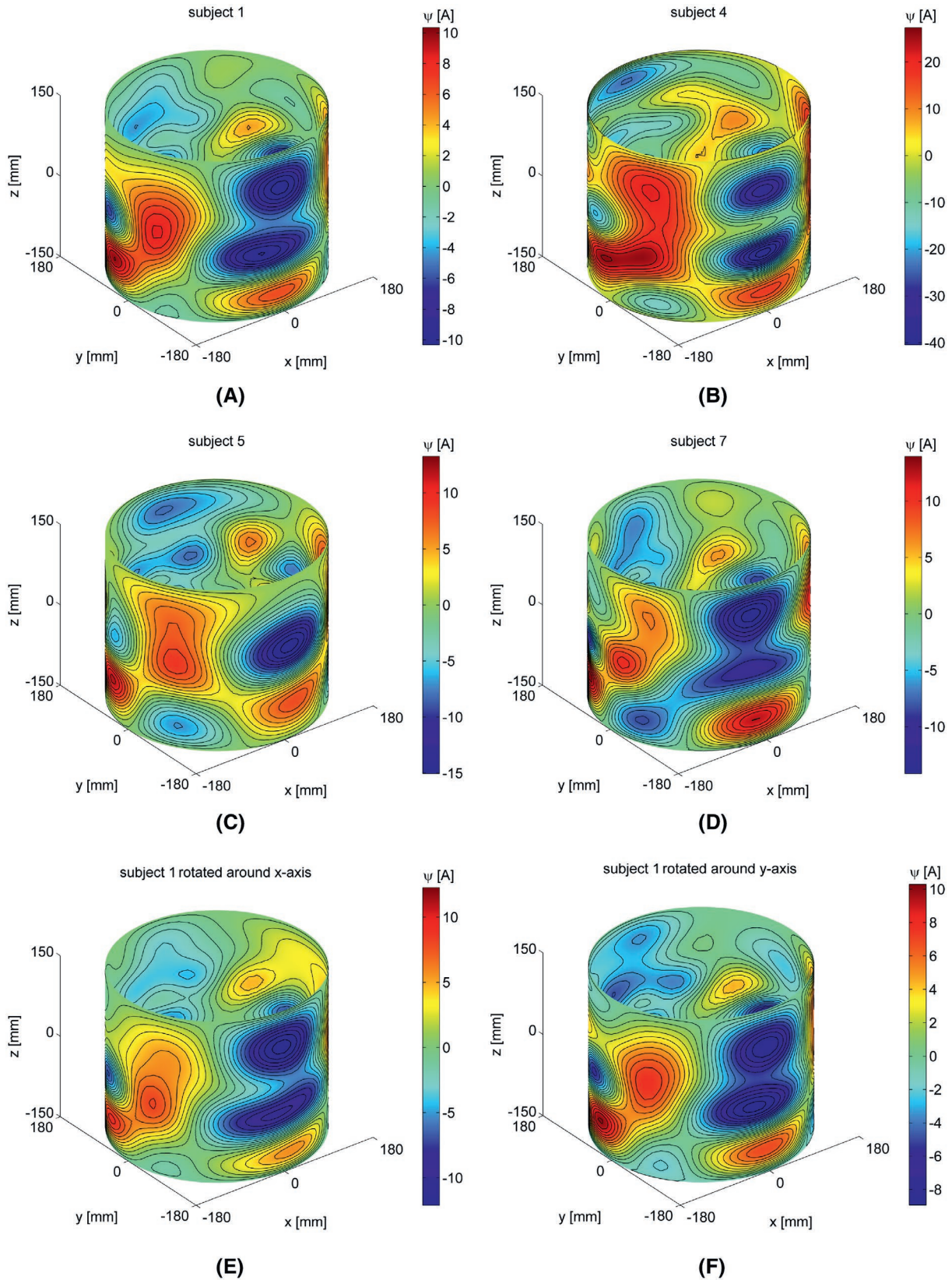


FIGURE 1 Stream functions for several selected subjects (A-D) in the reference head positions and subject 1 in other two positions after head rotations around the x (E) and y (F) axes, respectively. Here, the target order is equal to 5. The center of mass of a brain mask is at the origin. The head is oriented to face the negative y-axis and the top of the head points in the positive z-direction. The colorbars indicate the value of the stream function ψ in the units of A, the surface current density can be calculated according to Equation 2. Contour lines of the displayed stream functions visualize possible winding patterns. Here, the value of each stream function is scaled to a unit current flowing through individual contours

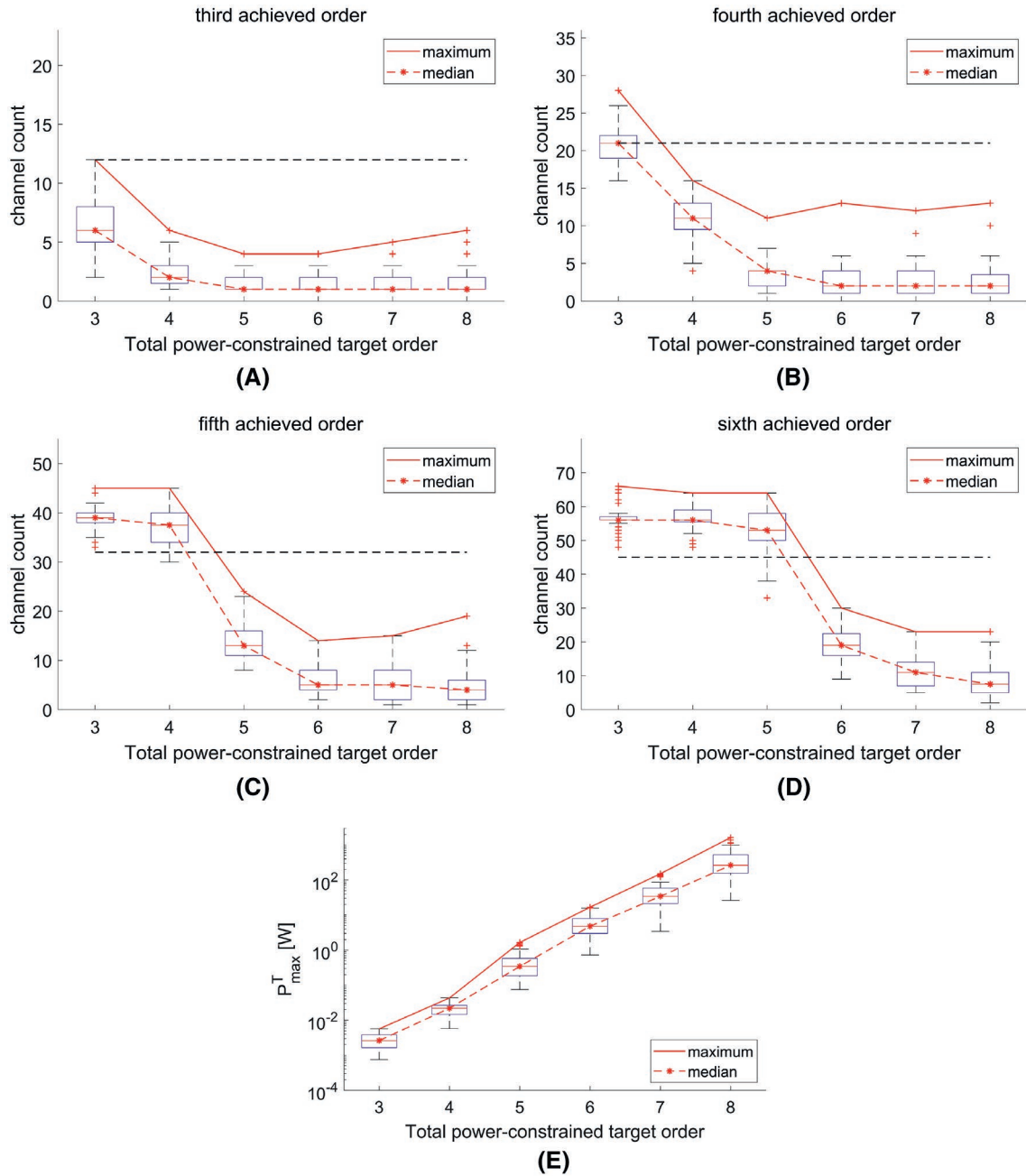


FIGURE 2 Box plot of the number of required components (referred to as channel counts) needed to achieve third-order (A), fourth-order (B), fifth-order (C), and sixth-order (D) SH shimming capability for all field maps in the training set. To provide a reference for the plotted channel counts, the numbers of SH functions corresponding to the given order are displayed as black dashed lines, defined as the total numbers of SH functions corresponding to the given order minus four. The box plot of maximum dissipated power P_{\max}^T [W] (E) for those target orders reveals that P_{\max}^T grows exponentially with the increase in target order. All those figures also suggest that higher dissipated power P_{\max}^T can lead to less channel count from the perspective of the median value of channel counts

not shown since it has a very similar layout as that in the reference head position (Figure 1A), with the corresponding rotation. Contrary to that, the coil layout after the head rotation around the x -axis shows the largest variation from the reference. The variation may be due to the fact that the head rotation around the x -axis leads to a stronger change of susceptibility-induced field distribution in the brain, as discussed in Maclaren et al.²⁹

3.2 | SVD method for shim coil design

Figures 2A-D and 3 show box plots of minimum numbers and maximum dissipated power P_{\max}^A of the components, which are used to obtain the third to sixth achieved order SH shimming capability for the original field maps in the training set, respectively. Here, all 84 column vectors of the matrix entering the SVD algorithm were calculated separately

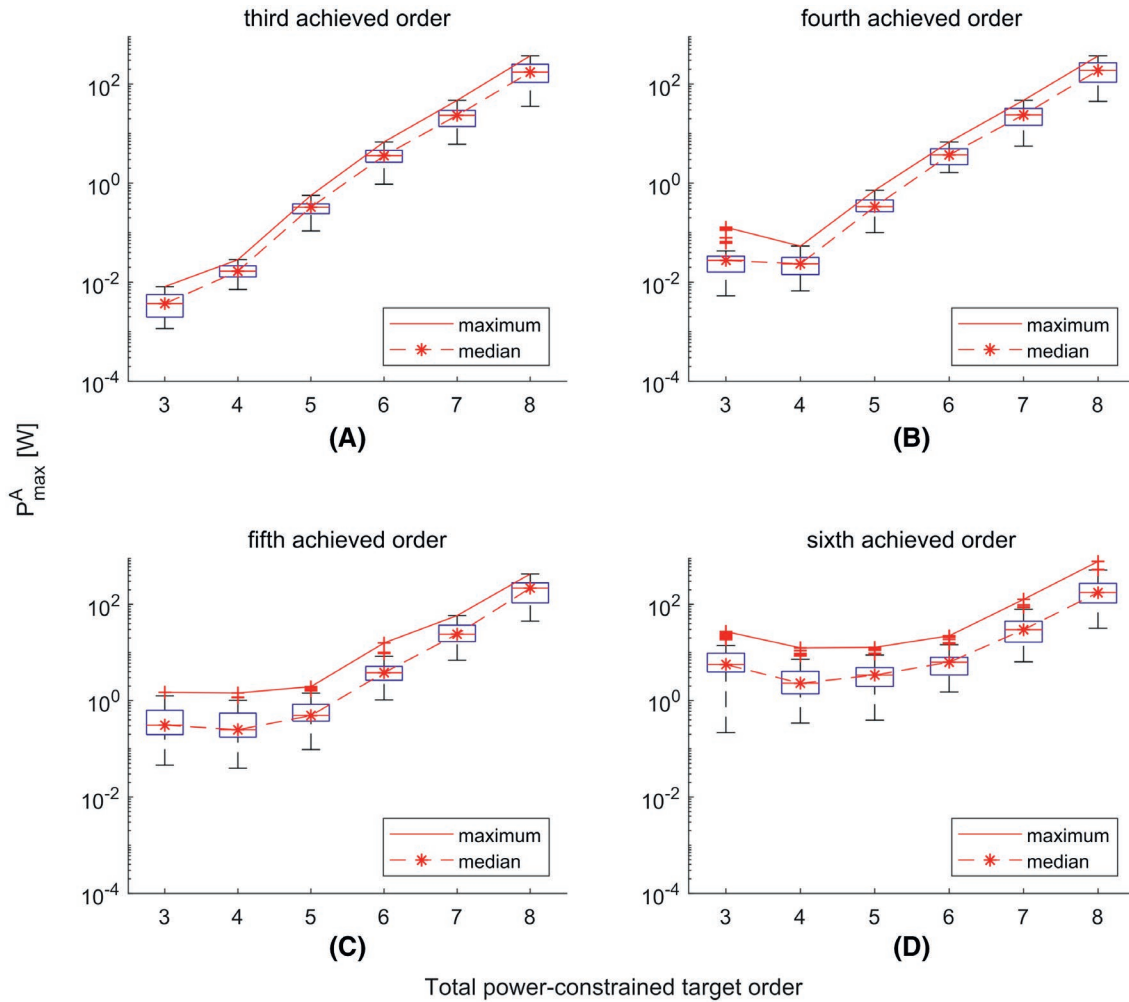


FIGURE 3 Box plot of maximum dissipated power P_{\max}^A [W] of required components needed to achieve third-order (A), fourth-order (B), fifth-order (C), and sixth-order (D) SH shimming capability for all field maps. The variations of the maximum and median values of these maximum dissipated power with respect to target order are depicted in red solid lines and red dashed lines with the star symbols, respectively. The outliers of the maximum dissipated power are plotted using the plus symbols

for different target orders ranging from the third to the eighth order, as shown on the x -axis of Figures 2A-D and 3. Figure 2E shows the box plot of dissipated power P_{\max}^T selected to solve Problem (1) for the corresponding target orders. In order to assess the number of required components, the total numbers of SH functions corresponding to the different orders (termed SH numbers) are also displayed in black dashed lines in Figure 2. Note that the SH numbers are defined as the total numbers of SH functions corresponding to the given order minus four, since constant and linear SH functions have already been used to pre-process brain field maps. The variations of the maximum and median numbers of components with respect to target orders are individually depicted in red solid lines and red dashed lines with the star symbols in Figure 2. The outliers of the minimum numbers are plotted using plus symbols.

As can be seen in Figure 2, with increasing target order, the median values of the number of required components

tend to decrease. Moreover, if a certain target order is equal to or greater than an achieved order, the median values of the number of components are significantly lower than SH functions corresponding to the achieved order. For example, the median values of all minimum numbers of components are only 50%, 52.4%, 40.625%, and 42.2% of the SH numbers if both the target orders and the achieved orders are equal to 3, 4, 5 and 6, respectively. If the target orders are selected to be one higher than the achieved orders, namely 4, 5, 6, and 7, then the median values of the number of components reduce to 16.67%, 19.05%, 15.625%, and 24.44% compared with the corresponding SH numbers. Although the selection of higher target orders may lead to an increase of dissipated power of the used components, as shown in Figure 3, it seems acceptable from an engineering perspective based on previously realized air-cooled coils. For example, the sixth target order and the fifth achieved order can be used in the coil array design since the maximum values of current and maximum

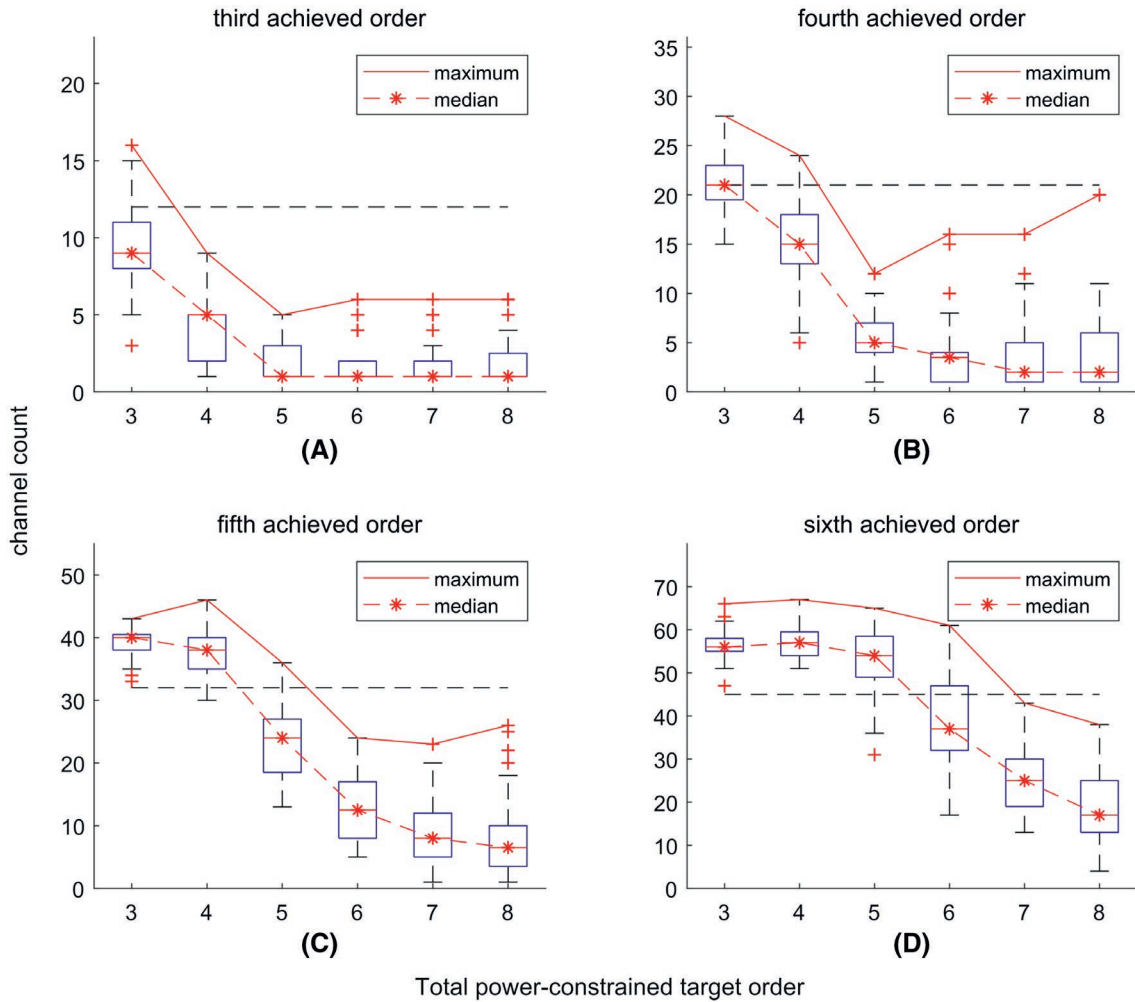


FIGURE 4 Box plot of channel counts needed to achieve third-order (A), fourth-order (B), fifth-order (C), and sixth-order (D) SH shimming capability in validation groups. To provide a reference for the plotted channel counts, the numbers of SH functions corresponding to the given order are displayed as black dashed lines, defined as the total numbers of SH functions corresponding to the given order minus four

power dissipation are 9.98 A and 15.77 W, respectively. In this example, each component has been discretized by its contours with 26 steps.

If a target order is lower than the achieved order, the median values of the number of components may be either slightly lower or higher than the SH numbers, as shown in Figure 2B-D, respectively. Furthermore, as shown in Figure 3, the median values of the maximum power dissipation remain within the same range as those in the case where the target order is equal to the achieved order. These results suggest that it is advantageous to use an equal or higher target order than the achieved order when defining the total number of required components.

Although the median values of the numbers of components have a decreasing tendency, the maximum number of components in some cases tend to first decline and then rise with the increase of the target order, as shown in Figure 2A-C. This U-shape variation suggests that using much higher

target order than its achieved order could lead to a suboptimal number of required components. In such cases, we can select the transition points, which indicate the points close to the local minimum on the U-shape tendency, to be the number of coil elements of the designed array since the maximum of the power dissipation has an increasing tendency with the target order. For example, as shown in Figure 2B, the target order at the transition point is equal to five and the maximum required number of components is equal to 11, which is the lowest requirement of the number of the coil elements to obtain a shimming capability better than fourth-order SH for all field maps.

Figure 2B-D also shows that the maximum number of components can be less than the total number of SH functions if a target order is equal to the achieved order. For example, when both the target order and the achieved order are equal to 5 or 6, the numbers of components for all the field maps in the training set are required to be 24 or 30, respectively.

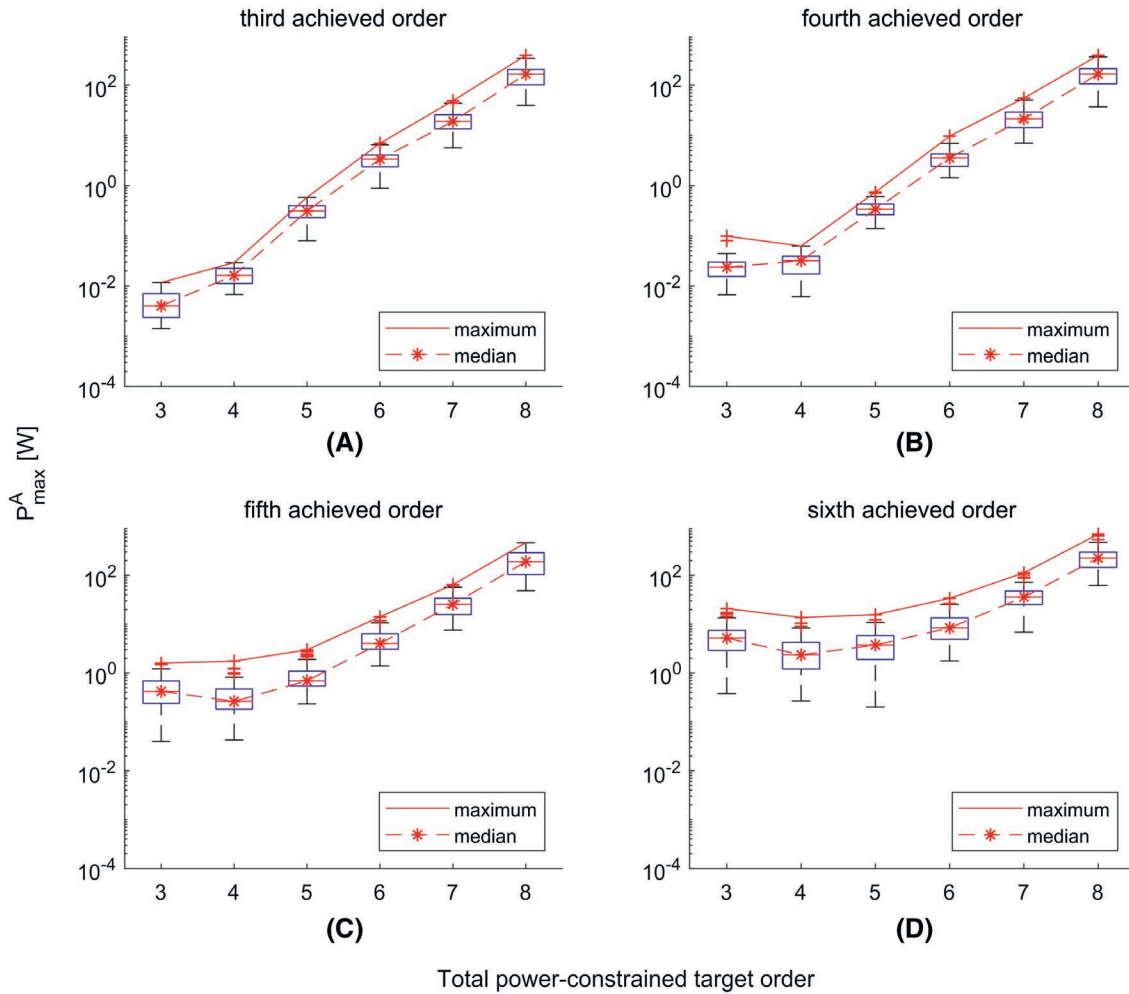


FIGURE 5 Box plot of maximum dissipated power P_{\max}^A [W] of required components needed to achieve third-order (A), fourth-order (B), fifth-order (C), and sixth-order (D) SH shimming capability in validation groups

However, to obtain the equivalent shimming capability to the SH fifth order (36 components for the full fifth-order SH basis) or sixth order (49 components for the full sixth-order SH basis), for more than 90% of all the field maps, only 19 or 24 components are needed, respectively.

3.3 | Shimming cross validation using leave-one-out technique

Figures 4 and 5 show box plots of minimum numbers and maximum dissipated power of the used components in all validation groups as described in Section 2.4. As can be seen, the median values of the maximum numbers of components also decrease with the increase of a target order. Moreover, if a target order is equal to or greater than an achieved order, the median values of the numbers of components also tend to be lower than the total numbers of the SH functions. For example, the median values of all numbers of components are less than 75%, 71.43%, 75%, and 82% of the corresponding SH numbers when both the target orders and the achieved orders are equal to 3, 4, 5, and 6, respectively. Furthermore, if the target orders are selected to be

one order higher than the achieved orders, that is 4, 5, 6, and 7, the median values of the numbers of components reduce to 41.67%, 23.8%, 39.06%, and 55.56% compared to the corresponding SH numbers. These results suggest that using a higher target order at the design stage can enhance the generalization ability of the resulting coil array.

Figure 4A-D also shows that the maximum numbers of components in some cases tend to follow a U-shape with the increase of the target order. In these cases, the values at the transition points can be selected as the numbers of coil elements of the designed array. For example, 12 and 24 can be selected as total numbers of coil elements to obtain fourth and fifth achieved order SH shimming capability for all field maps in the training set when the target orders are equal to 5 and 6, respectively.

3.4 | Shimming capability and coil element layouts of the designed coil-array

Figure 6A,B shows scatter plots of standard deviations for all field maps in the training set using 12 and 24 components,

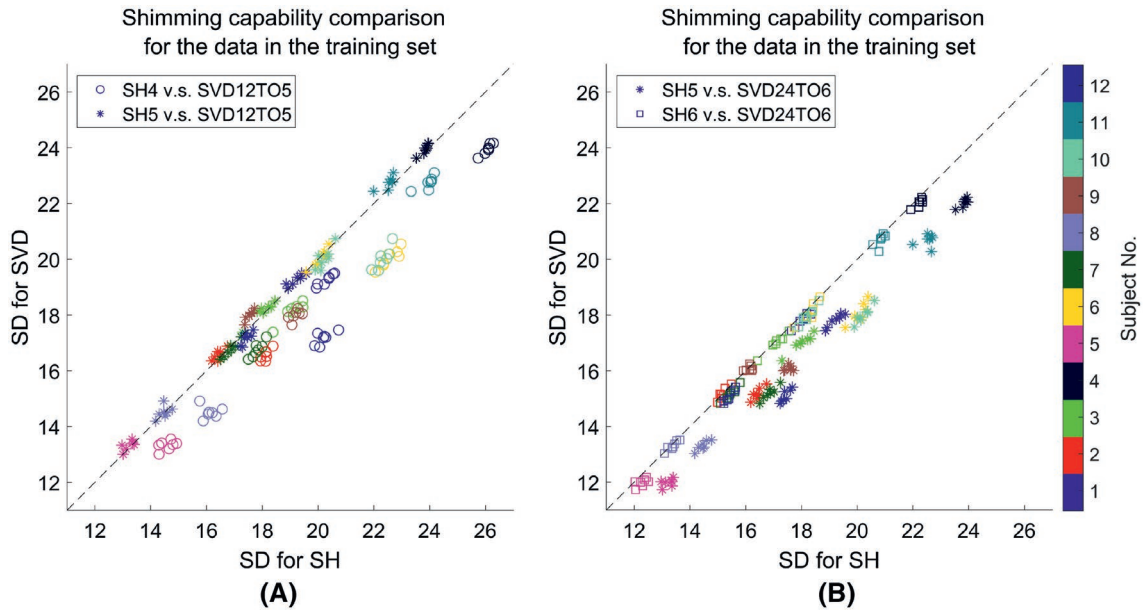


FIGURE 6 Comparison of standard deviation (SD) between SH shimming and SVD coil shimming for all data in the training set. Here, SH4, SH5 and SH6 indicate the fourth-, fifth-, and sixth-order SH shimming, respectively. SVD12TO5 and SVD24TO6 mean that 12 and 24 components are used for shimming when the target order (TO) are 5 and 6, respectively. Equal standard deviations between two methods are plotted in the dashed diagonal line. Data points corresponding to different human subjects are marked in different colors

respectively, and compared to high-order SH shimming. As can be seen, for all field maps, shimming using 12 and 24 components outperforms fourth- and fifth-order SH shimming, respectively. Furthermore, for more than 39.29 and 90.48 percent of all field maps, these components achieve an equal or better shimming capability compared to fifth- and sixth-order SH shimming, respectively.

Figure 7A-D depicts the first four components of the designed shim array of 12 components. As can be seen, these four components show distinctly different coil layouts in comparison to conventional SH coils.³⁰ Figure 7E shows a box plot of currents flowing through the 12 components to obtain a fifth achieved order SH shimming capability for all 84 field maps in the training set. As depicted, the median of currents flowing through the first SVD component has a more than three times higher amplitude than those of other components. This result may be related to the fact that the singular value of the first component is greater by a factor of over 2.7 than the singular values of the other components.

The performance of the designed coils was then evaluated in a test set consisting of data from 6 further subjects who had not been used during the design phase. Figure 8A presents a box plot of standard deviation (SD) of residual magnetic field inhomogeneity after shimming the field maps in the test set with SH and SVD coil. As can be seen, shimming using the 12 and 24 SVD components performed slightly better than the fourth- and fifth-order SH shimming, respectively. Figure 8B depicts the residual fields on three typical slices of a representative field map in the test set after shimming

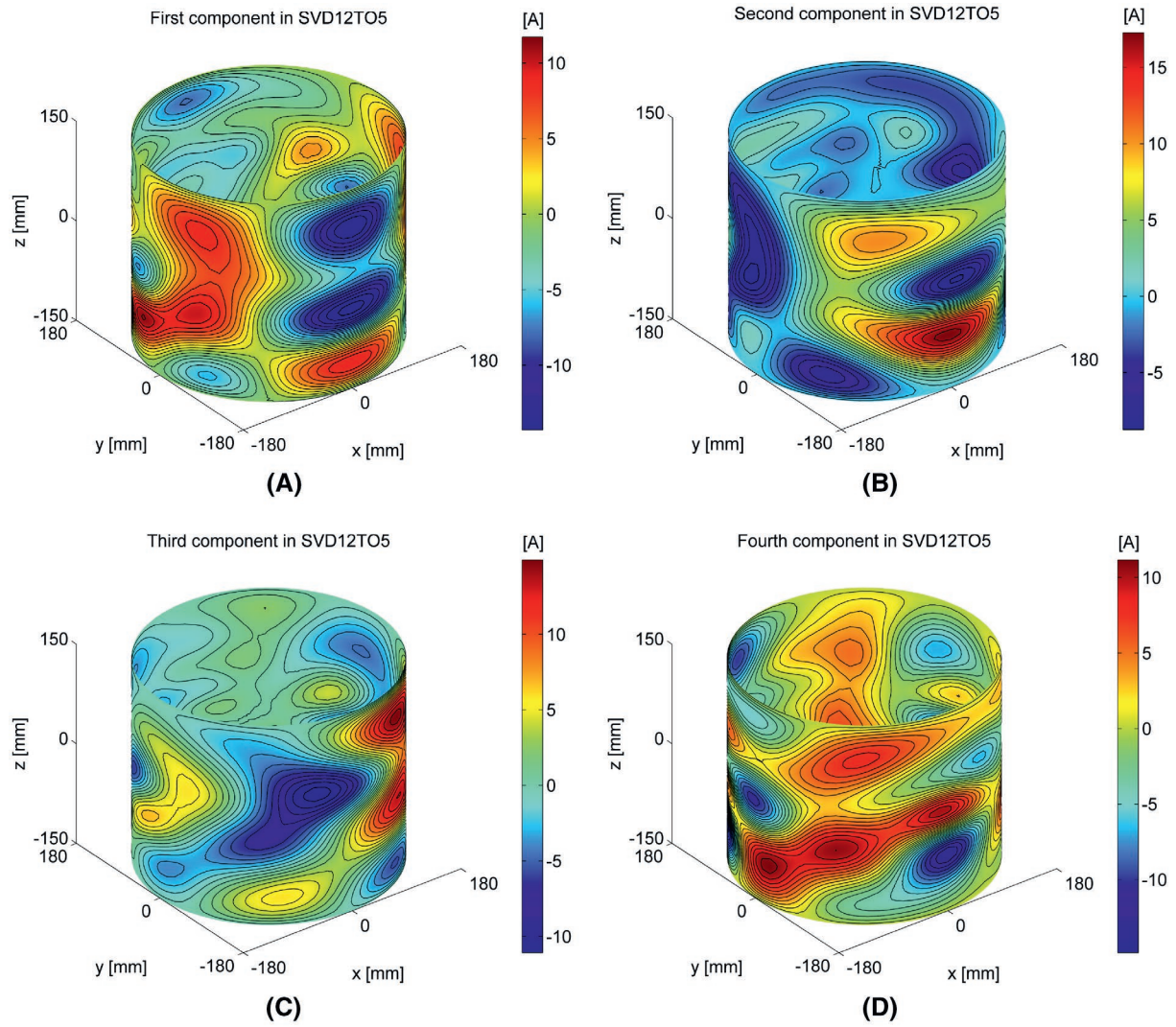
using the first and fourth SH shapes and SVD coil with 12 elements. As shown, the SVD coil shimming has a similar capability as the fourth-order SH shimming.

3.5 | Stability of the designed coil array

Figure 9 shows the variation of the 95% confidence interval of $\hat{\mu}_\sigma$ with respect to the number of subjects k in the bootstrap. Here, $\hat{\mu}_\sigma$ is calculated using the designed coil array with 12 coil elements. In order to assess the stability of the designed coil array, $\bar{\mu}_\sigma$ for all field maps in the original sample of 12 subjects is depicted by a dashed black straight line. The upper part of the confidence interval tends to decrease with increasing k . When the number of subjects k is equal to 12, the upper boundary of the confidence interval of $\hat{\mu}_\sigma$ is 20.75 % larger than $\bar{\mu}_\sigma$, indicating that a different sample of 12 subjects may lead to quite different designs and shimming capabilities. In order to bring the increase of the upper boundary under 5 %, the number of subjects k would need to be around 140.

4 | DISCUSSION

In this study, we have developed a novel approach for a shim coil array design based on the SVD method with the explicit consideration of the human head anatomy. Instead of directly applying SVD to multiple field maps of human brains, as described in Adalsteinsson et al¹⁶ and Li et al,¹⁷ here SVD has been applied to the matrix of stream functions. A similar



Currents flowing through each components in SVD12TO5 for all the data in the training set

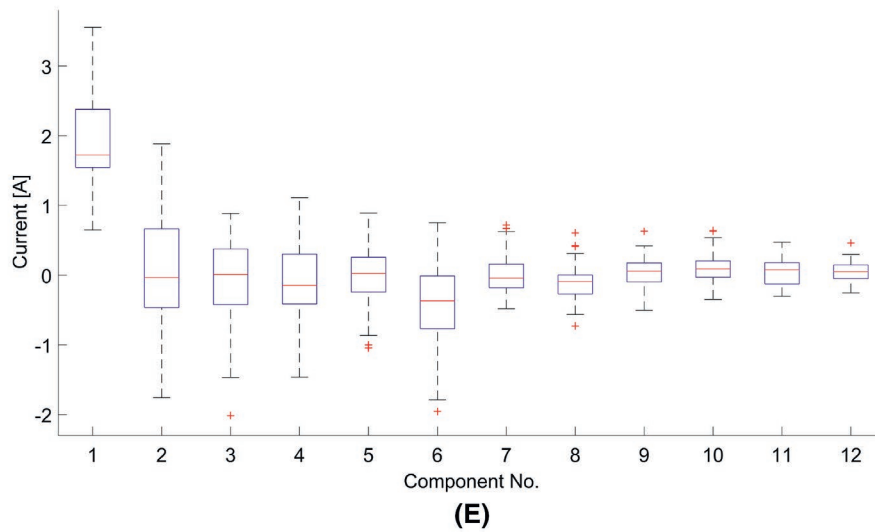
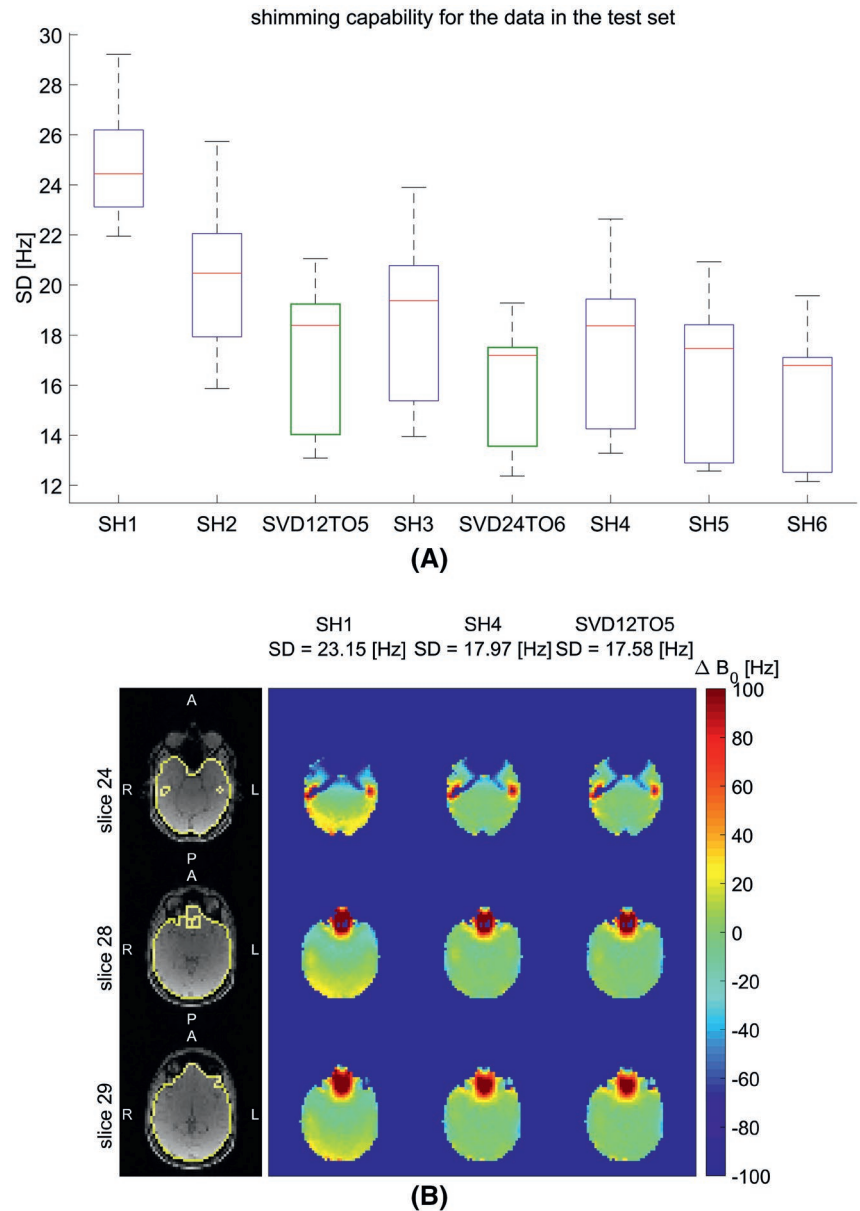


FIGURE 7 Stream functions (A-D) of the first four components and box plot of currents (E) flowing through the SVD12TO5 12 components for shimming of all the 84 field maps in the training set. For further details refer to the caption of Figure 1

FIGURE 8 Box plot (A) of standard deviation of the residual field inhomogeneity after different shimming methods for the data in the test set and the residual fields (B) on three typical slices of a representative field map in the test set after shimming using the first (SH1), fourth SH shapes (SH4), and SVD coil with 12 elements (SVD12TO5)



approach has been recently presented in a design for a gradient coil array with movable imaging volume.³¹ The input of the SVD algorithm in our method was composed of individual coil layouts optimized to achieve a given order SH shimming capability for each field map (given a constraint on total power dissipation) with each coil representing a column vector of the matrix. Contours of each resulting component can be used to construct an individual coil element of the shim coil array. Unlike the results of the SVD algorithm field maps in Li et al,¹⁷ the magnetic field generated by each coil element is spatially smooth over the human brain and naturally satisfies Maxwell's equations. Furthermore, the proposed protocol accounts for different possible head positions, which increases the usability of the designed shim array.

In the previous work,¹⁷ leave-one-out cross validation has already been used to evaluate the generalization ability

of the SVD modes of the field maps. Here, the cross validation technique has been applied to obtain a suitable total required number of components to balance the trade-off between generalization ability and fabrication challenges of the resulting shim coil array. Furthermore, the power dissipation of each element of a shim coil array can be calculated to provide additional clues for determining the total number of coil elements.

In a less recent publication,¹⁶ it was shown that the first SVD mode combined with up to second-order SH shapes outperforms up to third-order SH functions for the reduction of field inhomogeneities in validation data. This means that six bases (1 SVD mode plus 5 second-order SH shapes) are required if the field maps were measured after only a first-order SH shimming. This number of the bases is comparable to 5, which was the number of coil elements in

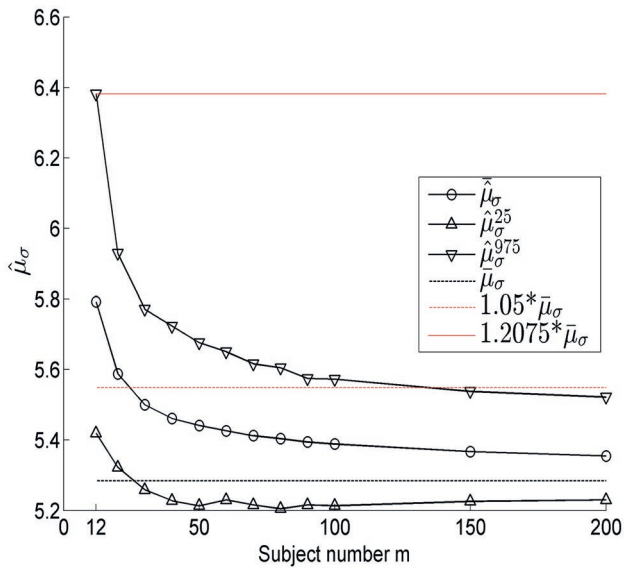


FIGURE 9 95% confidence interval of $\hat{\mu}_\sigma$ using the bootstrap technique. Here, $\hat{\mu}_\sigma$ is the mean of the standard deviation of the difference between the two resulting shimming fields generated by the designed coil array with 12 coil elements and the target order SH shapes for shimming of the residual field inhomogeneities

the present work if the target order and the achieved order are equal to 5 and 3, respectively, as shown in Figure 4A. These comparable results may be due to the high degree of similarity of field maps of normal human brains within the general population.

The validation data shown in Figure 4 reveal that using a target order equal to or lower than an achieved order did not allow us to obtain a smaller number of components than that of the corresponding SH functions when the achieved order was higher than 4. This result may be caused by relatively simple resulting stream functions from the individual shim coil design step, according to the method in Section 2.2. The authors³² have shown that the stream function for a field map has more wire loops for higher SH shimming fidelity. If the target order is too low, the resulting stream function does not capture the complexity of the target field map. After the SVD is performed on the matrix consisting of such stream functions for all field maps, more components are required to obtain a higher achieved order shimming fidelity.

As shown in Figures 2A-C and 4B,C, the maximum number of components tends to rise with the increase of the target order though the median values of the numbers of components have a decreasing tendency. This result may be due to relatively complicated resulting stream functions. If a target order is too high, the resulting stream function for each field map has more local wire loop structures according to Jia et al.³² Then, the SVD algorithm has difficulties finding a common basis in a set of rapidly oscillating functions. When the resulting SVD components are used for

shimming for a specific field map, more components may be required.

As shown in Figures 2 and 4, the total number of used components are typically determined by the maxima or the maximum outliers in the box-plots. One possible reason for the appearance of the outliers is the difference in the magnetic susceptibility distributions for individual human brains. Another possible reason is the different rotations for the same human brain. For example, as shown in Figure 6B, using 24 components did not allow us to achieve a sixth-order SH shimming performance for around 10 percent of the field maps. Even for the same subject, the sixth-order SH shimming capability for field maps corresponds to some but not all head positions. In order to achieve the goal for all field maps, one possible solution is to increase the number of used components to 30, as shown in Figure 2. The relationship between the head rotations and the number of the required components is a topic of an ongoing study at our institution.

It is worth noting that our results are obtained using field maps for whole brain shimming. Although the resulting shim coil array can also be used for reducing the field inhomogeneity within local regions in the brain, it may not be optimal in this case. Moreover, the proposed coil array may not be suitable to perform shimming over other human organs which have different susceptibility distributions. Fortunately, the proposed design method can be applied to create specific shim coil arrays for the local regions or other organs if field maps or the corresponding organs or areas are used in the design.

Stockmann et al² has simulated the shimming performance of their integrated RF/B₀ helmet arrays for human brain field maps acquired after second-order global SH shimming. Based on their results, 32-channel shim arrays plus 8-channel face loops have a shimming performance comparable to between the fourth- and fifth-order SH shimming. However, Figure 4C shows that the 24-channel coil elements achieve similar shimming fidelity for all validation data as the fifth-order SH shapes. This means that the total number of coil elements can be reduced by a factor of 1.25 compared to the RF helmet design. This reduction may be due to the fact that two shim coil arrays are mounted on different current-carrying surfaces and our shim coil array was designed specifically to reduce the field inhomogeneity of the human brain.

As can be seen in Figure 6A, some field maps in this study show higher standard deviations than some examples from the literature (e.g. Stockmann et al¹²). One of the possible reasons of the high standard deviation observed for some field maps in our data set is the large amount of anatomical diversity amongst the subjects enrolled in this study. Another reason can be the selection of the brain region to be shimmed, which in our study comprises the whole brain, including cerebellum and the most part of the brain stem. Furthermore, in our study we have paid a

great deal of attention to accurate segmentation of known regions of strong field inhomogeneities, such as temporal lobes and prefrontal areas.

This study only focuses on global static shimming of the entire human brain. However, dynamic slice-wise shimming of the human brain has attracted increasing interest in the past few years^{2,8,10,12,33} since dynamic shimming typically outperforms global shimming. Unlike multi-coils with local loops,^{8,10,12} each coil element of the resulting shim coil array has a global distribution of wire loops on the current-carrying surface. Like SH shim coils,³³ this global distribution might lead to eddy current-induced field perturbations on the \mathbf{B}_0 field during dynamic shimming. One possible solution to address this problem is to use a similar technique of pre-emphasis and \mathbf{B}_0 compensation as in Juchem et al.³³

There are several challenges associated with the practical implementation of the resulting coil designs: (i) current SVD components are all defined on the same current-carrying surface and (ii) do not account for the practical manufacturing constraints such as a finite wire spacing. Finally, as shown in Figure 7, the topology of the wire patterns is very irregular. The latter issue may be addressed by automated wire layout calculation routines, one such algorithm is being currently developed in our lab. Combined with machined manufacturing technologies, such as etching or water-jetting, the complexity of the underlying winding pattern can be effectively handled. The other two issues may be simultaneously handled by the following procedure: the field maps of all SVD elements can be calculated for a reasonable common region, e.g. an elliptical region encompassing typical brain dimensions, and used as target fields for finding the final stream function values on a set of concentric cylindrical surfaces. During this final design step, the p-norm ($\|\vec{J}\|_p := (\int_{\Gamma} |\vec{J}|^p d\Gamma)^{1/p}$ ($p > 2$)) of a surface current density³⁴ can be used to control the minimum width of wire tracks, leading to realizable coil element layouts. Following the implementation of these steps the final comparison to SH shimming with a larger number of SH functions will become feasible, as only then it will become possible both to compare the resulting electrical parameters and to assess the practical fabrication challenges.

The manuscript presents a novel shim coil design concept. The current results can be used as a preliminary data to guide further research work. For example, in order to increase the stability of the designed coil array, more field maps from a high number of subjects are needed during the design of a coil array, as shown in Figure 9. In order to reduce the cost of obtaining many field maps, the existing field maps from other projects, such as the human connectome project,³⁵ will be used in the future. Moreover, the use of a high number of field maps may become a challenge due to increased computational costs. Parallel computations using graphic processing units (GPUs) may be a solution that will be explored in future work.

5 | CONCLUSION

A novel approach based on the stream function method and the singular value decomposition has been presented and used to design a shim coil array matched to the human brain anatomy. The cross validation technique has been applied for finding an optimal number of elements of the coil array. The results demonstrate the validity of the proposed method to design a potentially physically realizable shim coil array matched to the human brain anatomy, which naturally satisfies the laws of electrodynamics. A bootstrapping technique has been leveraged to estimate the required number of brain field maps for the final coil design.

ACKNOWLEDGMENTS

This work was supported by the German Research Foundation (DFG) (Grant Number ZA 422/5-1, ZA 422/6-1, Reinhart Koselleck Project, DFG SCHE 658/12 and SCHE 658/13-1) and the European Research Council Proof-of-Concept Grant “mrSANE” grant agreement 755466.

ORCID

Feng Jia  <http://orcid.org/0000-0003-3593-2513>

Ali Aghaeifar  <http://orcid.org/0000-0002-6964-0992>

Sebastian Littin  <http://orcid.org/0000-0002-8190-1761>

REFERENCES

- Pohmann R, Speck O, Scheffler K. Signal-to-noise ratio and MR tissue parameters in human brain imaging at 3, 7, and 9.4 tesla using current receive coil arrays. *Magn Reson Med*. 2016;753:801–809.
- Stockmann JP, Wald LL. In vivo B_0 field shimming methods for MRI at 7 T. *NeuroImage*. 2018;168:71–87.
- Wu B, Li W, Avram AV, Gho S-M, Liu C. Fast and tissue-optimized mapping of magnetic susceptibility and T_2^* with multi-echo and multi-shot spirals. *NeuroImage*. 2012;593:297–305.
- Juchem C, de Graaf RA. B_0 magnetic field homogeneity and shimming for in vivo magnetic resonance spectroscopy. *Anal Biochem*. 2017;529:17–29.
- Pan JW, Lo K-M, Hetherington HP. Role of very high order and degree B_0 shimming for spectroscopic imaging of the human brain at 7 tesla. *Magn Reson Med*. 2012;68:1007–1017.
- Kim T, Lee Y, Zhao T, Hetherington HP, Pan JW. Gradient-echo EPI using a high-degree shim insert coil at 7 T: implications for BOLD fMRI. *Magn Reson Med*. 2017;78:1734–1745.
- Juchem C, Nixon TW, McIntyre S, Rothman DL, de Graaf RA. Magnetic field modeling with a set of individual localized coils. *J Magn Reson*. 2010;204:281–289.
- Juchem C, Nixon TW, McIntyre S, Boer VO, Rothman DL, de Graaf RA. Dynamic multi-coil shimming of the human brain at 7 T. *J Magn Reson*. 2011;212:280–288.

9. Jia F, Kroboth S, Layton KJ, et al. Using a matrix gradient coil for shimming of the human brain. *Magn Reson Mater Phys Biol Med*. 2016;293(Suppl 1):s77–s78.
10. Aghaeifar A, Mirkes C, Bause J, et al. Dynamic b_0 shimming of the human brain at 9.4 T with a 16-channel multi-coil shim setup. *Magn Reson Med*. 2018;80:1714–1725.
11. Aghaeifar A, Zhou J, Heule R, et al. A 32-channel multi-coil setup optimized for human brain shimming at 9.4 T. *Magn Reson Med*. 2019. <http://dx.doi.org/doi.org/10.1002/mrm.27929>
12. Stockmann JP, Witzel T, Keil B, et al. A 32-channel combined RF and B_0 shim array for 3 T brain imaging. *Magn Reson Med*. 2016;75:441–451.
13. Han H, Song AW, Truong T-K. Integrated parallel reception, excitation, and shimming (iPRES). *Magn Reson Med*. 2013;70:241–247.
14. Truong T-K, Darnell D, Song AW. Integrated RF/shim coil array for parallel reception and localized B_0 shimming in the human brain. *NeuroImage*. 2014;103:235–240.
15. Hudson P, Harris CT, Handler WB, Scholl TJ, Chronik BA. A single-axis composite shim coil insert for spectroscopy in the medial temporal lobe of the human brain. In Proceedings of the ISMRM 20th Scientific Meeting and Exhibition. Stockholm; 2010. p.221.
16. Adalsteinsson E, Conolly SM, Xu H, Spielman DM. Design of dedicated shim fields. In Proceedings of the ISMRM 7th Scientific Meeting and Exhibition, Pennsylvania; 1999. p. 477.
17. Li P-Y, Wu P-Y, Li Y-T, Chu Y-H, Lin F-H. Decomposition of off-resonance fields in brain MRI. In Proceedings of the ISMRM 27th Scientific Meeting and Exhibition, Paris; 2018. p. 4315.
18. Penny WD, Friston KJ, Ashburner JT, Kiebel SJ, Nichols TE. *Statistical Parametric Mapping: The Analysis of Functional Brain Images*. London: Elsevier; 2006.
19. Peeren GN. Stream function approach for determining optimal surface currents. *J Comput Phys*. 2003;191:305–321.
20. James G, Witten D, Hastie T, Tibshirani R. *An introduction to Statistical Learning with Applications in R*. New York: Springer Science+Business Media, LLC; 2013.
21. Efron B, Tibshirani RJ. *An Introduction to the Bootstrap*. London: Chapman & Hall/CRC; 1993.
22. Thesen S, Heid O, Mueller E, Schad LR. Prospective acquisition correction for head motion with image-based tracking for real-time fMRI. *Magn Reson Med*. 2000;44:457–465.
23. Smith SM. Fast robust automated brain extraction. *Human Brain Mapping*. 2002;17:143–155.
24. Robinson S, Schödl H, Trattng S. A method for unwrapping highly wrapped multi-echo phase images at very high field: umpire. *Magn Reson Med*. 2014;72:80–92.
25. Crozier S, Eccles CD, Beckey FA, Field J, Doddrell DM. Correction of eddy-current-induced B_0 shifts by receiver reference-phase modulation. *J Magn Reson (1969)*. 1992;97:661–665.
26. Welz AM, Cocosco C, Dewdney A, et al. Development and characterisation of an unshielded patloc gradient coil for human head imaging. *Concepts Magn Reson Part B*. 2013;43:111–125.
27. Hansen PC. Regularization tools: a MATLAB package for analysis and solution of discrete ill-posed problems. *Numer Algorithms*. 1994;6:1–35.
28. Bishop CM. *Pattern Recognition and Machine Learning*. New York: Springer Science+Business Media, LLC; 2011.
29. Maclaren J, Herbst M, Speck O, Zaitsev M. Prospective motion correction in brain imaging: a review. *Magn Reson Med*. 2013;69:621–636.
30. Hudson P, Hudson SD, Handler WB, Chronik BA. Finite-length shim coil design using a fourier series minimum inductance and minimum power algorithm. *Concepts Magn Reson Part B*. 2010;37:245–253.
31. Smith E, Freschi F, Repetto M, Crozier S. The coil array method for creating a dynamic imaging volume. *Magn Reson Med*. 2017;78:784–793.
32. Jia F, Kroboth S, Chu Y-H, et al. On the ultimate shimming performance in the human brain. *Magn Reson Mater Phys Biol Med*. 2017;303(Suppl 1):s301–s301.
33. Juchem C, Nixon TW, Diduch P, Rothman DL, Starewicz P, de Graaf RA. Dynamic shimming of the human brain at 7 T. *Concepts Magn Reson Part B*. 2010;37B:116–128.
34. Jia F, Littin S, Layton KJ, Kroboth S, Yu H, Zaitsev M. Design of a shielded coil element of a matrix gradient coil. *J Magn Reson*. 2017;281:217–228.
35. Fan Q, Witzel T, Nummenmaa A, et al. MGH-USC human connectome project datasets with ultra-high b-value diffusion MRI. *NeuroImage*. 2016;124:1108–1114.

How to cite this article: Jia F, Elshatlawy H, Aghaeifar A, et al. Design of a shim coil array matched to the human brain anatomy. *Magn Reson Med*. 2019;00:1–16. <https://doi.org/10.1002/mrm.28016>

Publication V

“Spread-Spectrum Magnetic Resonance Imaging”

K. Scheffler, J. Bause, A. Loktyushin, **A. Aghaeifar**, T. Steffen, B.
Schölkopf

Magnetic Resonance in Medicine, 82 (3), pp. 877-885 (2019)

DOI: [10.1002/mrm.27766](https://doi.org/10.1002/mrm.27766)

Spread-spectrum magnetic resonance imaging

Klaus Scheffler^{1,2}  | Alexander Loktyushin^{1,3} | Jonas Bause^{1,2} | Ali Aghaeifar^{1,2}  |
Theodor Steffen¹ | Bernhard Schölkopf³

¹High-Field MR Center, Max Planck Institute for Biological Cybernetics, Tübingen, Germany

²Department for Biomedical Magnetic Resonance, University of Tübingen, Tübingen, Germany

³Department of Empirical Inference, Max Planck Institute for Intelligence Systems, Tübingen, Germany

Correspondence

Klaus Scheffler, MPI for Biological Cybernetics, Spemannstrasse 41, 72076 Tübingen, Germany.
Email: klaus.scheffler@tuebingen.mpg.de

Funding information

Max-Planck-Gesellschaft; Deutsche Forschungsgemeinschaft, Grant/Award Number: DFG SCHE 658/12; Max Planck Society

Purpose: A novel method for the acceleration of MRI acquisition is proposed that relies on the local modulation of magnetic fields. These local modulations provide additional spatial information for image reconstruction that is used to accelerate image acquisition.

Methods: In experiments and simulations, eight local coils connected to current amplifiers were used for rapid local magnetic field variation. Acquired and simulated data were reconstructed to quantify reconstruction errors as a function of the acceleration factor and applied modulation frequency and strength.

Results: Experimental results demonstrate a possible acceleration factor of 2 to 4. Simulations demonstrate the challenges and limits of this method in terms of required magnetic field modulation strengths and frequencies. A normalized mean squared error of below 10% can be achieved for acceleration factors of up to 8 using modulation field strengths comparable to the readout gradient strength at modulation frequencies in the range of 5 to 20 kHz.

Conclusion: Spread-spectrum MRI represents a new approach to accelerate image acquisition, and it can be independently combined with traditional parallel imaging techniques based on local receive coil sensitivities.

KEYWORDS

acquisition acceleration, local magnetic fields, nonlinear field modulation, parallel imaging

1 | INTRODUCTION

Acceleration of imaging speed has been one of the most important challenges in MRI and spectroscopy during the last three decades. In the early days of MRI several minutes were required to capture a single slice of the human body using a spin echo sequence. Today, a 3D high-resolution dataset of the entire human brain can be measured within seconds. The FLASH sequence is one of the most prominent examples for rapid imaging.¹ With echo planar imaging a further significant acceleration was achieved by scanning multiple phase-encoded

echoes per repetition time instead of just one.² About two decades ago, the landscape for rapid MRI changed dramatically with the invention of parallel imaging techniques such as SMASH, SENSE, and GRAPPA.³⁻⁵ Parallel imaging uses the spatially confined sensitivities of local radio frequency receiver coils as additional information for spatial encoding to accelerate image acquisition. The most radical and ultimate extension of parallel imaging is to use one coil per voxel (OVOC) as introduced by Hennig,⁶ which, in principle, allows everything to be captured within microseconds. Many other rapid imaging techniques have since been proposed. For

example, UNFOLD, k-tBLAST/SENSE, or compressed sensing and its derivatives use sparse sampling in k-space and time, combined with prior knowledge to boost imaging speed further in certain applications.⁷⁻¹⁰ More recently, the use of nonlinear gradients for spatial encoding such as PatLoc, FRONSAC, and O-space imaging has been proposed with the potential to provide tailored spatially varying resolution, curved imaging slices that mirror physiological geometry, and faster parallel imaging capabilities with multichannel coils.¹¹⁻¹⁴ Both linear and nonlinear magnetic fields can be combined and used for image encoding, which offers significantly more degrees of freedom to encode the MR signal.

In conventional imaging, the scan of k-space (which is the Fourier transformed image space) is achieved by applying linear gradients along the principal axes. In most applications, k-space is acquired line by line on a Cartesian grid, or in some implementations along projections or spirals, to name just a few. The application of additional rapid magnetic field modulations during scan of k-space has already been demonstrated in the wave-CAIPI (preceded by similar techniques such as bunched phase encoding¹⁵ and zigzag sampling)¹⁶ and the FRONSAC approach.^{12,17} In wave-CAIPI, which is an extension of bunched phase encoding in combination with CAIPI,¹⁸ additional phase-shifted sinusoidal modulations are applied to phase encoding gradients during the readout. This converts the original k-space scan along a straight line into an extended corkscrew trajectory. The resulting improved distribution of k-space sampling points can be used to accelerate image acquisition if combined with parallel imaging. A similar principle is used in FRONSAC, except that the additional field modulation is achieved with global second-order nonlinear shim gradients superimposed on the underlying k-space trajectory produced by linear gradients. The simulated results achieved with FRONSAC demonstrate a faster coverage of k-space (along a similar corkscrew or oscillating trajectory to that in wave-CAIPI) and thus increased imaging speed.

Here we present a novel concept to boost MR imaging speed further called spread-spectrum MRI. Spread-spectrum MRI is based on the rapid dynamic modulation of local magnetic fields produced by an array of local current loop fields instead of using global field modulations via gradient or shim coils as done in wave-CAIPI or FRONSAC. The magnetic fields produced by local current coils are modulated dynamically during signal acquisition to superimpose local and unique phase variations onto the spin distribution, which can be interpreted as a unique fingerprint onto confined regions within the object. Spread-spectrum MRI distributes or spreads the basic bandwidth of gradient-encoded magnetization frequencies using distinct modulation frequencies (or even orthogonal noise patterns) originating from a certain spatial location of the object. This spatially unique information is then utilized to disentangle different parts of the object, and thus to boost imaging speed dramatically.

In other words, spread-spectrum MRI combines local nonlinear encoding with rapid modulation of k-space trajectories.

2 | METHODS

2.1 | Experimental setup

The experimental setup used to demonstrate accelerated acquisition is illustrated in Figure 1. All measurements were performed on a 9.4 T whole-body MR scanner with a patch antenna tuned to 400 MHz.¹⁹ The transmit/receive antenna was placed approximately 180 mm from the center of a cylindrical oil phantom (diameter 135 mm, length 220 mm). The phantom was surrounded by the eight local B_0 coils as depicted in Figure 1. Although the patch antenna had two receive channels, the data of only a single receive channel was used for image reconstruction for simplicity. In addition to the gradients GR, GP, and GS and the radio frequency excitation, the MR scanner triggered eight parallel current amplifiers via dedicated controllers (National Instruments I/O card type PXIe-6738), which were interfaced with a LabVIEW program. The current amplifiers were connected separately to the local square-shaped B_0 coils (50 mm × 50 mm, 50 windings) that injected spatially confined magnetic field modulation patterns into the measured sample placed in a cylinder with a diameter of 140 mm. Simultaneously to the acquisition of a conventional gradient echo sequence, different patterns of modulations are played out to eight local coils by the synchronized current waveform controller and amplifier. A priori measured magnetic field maps for the quantification of the B_0 field change evoked by the individual local coils at a certain current are then used for reconstruction of the MR signal acquired during local modulations of B_0 .

The field maps required for the spread-spectrum MRI reconstruction were determined for each coil, by performing two consecutive single-echo gradient echo measurements with a single axially oriented slice positioned approximately under the wires of the coils. The sequence triggered a half-sine-shaped current pulse with an amplitude of 0.1 A applied after the radio frequency pulse and before echo acquisition. The half-sine-length was 400 μ s and 500 μ s for the first and the second measurement, respectively. The other imaging parameters were as follows: echo time 4.8 ms, repetition time 500 ms, nominal flip angle 50°, field of view 160 mm × 160 mm, matrix size 128 × 128, slice thickness 2 mm, bandwidth per pixel 410 Hz. Images were reconstructed offline using in-house-developed Matlab routines followed by the subtraction of the phase of the two images acquired with the 500 μ s and 400 μ s dephasing period. The subtraction removed any phase perturbations caused by background field inhomogeneities and permitted sufficient mapping even in proximity to the local B_0 coils where the field gradient was high. The resulting difference phase maps were then converted into B_0 maps for each of the eight coils.

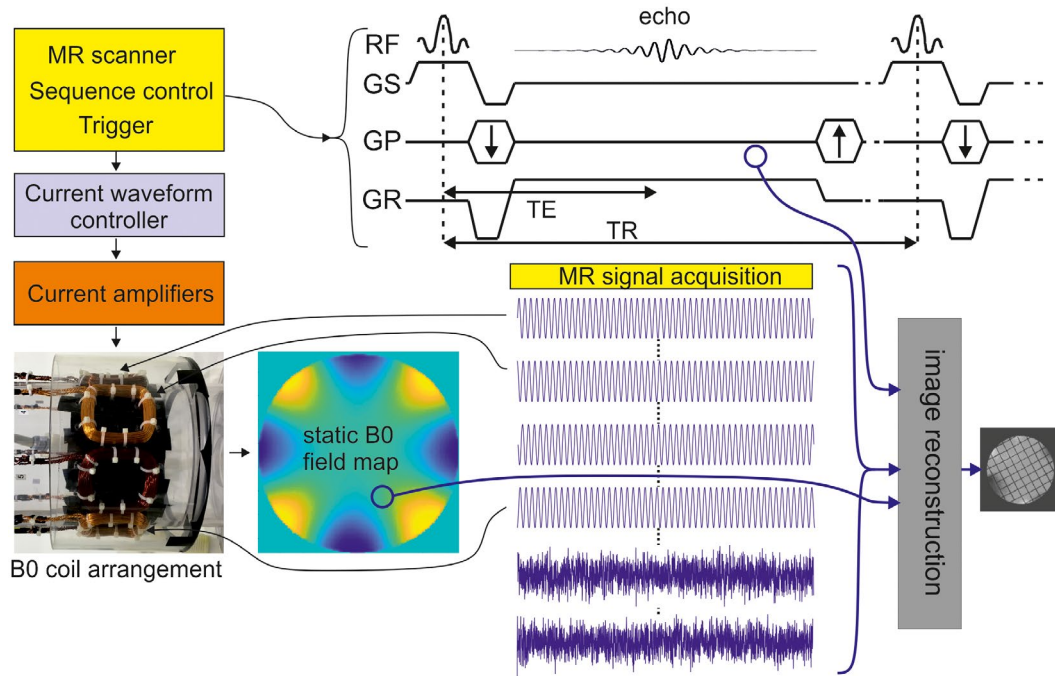


FIGURE 1 Experimental setup of spread-spectrum imaging. The MR scanner (top left) controls the timing and execution of the gradient echo sequence (top right) and sends a trigger before each MR signal acquisition period to the current waveform controller. Eight independent current waveforms are generated, amplified by current amplifiers and applied to the eight local coils during the MR acquisition period, i.e. during the flat top of the readout gradient. For example, current modulations can be phase-shifted sine waves (as in the measurements performed in this study) or even noise patterns. The modulated and phase-encoded gradient echoes together with the knowledge of the magnetic field induced by the local coils and its corresponding current time courses are used for image reconstruction. As in conventional parallel imaging, acceleration of acquisition time is achieved by measuring only every n th phase-encoded echo

The capabilities of spread-spectrum MRI were investigated by performing a 5 kHz/3A zero-to-peak sine wave modulation on each B_0 coil during signal readout. A phase increment of 45° between adjacent channels of the arrangement was applied. Applied current patterns were identical for each phase-encoded echo. The images with sinusoidal current modulations during the readout were acquired using the same sequence settings and slice position as the reference B_0 maps, but the trigger was adjusted such that the B_0 field modulations started synchronously with the data-sampling period. In order to be able to sample the full frequency spreading of the MRI signal, k-space oversampling in readout direction was increased from a factor of 2 to 8. Increasing the oversampling only changes the analog-to-digital converter dwell time but not the overall readout duration, if the bandwidth per pixel is kept at the same value. The used readout duration of 2.46 ms and gradient strength of 7.65 mT/m were therefore the same as for standard Cartesian encoding and resulted in approximately 12 field modulation cycles during each readout.

2.2 | Simulation setup

With the experimental setup depicted in Figure 1, which was designed to demonstrate the feasibility of accelerated imaging using spread-spectrum MRI, practical applications,

such as human brain imaging, are not feasible due to its small diameter of only 140 mm. We thus simulated an arrangement of eight square-shaped coils with an edge length of 90 mm placed on a cylinder with 250-mm diameter that provides sufficient space to fit a human head; see Figure 2. The black rectangle in Figure 2A represents the outline of the cylinder with 250 mm in diameter, where eight coils (in pink) are mounted, each rotated by 45° around the center of the cylinder. The color map shows the magnetic field produced by those coils in a center plane along the cylinder axis. Figure 2B is a plane perpendicular to Figure 2A along the white dashed line shown in Figure 2A. For a better visualization, a static current with opposite polarization between adjacent coils was used to calculate the field maps shown in Figure 2A and B. Figure 2C describes the magnetic field along the white line (± 90 mm) depicted in Figure 2B. Here, a current of ± 1 A (reversed polarity for opposing coils) through a single coil winding was assumed. According to Biot-Savart's law this field decays with $1/r$, where r is the distance to the coil wire. A linear approximation (dotted lines in Figure 2C) results in a gradient strength of about $20 \mu\text{T/m}$ (averaged along 180 mm) and $10 \mu\text{T/m}$ (averaged over 100 mm). For the simulations based on this setup, a reference image (depicted schematically in Figure 2B) acquired with a conventional gradient echo

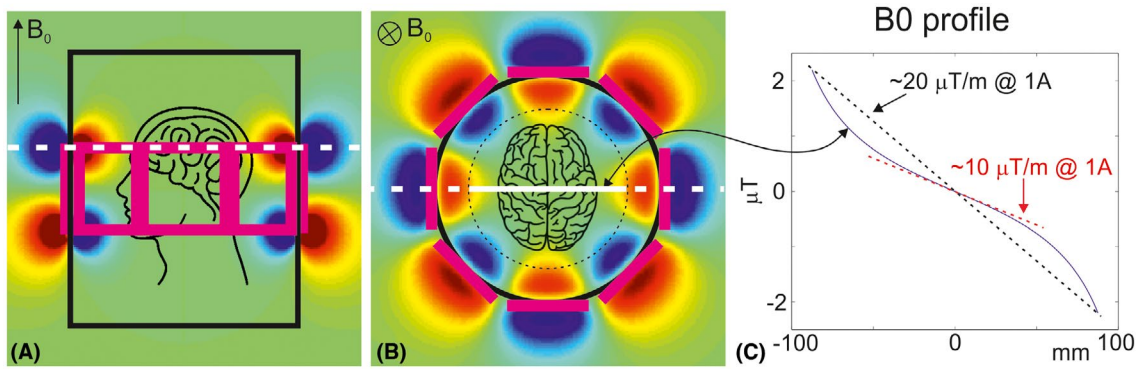


FIGURE 2 Illustration of the setup used for simulations. The underlying color maps in A and B represent magnetic fields generated by the eight local coils at a plane through the center of the cylinder (A) and a plane along the dashed white line in A (B). These maps were calculated using Biot-Savart's law and assuming opposite currents between adjacent coils. The resulting magnetic field within the dotted circle (180-mm diameter) and along the white line in B is shown in C including two linear field approximations (dotted lines) of 10 and 20 $\mu\text{T/m}$ for a current of 1 A (and -1 A for the opposing coil) through a coil with a single turn

sequence at 9.4T with an in-plane resolution of $0.85 \text{ mm} \times 0.85 \text{ mm}$ and a matrix size of 256×256 was used. Applied reconstruction algorithms are described in the following.

2.3 | Image reconstruction

In the presence of locally modulated magnetic fields, the measured signal \mathbf{s} at a k-space coordinate \mathbf{k} at time point t is given by the following equation:

$\mathbf{s}(\mathbf{k}, t) =$

$$\iiint \mathbf{m}(\mathbf{r}) \mathbf{p}(\mathbf{r}) \exp\left(-i\gamma(\mathbf{k}(t)\mathbf{r} + \sum_c \mathbf{B}_c(\mathbf{r}) \int_{t_1}^t f_c(\tau) d\tau)\right) dx dy dz \quad (1a)$$

$$\mathbf{k}(t) = \int_0^t \mathbf{g}(\tau) d\tau \quad (1b)$$

We assume that the measurement is performed with a single excitation/acquisition coil with a complex-valued sensitivity profile denoted as $\mathbf{p}(\mathbf{r})$. Without loss of generality, the terms describing relaxation effects are omitted in spatial encoding model (Equation (1a) and (1b)). The phase of the exponential term is composed of two parts. The term $\mathbf{k}(t)$ describes the k-space position related to the spatially linear gradients that are used to perform frequency and phase

played separately to each coil element c . The B_0 field profile of each coil element c is indicated by $\mathbf{B}_c(\mathbf{r})$, which was measured with the previously described two gradient echo measurements. $\mathbf{m}(\mathbf{r})$ is the object image to be reconstructed, and t_1 denotes the time of beginning of the modulation.

The continuous model has a discrete counterpart, where spatial encoding terms are described by the elements of the encoding matrix \mathbf{E} . Without loss of generality, let us consider a case in which a single 2D slice is acquired. Let K_x and K_y be the number of acquired k-space points in read-out and phase-encode direction, respectively. Further, let N_x and N_y be the number of pixels in spatial domain. We acquire a complex-valued spectrum $\mathbf{s} \in \mathbb{C}^{K_x \times K_y}$, and want to reconstruct the image $\mathbf{m} \in \mathbb{C}^{N_x \times N_y}$. The image acquisition process with local magnetic field modulation can be described by a discrete linear operator $\mathbf{E} \in \mathbb{C}^{(K_x K_y) \times (N_x N_y)}$. The acquisition process can therefore be described by a linear equation $\mathbf{s} = \mathbf{E}\mathbf{m}$. In case the currents injected into the loops are zero, the encoding matrix is an orthonormal Fourier transform matrix $\mathbf{E} = \mathbf{F}$. For ease of indexing let's reshape the encoding matrix as $\mathbf{E} \in \mathbb{C}^{K_x \times K_y \times N_x \times N_y}$. In the experiments and simulations described earlier a sine wave modulation $f_c(t) = \sin(t)$ of the local fields was applied that was identical for each phase encoding line. The elements of the matrix \mathbf{E} are then given by:

$$\mathbf{E}_{i,j,l,m} = \mathbf{F}_{i,j,l,m} \exp\left(-i\gamma \frac{\sum_c (a_c \mathbf{B}_{c,l,m} (\cos(2\pi w t_1 + \theta_c) - \cos(2\pi w t_i + \theta_c)))}{w}\right) \quad (2)$$

encoding (\mathbf{g} : linear magnetic field gradient vector, \mathbf{r} : spatial vector, τ and t : time). The second term $\sum_c \mathbf{B}_c(\mathbf{r}) \int_{t_1}^t f_c(\tau) d\tau$ corresponds to the sum of fields induced by the local magnetic field coils subject to an arbitrary waveform f_c . The waveform f_c represents the (unitless) current time course

Here, $\mathbf{B}_c \in \mathbb{C}^{C \times N_x \times N_y}$ is the B_0 field profile of a coil element c (where C is the total number of coil elements), w is the frequency of the spread-spectrum modulation, a_c is the modulation current amplitude, θ_c is the phase offset of the modulation. An extension of the model to the case of accelerated

acquisition is straightforward, for example, reduction of the number of phase encodings $j \in K_y$ and involves decreasing the number of rows in the matrix \mathbf{E} .

The image can be reconstructed by solving a linear equation systems $\mathbf{s} = \mathbf{E}\mathbf{m}$, which can be done for both general (Equation (2)) and separable (Equation (4); see following discussion) cases. In MR signal acquisitions with geometry factors (g -factor (4)) close to unity, computing the pseudoinverse of the encoding matrix \mathbf{E} and applying it to the measured k -space allow for a simple one-shot reconstruction. Otherwise, in case the g -factor is greater than unity, inversion of the system can be unstable and results become noisy. In such case, the following regularized optimization problem is solved:

$$\hat{\mathbf{m}} = \arg \min_{\mathbf{m}} (\|\mathbf{s} - \mathbf{E}\mathbf{m}\|_2^2 + \lambda |\text{TV}(\mathbf{m})|) \quad (3)$$

The regularization coefficient λ sets the weight of the total variation term ($\text{TV}(\mathbf{m})$) that penalizes blurring and ghosting artifacts in the reconstruction. The regularization term can be seen

$$s[k_x, y] = \sum_x \mathbf{m}[x, y] \exp \left(-i2\pi (k_x x / K_x) + \sum_c \mathbf{B}_c[x, y] \frac{\cos(2\pi w t_1 + \theta_c) - \cos(2\pi w t_{k_x} + \theta_c)}{w} \right) \quad (4)$$

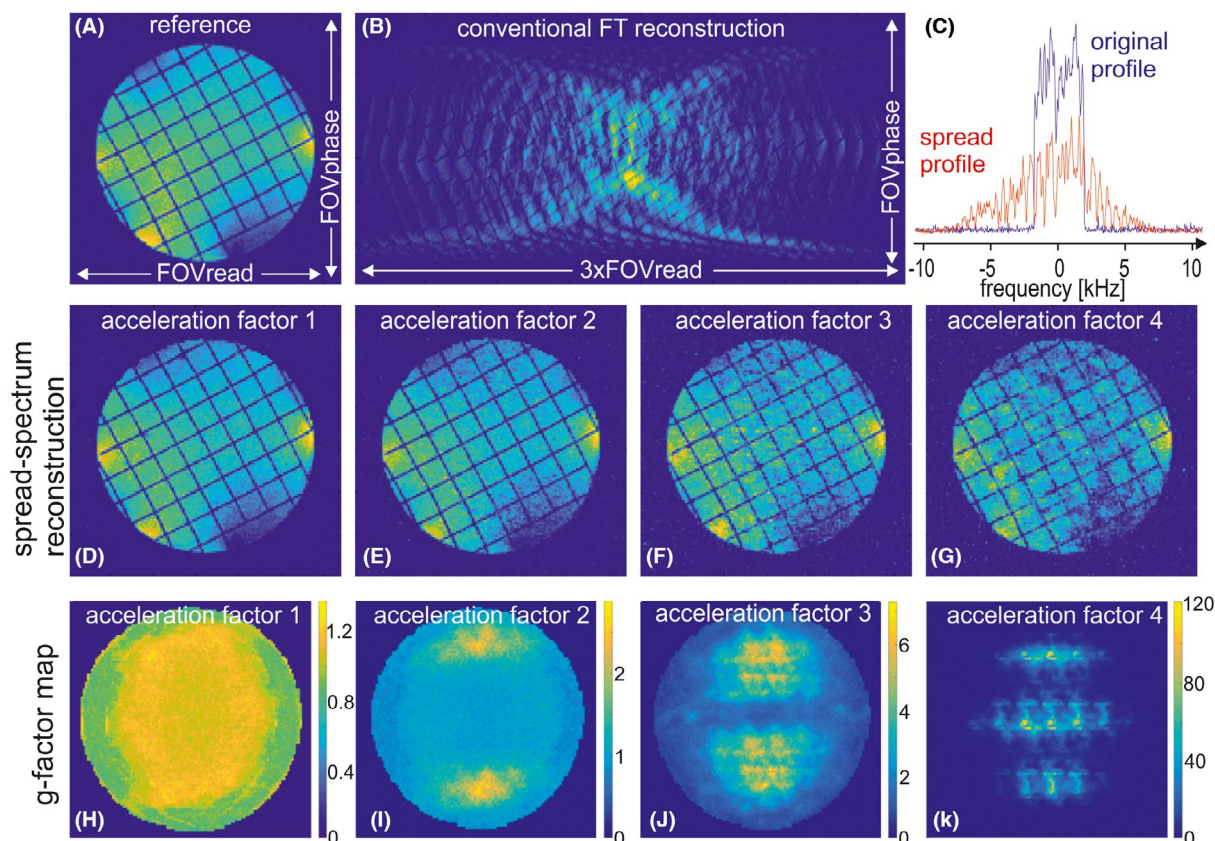


FIGURE 3 Experimental results achieved with spread-spectrum MRI. Top row: The application of phase-shifted 5-kHz current modulations leads to a spreading of the reference image A along readout direction (left–right) in the conventionally reconstructed image B. This frequency spread is also visible in the profiles (magnitude of the Fourier transformed central k -space line along readout direction with and without modulation) shown in C. The middle row shows spread spectrum reconstructed images of measured data with increasing acceleration factors, and the bottom row the corresponding g -factor maps, which indicate the noise amplification

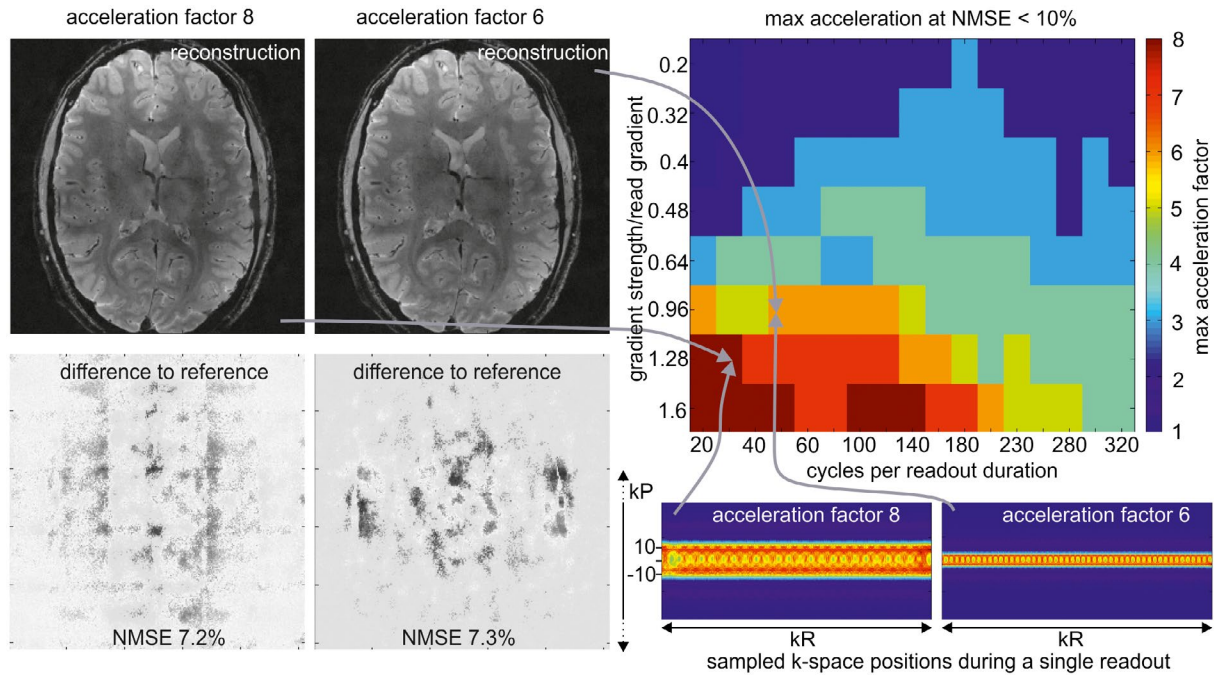


FIGURE 4 Simulated results achieved with spread-spectrum MRI. The column on the left shows simulated examples of reconstructed brain images accelerated by a factor of 6 and 8 and corresponding differences to the reference image. A modulation frequency of 24 and 32 cycles per readout gradient duration and a (linearly approximated) gradient strength of 1.28 and 0.96 relative to the readout gradient strength were applied to the local coils in the case of eight-fold and six-fold acceleration, respectively. These two combinations of modulation frequency and strength are marked by arrows in the matrix plot shown right. This plot gives an overview of achievable acceleration factors confined to reconstruction errors of below 10% NMSE, as a function of applied modulation strength and frequency to the local coils. Units are scaled to the strength and duration of the applied readout gradient. The two figures on the bottom right depict the sampled points in k-space along read (kR) and phase (kP) direction for acceleration factors of 6 and 8. Spreading along kP is about ± 10 and ± 4 phase encoding steps. NMSE, normalized mean square error

Here, k_x is the k-space index of the data sample in readout direction. In this representation, it is easy to see that the complex coefficients at each line in the hybrid space \mathbf{s}_y only depend on the magnetization values \mathbf{m}_y from the same line. In other words, no mixing of image voxel values in phase encode direction occurs and the image content is spread purely in readout direction. An advantage of such formulation is that the image reconstruction process can be made separable in phase encode direction in spatial domain, which results in smaller linear systems to be solved and faster convergence. However, in the more general case of arbitrary modulations for each phase encoding step or for non-Cartesian trajectories the optimization scheme shown in Equation 3 needs to be solved.

3 | RESULTS

3.1 | Experimental results

Experimental results achieved with this setup are summarized in Figure 3. Conventional 2D Fourier reconstruction of the phase-encoded and sine-wave-modulated echoes is shown in Figure 3B demonstrating a spread of the reference image along the readout direction. The profiles shown in Figure 3C are the magnitude of the Fourier transformed gradient echo acquired at the center of k-space

(no phase encoding) without (original profile, blue) and with 5-kHz field modulation (spread profile, red), showing a frequency-spread profile of about ± 5 kHz of the original profile. A phase increment of the 5-kHz sine waves of 45° between adjacent coils was applied. The second row shows reconstructed images acquired with local current modulation and acceleration factors of 1 to 4, i.e. using each k-space line (D), every other (E), every third (F), and every fourth k-space line (G), respectively. The degradation of image quality with increasing acceleration is quantified in Figure 3H to K as g-factor maps based on the pseudoreplica method.²¹ G-factors in the range of 1 to 1.5 represent only a minor amplification of reconstruction-related noise in the accelerated images, which is the case for the reference image H and the two-fold accelerated image I. Image degradation for higher g-factors is visible in Figure 3F and G. Reconstruction time was about 5 seconds on an Intel Core i7-3770K CPU operating at 3.50 GHz in combination with a Nvidia GeForce GTX TITAN GPU.

3.2 | Simulated results

The experimental results shown in Figure 3 have been acquired with a modulation frequency of 5 kHz at 3A

(zero-to-peak), which was the performance limit of the connected analog current amplifiers. Numerical simulations of this setup (not shown here) were able to demonstrate a theoretical acceleration factor up to 10 (with an image degradation of less than 10% normalized mean square error [NMSE] compared to the reference image) for modulation frequencies in the range of 10 to 20 kHz at peak currents of 6 to 8 A.

Examples of simulated reconstructions of the reference brain slice with acceleration factors of 6 and 8 using different modulation strength and frequency are depicted in Figure 4. As the reconstruction error is below 10% NMSE no differences in reconstruction quality or differences to the reference image (not shown here) are visible. The color map matrix shown at the right top represents maximum achievable acceleration factors resulting in reconstruction errors of below 10% NMSE as a function of applied modulation field strength and frequency to the local coils. To allow generalization of these simulations, the strength of the modulation fields is given as the ratio of the approximated linear field gradient strength generated by the local coils and the applied readout field gradient strength. The modulation frequency is given as the number of sine wave cycles per duration of the readout gradient.

In conventional imaging based on linear gradient field encoding, single points in k-space are sampled along a Cartesian trajectory or grid. Using nonlinear magnetic fields for encoding spreads each single point in k-space to a pattern or stamp of certain shape and size, similar to the O-space or FRONSAC methods that are based on spatially quadratically varying magnetic fields.¹²⁻¹⁴ The k-space pattern sampled along a single readout is shown in Figure 4 right bottom for two combinations of modulation strengths and frequencies. Without additional modulation, the sampling pattern is a single straight line along readout direction k_R . The spread of those patterns along phase encode direction (about ± 10 and ± 4 phase encoding steps for accelerations of 8 and 6, respectively) enables reduction of the number of linear phase encoding steps, leading to possible accelerations of a factor of 6 and 8. In general, higher-modulation amplitudes or fields increase k-space coverage along phase direction (k_P) and thus allow for higher acceleration. This is presented on the color map showing increasing maximum possible acceleration factors as a function of modulation strength.

4 | DISCUSSION

Spread-spectrum MRI is based on rapid local magnetic field modulation that enables acceleration of image acquisition. Acceleration factors of up to 4 were demonstrated experimentally in a phantom study using eight local coils modulated with 5 kHz. In order to estimate the practical performance

and limits of spread-spectrum MRI for human brain imaging, a larger setup consisting of eight coils arranged on a cylinder with 250 mm was simulated. In this simulation, only a single slice positioned in the region of largest field variations was considered, and local field modulations were combined with a conventional Cartesian k-space sampling using a linear readout gradient GR preceded by a stepwise increased phase encoding gradient GP. The required field strength generated by the local coils to achieve a certain acceleration factor scales (linearly, if local fields are approximated by a linear gradient as depicted in Figure 2C) with the strength of the used readout gradient GR. Depending on the targeted acceleration factor, the required local field strength is in the order of 20% to 150% of the strength of the applied readout gradient GR. Assuming a readout gradient strength GR of 10 mT/m (GR is in the order of 5 mT/m for conventional imaging, and 20 to 30 mT/m for fast imaging such as EPI and balanced SSFP) this corresponds to a required local field of 2 to 15 mT/m. In the approximation of a linear local field modulation, a pair of opposing wires with opposite current direction produce a gradient field of about 10 $\mu\text{T/m}$ per ampere, as shown in Figure 2C, Methods section. As an example, a coil with 25 turns will then generate a gradient field of 0.25 mT/m, and currents of 8 to 60 A are required to achieve a local modulation field of 2 to 15 mT/m. The inductance of such a 90 mm \times 90 mm, 25-turn coil is on the order of 100 μH (measured experimentally), resulting in a required driving voltage of 5 V (at 8 A and 1 kHz) up to 375 V (at 60 A and 10 kHz). This rough estimation of required currents and voltages is in the range of what small to medium current amplifiers are able to deliver. However, these estimations scale (about linearly) with the gradient strength used to sample k-space, and they scale (nonlinearly as depicted in the color map in Figure 4) with the targeted acceleration factor. For example, for an acceleration factor of 3 and a moderate readout gradient strength of 5 mT/m, currents in the range of 2 A to 3 A and frequencies of 4 kHz to 5 kHz are required, which leads to driving voltages of only about 5 V to 10 V for a 25-turn coil. Therefore, the required experimental effort for accelerated spread-spectrum MRI strongly depends on the specific application.

The presented experimental and theoretical results are based on phase-shifted sinusoidal modulation patterns. Thus, the resulting magnetic field pattern rotates within the imaging plane (Figure 2B) with the frequency of the applied sine wave. This corresponds to a rotation of the $1/r$ decaying magnetic fields shown in Figure 2C within the imaging slice. Using a linear field approximation (dashed lines in Figure 2C) the local coils generate a linear magnetic field gradient that rotates in a plane perpendicular to B_0 . In this linear approximation, the sampling of the measured MR signal in k-space is a superposition of a circle trajectory (from the modulated local coils) with a linear trajectory (from the readout gradient). This sampling trajectory is similar to the

wave-CAIPI corkscrew trajectory,¹⁷ which is generated by sinusoidal modulation of the linear gradients. The use of local, nonlinear magnetic modulation fields spreads this corkscrew trajectory into a dense band of k-space sampling points, as depicted in Figure 4. These trajectories show a certain similarity to the trajectories generated by the O-space or FRONSAC method¹²⁻¹⁴ resulting in a space variant resolution. However, in spread-spectrum MRI each single coil can be driven independently, leading to a much higher flexibility and degrees of freedom in possible modulation patterns as compared to only quadratically varying fields used in O-space or FRONSAC. This also offers the unique possibility to adapt local modulation fields to the underlying k-space trajectory generated by the linear imaging gradients with the goal to optimize the sampled k-space density across k-space. Independent local field modulation also allows optimization of combined acceleration with parallel imaging.

The achievable acceleration factor with spread-spectrum MRI depends on the field strength that is produced by the local modulation coils, and it varies along the spatial position along the local coil arrangement. As depicted in Figure 2, the strongest field modulation is along the dotted white line positioned along the coil windings perpendicular to the main static magnetic field B_0 in z-direction. Thus, possible acceleration factors significantly depend on the position and orientation of the imaging slice, and even no acceleration is possible for slices centered between opposing coil windings, i.e. where local fields from the coils cancel each other. Therefore, imaging acceleration is closely linked to the arrangement and number of local coils as well as to the spatial position and orientation of the imaging slice or position of the imaging volume for 3D imaging. This, however, also offers the possibility to design dedicated coil arrangements adapted to the specific requirements of certain imaging applications. As for any sequence, SNR is proportional to the square root of the total acquisition time (or sum of acquired ADC intervals) plus potential penalties for ill-conditioned problems reflected in an increased g-factor or NMSE. Therefore, presented acceleration factors of 6 or 8 shown in Figure 4 have a reduced SNR of $\sqrt{6}$ or $\sqrt{8}$, respectively.

Rapidly changed magnetic fields may stimulate nerves or muscles by inducing electric fields. The threshold for peripheral nerve stimulation is on the order of 50 T/s (rheobase, infinite duration of magnetic field change dB/dt).²² Assuming a local magnetic field modulation of 20 mT/m at 10 kHz to achieve high acceleration factors corresponds to a magnetic field change of about 40 T/s at a distance of 10 cm from the center of the specific coil arrangement shown in Figure 2A. Application of these rapidly changing fields thus seems to be feasible for human brain studies and is assumed to be even less problematic if smaller diameters of the B_0 arrangement can be used as in case of limb imaging.

This study was restricted to 2D imaging in combination with an underlying Cartesian k-space sampling, and the use

of only one receiver coil. Furthermore, all modulation coils were mounted at identical z-position on the cylinder. A further direction is thus to explore the potential of an array of local modulation coils distributed along the z and angular direction, similar to what is used for local shimming using matrix coils.²³ This will increase the flexibility of modulation patterns along all principal axes, which is mandatory for accelerated 3D imaging. Similarly, other k-space trajectories such as spirals or radial sampling combined with temporally varying local modulation patterns might further increase acquisition speed (see also O-SPACE reference). Furthermore, spread-spectrum MRI can be combined with parallel imaging, which is particularly advantageous if the overlap of individual radio frequency receive coil sensitivities and current coil field profiles is minimized. In case of spatially separated radio frequency coil and current coil profiles, individual acceleration factors generated with both spread-spectrum MRI and parallel imaging might be used independently for acquisition acceleration, resulting in a multiplication of acceleration factors.

ACKNOWLEDGMENTS

This work was supported by the Max Planck Society and the German research foundation (Reinhart Koselleck Project, DFG SCHE 658/12).

AUTHOR CONTRIBUTIONS

Klaus Scheffler, Alexander Loktyushin, and Jonas Bause contributed equally to this work.

ORCID

Klaus Scheffler  <https://orcid.org/0000-0001-6316-8773>

Ali Aghaeifar  <https://orcid.org/0000-0002-6964-0992>

REFERENCES

- Haase A, Frahm J, Matthaei D, Hänicke W, Merboldt KD. FLASH imaging: rapid NMR imaging using low flip-angle pulses. 1986. *J Magn Reson*. 2011;213:533–41.
- Mansfield P. Multi-planar image formation using NMR spin echoes. *J Phys C: Solid State Phys*. 1977;10:L55–L58.
- Sodickson DK, Manning WM. Simultaneous acquisition of spatial harmonics (SMASH): fast imaging with radiofrequency coil arrays. *Magn Reson Med*. 1997;38:591–603.
- Pruessmann KP, Weiger M, Scheidegger MB, Boesiger P. SENSE: sensitivity encoding for fast MRI. *Magn Reson Med*. 1999;42:952–962.
- Griswold MA, Jakob PM, Heidemann RM, et al. Generalized auto-calibrating partially parallel acquisitions (GRAPPA). *Magn Reson Med*. 2002;47:1202–1210.
- Hennig J, Zhong K, Speck O. MR-Encephalography: fast multi-channel monitoring of brain physiology with magnetic resonance. *Neuroimage*. 2007 Jan 1;34:212–9.

7. Madore B, Glover GH, Pelc NJ. Unaliasing by fourier-encoding the overlaps using the temporal dimension (UNFOLD), applied to cardiac imaging and fMRI. *Magn Reson Med.* 1999;42:813–828.
8. Parrish T, Hu X. Continuous update with random encoding (CURE): a new strategy for dynamic imaging. *Magn Reson Med.* 1995;33:326–336.
9. Tsao J, Boesiger P, Pruessmann KP. k-tBLAST and k-t SENSE: dynamic MRI with high frame rate exploiting spatiotemporal correlations. *Magn Reson Med.* 2003;50:1031–1042.
10. Lustig M, Donoho DL, Pauly JM. Sparse MRI: the application of compressed sensing for rapid MR imaging. *Magn Reson Med.* 2007;58:1182–1195.
11. Hennig J, Welz AM, Schultz G, et al. Parallel imaging in non-bijective, curvilinear magnetic field gradients: a concept study. *Magma.* 2008;21:5–14.
12. Wang H, Tam LK, Constable RT, Galiana G. Fast rotary nonlinear spatial acquisition (FRONSAC) imaging. *Magn Reson Med.* 2016;75:1154–1165.
13. Stockmann JP, Ciris PA, Galiana G, Tam LK, Constable RT. O-space images: highly efficient parallel imaging using second-order nonlinear fields as encoding gradients with no phase encoding. *Magn Reson Med.* 2010;64:447–56.
14. Wang H, Tam L, Kopanoglua E, Peters DC, Constable RT, Galiana G. O-space with high resolution readouts outperforms radial imaging. *Magn Reson Imaging.* 2017;37:107–115.
15. Moriguchi H, Duerk JL. Bunched phase encoding (BPE): a new fast data acquisition method in MRI. *Magn Reson Med.* 2006;55:633–648.
16. Breuer FA, Moriguchi H, Seiberlich N, et al. Zigzag sampling for improved parallel imaging. *Magn Reson Med.* 2008;60:474–478.
17. Bilgic B, Gagoski BA, Cauley SF, et al. Wave-CAIPI for highly accelerated 3D imaging. *Magn Reson Med.* 2006;73:2152–2162.
18. Breuer F, Blaimer M, Heidemann RM, Mueller MF, Griswold MA, Jakob PM. Controlled aliasing in parallel imaging results in higher acceleration (CAIPIRINHA) for multi-slice imaging. *Magn Reson Med.* 2005;53:684–691.
19. Hoffmann J, Shajan G, Budde J, Scheffler K, Pohmann R. Human brain imaging at 9.4 T using a tunable patch antenna for transmission. *Magn Reson Med.* 2013;69:1494–1500.
20. Ulyanov D, Vedaldi A, Lempitsky V. Deep image prior. 2017. arXiv preprint arXiv:1711.10925.
21. Robson PM, Grant AK, Madhuranthakam AJ, Lattanzi R, Sodickson DK, McKenzie CA. Comprehensive quantification of signal-to-noise ratio and g-factor for image-based and k-space-based parallel imaging reconstructions. *Magn Reson Med.* 2008;60:895–907.
22. Schaefer DJ, Bourland JD, Nyenhuis JA. Review of Patient safety in time-varying gradient fields. *J Magn Reson Imaging.* 2000;12:20–29.
23. Juchem C, Nixon TW, McIntyre S, Rothman DL, De Graaf RA. Magnetic field modeling with a set of individual localized coils. *J Magn Reson.* 2010;204:281–289.

How to cite this article: Scheffler K, Loktyushin A, Bause J, Aghaeifar A, Steffen T, Schölkopf B. Spread-spectrum magnetic resonance imaging. *Magn Reson Med.* 2019;82:877–885. <https://doi.org/10.1002/mrm.27766>